



HAL
open science

INVESTIGATION OF LOCAL AND INSTANTANEOUS PRESSURE IN A DYNAMIC FILTRATION MODULE (RVF TECHNOLOGY) TO INTENSIFY INDUSTRIAL MEMBRANE BIO-REACTOR (MBR)

Ming Cheng

► **To cite this version:**

Ming Cheng. INVESTIGATION OF LOCAL AND INSTANTANEOUS PRESSURE IN A DYNAMIC FILTRATION MODULE (RVF TECHNOLOGY) TO INTENSIFY INDUSTRIAL MEMBRANE BIO-REACTOR (MBR). Fluid mechanics [physics.class-ph]. INSA de Toulouse, 2022. English. NNT : 2022ISAT0008 . tel-03723893

HAL Id: tel-03723893

<https://theses.hal.science/tel-03723893>

Submitted on 15 Jul 2022

HAL is a multi-disciplinary open access archive for the deposit and dissemination of scientific research documents, whether they are published or not. The documents may come from teaching and research institutions in France or abroad, or from public or private research centers.

L'archive ouverte pluridisciplinaire **HAL**, est destinée au dépôt et à la diffusion de documents scientifiques de niveau recherche, publiés ou non, émanant des établissements d'enseignement et de recherche français ou étrangers, des laboratoires publics ou privés.



THÈSE

En vue de l'obtention du
DOCTORAT DE L'UNIVERSITÉ DE TOULOUSE
Délivré par l'Institut National des Sciences Appliquées de
Toulouse

Présentée et soutenue par
Ming CHENG

Le 5 avril 2022

**ÉTUDE DE LA PRESSION LOCALE ET INSTANTANÉE DANS UN
MODULE DE FILTRATION DYNAMIQUE (TECHNOLOGIE RVF) POUR
L'INTENSIFICATION DES BIOREACTEURS MEMBRANAIRES
INDUSTRIELS (BRM)**

Ecole doctorale : **SEVAB - Sciences Ecologiques, Vétérinaires, Agronomiques et
Bioingenieries**

Spécialité : **Ingénieries microbienne et enzymatique**

Unité de recherche :
TBI - Toulouse Biotechnology Institute, Bio & Chemical Engineering

Thèse dirigée par
Luc FILLAUDEAU et Philippe SCHMITZ

Jury

M. Ulrich KRUHNE, Rapporteur
M. Fethi ALOUI, Rapporteur
M. Luhui DING, Examineur
M. Alain LINE, Examineur
Mme Xiaomin XIE, Examinatrice
M. Luc FILLAUDEAU, Directeur de thèse
M. Philippe SCHMITZ, Co-directeur de thèse

THÈSE

En vue de l'obtention du

DOCTORAT DE L'UNIVERSITÉ DE TOULOUSE

Délivré par l'Institut National des Sciences Appliquées de Toulouse

Présentée et soutenue par

Ming CHENG

Le 5 April 2022

INVESTIGATION OF LOCAL AND INSTANTANEOUS PRESSURE IN A DYNAMIC
FILTRATION MODULE (RVF TECHNOLOGY) TO INTENSIFY INDUSTRIAL
MEMBRANE BIO-REACTOR (MBR)

ÉTUDE DE LA PRESSION LOCALE ET INSTANTANEE DANS UN MODULE DE
FILTRATION DYNAMIQUE (TECHNOLOGIE RVF) POUR L'INTENSIFICATION DES
BIOREACTEURS MEMBRANAIRES INDUSTRIELS (BRM)

Ecole doctorale: SEVAB - Sciences Ecologiques, Vétérinaires, Agronomiques et
Bioingenieries

Spécialité: Ingénieries microbienne et enzymatique

Unité de recherche: TBI - Toulouse Biotechnology Institute, Bio & Chemical Engineering

Ulrich KRUHNE (Professeur)	Université de Technologie du Danemark (DTU), PROSYS, Danemark	Rapporteur
Fethi ALOUI (Professeur)	Université Polytechnique Hauts-de-France, INSA Hauts-de-France, LAMIH, France	Rapporteur
Luhui DING (Professeur)	Université de Technologie de Compiègne (UTC), TIMR, France	Examineur
Alain Line (Professeur)	INSA de Toulouse, TBI, France	Examineur
Xiaomin Xie (Docteur)	Guangdong University of Technology et Guangdong Midea White Home Appliance Technology Innovation Centre Co. Ltd, Guangzhou, China	Examinatrice

Directeur(s) de Thèse :

Luc FILLAUDEAU (Directeur de Recherche) - INRAE, TBI, France, Directeur de thèse

Philippe SCHMITZ (Professeur) - INSA de Toulouse, TBI, France, Co-Directeur de thèse

Acknowledgement

This PhD work was carried out in TBI where I have spent three and half years, and it provided me a new insight into the world. Before that, I was not an ambitious person and I didn't even dare to imagine studying abroad. From 2018, a new chapter of my life began at INSA. I can feel that I have become more different, not only from an academic point of view, but also my daily life, which makes me stronger. At this special occasion, I would like to thank those who have been with me during this memorable time.

I would like to thank the financial support from China Scholarship Council (CSC), providing me with such a good opportunity to improve myself; I also thank TBI for offering me an excellent experimental platform; and I am grateful for the good learning environment in the EAD 7 and 8.

I would like to express my most sincere gratitude to my supervisors Luc Fillaudeau and Philippe Schmitz. You have not only broadened my mind to new horizons, but also guided me to refine my PhD project gradually. Your wisdom and kindness will guide me forward in the following work. I also appreciate Alain Line, who have helped me out from the data treatment and give me some new ideas in the experiments. Then, thanks to Claude Le Men for his help in the experimental set-up and data processing. Thanks to all of you for your help from the experiments to thesis writing, and even in my life.

I hope to show my gratitude to the jury members Ulrich Krühne, Fethi Aloui, thank you for spending time to review my manuscript, and the attendance of my PhD defence in the special time. Your comments and valuable advice would be appreciated.

Thanks to Yassim Boukazia and Susana Alonso for their help in my life when I first arrived. I would also like to thank Xiaomin Xie for sharing her experience and for her great contribution in the extensive review.

My kind colleagues also need to be acknowledged, especially Zibin Nan, Mei Mei, Ryma Laifa, Vincent Ngu and Ernest Simon for their company and help in daily life. Thanks to my Chinese friend Fan Chen, Bolin Shen, Zhou Shen, Ao Li, Nao Wu, Tianyi Zhang, Xiaoqian Li, Zhenhang Wu and Ye Tao, who always help me out in a hard time, share their happiness and food with me.

Finally, I would like to express my sincere gratitude to my dear family, especially my parents, for their endless love in the past 29 years. Thanks to my sisters for their encouragement and support. I am very grateful to my girlfriend Nana Su, for sharing the happiness and suffering with me.

Abstract

Dynamic filtration (DF) exhibits superior performances (high permeate flux, fouling limitation) to dead-end and cross-flow filtrations for various applications (water treatment, food engineering, bioprocess engineering). This PhD is devoted to exploring a technology called Rotating and Vibration Filtration (RVF) to get insight into its complex hydrodynamics at global and local scales, to understand and to explain its performances in membrane bioreactor (MBR). The objectives are to propose an exhaustive benchmarking and classification of DF modules, to develop an experimental device for local and instantaneous measurements of the driving force (pressure), then to describe pressure fluctuations using 3 different theoretical approaches, and finally to validate Computational Fluid Dynamics (CFD) simulation in laminar and turbulent regimes.

Combined with previous studies, the investigation of hydrodynamics in laminar and turbulent regimes were furtherly scrutinised to answer new scientific questions. Global, semi-local and local parameters have been characterized during experimental campaigns with Newtonian model fluids and 3 different impellers (Imp 1, 2 and 3). Then, the experimental data were confronted with numerical simulations.

For global approach, friction and power consumption curves were established as a function of mixing and feeding Reynolds number. The calculated mechanical power with the empirical correlation of local shear stress was underestimated. The balance between nominal power and thermal dissipation was investigated. For specific operating conditions (feeding flowrate, mixing rate, viscosity), the increase of temperature (inlet/outlet) superior to 5°C may be damageable for cell culture growth or bioproduction.

For semi-local and local approaches, the local pressure at the membrane surface was measured with a specially designed and instrumented porous substrate. Mean radial pressure and core velocity coefficient (k) were quantified versus flowrate, viscosity, radial position, impeller shape and mixing rate. The instantaneous pressure is decomposed into the time-averaged pressure and its fluctuating quantities using Statistical Analysis (SA), Probability Distribution Function (PDF) and Fast Fourier Transform (FFT). In turbulent regime, The "resonance frequency" of Imp 1 was clearly identified at 21.1 Hz, which induces the maximum pressure fluctuation that cannot be neglected during microfiltration process. Wherein, periodic pressure fluctuations dominate as opposed to random pressure signals. The empirical correlations are established to estimate their intensities as a function of rotation frequency and radial position. In laminar regime, the pressure fluctuation increases with the

mixing rate (0 to 30 Hz), but remains negligible (below 30 mbar) due to the sharp decline of the periodic contribution.

Considering CFD approach, the flow fields were simulated, and compared with local pressure and previous velocity measurements. The flow transition from separated to merged boundary layers is observed with the impeller rotation, which induces the unsteady flow. This technology provides the constructive ideas for optimizing the cell design.

Keywords: Dynamic filtration, Bibliography analysis, Hydrodynamics, Local and instantaneous pressure, Core velocity coefficient, Periodic and random pressure fluctuation, Resonance frequency, Signal reconstruction, CFD.

Résumé

La filtration dynamique (FD) affiche des performances supérieures (rétention, perméation) aux filtrations frontale et tangentielle pour diverses applications (biotechnologies environnementale, agro-industrielle et blanche). Ce doctorat explore l'hydrodynamique complexe aux échelles globale et locale du module «Rotating & Vibrating Filtration» (RVF) pour comprendre et expliquer ses performances dans les bioréacteurs à membrane (MBR). Les objectifs sont de proposer une revue exhaustive et une classification des modules de FD, de développer un dispositif expérimental pour des mesures locales et instantanées de la force motrice (pression), puis de décrire les fluctuations de pression en utilisant 3 approches théoriques, et enfin de valider la simulation numérique des écoulements (CFD) en régimes laminaire et turbulent.

Combinées aux travaux précédentes, l'hydrodynamique du module RVF en régimes laminaire et turbulent a été approfondie pour répondre à de nouvelles questions scientifiques. Les paramètres globaux, semi-locaux et locaux ont été caractérisés au cours de campagnes expérimentales avec des fluides modèles newtoniens et 3 agitateurs différents (Imp 1, 2 et 3).

Pour l'approche globale, des courbes de frottement et de consommation de puissance ont été établies en fonction du nombre de Reynolds d'agitation et de pompage. La puissance mécanique calculée avec la corrélation empirique de la contrainte de cisaillement locale était sous-estimée. L'équilibre entre la puissance nominale et la dissipation thermique a été étudié. Pour des conditions de fonctionnement spécifiques (débit d'alimentation, taux de mélange, viscosité), l'augmentation de la température (entrée/sortie) supérieure à 5°C peut être dommageable pour la croissance microbienne ou la bioproduction.

Pour les approches semi-locale et locale, la pression locale à la surface de la membrane a été mesurée avec un substrat poreux spécialement conçu et instrumenté. La pression radiale moyenne et le coefficient d'entraînement (k) ont été quantifiés en fonction du débit, de la viscosité, de la position radiale, de la forme du mobile et de la vitesse de rotation. La pression instantanée se compose des contributions moyenne et fluctuante qui sont identifiées en utilisant l'analyse statistique (SA), la fonction de distribution de probabilité (PDF) et la transformation rapide de Fourier (FFT). En régime turbulent, la "fréquence de résonance" a été identifiée à 21.1 Hz (Imp 1), ce qui induit la fluctuation de pression maximale qui ne peut être négligée pendant le processus de microfiltration. Dans ce cas, les fluctuations de pression périodiques dominant par opposition aux signaux de pression aléatoires. Des corrélations empiriques sont établies pour estimer leurs intensités en fonction de la fréquence de rotation

et de la position radiale. En régime laminaire, la fluctuation de la pression augmente avec le taux de mélange (0 à 30 Hz), mais reste négligeable (sous 30 mbar) en raison d'une forte diminution de la contribution périodique.

En dernier lieu, la CFD simule les champs d'écoulement pour une comparaison avec les mesures expérimentales de pression locale et de vitesse. La transition d'un écoulement avec des couches limites séparées à fusionnées est observée avec la vitesse de rotation (instabilité). Cette technique fournit des idées constructives pour optimiser la conception de la cellule.

Mots clés: Filtration dynamique, analyse bibliographique, hydrodynamique, pression locale et instantanée, coefficient de vitesse du noyau, fluctuation périodique et aléatoire de la pression, fréquence de résonance, reconstruction du signal, CFD.

List of scientific communications and publications

Journal articles:

- **M. Cheng**, X. Xie, P. Schmitz, L. Fillaudeau, Extensive review about industrial and laboratory dynamic filtration modules: Scientific production, configurations and performances, *Separation and Purification Technology*, 265 (2021) 118293. DOI: 10.1016/j.seppur.2020.118293
- **M. Cheng**, C. Le Men, A. Line, P. Schmitz, L. Fillaudeau, Methodology to investigate instantaneous and local transmembrane pressure within Rotating and Vibrating Filtration (RVF) module, *Separation and Purification Technology*, 272 (2021) 118955. DOI: 10.1016/j.seppur.2021.118955
- **M. Cheng**, C. Le Men, A. Line, P. Schmitz, L. Fillaudeau, Investigation of instantaneous and local transmembrane pressure in rotating and vibrating filtration (RVF) module: Comparison of three impellers, *Separation and Purification Technology*, 280 (2022) 119827. DOI: 10.1016/j.seppur.2021.119827

Conferences:

- **M. Cheng**, C. Le Men, A. Line, P. Schmitz, L. Fillaudeau, Investigation of instantaneous and local transmembrane pressure in RVF dynamic filtration module: comparison of three impellers, 13th ECCE and 6th ECAB, 20-23 September, 2021, online conference, Germany--- Oral presentation
- **M. Cheng**, C. Le Men, A. Line, P. Schmitz, L. Fillaudeau, A new experimental method to explore instantaneous and local transmembrane pressure within dynamic filtration module, 13th ECCE and 6th ECAB, 20-23 September, 2021, online conference, Germany--- Poster

Table of contents

Acknowledgement	I
Abstract	II
Résumé	IV
List of scientific communications and publications	VI
Table of contents	VII
List of figures	XIII
List of tables	XXI
Nomenclature	XXIII
Chapter I: Introduction	1
1 Background	1
2 From scientific progress to scientific questions	3
3 Thesis structure	5
Chapter II: Bibliography	7
1 Introduction	9
1.1 Conventional dead-end filtration and cross-flow filtration	9
1.2 Dynamic filtration	10
2 Scientific production related to dynamic filtration	13
2.1 Quantitative analysis	13
2.1.1 Scope of journals and research areas	14
2.1.2 Research institutions and scientific cooperation	15
2.1.3 Identification of research items	16
2.2 Qualitative analysis	19
2.2.1 Water treatment	20
2.2.2 Food processing	21
2.2.3 Bioprocess engineering	22
3 Specifications of Laboratory and Industrial Dynamic Filtration Modules	23
3.1 Classification of dynamic filtration modules	23

3.2	Rotating systems	29
3.2.1	Rotating membrane modules	29
3.2.1.1	<i>Rotating disk membrane</i>	29
3.2.1.2	<i>Rotating rectangular membrane</i>	31
3.2.1.3	<i>Rotating cylinder membrane</i>	32
3.2.1.4	<i>Rotating hollow fibre</i>	34
3.2.2	Rotating mechanical device module	34
3.2.2.1	<i>Rotating disk</i>	34
3.2.2.2	<i>Rotating impeller</i>	38
3.2.2.3	<i>Rotating cylinder</i>	40
3.2.3	Rotating disk and membrane module	40
3.3	Oscillating system	41
3.3.1	Oscillating filtration cell modules	41
3.3.1.1	<i>Oscillating disk cell</i>	41
3.3.1.2	<i>Oscillating rectangular cell</i>	42
3.3.2	Oscillating membrane module	43
3.3.2.1	<i>Oscillating rectangular membrane</i>	43
3.3.2.2	<i>Oscillating cylinder membrane</i>	45
3.3.2.3	<i>Oscillating hollow fibre membrane</i>	45
3.3.3	Oscillating spacers module	46
3.4	Oscillating and vibrating system	47
4	Characterization of fluid flow in dynamic filtration	49
4.1	Global approaches	49
4.1.1	Dimensionless analysis	49
4.1.1.1	<i>Reynolds number</i>	49
4.1.1.2	<i>Taylor number</i>	51
4.1.1.3	<i>Mass transfer</i>	52
4.1.2	Friction and power consumption curves	53
4.2	Semi-local approaches	54
4.2.1	Radial pressure and core velocity coefficient	54
4.2.1.1	<i>Radial pressure</i>	54
4.2.1.2	<i>Core velocity coefficient</i>	56

4.2.2	Shear rate and shear stress	58
4.2.2.1	<i>Rotating systems</i>	59
4.2.2.2	<i>Oscillating systems</i>	60
4.2.2.3	<i>Oscillating and vibrating systems</i>	62
4.3	Local approaches	62
4.3.1	Local velocity and shear stress	62
4.3.1.1	<i>Particle Image Velocimetry (PIV)/ Particle Tracking Velocimetry (PTV)</i> 63	
4.3.1.2	<i>Molecular Tagging Velocimetry (MTV)</i>	63
4.3.1.3	<i>Laser Doppler Velocimetry (LDV)</i>	63
4.3.1.4	<i>Electrochemical method</i>	63
4.4	Computational Fluid Dynamics (CFD)	64
5	Discussion	65
5.1	Energy demand associated with DF module	65
5.1.1	Mechanical power.....	66
5.1.2	Pumping power.....	67
5.1.3	Specific energy demand.....	68
5.2	Specifications and decision tree for DF application.....	70
Chapter III: Materials and Method		73
1	Experimental set-up and instrumentation	74
1.1	RVF module.....	74
1.2	Impeller configuration	75
1.3	Experimental set-up.....	75
1.4	Data acquisitions	78
2	Experimental strategies and operating conditions	79
2.1	Experimental strategies.....	79
2.2	Operating conditions and fluids	79
2.2.1	Water.....	80
2.2.2	BREOX solutions	80
3	Global investigation: friction and power consumption curve	81

3.1	Raw data	81
3.2	Friction curve	81
3.3	Power consumption curve	82
3.4	Energy balance	82
3.4.1	Thermal power	83
3.4.2	Mechanical power	83
4	Semi-local investigation: core velocity coefficient	84
5	Local investigation: instantaneous pressure	85
5.1	Statistical analysis (SA)	85
5.2	Probability distribution function (PDF)	86
5.3	Fast Fourier transform (FFT)	87
5.4	Reconstruction of PDF with periodic and random functions	87
6	Computational Fluid dynamic (CFD)	89
6.1	Laminar regime	89
6.1.1	Computational domain	89
6.1.2	Model	89
6.1.3	Boundary conditions	90
6.1.4	Mesh	90
6.2	Turbulent regime	91
6.2.1	Computational domain	91
6.2.2	Model	91
6.2.3	Boundary conditions	92
6.2.4	Mesh	92
Chapter IV:	Results and Discussion	94
1	Global investigations	95
1.1	Pumping power	95
1.1.1	Pressure drop	95
1.1.2	Friction curve	95
1.2	Mixing power	97
1.2.1	Net power	97

1.2.2	Power consumption curve	98
1.3	Thermal balance	99
1.3.1	Thermal increase	99
1.3.2	Thermal power	99
1.3.3	Energy balance	100
2	Local pressure at the membrane surface	103
2.1	Mean pressure	103
2.1.1	Mixing pressure	103
2.1.2	Core velocity coefficient	104
2.1.2.1	<i>Impeller geometry</i>	<i>104</i>
2.1.2.2	<i>Flowrate</i>	<i>105</i>
2.1.2.3	<i>Mixing rate</i>	<i>106</i>
2.1.2.4	<i>Rotation direction</i>	<i>106</i>
2.1.2.5	<i>Viscosity</i>	<i>107</i>
2.2	Instantaneous pressure	108
2.2.1	Data convergence	108
2.2.2	Raw data	108
2.2.3	Turbulent regime	110
2.2.3.1	<i>SA</i>	<i>110</i>
2.2.3.2	<i>PDF</i>	<i>113</i>
2.2.3.3	<i>FFT</i>	<i>115</i>
2.2.3.4	<i>Modelling</i>	<i>117</i>
2.2.3.5	<i>Comparison of fluctuating intensity</i>	<i>119</i>
2.2.3.6	<i>Signal reconstruction</i>	<i>120</i>
2.2.4	Laminar regime	121
2.2.4.1	<i>SA</i>	<i>121</i>
2.2.4.2	<i>FFT</i>	<i>122</i>
2.2.4.3	<i>Modelling</i>	<i>122</i>
2.2.5	Viscosity	123
2.2.5.1	<i>SA</i>	<i>123</i>
2.2.5.2	<i>FFT</i>	<i>124</i>
3	CFD	126

3.1	Laminar regime	127
3.1.1	Validation of numerical simulation	127
3.1.2	Local velocity	129
3.1.3	Local pressure	131
3.1.3.1	<i>Mixing rate</i>	132
3.1.3.2	<i>Viscosity</i>	135
3.1.3.3	<i>Blades surface area</i>	135
3.1.3.4	<i>Number of blades</i>	137
3.1.3.5	<i>Impeller/membrane gap</i>	139
3.1.4	Local shear stress	141
3.1.4.1	<i>Mixing rate</i>	141
3.1.4.2	<i>Viscosity</i>	144
3.1.4.3	<i>Blades surface area</i>	145
3.1.4.4	<i>Number of blades</i>	146
3.1.4.5	<i>Impeller/membrane gap</i>	148
3.2	Turbulent regime	149
3.2.1	Validation of numerical simulation	149
3.2.2	Local velocity	150
3.2.3	Local pressure	152
3.2.4	Local shear stress	152
Chapter V: Conclusions and Perspectives		156
1	Scientific context	156
2	Answer to our initial scientific questions	157
3	Our highlights and perspectives	159
References		161
Annexes		180

List of figures

Fig. I.1 Schematic diagram of dynamic filtration module and their investigations.....	1
Fig. I.2 Scientific progress and investigation with RVF module.	4
Fig. II.1 Comparison between Dead-end filtration (DEF), Cross-flow filtration (CFF) and dynamic filtration (DF).	10
Fig. II.2 Number of publications and citations per year (Source: Core Collection-WoS (Thomson-Reuter), period: 1991 to 2020).....	14
Fig. II.3 Institution's cooperation network.	16
Fig. II.4 Keywords co-occurrence network.	17
Fig. II.5 Distribution map of keywords and nodes time-zone associated with DF.....	19
Fig. II.6 Application fields and filtration types associated with dynamic filtration.	20
Fig. II.7 Friction curve established with RVF lab-scale module [6].....	54
Fig. II.8 Power consumption curve established with RVF lab-scale module [6].....	54
Fig. II.9 Determination of hydrodynamic performances, evolution of the radial pressure distribution versus the radius and the rotational speed [6]	56
Fig. II.10 Evolution of core velocity coefficient, $K\theta$ as a function of gap-to-radius ratio, z/R_m . Values are reported from literature for DF modules using confined rotating impeller close to the membrane and established under laminar or turbulent regimes [8].....	58
Fig. II.11 Filtration modes, (a). Single-pass continuous filtration (b). Continuous filtration with partial retentate recycle (Feed & Bleed).....	66
Fig. II.12 Main criteria and knowledge gap in DF application.....	71
Fig. III.1 Schematic diagram of Rotating and Vibrating Filtration module. (a) RVF module; (b) one dismantled filtration cell; (c) and (d) home designed and instrumented porous substrate for local pressure measurements; (e) configuration of filtration cell.....	74
Fig. III.2 Impeller configuration.	75
Fig. III.3 Experimental set-up.....	76
Fig. III.4 Global measurement with water at 300 L/h and 40 Hz.	81
Fig. III.5 The spectrum of instantaneous pressure and data treatment. (a) instantaneous and mean pressure; (b) fluctuating pressure and its standard deviation; (c) probability analysis at 5 and 20 Hz; (d) fluctuating pressure on frequency domain at 20 Hz.	85
Fig. III.6 PDF at 20 Hz. Model reconstruction of PDF with periodic and random functions.	88
Fig. III.7 Schematic of RVF cell. (a) is the top view and (b) is the side view.	90

Fig. III.8 Mesh geometry	91
Fig. III.9 Mesh geometry. (a) 1/36 of rotating disk and (b) 1/3 of rotating impeller.	92
Fig. IV.1 The pressure drop of the RVF module as a function of the mixing rate. (a) the pressure drop for different flowrate (Q_F : 50-300 L/h); (b) the pressure drop for different viscosity (μ : 0.001-0.6 Pa.s).	95
Fig. IV.2 Euler number with mixing versus feeding (a) and mixing (b) conditions, respectively.	96
Fig. IV.3 Euler number without mixing versus feeding condition (0.001-0.6 Pa.s for Imp 1, 0.001 Pa.s for Imp 2 and 3).	96
Fig. IV.4 Friction curve for different impeller configuration. (a) Imp 1 (μ : 0.001-0.6 Pa.s), (b) Imp 2 ($\mu=0.001$ Pa.s) and (c) Imp 3 ($\mu=0.001$ Pa.s).	97
Fig. IV.5 Net power for Imp 1 as a function of mixing rate. (a) turbulent regime ($\mu=0.001$, 0.01 Pa.s); (b) laminar regime ($\mu=0.05$, 0.2, 0.6 Pa.s).	98
Fig. IV.6 Power consumption curves for three impellers from laminar to turbulent regime. ...	98
Fig. IV.7 Thermal increase of the fluid in the RVF as a function of mixing rate. (a) Different flowrate (water) for Imp 1 and 100 L/h for Imp 2 and 3; (b) different fluid (μ : 0.001-0.6 Pa.s) for Imp 1.	99
Fig. IV.8 Thermal dissipation in the RVF as a function of mixing rate for Imp 1. (a) Different flowrate (water, μ : 0.001 Pa.s, Q_F : 50-300 L/h,) and impeller; (b) different flowrate (Q_F : 12-200 L/h) and viscosity (BREOX solution, μ : 0.01-0.6 Pa.s).	100
Fig. IV.9 Comparison of thermal dissipation and mechanical power as a function of net power for Imp 1. (a) turbulent regime ($\mu=0.001$ Pa.s, N : 0-50 Hz) (b) laminar regime ($\mu=0.6$ Pa.s, N : 0-30 Hz).	101
Fig. IV.10 Mixing pressure as a function of mixing rate and radius for three impellers. (a) Imp 1, (b) Imp 2 and (c) Imp 3. Operating conditions: $\mu=0.001$ Pa.s, N : 0-50 Hz, $Q_F=50$ L/h.	103
Fig. IV.11 Mixing pressure as a function of mixing rate at R5. (a) turbulent regime (μ : 0.001, 0.01 Pa.s, N : 0-50 Hz, Q_F : 50-300 L/h, Imp 1, r : 53.9 mm); (b) laminar regime (μ : 0.05, 0.2, 0.6 Pa.s, N : 0-40 Hz, Q_F : 12-130 L/h, Imp 1, r : 53.9 mm).	104
Fig. IV.12 Mean core velocity coefficient for three impellers. (a) Imp 1, (b) Imp 2 and (c) Imp 3. Operating conditions: water, μ : 0.001 Pa.s, N : 0-50 Hz, Q_F : 50-300 L/h, r : R1-R8.	104
Fig. IV.13 Core velocity coefficient for different flowrates. (a) Imp 1, (b) Imp 2 and (c) Imp 3. Operating conditions: water, μ : 0.001 Pa.s, N : 0-50 Hz, Q_F : 50-300 L/h, r : R1-R8.	105
Fig. IV.14 Core velocity coefficient for different mixing rates. (a) Imp 1, (b) Imp 2 and (c) Imp 3. Operating conditions: water, μ : 0.001 Pa.s, N : 0-50 Hz, Q_F : 50 L/h, r : R1-R8.	106

Fig. IV.15 Core velocity coefficient for the different rotation directions. Operating conditions: water, μ : 0.001 Pa.s, N: 0-50 Hz, $Q_F=50$ L/h, r: R2, R4, R5, R7.....	107
Fig. IV.16 Core velocity coefficient of different fluids. Operating conditions: μ : 0.001-0.6 Pa.s, N: 0-50 Hz, Q_F : 12-50 L/h, r: R2, R4, R5, R7.	108
Fig. IV.17 Statistical convergence of raw data.....	108
Fig. IV.18 Raw data analysis for three impellers with water. (a), (b) and (c) are the evolution of instantaneous pressure versus mixing rate for three impellers at R6; (d), (e) and (f) are the evolution of instantaneous pressure versus local radius for three impellers at 20 Hz.	109
Fig. IV.19 Raw data analysis for different fluids with Imp 1. (a), (b) (c) and (d) are the evolution of instantaneous pressure at R6 and mixing rate of 10, 20, 30 and 50 Hz, respectively.	110
Fig. IV.20 Standard deviation of instantaneous pressure for Imp 1 at different conditions (flowrates, mixing rates and back pressures) with water.	111
Fig. IV.21 Statistical Analysis. (a), (b) and (c) are the evolution of standard deviation versus mixing rate for three impellers; (d), (e) and (f) are the coefficient of variation versus mixing rate for three impellers.	112
Fig. IV.22 High order items distribution. (a), (b) and (c) are the skewness distribution for three impellers; (d), (e) and (f) are the flatness distribution for three impellers. The dashed line indicates the S and F in a normal distribution.....	113
Fig. IV.23 PDF at different conditions. (a), (b) and (c) are the PDF versus mixing rate for three impellers; (d), (e) and (f) are the PDF versus radius for three impellers.....	114
Fig. IV.24 PDF analysis for Imp 1. (a) the probability distribution of fluctuating pressure at R6; (b) the evolution of PDF width (peak-to-peak/2) versus mixing rate.	115
Fig. IV.25 Frequency domain analysis with FFT at 20 Hz. (a), (d), (g) and (j) are Imp 1; (b), (e), (h) and (k) are Imp 2; (c), (f), (i) and (l) are Imp 3.	116
Fig. IV.26 Cumulative amplitudes at R6. (a) Imp 1; (b) Imp 2; (c) Imp 3.....	117
Fig. IV.27 Total energy input I_P+I_R (a, b, c) and periodic contribution $I_P/(I_P+I_R)$ (d, e, f) as a function of mixing rate and radius for Imp 1, Imp 2 and Imp 3, respectively.	118
Fig. IV.28 Fluctuating intensities for Imp 1 as a function of mixing rate and radius. (a) periodic intensity; (b) random intensity.	119
Fig. IV.29 The evolution of pressure fluctuations (standard deviation, peak-to-peak/2, amplitude from FFT at 3N and total energy from modelling) as a function of mixing rate. .	120
Fig. IV.30 Signal reconstruction of instantaneous pressure with empirical correlations (continuous and fluctuating components at R6). Dots and lines correspond to the	

experimental and reconstructed signal, respectively.....	121
Fig. IV.31 Standard deviation of pressure fluctuation at different mixing rates and radii.....	122
Fig. IV.32 Evolution of cumulative amplitude from FFT versus mixing rate.	122
Fig. IV.33 Spectrum of total energy input and periodic contribution as a function of mixing rate and radius.	123
Fig. IV.34 Viscous effect on the standard deviation of pressure fluctuation. Operating conditions: μ : 0.001-0.6 Pa.s, N: 0-30 Hz, r: R6 and R8.	124
Fig. IV.35 Viscous effect on the amplitude at 3N of pressure fluctuation. Operating conditions: μ : 0.001-0.6 Pa.s, N: 0-30 Hz, r: R6 and R8.	124
Fig. IV.36 Explorations and actions in CFD approach within RVF module (L: laminar regime, T: turbulent regime)	126
Fig. IV.37 Horizontal velocity profile at z-direction and r=45 mm for PIV measurement and CFD simulation. Operating conditions: μ : 0.81 Pa.s, N: 2 Hz, Q_F : 45 L/h.....	128
Fig. IV.38 Comparison of pressure profile for experimental results and numerical simulation. (a) Mixing pressure as a function of mixing rate; (b) pressure fluctuation for different mixing rates at R6. Operating conditions: μ : 0.18 Pa.s, N: 0-30 Hz, Q_F : 25 L/h. Dots are experimental data and curves show CFD simulation.....	129
Fig. IV.39 Velocity field in the filtration cell. Operating conditions: μ : 0.2 Pa.s, N: 20 Hz, Q_F : 25 L/h.....	130
Fig. IV.40 Tangential velocity along the z-direction. (a) is the velocity distribution at different positions; (b) and (c) are the velocity distribution for different mixing rates at A and C, respectively. A (between two blades), B (leading edge), C (on the blade) and D (trailing edge) with a radius of 60 mm; E, F and G with a radius of 50, 40 and 30 mm, respectively. Operating conditions: μ : 0.2 Pa.s, N: 20 Hz, Q_F : 25 L/h.	130
Fig. IV.41 Tangential velocity along the z-direction. (a) and (b) are velocity distribution at different positions for Imp 1; (c) is the velocity distribution for the full disk. Operating conditions: μ : 0.05-0.6 Pa.s, N: 20 Hz, Q_F : 25 L/h, Imp1 and full disk.	131
Fig. IV.42 Pressure field for different mixing rates with Imp 1. (a), (b) and (c) are on the membrane surface; (d), (e) and (f) are the cross-section with 0° to x-axis (black dashed line); (g), (h) and (i) are the cross-section with 60° to x-axis (red dashed line). Operating conditions: μ : 0.2 Pa.s, N: 10, 20 and 30 Hz.	132
Fig. IV.43 Pressure distribution as a function of mixing rate. (a) and (b) are the mixing pressure; (c) and (d) are the standard deviation of pressure fluctuation. Operating conditions: μ : 0.2 Pa.s, N: 0-50 Hz, r: R2, R4, R6 and R8, Imp 1 for (a) and (c), Imp 4-60° (three blades)	

for (b) and (d).....	133
Fig. IV.44 Pressure distribution as a function of radius. (a) and (b) are the mixing pressure; (c) and (d) are standard deviation of pressure fluctuation. Operating conditions: μ : 0.2 Pa.s, N: 0-50 Hz, r: 25-67.5 mm, Imp 1 for (a) and (c), Imp 4-60° (three blades) for (b) and (d).	134
Fig. IV.45 Core velocity coefficient for different radii. Operating conditions: μ : 0.2 Pa.s, N: 0-50 Hz, Q_F : 25 L/h, r: R1-R8.....	134
Fig. IV.46 Pressure distribution as a function of viscosity. (a) is the mixing pressure; (b) is the standard deviation of pressure fluctuation. Operating conditions: μ : 0.05-0.6 Pa.s, N: 10-50 Hz, r: R6.....	135
Fig. IV.47 Pressure field at the membrane surface for different impeller geometries. (a) is the geometry 30° blade, which angle length varies from 0 to 120°; from (b) to (h) are the three blades impeller with the increased surface area from 0 to 90°; (i) is the full disk. Operating conditions: μ : 0.2 Pa.s, N: 20 Hz.	136
Fig. IV.48 Pressure distribution with the increased angle of blades. (a) is the mixing pressure; (b) is the standard deviation of pressure fluctuation. Operating conditions: μ : 0.2 Pa.s, N: 0-30 Hz, r: R6.....	137
Fig. IV.49 Evolution of pressure fluctuation for different kinds of blades. Operating conditions: μ : 0.2 Pa.s, N: 20 Hz, r: R6.	137
Fig. IV.50 Pressure field at the membrane surface for different impeller geometries. From (a) to (e) are the impeller with the increased number of blades (30°) from 2 to 8. Operating conditions: μ : 0.2 Pa.s, N: 20 Hz.	138
Fig. IV.51 Pressure distribution with the increased number of blades. (a) is the mixing pressure; (b) is the standard deviation of pressure fluctuation. Operating conditions: μ : 0.2 Pa.s, N: 0-30 Hz, r: R6.....	138
Fig. IV.52 Evolution of pressure fluctuation for different numbers of blades. Operating conditions: μ : 0.2 Pa.s, N: 20 Hz, r: R6.	139
Fig. IV.53 Pressure field at the membrane surface with different gaps between impeller and membrane. (a) is the illustration of cell geometry; from (b) to (h) are the increased gap from 2 to 10 mm. Operating conditions: μ : 0.2 Pa.s, N: 20 Hz.	140
Fig. IV.54 Pressure distribution with the different gaps. (a) is the mixing pressure; (b) is the standard deviation of pressure fluctuation. Operating conditions: μ : 0.2 Pa.s, N: 0-30 Hz, r: R6.....	141
Fig. IV.55 Shear stress field for different mixing rates with Imp 1. (a), (b) and (c) are on the membrane surface; (d), (e) and (f) are the cross-section with 0° to x-axis (black dashed line);	

(g), (h) and (i) are the cross-section with 60° to x-axis (red dashed line). Operating conditions: μ : 0.2 Pa.s, N: 10, 20 and 30 Hz.	142
Fig. IV.56 Shear stress distribution as a function of mixing rate. (a) and (b) are the mean shear stress; (c) and (d) are the standard deviation of local shear stress. Operating conditions: μ : 0.2 Pa.s, N: 0-50 Hz, Imp 1 for (a) and (c), Imp 4- 60° (three blades) for (b) and (d).	143
Fig. IV.57 Shear stress distribution as a function of radius. (a) and (b) are the mean shear stress; (c) and (d) are the standard deviation of local shear stress. Operating conditions: μ : 0.2 Pa.s, N: 0-50 Hz, Imp 1 for (a) and (c), Imp 4- 60° (three blades) for (b) and (d).	144
Fig. IV.58 Shear stress distribution as a function of viscosity. (a) is the mean shear stress; (b) is the standard deviation of local shear stress. Operating conditions: μ : 0.05-0.6 Pa.s, N: 0-50 Hz, r: R6.	144
Fig. IV.59 Estimation of local shear stress at the membrane surface. Operating conditions: μ : 0.05-0.6 Pa.s, N: 0-50 Hz, r: R1-R8.	145
Fig. IV.60 Shear stress field at the membrane surface for different impeller geometries. (a) is the geometry of a blade; from (b) to (h) are the three blades impeller with the increased surface area from 0 to 90° ; (i) is the full disk. Operating conditions: μ : 0.2 Pa.s, N: 20 Hz.	146
Fig. IV.61 Shear stress distribution with the increased angle of blades. (a) is the mean shear stress; (b) is the standard deviation of local shear stress. Operating conditions: μ : 0.2 Pa.s, N: 0-30 Hz, r: R6.	146
Fig. IV.62 Shear stress field at the membrane surface for different impeller geometries. From (a) to (e) are the impeller with the increased number of blades (30°) from 2 to 8. Operating conditions: $\mu=0.2$ Pa.s, N=20 Hz.	147
Fig. IV.63 Shear stress distribution with different numbers of blades. (a) is the mean shear stress; (b) is the standard deviation of local shear stress. Operating conditions: $\mu=0.2$ Pa.s, N: 0-30 Hz, r: R6.	147
Fig. IV.64 Shear stress field at the membrane surface with different gaps between impeller and membrane. (a) is the illustration of cell geometry; from (b) to (h) are the increased gap from 2 to 10 mm. Operating conditions: $\mu=0.2$ Pa.s, N=20 Hz.	148
Fig. IV.65 Shear stress distribution with different gaps. (a) is the mean shear stress; (b) is the standard deviation of local shear stress. Operating conditions: $\mu=0.2$ Pa.s, N: 0-30 Hz, r: R6.	148
Fig. IV.66 Angular velocity profile at z direction. (a) $s/R=0.08$, $Re=10^6$, (b) $s/R=0.127$, $Re=1.6 \times 10^6$. Operating conditions: μ : 0.001 Pa.s, N: 35/56 Hz, Q_F : 0 L/h.	149
Fig. IV.67 Velocity field in the filtration cell. Operating conditions: 60° three-blade impeller,	

μ : 0.001 Pa.s, N: 20 Hz, Q_F : 50 L/h.....	150
Fig. IV.68 Tangential velocity along the z-direction. (a) velocity distribution at different positions (radius, angle) for 60° three-blade impeller; (b) velocity distribution at different radii for the disk. A (between two blades), B (leading edge), C (on the blade) and D (trailing edge) with a radius of 60 mm; E, F and G with a radius of 50, 40 and 30 mm, respectively. Operating conditions: μ : 0.001 Pa.s, N: 20 Hz, Q_F : 50 L/h.	151
Fig. IV.69 Tangential velocity along the z-direction. (a) velocity distribution between the membrane and the blade; (b) velocity distribution between two membranes. Operating conditions: μ : 0.001 Pa.s, N: 10, 20, 50 Hz, Q_F : 50 L/h.	151
Fig. IV.70 Pressure distribution as a function of radius. (a) is the mixing pressure, (b) is the standard deviation of pressure fluctuation. Operating conditions: μ : 0.001 Pa.s, N: 10, 20, 50 Hz, Q_F : 50 L/h.....	152
Fig. IV.71 Shear stress field at the membrane surface. Operating conditions: μ : 0.001 Pa.s, N: 20 Hz, Q_F : 50 L/h.....	153
Fig. IV.72 Shear stress distribution as a function of radius. (a) is the mean shear stress, (b) is the standard deviation of shear stress fluctuation. Operating conditions: μ : 0.001 Pa.s, N: 10, 20, 50 Hz, Q_F : 50 L/h.....	153
Fig. IV.73 Estimation of local shear stress at the membrane surface. Operating conditions: μ : 0.001 Pa.s, N: 10, 20, 50 Hz, Q_F : 50 L/h.	153

Annexes

Fig. S 1 Impeller geometry with difference surface area. No blades and full disk indicate 0 and 120°, other three impellers equip with three blades and the angle from 20 to 90°.....	180
Fig. S 2 Impeller geometry with difference number of blades. The impellers equip with 2 to 8 blades (30°).....	180
Fig. S 3 The comparison of velocity, pressure and shear stress for different meshes. (a) tangential velocity along the z-axis; (b) and (c) are the pressure and the shear stress along the θ direction.	181
Fig. S 4 Core velocity coefficient for different flowrates. Operating conditions: water, μ =0.001 Pa.s, N: 0-50 Hz, Q_F : 50-300 L/h, r: R1-R8.....	181
Fig. S 5 Local pressure as a function of back pressure. Operating conditions: μ =0.2 Pa.s, N: 20 Hz, r: R6, Q_F =25 L/h.....	182
Fig. S 6 Local pressure as a function of feeding flowrate. Operating conditions: μ :0.2 and 0.6	

Pa.s, N: 20 Hz, r: R6, Q_F: 6-183 L/h.....182

Fig. S 7 Structured mesh of rotating disk system (10° of the disk). (a) is the formation of structured mesh, (b) and (c) are the poor (boundary layer 1) and high (boundary layer 1 and 2) quality of mesh, respectively.....183

List of tables

Table II.1 Top 5 most productive journals considering the number of articles and citations (source: WoS).....	14
Table II.2 Top 9 most productive institutions (source: WoS).	15
Table II.3 Clusters of research hotspots.	17
Table II.4 Top 10 keywords with the strongest citation bursts.	18
Table II.5 Classification of DF modules according to the movement and shape.....	23
Table II.6 Classification and specification of DF modules (d: membrane diameter, S: membrane surface area, N/F: maximum rotating, vibrating and/or oscillating speed/ frequency, A: amplitude, displacement or vibrating angle, TMP: maximum operating transmembrane pressure).....	24
Table II.7 Dimensionless numbers used to describe hydrodynamic within Dynamic Filtration device (d: diameter, u: velocity, Q: flowrate, r: radius, d _h : hydraulic diameter, r _h : hydraulic radius, d _o : outer diameter; d _i : inner diameter, u _z , axial flow velocity, N: mixing rate, d _m : rotor diameter, k: core velocity coefficient, ω: angular velocity, h: rotor height, α: inclination angle of conical rotor, s: characteristic length scale, F: oscillating/ vibrating frequency, H: vertical distance).	50
Table II.8 Four flow pattern in rotating system.	51
Table II.9 Core velocity coefficient of different DF filters.....	57
Table II.10 Shear rate of four flow regimes in a rotation system.	59
Table II.11 Specific energy demand in different modules.	69
Table II.12 Resume of available data about hydrodynamics and applications with the different types of DF modules.	72
Table III.1 Radial distribution of pressure taps at the membrane surface (porous substrate)..	74
Table III.2 All sensors used in the experiment.....	77
Table III.3 All equipment used in the experiment.....	77
Table III.4 Data acquisitions in the experiments.	79
Table III.5 Operating conditions for global and local pressure measurements.....	79
Table III.6 Signal decomposition into periodic and random contributions (P _P (t): periodic signal, P _R (t): random signal, A: amplitude, f: frequency, φ: phase, σ: standard deviation, E _P (x) and E _R (x) are the PDF.).....	87
Table IV.1 Established friction curves for three impellers.....	97

Table IV.2 Numerical coefficient for the thermal dissipation based on the equation: $\Phi T = aN^2$.	100
Table IV.3 Information on the data treatment.	119
Table IV.4 Signal reconstruction for Imp 1 at R6, with the value of the two parameters to estimate the instantaneous pressure. A and σ are calculated from the convolution of PDF functions.	121
Table IV.5 Validation of CFD simulation based on velocity and pressure field.	127

Annexes

Table S 1 Effect of blade surface area on core velocity coefficient.	183
Table S 2 Effect of blade number on core velocity coefficient.	184
Table S 3 Effect of impeller/membrane gap on core velocity coefficient.	184

Nomenclature

Abbreviation

AVM	axial vibration membrane
BDF	biodruck-filter
BOD	biological oxygen demand
BSA	bovine serum albumin
CAPEX	capital expenditure
CFD	computational fluid dynamics
CFF	cross-flow filtration
CFD	computational fluid dynamics
COD	chemical oxygen demand
Cond	conductivity
CP	concentration polarization
CR	cross rotational
CRD	compact rotating disc filter
CRDM	retentate recycling process
CSAF	controlled shear affinity filtration
CSF	controlled shear filtration
CTF	Couette-Taylor flow
CU	current
DCF	dynamic cross-flow filter
DEF	dead-end filtration
DF	dynamic filtration
DMF	dynamic membrane filter
DP	differential pressure
DRDM	retentate non-recycling process
FFT	fast Fourier transform
FMX	anti-fouling membrane unit
HF	hollow fiber
HSR-MS	high shear rotary membrane system
IREC	Catalonia Institute for Energy Research
ISBM	intermeshed spinning basket membrane
LDA	laser doppler anemometry
LDV	laser doppler velocimetry
LLR	Log-likelihood Ratio
MBR	membrane bioreactors
MF	microfiltration
MMV	magnetically induced membrane vibration
MSD	multi-shaft disk
MSDF	modular span disk filtration
MTV	molecular tagging velocimetry
NF	nanofiltration
OFSM	oscillatory flat surface membrane

OPEX	operational expenditure
PAAS	poly acrylic acid sodium
PDF	probability distribution function
PEG	polyethylene glycol
PES	polyether sulfones
PG	pressure gauge
PR	relative pressure
PVDF	polyvinylidene difluoride
PIV	particle image velocimetry
PMA	copolymer of maleic acid and acrylic acid
PMMA	polymethyl methacrylate
PTFE	Polytetrafluoroethylene
PTV	particle tracking velocimetry
RCF	rotating cross-flow
RDM	rotating disk module
RD-M	rotating disk-membrane
R-HFM	rotating hollow fiber membrane
RO	reverse osmosis
RVF	rotating and vibrating filtration
SA	statistical analysis
SBM	spinning basket membrane
SBR	styrene butadiene rubber
SS	single stirred
SSDF	signal shaft disk filter
SST	Shear Stress Transport
TEN	tension
TMP	transmembrane pressure
UF	ultrafiltration
UHT	ultra-high temperature processing
URV	Rovira Virgili University
USVM	uniform shearing vibration membrane
UTC	University of Technology of Compiègne
VCF	volume concentration factor
VERO	vibration enhanced reverse osmosis
VHM	vibrating hollow fiber microfiltration
VMBR	vibrating membrane bioreactor
VMF	vibrating membrane filtration
VRM	vacuum rotation membrane
VSEP	vibratory shear enhanced processing
WoS	web of science

Latin letter

<i>A</i>	amplitude	m
<i>a, b</i>	numerical constants	/

C	concentration	/
C_p	specific heat capacity	J/(kg.°C)
D	diffusion coefficient	m ² /s
d	diameter	m
d_h	hydraulic diameter	m
d_i	inner diameter	m
d_m	rotor diameter	m
d_o	outer diameter	m
Da	Darcy number	/
E	Specific energy demand	kWh/m ³
Ek	Ekman number	/
Eu	Euler number	/
$E_P(x)$	periodic PDF	mbar ⁻¹
$E_R(x)$	random PDF	mbar ⁻¹
F	oscillating/ vibrating frequency, flatness	Hz
f	velocity factor, friction factor	/
G	gain of the system	/
H	vertical distance	m
h	rotor height	m
I	tension	A
I_P	periodic intensity	mbar
I_R	random intensity	mbar
J	Flux	m/s
J_{SS}	steady-state flux	m/s
K	numerical coefficient	/
k	core velocity coefficient	/
k_m	transfer coefficient	/
L	channel length	m
L_p	permeability	m/(s·Pa)
m	sampling number	/
N	mixing rate	Hz
N_0	intrinsic frequency	Hz
N_p	Power number	/
N_r	resonance frequency	Hz
P	power consumption	W
P_0	pressure without the rotation of impeller	mbar
$P(f)$	pressure at frequency f	mbar
$P(N, r, t)$	instantaneous pressure	mbar
P_M	mechanical power	W
P_P	pumping power	W

P_T	total power	W
P_{in}	inlet pressure	Pa
P_{out}	outlet pressure	Pa
P_p	permeate pressure	Pa
Δp	pressure drop	Pa
ΔP	transmembrane pressure	Pa
ΔP_{ag}	additional pressure	Pa
$\widetilde{P}_P(t)$	periodic signal	mbar
$\widetilde{P}_R(t)$	random signal	mbar
$\bar{P}(N, r)$	mean time pressure	mbar
$\tilde{P}(N, r, t)$	fluctuating pressure	mbar
Q	flowrate	m ³ /s
Q_c	circulation flowrate	m ³ /s
Q_f	feeding flowrate	m ³ /s
Q_p	permeate flowrate	m ³ /s
Q_r	retentate flowrate	m ³ /s
r	radius	m
R_h	hydraulic resistance	m ⁻¹
R_m	rotor radius	m
r_h	hydraulic radius	m
r_i	inner radius	m
r_o	outer radius	m
Re	Reynolds number	/
Re_a	Reynolds number for axial flow in annulus	/
$Re_{feeding}$	Reynolds number for feeding	/
Re_{mixing}	Reynolds number for mixing	/
Re_Q	Reynolds number in the tube	/
Re_r	Reynolds number in rotating system	/
Re_s	Reynolds number for rotating cone	/
Re_v	Reynolds number in oscillating/ vibrating system	/
S	membrane surface area, skewness	m ²
s	characteristic length scale, gap	m
Sh	Sherwood number	/
Sc	Schmidt number	/
T	period, temperature	Hz
t	time	s
Δt	time interval	s
Ta	Taylor number	/
U	current	V

U_{θ}	tangential velocity	m/s
u	velocity	m/s
u_z	axial flow velocity	m/s
\bar{u}	mean velocity of fluid	m/s
ν	kinematic viscosity	m ² /s
ν_0	amplitude of velocity	m
y	gap	m
z	gap between rotor and membrane, or between two cylinders	m

Greek letter

α	inclination angle	°
β	relative standard deviation of pressure	mbar
ϵ	dumping factor	/
σ_P	standard deviation of pressure	mbar
σ_{τ}	standard deviation of shear stress	Pa
φ	phase	°
γ	shear rate	s ⁻¹
γ_{av}	average shear rate	s ⁻¹
γ_{max}	Maximum shear rate	s ⁻¹
γ_R	shear rate at rotor surface	s ⁻¹
γ_S	shear rate at membrane surface	s ⁻¹
δ	limiting layer thickness	m
Δ	minimum cumulative error	/
μ	dynamic viscosity	Pa.s
μ_p	permeate viscosity	Pa.s
ρ	density	kg/m ³
τ	shear stress	Pa
ω	angular velocity	rad/s
η	mechanical efficiency	/
Φ_M	mechanical power	W
Φ_N	net power	W
Φ_T	thermal power	W

Chapter I: Introduction

1 Background

Membrane bioreactors (MBR) are now largely applied in biotechnology (e.g., food biotechnology, environmental, industry, health, etc.) [1-3]. Then, dynamic filtration (DF) stands as a highly relevant alternative to classical filtration techniques such as dead-end and crossflow filtrations. Indeed it can be considered a more efficient filtration technology [4]. In particular, the so-called Rotating and Vibrating Filtration (RVF) module is a promising dynamic filtration module. It has been investigated intensively in our laboratory for bioprocess engineering applications for several years.

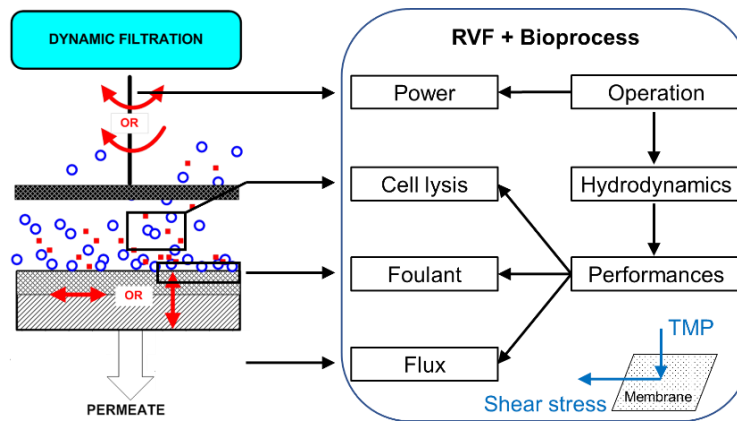


Fig. I.1 Schematic diagram of dynamic filtration module and their investigations.

Many dynamic filtration devices have been investigated in the past 30 years (Fig. I.1). Their hydrodynamics and their geometrical configuration appear to be determinant factors in optimizing their overall performances. Most of the research focused on global performances (efficiency, fouling reduction, retention-permeation locks, etc.), whereas few works were associated with local parameters (hydrodynamics, fouling nature, and structure). In RVF module, local and global hydrodynamics were specifically investigated by Xiaomin XIE (PhD, 2017) [5]. Measurements and analysis of local parameters such as local velocity, shear stress, and flow pattern/ coherent structure have contributed to a better understanding of local phenomena and their subsequent role in process efficiency. Another critical factor in optimizing the overall performance of a biological process is the configuration of the MBR. Their performances are strongly influenced by the complex interactions between gas and liquid hydrodynamics as well as the microorganism activities. The specificity of microbial bio-reactions in relation to irreducible couplings between heat and mass transfers and fluid

mechanics, led to complex and dynamic systems [1].

The hydrodynamics in the DF module is related to the dimensionless Reynolds number, and their correlation with the Darcy number and power number can be used to estimate energy consumption [6]. Semi-local approaches include the additional pressure and local shear rate. In rotating systems, the mixing pressure caused by the rotating disk or impeller is related to the core velocity coefficient, but this theory has not been reported in vibrating systems. The empirical correlations to estimate local shear rate was proposed according to the operating conditions and specific cell geometries [7]. For local approaches, the experimental measurement allows the visualization of velocity, pressure and shear fields, then compared to computational fluid dynamics (CFD) technology [7-9].

Some researchers have found the empirical relations between steady-state permeate flux and local shear rate [10-12]. The average shear rate is commonly used as a primary indicator for evaluating filtration systems. In spite of the fact that an increase in shear implies a higher permeate flux, it is also essential to account for the unit energy consumption, irreversible fouling and fluid sensitivity. The theory of critical and threshold flux was promoted in order to limit the increase of foulant, with the relevant TMP usually being a time-mean value [13, 14]. In a rotating disk module, the disk with vans yields higher permeate flux than smooth discs at the same shear rate [15], which is explained by both shear and pressure magnitudes and their fluctuations. In microfiltration, transmembrane pressure (TMP) can be maintained at very low values (~100 mbar), and then high-pressure fluctuation (same order of magnitude as TMP) could contribute to surface cake layer and internal reversible fouling destabilization.

This PhD thesis focuses on the investigation of local hydrodynamics in a defined DF module in relation to its applications in bioprocess. A dynamic filtration device, called RVF is specifically scrutinized. This DF device consists of several filtration chambers in series. Each filtration chamber includes two crown membranes and a specially designed impeller with three flat blades, rotating continuously (up to 50 Hz) to generate high stress (shear and pressure) as well as a hydrodynamic perturbation in the narrow membrane-blade gap. This module enables increased permeability by reducing the volume of the filtration loop, uncoupling the feeding flow rate and the local shear rate at the membrane surface, and operating at low transmembrane pressure (TMP). This PhD work is devoted to exploring RVF technology in order to get insight into its complex hydrodynamics at global and local scales, to understand and explain its performances in membrane bio-reactor (MBR), and to define the “best” operating conditions and device configurations for bioprocess intensification under realistic energetic constraints.

2 From scientific progress to scientific questions

In conventional membrane filtration, TMP is the primary driving force, determined by the fluid type and membrane pore size. An increase in TMP allows higher permeate flux, while it also accelerates the accumulation of matter at the membrane surface and then the formation of the cake layer (hydraulic resistance). Cross-flow filtration (CFF) aims to take benefit of the shear forces generated by tangential flow to reduce cake build-up. The retention-permeation lock remains a knowledge bottleneck in many applications. In CFF, considering the coupling between TMP, high local shear stress and feeding velocity, the threshold and critical fluxes have been defined in order to model the cake layer formation.

In dynamic filtration, the mechanical movement of one element (ex., impeller for RVF module) has been introduced to increase the shear forces in order to intensify filtration. Confined filtration device, generation of complex hydrodynamics into filtration chamber and the uncoupling between local shear and feeding flowrate are factors of complexity for process engineers. Then, it is still crucial to deeply investigate the local hydrodynamics (flow regime, velocity, pressure and shear stress fields) inside the filtration cell and to better understand the mechanisms that take place close to the membrane during the filtration operation. The flow variables should be associated with the operating conditions and the rheological behavior of fluids.

Since 2000, RVF module has been scrutinized in order to identify qualitative and quantitative performance (brewing and wine making) or critical operating conditions (cell lysis). Characterizing and understanding its complex hydrodynamics is challenging and can be explored through global, semi-local and local approaches, as well as CFD simulation. Fig. I.2 illustrates the existing results and the targeted objectives within this PhD work.

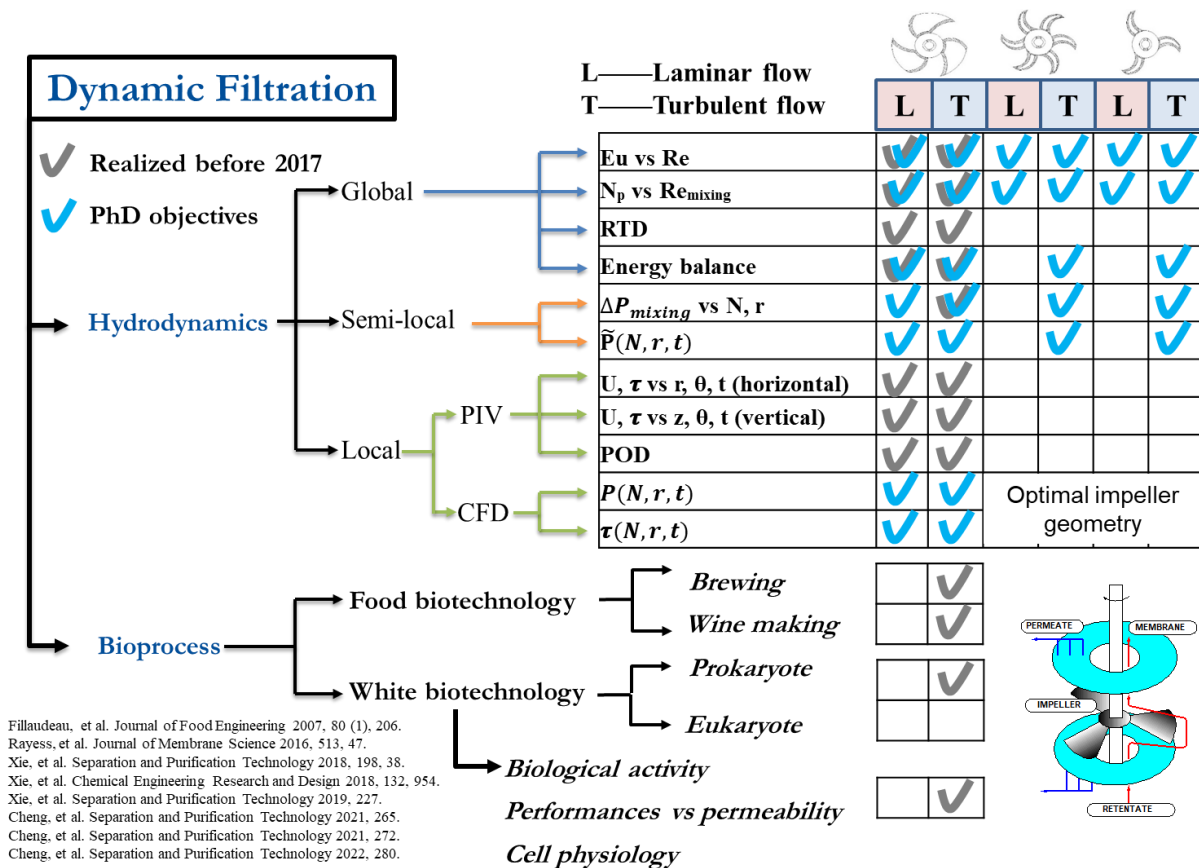


Fig. I.2 Scientific progress and investigation with RVF module.

Several scientific questions are addressed:

- (1) How to estimate the global parameters (pumping and mechanical power) with operating conditions?
- (2) How to know the local and instantaneous pressure and shear stress, what are their intensity and frequency?
- (3) What are the best operating conditions (flow regime, mixing rates, flowrates and back pressure)?
- (4) What are the best filtration cell configuration (membrane/impeller gap and impeller geometry)?
- (5) How do the mean/ fluctuating values of pressure and shear stress impact on filtration performance?
- (6) How do the microorganisms react to the increase in temperature and mechanical stress inside the filtration cell (cell lysis)?
- (7) How to enhance the filtration performance during bioprocess (flow regime, operating conditions and device configuration)?

3 Thesis structure

PhD work aims to study the local and instantaneous pressure in RVF module to intensify industrial membrane bio-reactor (MBR). The time series pressure due to the rotation of the impeller in the RVF is explored intensively using dedicated experiments. CFD simulations on one filter cell of the RVF are also performed. Once validated by experimental results, they are used to scrutinize the local hydrodynamics on a large range of parameters, not only for the pressure, but also for the local shear stress. This manuscript is structured by three main parts: i) an extensive review of DF; ii) methodological development and data treatment and iii) experimental results, data treatment, interpretation, and comparison with CFD simulation.

❖ Chapter II: Bibliography (extensive review about dynamic filtration)

This chapter provides an extensive review about industrial and laboratory dynamic filtration modules, scientific production, configurations and performances are analyzed and discussed. Firstly, a bibliography analysis of dynamic filtration was performed based on the WoS database; Secondly, all dynamic filtration devices from the lab, pilot to industrial scale were carefully described and classified; Then, an overview of the different methods and techniques to investigate the local hydrodynamics are introduced; Finally, a decision tree based on energy consumption and reported applications was proposed to highlight the knowledge gap for future scientific research and industrial applications.

❖ Chapter III: Materials and Methods

A dedicated methodology was developed by considering pressure evolution versus time and space associated with impeller shape and rotation. This chapter is devoted to (i) the description of experimental set-up and instrumentation, (ii) the presentation of experimental strategies and operating conditions, (iii) the explanation of data treatment from global to local approaches, and (iv) the construction of CFD model. Data treatment of pressure signals constitutes a challenging step in order to extract all components (mean, amplitude, frequency, periodic and random) through Statistical Analysis, Probability Distribution Function and Fast Fourier Transform, up to signal reconstruction. Finally, the methodology for CFD simulation (COMSOL Multiphysics) within RVF module is detailed in laminar and turbulent regimes.

❖ Chapter IV: Results and Discussions

This chapter is dedicated to presenting and comparing the effects of operating parameters in the RVF module. The main scientific questions raised above are answered based on experimental results and CFD simulations. More details are given below:

(1) Global investigations

The empirical correlations are introduced to estimate power consumption (mixing, pumping and thermal power) in laminar and turbulent regimes. Based on the net power input, the power consumption curve was established. The friction curve derived from effective pumping power (pressure drop) was presented as a function of mixing and feeding Reynolds number. In addition, the increase in temperature (two filtration cells) due to the thermal dissipation can be expressed by the mixing rates.

(2) Local pressure

The local pressure at the membrane surface was measured with the specially designed and instrumented porous substrate, including mixing and fluctuating components. The core velocity coefficient is defined to quantify mixing pressure versus feeding flowrate, mixing rate, viscosity and impeller shape. The pressure fluctuations are analysed and modelled to reveal their magnitude and frequency at different positions along the membrane surface.

(3) CFD simulation

For laminar regime, the simulations are performed on a geometry that consists of 1/3 of the filtration cell (Imp 1), taking benefit of the asymmetry of the system. Different operating conditions and cell geometries are explored. The velocity profile depicts the variation of fluid flow due to the rotation of the impeller. This contributes to explaining the time variations of pressure at the membrane surface.

For turbulent regime, the validation of numerical simulation was performed based on the velocity distribution of the rotating full disk system. To investigate the local pressure and shear stress at the membrane surface, the Shear Stress Transport (SST) $k-\omega$ model was selected to solve the flow close to the wall.

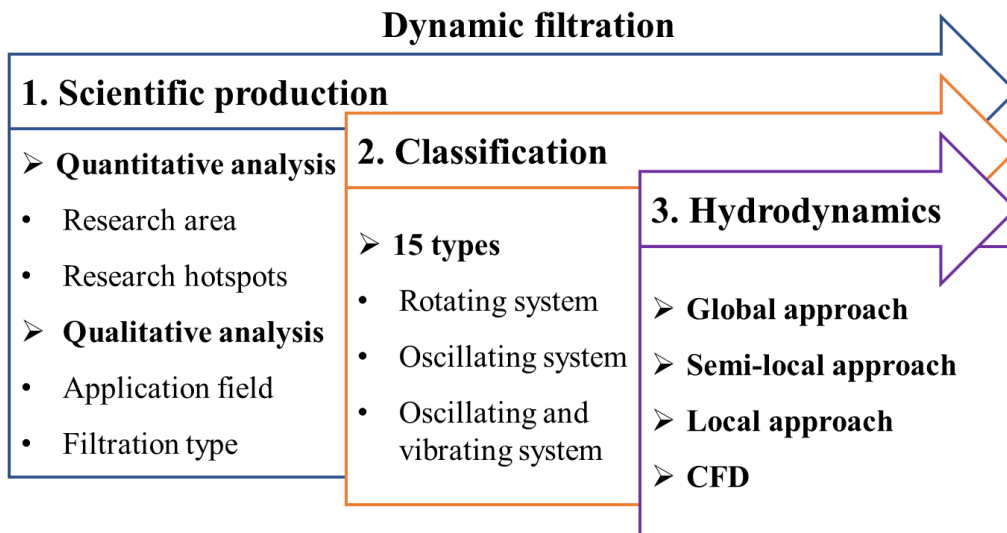
Finally, the overall conclusions of this manuscript are presented in chapter V, which highlights that the pressure and shear stress fluctuations are the potential parameters to enhance filtration. Particularly, the identification of resonance phenomena, their theoretical meaning and applications need further research.

Chapter II: Bibliography

This chapter provides an extensive review about industrial and laboratory dynamic filtration modules: scientific production, configurations and performances. By maintaining a high shear rate, dynamic filtration (DF) provides excellent performances in controlling fouling and improving flux during filtration. Many DF devices comprising a mechanical movement generated by the rotation, oscillation and/ or vibration of one element have thus been developed. Based on the bibliometric analysis, new applications and technologies related to DF have become a new research hotspot. Major applications were reported in food processing, water treatment and bioprocess engineering. With a precise definition of the concepts of oscillation and vibration, 55 DF modules have been classified into 15 different types according to movement and shape (filtration cell, membrane, impeller, disk...). But it appears that it remains a great challenge to complete the knowledge on the flow of fluid inside DF modules because of their complex geometries. Global, semi-local and local investigations of hydrodynamics have been detailed. They not only make it possible to estimate performances but also help to calculate energy consumption according to operating conditions. In this review, the main characteristics of DF devices and existing applications are presented. These empirical results are already very useful for the selection of DF devices for a dedicated application. However, a better understanding of local temporal variations in pressure and shear stress is still necessary to refine the choice of a device and the operating conditions. The overarching aims propose to report the main criteria that will help engineers to select DF modules or to identify the scientific and/ or technological bottlenecks about hydrodynamics or applications.

Highlights:

- (1) Bibliography overview of dynamic filtration (application, research items, trends and stakeholders);
- (2) Classification and specification of laboratory and industrial Dynamic Filtration Modules;
- (3) Characterization of fluid flow within dynamic filtration modules;
- (4) Main criteria to select dynamic filtration modules (critical conditions, performances, power).



1 Introduction

Membrane separation technology has become widely used in the bioprocess and food processing industry (dairy, juice, wine, water) [3, 16]. Among three-phase reactors, membrane bioreactors (MBR) appeared in the 70s and were primarily applied in the biotechnology field: white biotechnology, pharmaceutical and food industries [1-3]. However, membrane processes are yet to identify as an industrial alternative by users. The choice of membrane process is a multi-criteria and fundamental approach including diversities of (i) mass transfer processes (from electro-dialysis up to microfiltration), (ii) the geometry of module (plane, filter-press, tubular, spiral wound, hollow fiber), (iii) the nature of membrane (mean pore diameter and associated distribution/chemical nature: organic, mineral, metal, composite) and (iv) the operating mode (dead-end, cross-flow or dynamic filtration) and technology dedicated to fouling limitation (co-current, back-filtration, back-shock, back-flush,...). The overarching aim is to improve qualitative and quantitative performances of separation processes, in other terms, their intensification and efficiency in biological, chemical, and food processes. Retention could be described as mechanical and/or physico-chemical retention, but the mechanisms of retention result from a complex balance between the local hydrodynamic conditions, the product, the nature and the membrane cut-off.

1.1 Conventional dead-end filtration and cross-flow filtration

In conventional dead-end filtration (DEF) (Fig. II.1), the feeding flux is perpendicular to the permeation, and the fouling will accumulate at the membrane surface. Transmembrane pressure (TMP) increases with the formation of the cake layer, resulting in lower filtration efficiency. Cross-flow filtration (CFF), also known as tangential flow filtration, was typically designed to reduce the impact of fouling by applying a tangential feeding flow passing over the membrane and removing some of the deposits from the surface. Increasing feeding flowrate is one of the conventional ways to enhance performances in CFF. However, energy consumption rapidly increases with pumping power, proportional to the cube of flowrate in a turbulent flow regime [17].

A large number of hydrodynamic techniques have been proposed to limit or manage fouling by modifying dead-end and cross-flow filtration modules to improve performance. The main technologies are introduced below:

- The periodic shutdown of transmembrane pressure [18, 19];

- Co-current operation (homogeneity of TMP along with the diaphragm) [20];
- Reversal of the permeation flow (backflush) [21];
- The back-shock process (periodic inversion of the permeate flow, effective backflush time of less than 0.1 s) [22];
- Cleaning by generating non-stationarity in the tangential flow: generation of Dean or Taylor vortices [23-25], installation of static turbulence promoters such as baffled channel or stamped membrane [26, 27], pulsed flow [28], generation of two-phase flow (gas-liquid, liquid-solid) [29], ultrasound [30].

Although the impressive results to control fouling with these methods, the performance limitation of previous configurations and operating modes led engineers and researchers to propose an alternative named Dynamic filtration (DF).

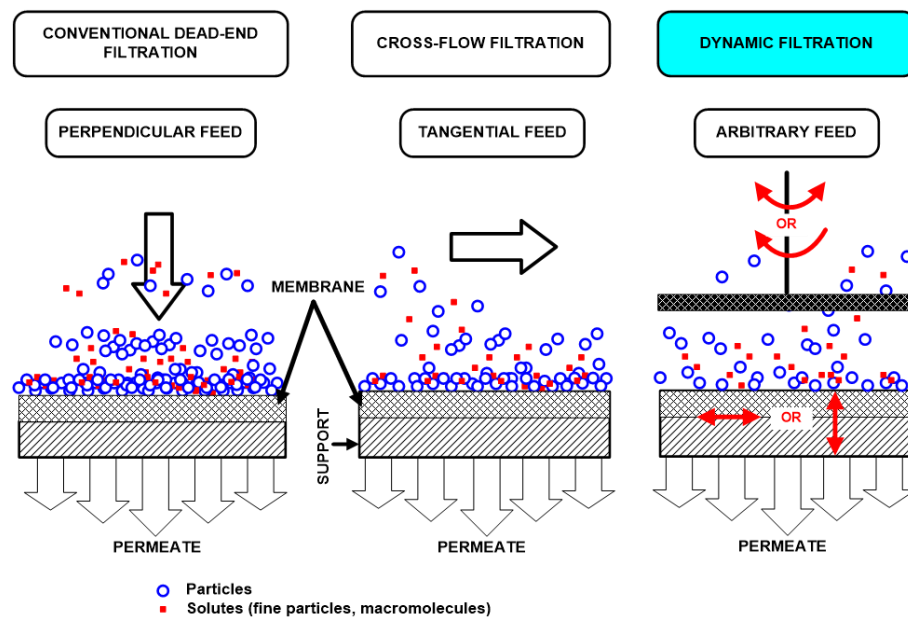


Fig. II.1 Comparison between Dead-end filtration (DEF), Cross-flow filtration (CFF) and dynamic filtration (DF).

1.2 Dynamic filtration

Dynamic Filtration, also named Shear Enhanced Filtration, appears as a promising and alternative way compared to DEF and CFF. DF is characterized by the mechanical movement of devices to create high shear stress at the membrane surface, resulting in uncoupling between local shear rate and TMP from feeding flowrate. As shown in Fig. II.1, the permeate flux is not limited by the feeding flowrate but is determined by local hydrodynamic

conditions. The rotating disk/impeller/cylinder or membrane, oscillating and vibrating device or membrane, or other mechanical motion can generate locally high shear rates approximately up to $3 \times 10^5 \text{ s}^{-1}$ without large feeding flow rates [11]. Taking advantage of this technology, DF performs its outstanding behaviors in permeability and productivity, which leads to an effective and economical process, and those major expected advantages are [4, 31]:

- Enhanced local shear rates (magnitude and time fluctuation) at the membrane surface;
- Application of low TMP;
- Reduction of fouling magnitude, which generates higher permeate flux and requires lower filtration area;
- Reduction of loop dead volume;
- Significant energy-saving (Power/ Permeate flux or Energy/ Permeate volume).

Many studies [32-34] have shown an improvement in efficiency and fouling control with DF. However, additional motion modules will also generate a series of defects. The drawbacks of DF modules are mainly attributed to their mechanical and hydrodynamics complexities:

- **Technical limitations:**
 - The complex mechanical configuration of devices may generate higher capital and operational investment, especially when scaling up;
 - The increase in the filtration area for scaling-up can be difficult.
- **Hydrodynamic limitations:**
 - Characterization of internal flow patterns is difficult (global performances and space-time resolution of velocity and pressure fields);
 - Local high shear stress may generate energy dissipation and subsequent local thermal increase.

For process engineers, the balance between advantages and drawbacks should be established for industrial applications through rational criteria, generally derived from lab-scale investigations. These strategies include estimating local and global parameters, theoretical models and computational fluid dynamics (CFD) simulation, practical filtration performances and energy consumption. More and more new devices and investigations are emerging to deal with these issues.

In 1994, Mikulasek [35] reviewed the typical methods to reduce concentration polarization and membrane fouling thanks to chemical, physical and hydrodynamic methods. The dynamic effects of rotating and oscillating to promote instabilities of flow were detailed.

The anti-fouling mechanisms in rotating filtration were summarized by Lee and Lueptow (2004) [36], and they also described the recent efforts to apply rotating filtration to reverse osmosis (RO). Jaffrin (2008, 2012) [4, 37, 38] and Ding et al. (2014, 2015) [31, 39] summarized the industrial dynamic filtration modules with rotating and oscillating. The hydrodynamics inside the filtration cell was specialized concerning the shear rate and radial pressure. The empirical equation $J = a\gamma^b$ linked the permeate flux (J) and mean shear rate (γ) with two constants, a and b . Outputs from a review of available data from studies of rotating and vibrating membrane filters, as well as vibrating hollow fiber membranes, provide a direct correlation between performances (flux) and local hydrodynamics (shear rate) [12]. However, confusion remains between the mean and maximum shear rates. Meanwhile, there is still no clear classification of dynamic filtration devices.

In this review, the bibliometric analysis was conducted to confirm the research trends about DF modules over the years and summarized its application field and filtration type. Due to the diversity of DF devices, the industrial or lab-scale modules were classified into 15 types according to the mechanical movement form and shape. The use of the available information related to internal hydrodynamics of DF allows the prediction of local performance and power consumption. They were combined with practical application requirements to guide the selection of appropriate industrial equipment.

2 Scientific production related to dynamic filtration

The database interrogation was carried out to review scientific publications and to gain insight into research hotspots. The scientific database Web of Science (WoS) Core Collection (Thomson-Reuter) was used to identify relevant articles concerning “dynamic filtration” and with the following methodology.

- Database: Web of Science Core Collection
- Profiles: (dynamic filtration) AND (membrane) AND (high shear OR shear enhanced OR rota* OR vibra* OR oscilla*)
- Field: Topic (Title, Abstract, Keywords)
- Period: 1975 to 2020 (Updated: February 30, 2020).

Citespace [40] is one of the most commonly used tools in the visual exploration of scientific literature. It was adopted as a research tool for quantitative analysis, while qualitative analysis was associated with its application fields and filtration types to identify the investigated scientific problematics. The working database was established by filtering the related publications about dynamic filtration from WoS.

2.1 Quantitative analysis

Out of 251 extracted articles, 150 publications are related to “dynamic filtration” including research articles (142, 94.7%), proceedings papers (22, 14.7%), reviews (6, 4.0%), and book chapter (2, 1.3%). Fig. II.2 shows the number of papers per year from 1991 to 2020. During the period 1975-1990, no article was found in WoS. The average number of publications per year was 1.8 ± 0.8 between 1991 and 2001, and increased rapidly to 11.8 ± 3.4 during 2002-2019, even up to 16 in 2018. The number of citations almost grows exponentially and is strongly correlated with the publication rate. 2544 citations between 2002 and 2019, equivalent to a 19.6 citations/articles ratio. This basic figure indicates an increasing research activity, scientific and industrial interests in DF.

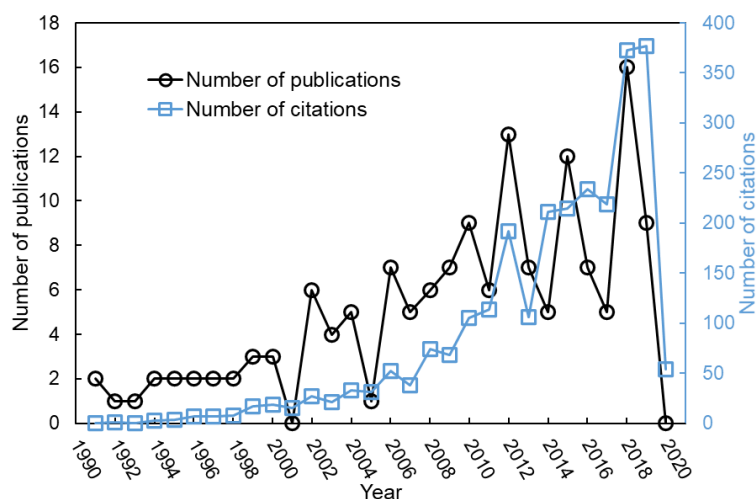


Fig. II.2 Number of publications and citations per year (Source: Core Collection-WoS (Thomson-Reuters), period: 1991 to 2020)

2.1.1 Scope of journals and research areas

Five research areas represent almost 90% of articles. Engineering (in general) accounts for 78.7% of total publications, which include 118 articles, whereas Polymer Science and Water Resources rank second and third places with only 31 (20.7%) and 28 (18.7%) articles, respectively. Biotechnology & Applied Microbiology, Chemistry and Environmental Science & Ecology also account for a significant proportion. Besides, DF modules have been reported in the other 11 categories, such as Food Science Technology, Agriculture, Mechanics, Physics, Energy & Fuels, etc.

Table II.1 Top 5 most productive journals considering the number of articles and citations (source: WoS)

Journal	TA (P)	TC (P)	Category
JOURNAL OF MEMBRANE SCIENCE	31 (20.7)	1143 (43.5)	ENGINEERING; POLYMER SCIENCE
DESALINATION	20 (13.3)	298 (11.4)	ENGINEERING; WATER RESOURCES
SEPARATION AND PURIFICATION TECHNOLOGY	14 (9.3)	203 (7.7)	ENGINEERING
BIOTECHNOLOGY AND BIOENGINEERING	7 (4.7)	165 (6.3)	BIOTECHNOLOGY & APPLIED MICROBIOLOGY
CHEMICAL ENGINEERING RESEARCH DESIGN	6 (4.0)	32 (1.2)	ENGINEERING

TA: Total article; TC: Total citation; P: percentage (%)

According to the Citation report for 150 selected results, the articles related to DF were

published by 26 journals among 23 WoS subject categories. The five most productive journals with the number of articles and categories of journals are shown in Table II.1. Total articles and citations rate in each journal follows the same trend with a dominant position for the Journal of Membrane Science.

2.1.2 Research institutions and scientific cooperation

Table II.2 shows the top 9 most productive institutions with the same indicators. The leading institution is University of Technology of Compiègne, UTC (France), which published the most articles accounting for 30.0% of the total, and almost half of them were in cooperation. Afterward, Rovira Virgili University, URV (Spain), Jadavpur and Calcutta University (India) and Nagoya University (Japan) published relatively few articles, but they all exceeded five. Then followed by IREC (Spain) and Tamkang University (China).

Table II.2 Top 9 most productive institutions (source: WoS).

Institution	TA(P)
UNIV TECHNOL COMPIEGNE	45 (30.0)
UNIV ROVIRA VIRGILI	9 (6.0)
JADAVPUR UNIV	8 (5.3)
UNIV CALCUTTA	7 (4.7)
NAGOYA UNIV	6 (4.0)
IREC	5 (3.3)
TAMKANG UNIV	5 (3.3)
DALIAN UNIV TECHNOL	4 (2.7)
UNIV TOULOUSE	4 (2.7)

TA: Total article; P: percentage (%)

113 institutions (academics or private companies) and 99 collaborative links were illustrated by the cooperation network (Fig. II.3). The size of the nodes represents the scientific activity, and the links inform the cooperation between the academic institutions and/ or private companies. As for the major network, the dominant position is led by UTC (France) from the 7 most massive clusters, which published 45 articles and linked with other 12 institutions, but mainly concentrated from 2000 to 2010. Another major one emerged at University of Toulouse. It has 5 collaborators, among 4 of them are connected. Furthermore, the bilateral national cooperation in India, Korea, and China, the international collaborations between Tamkang University (China) and Nagoya University (Japan), URV (Spain) and UTC (France) indicates a high degree of cooperation. In Fig. II.3, the color informs about the production year. Most productive institutions have come from China, France and Korea in the

last four years.

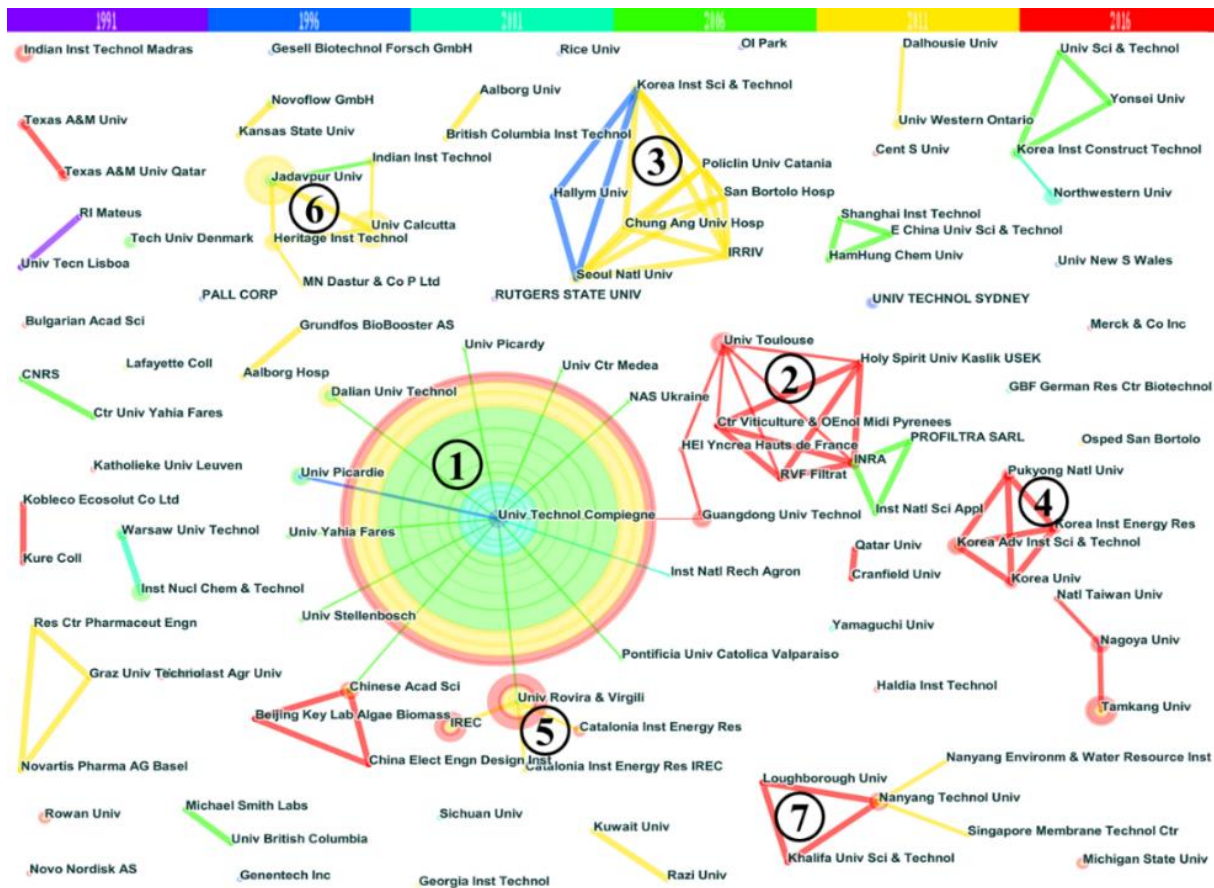


Fig. II.3 Institution's cooperation network.

2.1.3 Identification of research items











Generally, the keywords are associated with the core content of the publications; the higher frequency of occurrence in specific fields reflects the research hotspots. Fig. II.4 lists the co-occurrence network of high-frequency keywords (count \geq 3, representing more than 75% of total keywords) related to DF. Most of these keywords correspond to filtration types (microfiltration, ultrafiltration, nanofiltration and reverse osmosis), DF modules (rotating membrane, perforated disk, overlapping ceramic membrane, ...), treated fluids (microalgae, dairy wastewater, biofuel, chicory juice, emulsion...), performances (permeate flux, critical flux, threshold flux, shear stress/ rate...) and CFD simulation.

summarized in 4 dominants:

- DF technologies, such as rotating disk, vibratory disk, rotating membrane filter, shear enhanced filtration and vibration;
- Applications include yeast cells, dairy effluent, microalgae, alpha-lactalbumin, etc.;
- Hydrodynamics and performances associated with flux behavior, turbulent flow, shear stress, concentration polarization and mass transfer;
- Simulations (dynamic simulation).

Table II.4 presents the top 10 keywords citation bursts about DF between 1991 and 2019. It is noticeable that all keywords alternate between technologies, applications and performances. Dynamic filtration ranked the first position with strength was bursting from 2000 to 2005. Meantime, skim milk, ultrafiltration, performance and crossflow microfiltration also stood as the hot pots before 2010. Afterward, the scientific interest evolves from the description of fouling mechanisms (concentration polarization, permeate flux and threshold flux) to new applications (microalgae) and technological developments.

Table II.4 Top 10 keywords with the strongest citation bursts.

Keywords	Year	Strength	Begin	End	1991-2019
dynamic filtration	1991	4.2973	2000	2005	
skim milk	1991	2.5107	2004	2009	
ultrafiltration	1991	3.1852	2004	2009	
performance	1991	2.7155	2008	2010	
cross flow microfiltration	1991	2.4962	2009	2010	
concentration polarization	1991	2.5581	2011	2012	
permeate flux	1991	3.0425	2011	2013	
microalgae	1991	2.9145	2014	2019	
technology	1991	2.3293	2015	2019	
threshold flux	1991	3.0737	2015	2017	

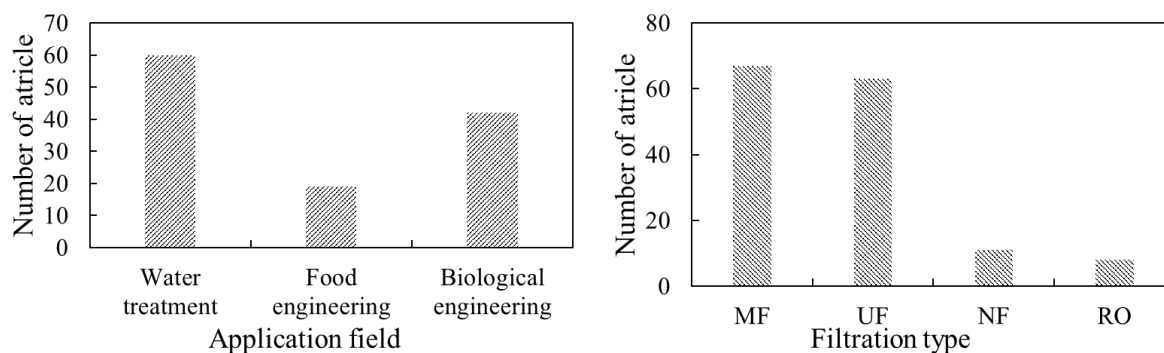


Fig. II.6 Application fields and filtration types associated with dynamic filtration.

According to the types of fluid, microfiltration (MF) and ultrafiltration (UF) were widely applied for separating fine particles from liquids, while nanofiltration (NF) and reverse osmosis were commonly used for removing dissolved constituents. As presented in Fig. II.6, MF (67 articles) and UF (63 articles) stand as the most frequent processes compared with NF (11 articles) and RO (8 articles). In MF, the articles mainly concerned large suspended solids removal such as biotic suspension (cell harvest, yeast suspension, microalgae suspensions), mineral suspension, sludge dewatering and model suspension. In UF, DF modules were tested with skim milk, soymilk, juice, surfactant solution, BSA suspension, and oily emulsions. Besides, DF treatment of wastewater from food processing presented a high-efficiency removal of chemical oxygen demand (COD) and biological oxygen demand (BOD). NF and RO are mostly used for a deeper treatment of separation, such as dissolved metals and salts removal, and drinking water purification.

In all processes (MF, UF, NF and RO), most membrane materials were organics (94 out of 119). In contrast, inorganic membranes (34) such as ceramic membranes and metal oxide membranes, were mainly used in MF processes.

2.2.1 Water treatment

In water treatment (60 articles), researchers investigated DF to treat industrial and municipal wastewater and rarely drinking water. Experimental fluids were mostly synthetic model fluids and suspensions, whereas others used wastewater from the treatment plants (paper mill [41, 42], detergent [43] and food industries [44, 45], sludge from anaerobic membrane reactor [46, 47]). Due to the complex composition of industrial wastewater, simple solutions, emulsions and solid-liquid suspensions were preferred as test fluids. Simple solutions were used to mitigate toxic pollutants (halogenated organic compounds [48, 49], 2-MIB and geosmin [50], polyvinyl alcohol [51], heavy metal ions [52, 53] and sodium

dodecylbenzene sulfonate [54, 55]), artificial seawater (NaCl, KCl, MgCl₂, CaCl₂, and MgSO₄) [56, 57], viscous solutions (polyethylene glycol-6000 [58-60], carboxymethyl cellulose [61], ethanol [62]), soluble salts (CaSO₄ [63], NaCl [64]), model wastewater in dairy process [65-71] and space mission [72]. For emulsion, oil/water mixtures with surfactants were considered [73-79]. Solid-liquid suspensions with dispersed particles as model effluent included bentonite [80], polymethyl methacrylate (PMMA) [81-83], styrene butadiene rubber (SBR) latex [84], polystyrene latex [85], CaCO₃ [86-90], SiO₂ [91-94], Al₂O₃ [95], ZnO, Fe(OH)₃ [96, 97] and hollow glass microspheres [98].

The permeation/retention bottlenecks were scrutinized versus operating conditions (effluent, concentration, temperature, TMP) and device configurations (geometry of DF modules, shear rate, membrane nature and cut-off). Most of the works reported qualitative performances (flux, steady-state flux, hydronic resistance, concentration factor, volume reduction ratio, rejection rate, concentration polarization) to establish the empirical correlations (flux versus shear rate/ shear stress). Computational fluid dynamics [56, 64, 70, 82, 93, 98] was used to simulate local and global performances (shear rate/ shear stress, flux) within the filtration cell and membrane surface. Only one article used PIV (particle image velocimetry) [80] to examine the local hydrodynamics and compared it with the filtration performances.

2.2.2 Food processing

In food processing (19 articles), DF was applied in liquid food production (dairy, brewing and extract juice). 12 articles (63%) were related to the concentrations of milk protein from casein micelle [11, 99-105] and the separation of α -lactalbumin and β -lactoglobulin [106-109]. The fluids commonly came from commercial UHT skim milk and low heat powder milk. Defatted soy milk was also used to recover trypsin inhibitor and soy milk protein [110]. Microfiltration in brewing (rough and clarified beer) [111] and wine-making (crude simulated and filtered wine) [112] were investigated with DF. Retention/permeation performances were reported in terms of product quality and cost-effectiveness. Juices of sugar beets [113], *Alfalfa* [114, 115] and *Jerusalem Artichoke* [116] contain a large number of nutritional compounds, such as sugar, leaf protein and inulin, which have been separated, purified and/or concentrated by ultrafiltration with DF.

All works are associated with technical locks about product concentration and quality. Performances versus volume reduction ratio and modeling of hydraulic resistance stand as major scientific questions. To increase filtration efficiency, optimizations of operating

conditions and modifications of DF geometrical configurations are handsome strategies. The filtration performances do not only focus on the permeate flux but also on permeate quality (purification and separation rate). These analyses mainly rely on the permeate/retentate turbidity, coloration or conductivity, and the concentration or °Brix of target products. It should be mentioned that membrane selectivity (membrane materials, structure and cut-off) is a critical issue for some particular compositions.

2.2.3 Bioprocess engineering

For bioprocess engineering, 42 papers were carried out associated with DF modules due to their wider coverage (cell productions: prokaryote, eukaryote, microalgae, animal cells; biomolecule productions: recombinant proteins, antibody, exopolysaccharides, etc.). Most of tested fluids are biological suspensions (fermentation broth) containing microalgae [34, 117-132], yeast [10, 11, 13, 15, 133-140], bacteria [141-143] and animal cell [144-146]. Other dispersions were produced by commercial or fermented biological products, including bovine serum albumin (BSA) [147-149], polygalacturonic acid 140, α -lactose monohydrate [150], ibuprofen [150], recombinant human growth hormone [151] and monoclonal antibody [152]. Within the research, 17 publications (40%) focused on the concentration and separation (biomass) of microalgae and constituted a new hotspot over the last decade. *Saccharomyces cerevisiae* (baker's yeast) was commonly used in DF for its widespread applications in the biotechnological industry. Model suspensions were formed by the mixture of yeast with ultrapure osmosed water [11, 15] and buffer [13, 136] or directly extracted from fermentation broth [133, 134].

In bioprocess engineering, flux decline induced by the fouling layer was discussed. Methods to improve critical flux are generally consistent with water treatment and food processing, but cell viability needs to be considered under high shear stress [106, 153]. Several publications are dedicated to the formation of cell cake layers, which exhibit high specific filtration resistance due to their high compressibility. The empirical correlations between cake mass and operating conditions (TMP and wall shear stress) were reported and interpreted [121]. CFD has been combined with experimental data to investigate local operating conditions with biological fouling within DF devices [121, 123, 124, 146, 148-150].

3 Specifications of Laboratory and Industrial Dynamic Filtration Modules

3.1 Classification of dynamic filtration modules

In recent decades, many efforts and a great number of studies have been achieved to develop novel DF modules at the lab or pilot-plant scales. From scientific and technical literature, 55 modules with 85 configurations were designed and produced by 29 industries and 21 laboratories. Reviewing the existing DF modules, they can be classified by the type of movement, including rotation, oscillation and vibration. These movements can occur to the membrane, the mechanical device (disk, impeller and cylinder) or the whole filtration module. Oscillating and Vibrating movements are easily confused, and there is no clear definition to distinguish them. In this paper, oscillation and vibration are defined as mechanical movement, which can be perpendicular and parallel to the direction of permeate flux, respectively. Based on the shapes of the moving part and the membrane, the 55 identified modules could be classified into 15 types considering the movement form and part (Table II.5). Table II.6 reports the technical specifications (trade name, filtration area, maximum rotating speed, oscillating or vibrating frequencies) of all modules.

Table II.5 Classification of DF modules according to the movement and shape.

Movement form	Movement part	Shape of movement part	Shape of membrane	Type	
Rotating	Membrane	Disk	Disk	1	
		Rectangular	Rectangular	2	
		Cylinder	Cylinder	3	
		Hollow fiber	Hollow fiber	4	
	Mechanical device	Mechanical device + Membrane	Disk	Disk	5
			Impeller	Disk	6
			Cylinder	Cylinder	7
Oscillating	Filtration module	Disk + Membrane	Disk	8	
		Cylinder	Disk	9	
	Membrane	Rectangular	Rectangular	10	
		Rectangular	Rectangular	11	
		Cylinder	Cylinder	12	
		Hollow fiber	Hollow fiber	13	
Spacers	Rectangular	Rectangular	14		
Oscillating + Vibrating	Membrane	Hollow fiber	Hollow fiber	15	
Vibrating	/				

Table II.6 Classification and specification of DF modules (*d*: membrane diameter, *S*: membrane surface area, *N/F*: maximum rotating, vibrating and/or oscillating speed/frequency, *A*: amplitude, displacement or vibrating angle, *TMP*: maximum operating transmembrane pressure)

Type	Manufacturer	Configuration	Status	Membrane size (mm)	S (m ²)	N/F (rpm, Hz), A (mm, °)	TMP (bar)	Fluid	Ref	
1	Spintek, Huntington Beach, CA, USA	Spintek ST II	Industrial	d=340	0.05-2.3	1200 rpm	10	/	[154]	
		Spintek ST IIL	Lab	d=203 (2)	0.05	1800 rpm	3.1	Cutting oil emulsion	[155]	
	Spintek, Los Alamitos, CA, USA	High shear rotary membrane system, HSR-MS	Lab	d=74-267	0.0492	1750 rpm	5.17	Wastewater, O/W emulsion	[156-161]	
	Novoflow GmbH, Rain/Lech, Germany	Single shaft disk filter, SSDF-312	Industrial	d=312 (75-100)	40	/	/	/	/	[162]
		SSDF-500+	Industrial	d=550 (75)	50	/	/	/	/	
		Compact rotating disk filters CRD	Lab	d=152 (3)	0.108	1800 rpm	1	Oily wastewater	[73]	
	Diva Envitec Pvt. Ltd., India	Modular spin disk filtration, MSDF	Industrial	/	1-100	/	/	/	[163]	
	Fraunhofer IGB, Germany, membrane supplier: KERAFOLE	Rotating disk filter	Industrial	/	/	/	0.5-1.2	/	[164]	
	Mio Vigneto Products, Automatic Filter System	Rocket M7	Industrial	(35)	7	/	/	/	[165]	
	ANDRITZ KMPT GmbH, Vierkirchen, Germany	Rotational dynamic filtration, DCF 152/S	Lab	d=152	/	1150 rpm	/	Water/ ethanol	[62]	
	HUBER (Berching, Germany), Vacuum Rotation Membrane VRM® Bioreactor	Vacuum rotation membrane bioreactor, VRM 20/36	Industrial	/	108	1.8 rpm	0.3	Wastewater	[166]	
		VRM	Industrial	d=4500	540	/	/	/	[167]	
	Hitachi, Japan	AQUA UFO	Industrial	/	/	/	/	/	[4]	
ANDRITZ KMPT (Vierkirchen, Germany), membrane supplier: KERAFOLE	Dynamic cross-flow filter, DCF	Lab	d=152 (6)	0.138	1110 rpm	5.5	Microalgae	[118, 119]		
Westfalia Separator, Aalen, Germany	Multi shafts disks, MSD, two-shaft laboratory pilot	Lab	d=90 (12)	0.121	2000 rpm	2.5	CaCO ₃	[86, 89, 168]		
	MSD, eight-shaft pilot	Industrial	d=31.2	80	/	/	/	[38]		
2	Gurpreet Engineering Works, Kanpur, UP, India	Spinning basket membrane, SBM	Lab	130×55 (4)	0.0286	600 rpm	9.7	PEG 6000, BSA, Polyving alcohol	[51, 59, 148, 169]	
		Intermeshed spinning basket membrane, ISBM	Lab	105×55 (8)	0.046	480 rpm	9.7	BSA	[149]	
	Key Laboratory of Industrial Ecology and Environmental Engineering, Dalian University of	/	Lab	300×30 (2)	0.018	160 rpm	0.065	Kaolin, yeast, CaCO ₃	[170]	
		/	Lab	230×20 (2)	0.0092	/	/	Halogenated compounds in water	[48]	

Chapter II: Bibliography

Type	Manufacturer	Configuration	Status	Membrane size (mm)	S (m ²)	N/F (rpm, Hz), A (mm, °)	TMP (bar)	Fluid	Ref
	Technology, China								
3	Hemascience, Santa Ana, CA, USA	Plasmacell filter	Industrial	/	/	/	/	/	[171]
	Faculty of Engineering, University of Regina, Canada	/	Lab	/	/	10000 rpm	0.25	Oily-wastewater	[172]
	Membrex Inc. Fairfield, USA	Benchmark Biopurification system	Lab	/	0.02	2000 rpm	1.4	Yeast	[133]
	Department of Chemical Engineering, Nagoya University, Japan	/	Lab	$2\pi \times 15 \times 500$	0.0471	1500 rpm	1.51	PMMA	[81]
		/	Lab	$2\pi \times 15 \times 320$	0.03016	5000 rpm	1.51	PMMA, O/W	[77, 78, 83]
	Department of Mechanical Engineering, Northwestern University, USA	Rotating reverse osmosis	Lab	$2\pi \times 241 \times 127$	0.0192	180 rpm	10	CaSO ₄ , model wastewater	[63, 72]
	Millipore Co.	/	Lab	$2\pi \times 26 \times 670$	0.1094	600 rpm	/	SiO ₂	[92, 94]
	Department of Chemical Engineering, Universit� de Technologie de Compi�gne, France	/	Lab	$2\pi \times 5 \times 45$	0.0014	7000 rpm	1	Al ₂ O ₃	[95]
	Suker AG, Winterthur, Switzerland	Biodruck-filter, BDF-01	Lab	$2\pi \times 33 \times 200$	0.04	3000 rpm	0.7	Yeast	[173]
4	Facultad de Ciencias-Seccion de Qu�mica, Universidad La Laguna, Spain	Rotating hollow fibre membrane, R-HFM	Lab	/	0.047	330 rpm	0.4	Anaerobic suspensions	[47]
5	University of Technology of Compi�gne, France	Rotating disk module, RDM-1	Lab	d=154	0.019	3000 rpm	10	CaCO ₃ , yeast, skim milk, juice, broth, dairy effluent, microalgae, PAA-Cd complex	[11, 14, 15, 33, 43, 66, 67, 70, 71, 74, 75, 87, 88, 99, 106, 108, 110, 114, 115, 141, 174-184]
		RDM-2	Lab	d=260	0.046	1500 rpm	2	Skim milk	[183]
	School of Chemistry and Chemical Engineering, Central South University, China	Rotating disk module	Lab	d=176	0.0242	3000 rpm	2.5	Cd ²⁺ , Zn ²⁺	[185, 186]
	Department of Chemical and Materials Engineering, Tamkang University, Taiwan, China	Rotating-disk dynamic filter-1	Lab	d=38	0.00112	3000 rpm	1	Microalgae, PMMA, artificial seawater	[57, 82, 93, 121]
		Rotating-disk dynamic filter-2	Lab	d=155	0.0377	3000rpm	1	Microalgae	[124]
	Pall Corp., Dreieich, Germany	Dynamic membrane filter, DMF LAB6 system	Lab	d=151	0.0137	3450 rpm	2	Yeast, coli	[134, 145, 153, 187]
	Grundfos BioBooster, Bjerringbro, Denmark	Rotating cross-flow, RCF MBR	Lab	d=312	0.12	350 rpm	15	/	[7]
	BKT Water & Energy, Korea	Anti-fouling membrane filtration system FMX-S	Industrial	/	94.9	270 rpm	15	/	[188]
FMX-E		Industrial	/	40	270 rpm	5	/		
FMX-P		Industrial	/	0.0873-3.16	290-350 rpm	30	/		

Chapter II: Bibliography

Type	Manufacturer	Configuration	Status	Membrane size (mm)	S (m ²)	N/F (rpm, Hz), A (mm, °)	TMP (bar)	Fluid	Ref
		FMX-B	Lab	d=150	0.0146	1600 rpm	1	Microalgae	[123, 126, 128]
	Miltenyi Biotec, Germany	Life 18 disk separator	Industrial	/	/	/	/	/	[189]
	Michael Smith Laboratories, Canada	Controlled shear affinity filtration (CSAF)	Lab	d=30	0.0014	/	/	/	[190]
	Gesellschaft für Biotechnologische Forschung mbH, Biochemical Engineering Division, Germany	Controlled shear filtration, CSF	Lab	d=90	0.0515	/	/	BHK cell	[144]
6	Bokela GmbH, Karlsruhe, Germany	Dynotest	Lab	/	0.013	/	7	Alpha-lactose monohydrate suspension	[150]
		DYNO	Industrial	/	0.13-12	/	6	/	[191]
	Metso Paper Co, Raisio, Finland	Cross Rotational (CR)-Filter, CR 200/1	Lab	d=200 (1)	0.054	/	/	Paper mill waste	[192-194]
		CR 250/2	Lab	d=250 (2)	0.18	/	10		[195]
		CR 500/5	Industrial	d=500 (5)	1.75	470 rpm	2.7		[196]
		CR 550 / 15 to 30	Industrial	d=550 (15-30)	7.5-15	/	/		[39]
		CR 1000/ 26 to 60	Industrial	d=1000 (26-60)	35-84	/	/		[39]
		CR 1000/10	Industrial	d=1000 (10)	13.5	365 rpm	1		[193]
	CR 1010/70 to 100	Industrial	d=1010 (70-100)	98-140	/	/	[39]		
	RVF Filtration, Paris, France	Rotating and vibrating filtration, RVF	Lab	d=142 (4)	0.024 per cell (1 to 5 cells)	50 Hz	3	Beer, wine, viscous, solution	[6, 8, 111, 112, 197, 198]
RVF 5		Industrial	d=800 (10)	1 per cell (1 to 5 cells)	30 Hz	20	Waste water, chemical sludge	[199, 200]	
7	Fann Instrument Company, Houston, Texas, USA	Fann 90 Dynamic HPHT® Filtration System	Lab	/	/	300 rpm	7	Drilling fluid	[201]
	Department of Nuclear Methods in Process Engineering, Dorodna, Warsaw, Poland	Helical Couette-Taylor flow (CTF) filtration module	Lab	/	0.04	2800 rpm	0.7	Radioactive wastes, wastewater	[52, 53]
8	Gurpreet Engineering Works, Kanpur, UP, India	Rotating disk-membrane, RD-M	Lab	/	0.00246	Membrane:600 rpm stirrer: 1000 rpm	10	BSA, PEG6000, kraft black liquor	[41, 42, 58, 60, 147]
	Krauss-Maffei DCF, Andritz KMPT GmbH, Vierkirchen, Germany	Dynamic cross-flow filtration, DCF	Lab	d=152 (4)	0.14	1000 rpm	5	Skim milk	[105]
9	New Logic, CA, USA	Vibratory shear enhanced processing, VSEP series L 101	Lab	d=135	0.05	55-60.75 Hz	15	Skim milk, simulated tannery wastewater, microalgae, latex solution	[34, 44, 65, 84, 100, 101, 127, 131, 181, 202]
		VSEP series LP	Lab	/	1.53	/	40	Microalgae	[122]
		VSEP series L	Lab	/	0.446	/	40	/	[203]

Type	Manufacturer	Configuration	Status	Membrane size (mm)	S (m ²)	N/F (rpm, Hz), A (mm, °)	TMP (bar)	Fluid	Ref
		VSEP series P	Lab	/	1.57	/	40	/	
		VSEP series B	Lab	/	0.0111	/	10	/	
		VSEP series P-50	Lab	/	4.65	/	40	/	
		VSEP series i18	Lab	/	13.9-26.9	35-49 Hz	38	/	
		VSEP series i36	Lab	/	41.8-55.7	38-55 Hz	38	/	
	VSEP series i84	Lab	/	up to139	43-55 Hz	38	/		
	Pall Filtration, East Hills, NY, USA	Vibrating membrane filtration, VMF-PALLsep PS 10	Lab	/	0.2	55-55.75 Hz	2	BSA	[204]
		VMF-PALLsep Biotech Module	Industrial	/	0.2-5	/	3.5	/	[205]
10	Department of Mechanical Engineering, Texas A&M University, College Station, TX, USA	Vibration enhanced reverse osmosis (VERO) membrane	Lab	30×20	0.0006	60 Hz, 1.2 mm	55	Simulated seawater	[56, 64]
11	Chemical and Biochemical Engineering Department, Western University, London, Ontario, Canada	Oscillatory flat surface membranes, OFSM	Lab	89×68	0.006	25 Hz, 30 mm	0.6	Yeast	[137, 139, 206-209]
	State Key Laboratory of Pollution Control and Resource Reuse, Tongji University, China	Uniform shearing vibration membrane, USVM	Lab	/	0.02	5 Hz, 20 mm	0.7	Microalgae	[210]
	Faculty of Bioscience Engineering, Katholieke Universiteit Leuven, Belgium	Magnetically induced membrane vibration, MMV	Lab	/	0.016-0.0215	60 Hz, 20 mm	0.3	Wastewater, microalgae, anaerobic sludge, lignocelluloses hydrolysate	[46, 211-215]
	State Key Laboratory of Pollution Control and Resource Reuse, Tongji University, China	Axial vibration membrane, AVM	Lab	/	0.02	15 Hz, 40 mm	0.7	Microalgae	[216-218]
12	Department of Chemical Engineering, University of Engineering & Technology Peshawar, Pakistan	Oscillating membrane module	Lab	/	/	0-100 Hz, 0-10 mm	0.4	Oil in water emulsion	[79]
	Chemical Engineering Department, Loughborough University, Leics, UK	Azimuthal and axial oscillation filtration	Lab	/	/	100 Hz, 3 °	0.3	Suspension of calcite	[219]
13	IMI Institute for R&D, Israel Chemicals Group, Israel	Vibrating hollow fibre microfiltration, VHM	Lab	/	0.0057	10 Hz, 40mm	/	Yeast	[220]
	School of Civil and Environmental Engineering, Nanyang Technological University, Singapore	Vibrating submerged hollow fibre membranes	Lab	/	/	0-15Hz, 0-12mm	0.4	Bentonite	[80]

Chapter II: Bibliography

Type	Manufacturer	Configuration	Status	Membrane size (mm)	S (m ²)	N/F (rpm, Hz), A (mm, °)	TMP (bar)	Fluid	Ref
	CAPEC, Department of Chemical Engineering, Technical University of Denmark, Denmark	HF membrane filter	Lab	/	0.0256	30 Hz, 1.175mm	0.25	Enzyme, yeast	[13, 136, 221, 222]
14	Nanyang Environment and Water Research Institute, Nanyang Technological University, Singapore	Spacer vibration of submerged flat sheet membranes	Lab	50×70×2	0.007	2 Hz, 12 mm	0.4	Bentonite and alginate solution	[223]
15	School of Chemical Engineering, The University of New South Wales, Australia	Transverse vibrating hollow fibre membrane	Lab	/	/	58 Hz, 5 mm	0.2	Yeast, milk	[138, 224]
	Department of Nephrology, San Bortolo Hospital, Italy	Shaking HF membrane module	Lab	/	/	20 Hz, 20 mm (20 °)	/	/	[225, 226]
	School of Chemical Engineering, The University of New South Wales, Australia	Rotational vibrating hollow fibre membrane	Lab	/	0.0131	10.3 Hz, 18.3-55°	0.8	Yeast	[32]
	School of Water Resource and Civil Engineering, Northeast Agricultural University, China	Vibration hollow fibre membrane	Lab	/	0.0045	2 Hz, 180 °	0.6	Microalgal	[132]
	Institute of Oceanic and Environmental Chemical Engineering, Zhejiang University of Technology, China	Pendulum type oscillation, PTO	Lab	/	0.2	70 rpm, 50 mm	/	Oily wastewater	[227]

3.2 Rotating systems

Rotating systems can be split into three categories: rotating membrane modules (21 modules), rotating mechanical devices (14 modules) and the association of rotating membrane and mechanical devices (2 modules).

3.2.1 Rotating membrane modules

3.2.1.1 Rotating disk membrane

The disk membranes are one of the most commonly used in rotating membrane filters. From the literature, 10 modules (corresponding to 16 configurations, Table II.6) were designed and produced by local companies. These modules consist of membranes mounted onto the porous support driven by one or more central shafts. Such supports can be one or more rotary disks, allow a flexible configuration, and lead to easy scale-up with larger filtration area capacity. Cell design, geometrical configurations and operating conditions are the most critical parameters to optimize module efficiency.

In high shear rotary membrane system (HSR-MS) [157-161], flat round membrane disk packs are attached to the highly porous nylon meshes. A solid disk pack is placed between two meshes and sets on a hollow rotating shaft for permeation channels. By the central shaft rotation, the maximum liquid velocities close to the membrane can reach up to 18 m/s, compared to 4.5 m/s for conventional cross-flow UF systems [161]. Henrik et al. [62] tried to add a metal insert in the rotary membrane chamber. It generates disturbances in the bulk flow, which increase the filtration pressure.

Industrial applications of DF modules require technical improvements in order to increase the filtration area. A compact rotating disc filter (CRD) is a lab-scale module with 3 disk membranes compressed on the same hollow rotating shaft. In wastewater treatment, it has an available effective filtration area of 0.1 m² [73]. Signal shaft disk filter (SSDF-312) can equip with 75-100 filter disks mounted on a single shaft with a 10-15 m² filter area [162].

With the same concept, modular span disk filtration (MSDF) is manufactured by Novoflow GmbH (Germany), with a lot of disk membranes mounted on a single shaft, and the filtration area ranging from 1 m² up to 100 m² [163]. Vacuum rotation membrane (VRM, HUBER, Berching, Germany) filtration unit also designed with an available large-scale membrane area (diameter approx. 2.3 and 3.2 m, and membrane surface approx. 900 m² and 3840 m²) and coupled with a powerful aerator to clean the contaminated membrane [166, 167, 228]. Rocket M7 was designed for the purification of grape juice in winemaking; 35 disk

membranes (total filtration area of 7 m²) were installed in the rotating shaft and driven by a 3 kW power motor [165].

Besides, some systems equipped with multi-shaft (rotate in the same direction), overlapping membranes were developed and well-studied. A two-shaft system, Dynamic cross-flow filter (DCF) commercialized and made by KMPT, was tested with microalgae for biofuel production [118, 119]. In the optimized condition, pilot experiments achieved a concentration factor up to 200 and permeability up to 600 L/h/m²/bar (with pre-concentration) [118]. Another two shafts filter, a lab-scale Multi-shaft disk (MSD, Westfalia Separator, Aalen, Germany) module, was studied by Ding et al. [86, 89, 168]. They found that the permeate with two shafts module is about twice higher than the static membrane module with the same azimuthal rim velocity. The overlapping of disks generates the maximum shear rate [86]. With this knowledge, a larger MSD system was commercialized by Westfalia Separator. It is equipped with 8 shafts and fixed a pile of membrane-disks; all shafts and membrane-disks rotate at the same speed [38].

Bendick et al. [156, 157] used the zirconium dioxide ceramic MF membrane in HSR-MS to treat shipboard wastewaters (bilge water, blackwater and thermal destruction quench water). They changed different hub sizes resulting in various membrane diameters and different angular speeds of the membrane. For every 100 rpm increase in angular velocity, steady-state flux increased on average by 26 L/(h·m²). While expanding the filter disk diameter also provides excellent performance per disk at a lower rotation speed and reduces the number of discs required.

He et al. [89] modified the configuration of MSD (2 shafts). Previously, each shaft equips with 6 ceramic membranes (0.2 μm). The permeate flux for 12 membranes was 520 L/(h·m²) when filtering 200 g/L of CaCO₃, while it was reduced to 503 L/(h·m²) when working with 6 membranes. However, after replacing one of the ceramic membranes on each shaft with a smooth disk or a disk with 8 vans, the permeate flux was further improved to 740 or 816 L/(h·m²), respectively. With the same module, Tu and Ding [87] replaced the ceramic membrane with nylon membranes of the same size and pore diameter to concentrate CaCO₃. Maximum permeate flux was observed for the nylon membrane to reach 850 L/(h·m²) compared to 760 L/(h·m²) for the ceramic membrane. In the fractionation of milk protein, Espina et al. [106] found that the PVDF membrane performed better than the ceramic one regarding permeate flux and casein rejection. In another paper [108], the concentrated fluid from the MF for ceramic membrane achieved the transmissions of α-lactalbumin and β-lactoglobulin between 0.8 and 0.98, for further filtration with UF was applied to separate

them.

In UF, the West Virginia University team compared the performances of polymeric (100 kDa) and ceramic (0.11 μm) membranes for treating oily wastes from metal-working. The latter was superior to the polymeric membrane in terms of permeate flux and quality, as well as for cleaning and durability [158]. With CRD, oily wastewater with different concentrations was treated in MF and UF (ceramic membrane). High oil (>99%) and TOC (>98%) rejection rates were achieved with both membranes; their performances were independent of the rotational speed and the feed concentration [73]. With VRM, the wastewater treatment was performed at a very low rotational speed (1.8 rpm), and UF polyether sulfone flat membranes (NADIR P-150F) were compacted with a total filtration area equal to 108 m^2 . The COD in the final permeate flux was reduced to 3 mg/L without suspended solids for an initial retentate concentration equal to 601 mg/L. Moreover, the membrane immersed in wastewater could be used longer due to the air scouring [166].

3.2.1.2 Rotating rectangular membrane

Only two modules (lab scale) were identified with rotating rectangular membranes, but their designs are entirely different.

Gurpreet Engineering Works in India [51, 59, 148, 169] developed the first module named Spinning basket membrane (SBM). Four flat rectangular membranes (each of dimension $65 \times 145 \text{ mm}^2$ with an effective area of $55 \times 130 \text{ mm}^2$) are fitted on alternate sides of adjacent radial arms, and the other side remains impermeable. These arms are driven by a hollow shaft and allow the permeate to pass. In continuous running, the membrane filtration cycle rotated as a normal run, followed by a short time cleaning cycle rotated in the reverse direction. With the same theory, the intermeshed spinning basket membrane (ISBM) consists of two identical spinning baskets, which are intermeshed with a phase difference of 45° and able to operate at the same speed but in a reverse direction [149]. Sarkar et al. [59] investigated the separation of PEG 6000 with the SBM module and PES (5kDa) UF membrane. It indicated superior performance in terms of shear enhancement and flux recovery compared with other shear enhanced systems, namely the single stirred (SS) and the rotating disk-membrane (RD-M) modules. The steady flux of the SBM module was 45-95% higher than its RD-M counterpart; in comparison with SS, it was 300-450% enhanced when rotating at 62.5 rad/s. With its inbuilt cleaning facility, the module restricts the flux decline within 15% of its start-up value, even after 21 h of continuous running. In the UF of Bovine Serum Albumin, the average permeates flux of ISBM was observed to be approximately 1.8 times higher than that of the SBM module due to comparatively higher membrane shear

stress. Maximum permeate flux was evaluated to be as high as $2.4 \times 10^{-4} \text{ m}^3/(\text{m}^2 \text{ s})$ at moderate transmembrane pressure and rotational speed (588 kPa and 52.36 rad/s). It also showed better performance in treating extremely fouling feed solutions than other standard membrane units [148, 149].

The second module is named helical lab-scale filter [48, 49, 170]. Two pieces of the flat membranes are supported on an aluminum spacer to maintain the helical angles (0° , 180° , 270° , 360° and 450°). A tubing outlet is assembled in the central of the aluminum spacer, for one side is sealed out and allowed for the collection of permeate water. The filter sheet is immersed in the tube container and driven by a DC motor, which is able to rotate at the speed of 75 and 160 rpm. Different particle suspensions (yeast, kaolin and CaCO_3) were tested in MF with dynamic membranes (PES, $0.22 \mu\text{m}$) with a total filtration area of 0.018 m^2 . 360° stood as an optimal helical angle considering the permeate flux, and the energy consumption for this condition was smaller (0.069 kWh/m^3) than the rotating flat membrane (0.081 kWh/m^3). The order of membrane fouling was yeast > kaolin > nano- CaCO_3 at the same concentration of 5.0 g/L , even the mean diameter of yeast is smaller than others [170]. To remove halogenated compounds (Cl^- , Br^-) in water, pre-coated nano- CaCO_3 dynamic membranes with an effective area of 0.0092 m^2 were applied in the batch and the continuous photocatalytic experiments. This coated (fouling) layer enhanced the filtration performances and the retention of photocatalysts [48, 49].

3.2.1.3 Rotating cylinder membrane

In 1967, Sherwood et al. [229] suggested a rotating cylinder filter in reverse osmosis for salt and water transport, including an inner cylinder membrane rotating in a cylindrical stationary housing. 8 other modules with similar configurations have been reported in the literature. The reduction of membrane polarization is improved by taking advantage of Taylor vortices in the annular gap of the filter apparatus [173].

Early-commercialized filters, Biodruck-filter (BDF-01, Sulzer AG, Winterthur, Switzerland) was dedicated to cell harvesting and cell debris removal [173], with 66 mm diameter and 200 mm length inner cylinder membrane (0.04 m^2 filtration area) at rotation speed up to 3000 rpm. With the Teflon membrane ($0.2 \mu\text{m}$), 3.3 and 10 concentration ratios were tested. Flux increments have been observed during the increase of rotation speed and TMP. In *E. coli* broth concentration, the Biodruck-filter showed a significantly higher flux (about three-fold) than cross-flow filtration techniques over a broad concentration range.

Murase et al. [81] described the same dynamic microfiltration system with a rotating ceramic membrane ($0.2 \mu\text{m}$ alumina ceramic membrane). Polymethyl methacrylate as slurry

material was circulated in the annular gap of 3.3 mm. The same fluid was treated with the increase in outer cylinder diameter to achieve a larger gap (12.5 mm) in the filtration cell. PMMA solutions were diluted with glycerin at concentrations of 72, 53 and 0% to obtain different viscosities. Results showed that high-speed rotating dynamic filtration was considered to be more useful when the slurry has a higher viscosity [83]. In the separation of oil in water emulsion, high rotation speed helped limit the oil layer at the membrane surface. With additional suspended particles in the emulsion, a further increase in steady-state flux was observed from 5.41×10^{-4} to 1.14×10^{-3} cm/s in 49 kPa, from 5.1×10^{-4} to 4.65×10^{-3} cm/s in 147 kPa [78].

Park et al. (1994) [92] and Choi et al. (1999) [94] investigated another module from Millipore Co. Different gap ratios of 0.17, 0.54 and 0.65 (inner cylinder radius: 5.2 cm) were achieved by changing the diameter of the outer cylinder. Fine silica particles filtered with MF-cellulose ester membrane (with a total filtration area of 0.1094 m²) rotating varied from 0 to 62.8 rad/s. At a higher rotating speed of 41.8 rad/s, filter flux decreased for the cake layer formation during the initial transient period. The fouling accumulation and sweeping effect came to equilibrium after 2 hours of work, resulting in the pseudo steady-state filtrate flux. This value would decrease for higher concentration fluids, but normalized filtrate flux seemed to be constant. In the range of tests, normalized filtrate flux increased by reducing the gap ratio or working at a higher rotation speed; a linear relationship was observed with Taylor number (Ta) when $\omega > 34.1$ rad/s [92].

A company 'Mebrex' [133], developed a Benchmark Biopurification System for the steroid recovery from yeast suspensions. It equips with a 100000 molecular weight cut-off hydrophilized polyacrylonitrile membrane (0.02 m² surface area). Steroid recovery in the permeate showed a significant increase with the Taylor number and obtained the best recovery conditions at $Ta=2346$ (2000 r/min).

Lee and Lueptow [63, 72] took advantage of Taylor-Couette flow instabilities to reduce the flux decline related to concentration polarization and membrane fouling in reverse osmosis. Commercial polymeric RO membranes with an outer radius of 2.41 cm and length of 12.7 cm (corresponded to the total area of 0.0192 m²) were applied in the filtration of space mission wastewater (wash water, condensate, and urine). Rotational speed and TMP showed to enhance the flux and rejection in rotating RO [72]. In the concentration test of CaSO₄, the permeate flux for rotating RO at $\omega=180$ rpm remained constant up to a volume concentration factor (VCF) of 4.2. Further treatment would lead to a sharp decrease in permeate flux due to the scale formation of soluble salts [63].

With the same concept, a plasmapheresis filter was commercialized for plasma collection. An inner cylinder (capacity, 7 ml) was assembled in the filter, driven by a magnet, and rotated inside the cell. Blood was separated for the centrifugal force and reached into the collection system, which permits the collection of 500 mL of plasma within 30 min [171].

The last one was described by Amgar [172] in oily-water systems. Three parameters (membrane rotation speed, membrane radius and azimuthal velocity profile) were investigated, the rejection capacity of the membrane and fouling problem were reported. With the rotation of the membrane, due to the centrifugal force, the oil droplets will gather in the middle and reduce the membrane fouling. The rejection rate of the oil phase increase with the rotation speed and diameter of the membranes.

3.2.1.4 Rotating hollow fibre

One module equipped with hollow fiber (HF) membranes has been investigated in a rotating system, named rotating hollow fiber membrane (R-HFM) [47]. In a 3 L tank (inner diameter of 0.15 m), 97 fibers package were assembled vertically, and each fiber shows a length of 0.08 m with an outer diameter of 1.9 mm. The membrane modules have an average pore size of 0.04 μm and a nominal membrane surface area of 0.047 m^2 . Compared with the conventional strategy, HF membranes were immersed in the filtrate, but one top header of membranes rotated to restrict the cake layer formation. In the UF of anaerobic suspensions, the fouling rate increased with permeate flux. The turbulence promoters were introduced to evaluate the effectiveness of fouling limitations. With the increase of permeate flux from 8 to 14 $\text{L}/(\text{m}^2\cdot\text{h})$, this value decreased from 44.4% to 40.7% within the conventional gas-sparging membrane module, while sharply improving to 96% and 93% at the rotation speed of 260 rpm [47].

3.2.2 Rotating mechanical device module

3.2.2.1 Rotating disk

Unlike the rotating membrane system, the filter cake layer formation was limited by the rotation of external mechanical devices (such as disks, impellers or cylinders). 9 rotating disk modules (14 configurations) have been well documented in the literature. They solved the problem of flux decline by the design of inlet/outlet, disk structure, and the distance between rotating disk and membrane, mixing rate and TMP.

Dynamic Membrane Filter (DMF, Pall Corp., Cortland, NY) appeared as the first commercial system [134, 153, 187]. This filtration unit houses a 6-in.-diameter stainless-steel

solid disk with a maximum rotating speed of 3450 rpm rotating in the clockwise direction only. The gap between the membrane (7.5 cm radius and a total area of 0.0137 m²) and the rotating disk is 4 mm. The feed entered the system from the center at the bottom side of the rotating disk, flowing into the gap between the stationary membrane and disk toward the center where the concentrate or retentate was collected. Lee et al. [134] used this system installed with the MF membrane to filtrate yeast suspension. Results showed no significant difference in flux with three different membranes (PVDF, 0.45 and 1.2 μm pore size for Nylon). Both Nylon membranes reached steady flux earlier than the PVDF membrane, at about 40 min. But 1.2 μm Nylon membrane performed better by 1.4 times higher than the 0.45 μm one according to their concentration factor profile. Moreover, compared with the conventional cross-flow system, steady flux and average shear rate of DMF were 100 L/(h·m²) and 12000 s⁻¹, which were 5 and 7.5-fold higher than cross-flow systems, respectively.

Rotating Disk Module (RDM) has been largely reported concerning the filtration performances [11, 14, 15, 33, 43, 66, 67, 70, 71, 74, 75, 87, 88, 99, 106, 108, 110, 114, 115, 141, 174-184]. 2 modules were built similar to DMF, but with different sizes, both include a disk that rotates inside a cylindrical housing around a hollow shaft, through which the retentate is evacuated. But the larger module (RDM-2) receives a 460 cm² annular membrane area, compared with a 190 cm² flat disk membrane in a smaller one (RDM-1). The module performances for 5 inlet/outlet configurations (lateral housing wall, back plate or axial) were compared at a 3 mm disk-membrane gap. The highest permeate flux was obtained at high speeds with the inlet at the backplate and axial retentate outlet. With the increase of the disk-membrane gap from 4 to 18 mm, almost no effect on the permeate flux was observed. In the gap of 10 mm, by equipping the disk with nylon mesh in module 1, or eight pairs of 2-mm aluminum rods in module 2, permeate flux increased due to the increment of core velocity coefficient [174]. The gap ratio (disk-membrane gap divided by disk radius) seems relevant to this coefficient [11, 15, 183]. Bouzerar et al. [88] applied RDM in MF of CaCO₃ suspension. First, the disk speed was decreased in steps from 1500 rpm to rest in order to evaluate steady-state flux. Then speed was raised again to 1500 rpm to investigate the irreversibility of fouling. Initial peripheral pressure was fixed at 15 kPa, and experiments were performed with 0.1 μm PVDF membranes. Final permeate flux almost kept the same value but represented only 64% of the initial one when conducted at 50 kPa. When the rotation speeds up to 1100 rpm, permeate flux increases with radius, and fouling almost disappears at $r > 4$ cm. But in the central part, relatively lower local velocity was not able to eliminate the cake layer. In dairy wastewater treatment [66], the RDM configuration was a

disk equipped with 4 pairs of 6 mm-high vanes (disk membrane-gap not specified), which can rotate up to 2500 rpm. Performances were scrutinized versus shear rate (0.169×10^5 to $2.05 \times 10^5 \text{ s}^{-1}$), TMP (3 to 7 bar), temperature (35 to 55°C) and membrane cut-off (30 to 10 kDa). Flux decline was observed due to membrane blocking by lactose and milk protein. Shear rate and TMP showed a great effect on membrane fouling control and contributed to the cleaning process. Evaluating the membrane permeability recovery rate, concluded that a high shear rate combined with a cleaning agent is more conducive to fouling elimination. Low TMP presented that the concentration polarization of casein micelles and the cake layer was reduced on the membrane surface [71]. In the concentration tests of leaf protein (MF, UF), Zhang et al. [114] modified the loop operation of the RDM module into the retentate recycling process (CRDM) and retentate non-recycling process (DRDM). At rotation speed of 1000 rpm, TMP of 3 bar for MF and 4 bar for UF, results indicated the least flux decline, smallest irreversible fouling and highest permeability recovery after membrane cleaning in CRDM, while DRDM obtained the best leaf protein rejection due to the secondary filtration effect. In the treatment of detergent wastewater, NF was performed after the pre-treatment in UF. The permeate flux in NF increased linearly with TMP to reach 450 L/(m²·h) at 40 bar at the rotation speed of 2000 rpm, while it reached a plateau at 350 L/(m²·h) above 35 bar without pre-treatment in UF. The rejection of conductivity and COD could be more than 90% when the TMP is up to 20 bar. Increasing feed pH (4.5 to 9.9) and temperature (25 to 45°C) seemed to enhance electrostatic repulsion and led to the increase of permeate flux, but conductivity rejection showed the opposite trend [43]. In this rotating system, the net power consumed by the rotating disk was proportional to the square of rotation speed. Disk with vanes presented much higher net power than smooth disk in the same condition. However, it was opposite with specific energy consumption [74, 141]. There were other studies focused on various test fluids [15, 43, 54, 55, 67, 96, 99, 110, 117, 142, 143, 190, 230], and were often compared to the other DF systems [11, 69, 75, 87, 97, 102, 103, 106-108, 113, 231].

The anti-fouling membrane filtration system (FMX) was produced by BKT Water & Energy (Korea), equipped with high-speed rotating vortex generators. They were veined discs and had two uneven and asymmetric surfaces. Standard class FMX-S and economic class FMX-E were proposed with a filtration area of 95 m² and 40 m². In the pilot-scale, FMX-P compacted several membranes on the rotating shaft in series and reached the space between 0.0873 m² to 3.16 m² [188]. FMX-B only equipped one rotating disk of 145mm diameter and 10mm thickness in the filtration cell (20 mm height). Membrane (surface area of 0.0146 m²) was installed at the bottom of the module, while the feed inlet and concentrate outlet were

connected to the upper surface. With this module, a CFD simulation was performed by Kim et al. [123]. Fluid velocity and average shear stress of a perforated disk on the membrane surface were found to be 2 and 7-fold higher than an unperforated disk, respectively. As the average shear stress increased from 0.23 (0 rpm) to 28.99 Pa (800 rpm), the microalgal fouling resistance reduced by 87%, and the plateau permeate flux was increased 6.7-fold to 381 L/(h·m²). Effect of rotation speed, TMP, membrane cut-off or biomass concentration on filtration performances had been illustrated to be associated with permeate flux and fouling resistance [126, 128].

Another rotating disk module derived from Central South University (China) was assembled to separate heavy metal from wastewaters [185, 186, 232]. It shared the same configuration of the inlet and outlet with the RDM module. A disk with a radius of 83 mm was driven by a rotating shaft in an 88 mm inner radius circular housing, enable to speed up to 3000 rpm. The model waste of lead nitrate was fully complexed with poly acrylic acid sodium (PAAS) or copolymer of maleic acid and acrylic acid (PMA), then removed by UF. These metal complexes were sensitive to the high shear rate. The results indicated that the critical shear rate of the PMA-Pb complex was less than that of the PAA-Pb complex. But the former case was preferred for the treatment of lead contained wastewater due to its higher load capacity of Pb (II) and easier regeneration [232]. For the separation of Zn (II) from aqueous solutions, the critical shear rate for PAA-Zn complexes was $1.58 \times 10^5 \text{ s}^{-1}$ at pH 7.0 [186]. Another publication investigated the critical speed of two disks (smooth disk and disk with 6 vans) to remove the PAA-Cd complex. The critical shear rate for both disks was calculated to be $1.31 \times 10^5 \text{ s}^{-1}$ at pH 6.0, and the rejection of Cd reached 99.7% [185].

A rotating-disk dynamic filter was designed by Tamkang University (China) [57, 82, 93, 121]. The diameter and height of the chamber are both 38 mm. Two vanes (10 mm×10 mm×1 mm) are placed beneath a rotating disk with a diameter of 30 mm. A low circular inlet and a high circular outlet are connected to the chamber for feed inflow and concentrate outflow. A circular membrane is installed on the porous bottom plate with a filtration area of $1.12 \times 10^{-3} \text{ m}^2$ [121]. In MF, SiO₂ was separated from artificial seawater. The pseudo-steady filtration flux was only 1.65 m³/(m²·s) for a static disk, but it increased by 170% as ω increased to 500 rpm at a distance of 1.5 mm between vanes and membrane. This increase in the flux was more considerable for a smaller gap of 0.8 mm, and the filtration flux increased 2.4-fold as ω rose from 0 to 500 rpm [57]. From another article, 2 vanes disk (Type 1), 4 vanes disk (Type 2) or 2 vanes disk with circular orifices (Type 3) was able to rotate 15 mm above the membrane. It indicated that increasing the disk rotation speed or the number of vanes improves the mean

filtration flux, and the holes in the disk have no effect on flux enhancement. The specific filtration flux (flux divided by energy) could be ordered as Type 3 > Type 1 > Type 2, and it also decreased with the increase of rotation speed [93]. For the same purpose, a larger module with a filtration area of 0.0377 m² was established by Hwang et al. [124]. By modifying the disk, 6 types of disks were constructed with different concepts (distance between disk and membrane, number of vans and vans' structure). Considering the filtration flux and power consumption, disk and disk with 2 vans (has an uneven rectangular cross-section) showed to be the optimal designs, and even 4 uniform vans could generate the highest shear stress and result in the highest permeate flux.

A particular configuration of the rotor could be observed in the controlled shear filtration (CSF) module [144]. It has a conical rotor (inclination angle of 4°) of 70 mm diameter rotating at 0.2 mm above a PVDF membrane (51.5 cm² effective filtration area) for MF of recombinant BHK cell suspension. The threshold level of shear stability was determined during the sharp decrease of cell viability for the step improvement of rotating speed. An optimal growing cell showed better resistance with shear stress up to 17.2 N/m² instead of 7.12 N/m² for a lower growing cell. Compared with traditional cross-flow filtration, constant flux 30 L/(h·m²) and cell viability percentage 83% greatly improved to 97%-91%, 290 L/(h·m²) with CSF, respectively. Almost with the same configuration, the controlled shear affinity filtration (CSAF) module was investigated with CFD simulation. A new rotor (0.2 mm gap to the membrane) was designed with a variable inclination angle, which permitted the constant shear stress at all radial positions except the center-point. Meanwhile, the threshold shear stress of 0.17 Pa was achieved across virtually the entire membrane surface at a rotor speed of 250 rpm. It was 60% less than the rotor speed required in the original CSAF device [190].

In rotating cross-flow (RCF) MBR [7], a 156 mm radius of the membrane is placed in the support. With a gap of 5 mm, a disk of 140 mm radius can rotate between 50 and 350 rpm. In a single-use medical product LIFE 18-Disk Separator, which was designed to separate plasma from whole blood, two membranes are configured with a spinning disk rotating between them within a plastic housing and only reaches 50 ml for the volume [189].

3.2.2.2 Rotating impeller

Similar to the rotating disk module, the shape of the impeller also draws much attention. 3 modules were developed into 10 configurations by compacting even up to hundreds of membranes in the filtration cell and increasing the diameter of membranes for large-scale applications.

Cross Rotational Filters (CR-filters) were designed by Metso-Paper corp., equipped with two-blade impellers between two membranes. The company proposed several scales for users; the diameter could range from 200 to 1010 mm, e.g., the Opti Filter CR-1010/100, with 100 cassettes of 1010 mm diameter, achieves filtration area up to 140 m² [192-194, 233]. The DYNO (Bokela GmbH, Karlsruhe, Germany) filter was installed with a blade-like rotor for each filtration cell and reached 12 m² of total membrane area [191]. The same concept also has been applied to the Rotating and Vibrating Filtration (RVF) module. A lab-scale RVF module has two identical filtration cells. Each consisted of a three-blade impeller with 135 mm diameter and 8 mm thickness, rotating in a 14 mm gap between two porous substrates, which can operate up to 50 Hz [6, 111].

Gursch et al. [150] reported the continuous manufacturing of active pharmaceutical ingredients with a lab-scale Dynotest system, aluminum oxide disk membranes (0.5 μm) were equipped with a total filtration area of 0.013 m². A material-dependent linear relationship of the permeate flow as a function of cumulated feed flow was found with different fluids; slope k made it possible to establish a constant concentration factor to predict filtration performance for any given product.

In the paper industry, Jutta et al. [196] described the UF process with a CR module; polymeric and ceramic membranes ranging from 8 to 200 kDa were tested. It was shown that the relatively low cut-off (30 kDa) hydrophilic C30G membrane made from regenerated cellulose had higher fluxes both at neutral and acidic pH. It could last six days of filtration with good permeation. The same reports also have been investigated in NF and RO [194, 233].

Rayess et al. [112] employed MF (PES and PTFE, 0.2 μm) with the RVF module in wine clarification. In the filtration of crude simulated wine, the permeability of PTFE membranes was slightly higher than PES membrane with $N=0$ Hz, but it is the opposite during filter wine filtration respectively, for 1676 L/(h·m²·bar) (PES) and 170 L/(h·m²·bar) (PTFE). When N was increasing, PES seemed to be sensitive to the mixing effect, while PTFE showed to be unaffected by the frequency increase. Fillaudeau et al. [111] also tested two ceramic membranes (0.6 to 4 μm) with rough beer. In this research, the driving force at the membrane surface and the core velocity coefficient associated with fluid dynamics were determined with water. Afterward, the performance of RVF was evaluated for two different rough beers and model beers, which resulted in the ceramic membrane achieving a more satisfying quality and flux value than traditional filtrations.

3.2.2.3 Rotating cylinder

As discussed in the rotating cylinder membrane, studies on fixed membrane cylinders have also been reported. 2 modules have been designed in the lab-scale application.

The application of helical Couette-Taylor flow (CTF) [52] could help to reduce fouling in the process of filtration. A tubular membrane module is configured with a tubular metallic membrane (diameter of 30/34 mm, filtration area of 0.04 m²) as a housing and a coaxial inner cylinder as a rotor (diameter of 20 mm). In order to be applied to radioactive wastes, cobalt ions solution was fed in UF with the metallic membrane. After 720 min circulation, the permeate flux decreased to 8 L/(m² s) without mixing. Due to the instability of the flow, it was almost 3-fold when the inner cylinder was rotating up to 1500 rpm. Further improvement in the rotation speed seemed to have little effect on the permeation [52]. The optimal hydrodynamic conditions were established by response surface methodology. The maximal permeate flux and the minimal flux decline were observed at TMP of 70kPa, retentate flowrate 108 L/h and rotating speed of 2800 rpm [53].

DYNAMIC HPHT Filtration system [201] equipped with a rotating cylinder, which could simulate the build-up of filter cake on the formation. A 6.3 mm thick porous walled cylinder (inner diameter of 25.8 mm) as the filter medium and rotating shaft of 19 mm diameter is placed within a 250 ml high-pressure and high-temperature cell. The mud sample sheared in the annulus formed between the inside diameter of the filter core and the rotating shear shaft. A ceramic filter (5-90 μm) was used in the MF of the drilling fluid. The experimental results fitted with the Boluk-Balavi equation, which could help evaluate the spurt loss volume, the initial rate of fluid volume loss (flux), blocking and cake erosion in DF [201].

3.2.3 Rotating disk and membrane module

The request for DF of large shear stress led to the introduction of a rotating disk and membrane system (2 modules). Disk and membrane are mounted on different shafts and could rotate in the reverse direction.

A shear-enhanced system, namely rotating disk-membrane (RD-M) module, was investigated on microfiltration of black liquor [41, 42], Ultrafiltration of PEG 6000 and Bovine serum albumin [58, 60, 147]. The membrane was placed on disk-shaped porous support with an effective filtration area of 24.6 cm². A stirrer is provided inside the cell, having the same diameter as that of the membrane. They rotate in the opposite direction and give a maximum shear rate of $2 \times 10^5 \text{ s}^{-1}$ at the membrane surface. In the UF of BSA, the

increment of membrane rotation speed, stirring speed, and TMP are likely to improve the permeate flux. It has been demonstrated that 79.7% of steady-state permeate flux decreased on increasing bulk concentration from 1 g/L to 30 g/L, resulting in the mean residence time increasing from 0.17 s to 0.28 s. However, TMP did not affect residence time by increasing 294 kPa to 882 kPa [147]. The influence of membrane disc rotation was found to increase the flux substantially, more than so obtained by stirrer rotation. Nevertheless, the pre-treatment steps proved to be highly efficient in minimizing flux decline [41, 42].

By modifying dynamic cross-flow filtration (DCF), Johannes et al. [105] described a new module. Two rotating shafts equipped with two ceramic membrane disks and one smooth metal blind disk individually, resulting in a membrane filtration area of 0.14 m². The disks from each shaft overlapped each other by 26.4% of their surfaces. As a result, MF (0.06 µm pore size) of pasteurized skim milk (3.4%, w/w, protein) could preferably be applied in small-scale manufacture of milk retentate for protein contents of $\geq 14.8\%$ (w/w).

3.3 Oscillating system

Considering the movement part, oscillating could happen in the whole filtration cell (3 modules with 12 configurations) or just occur in the membrane (9 modules with 9 configurations). These motions could be azimuthal, horizontal or axial oscillation. In addition, the spacer oscillation (1 module) also promoter turbulence in the flow.

3.3.1 Oscillating filtration cell modules

3.3.1.1 Oscillating disk cell

Disk membranes are placed on the support to permit the collection of permeate and filtration cells oscillated in the azimuthal direction to generate high shear stress. With this knowledge, 2 companies have designed 11 configurations in lab and industrial applications.

Commercialized by New Logic (USA), vibratory shear enhanced processing (VSEP) [10, 34, 44, 84, 100, 101, 127, 131, 202] represented the first vibrating filtration device. These filtration bodies, consisting of alternative overlapping membranes or membrane-coated disks in series, are mounted on a torsion bar driven by a motor. It can reach 130 m² filtration area per module and scale up by installing more membrane modules. A similar principle was introduced in the vibrating membrane filtration module (PallSep-VMF) [204]. Industrial VMF biotech modules were available in 0.2, 1 and 5 m² surface areas for more flexibility and easy scale up or scale down [205].

The VSEP L101 was a relatively small pilot-scale module. An annular membrane with an area of 503 cm² in a circular housing (with a gap of 3.5 mm) is placed at the top of a vertical shaft, and driven by a torsion spring. This shaft amplified the vibrations to reach the amplitude from 6.35 to 31.75 mm, corresponding to the frequency between 55 and 60.75 Hz. The feed and retentate channels are distributed on both sides of the rotating shaft at the bottom plate. The permeation through the membrane was collected through the holes in the membrane plate support [202]. Akoum et al. [10] investigated the MF of yeast suspensions and the UF of BSA solutions with this module. In the case of yeast MF, the permeate flux was found to be proportional to $\gamma^{0.19}$ at a frequency below 59.7 Hz and to $\gamma^{0.50}$ at a higher frequency. In the UF of BSA, the permeate flux was proportional to $\gamma^{0.426}$ at all frequencies. As for the treatment of dairy process water, the membrane oscillated at 60.75 Hz and 40 bar, the highest permeate flux in NF was 270 L/(m²·h) and the initial COD reduced from 36000 to 94 mg/L. While in RO, final permeate flux was 240 L/(m²·h) and 36 mg/L COD [68]. Frappart et al. [69] compared the filtration performance of VSEP and RDM with dilute skim milk in RO. The permeate flux for the VSEP working at resonant frequency (60.75 Hz) was very close to the result for RDM rotating at 2000 rpm. The same device has also been applied to other suspensions, such as tannery wastewater [202], latex solution [84], metal working emulsions [76] and microalgae [34, 125, 127].

PallSep PS10 VMF unit consists of two membrane discs, both covered with a hydrophobic PTFE membrane on both sides, giving a total membrane surface area of 0.2 m². The feed is delivered to the first membrane disc through a feed channel at the bottom endplate of the VMF membrane assembly. Each membrane disk has 18 circular holes (8.5 mm diameter), whose 12 holes are located at 270 mm on the outer edge and 6 holes at 26 mm in the inner diameter of the disc. The fluid then flows outward in the retentate channel and inwards tangential to the membrane surface towards 6 equally spaced, which is collected in a series of grooves and exits the VMF system through the top end plate permeate port. In the recycle mode of 200 g/L yeast suspension, a decline in permeate flux was observed until a steady-state was achieved after about 20 min with the vibration at 19.5 mm amplitude. Without any vibration, permeate flux fell to zero in 10 min at the same cross-flow rate of 1 L/min. In the concentration tests of yeast suspension, increased the gap width from 1.4 to 4.2 mm, the maximum solids loading capacity was improved from 561 to 633 g/L. It also indicated that the volume concentration factor would increase with a larger gap width [204].

3.3.1.2 Oscillating rectangular cell

Another lab-scale oscillating filtration cell is vibration enhanced reverse osmosis

(VERO) [56, 64, 234], derived from Texas A&M University (USA). A linear actuator was used to vibrate the RO membrane desalination cell at the given vibration curve shape, frequency, and amplitude. Feed solution enters from the left feed port at the top plate, flows into the membrane channel, and leaves the desalination cell through the retentate port on the other side of the top plate. The permeate flow is collected by the permeate carrier and flows out through the permeate ports at the bottom plate. The height of the feed channel is 0.78 mm and placed with a feed spacer, which is just above the flat rectangular membrane of 60 cm² (20 cm×3 cm) filtration area. With this module, Su et al. [56] investigated the desalination of artificial seawater in 3 feeding flowrates related to Reynolds numbers 344, 516 and 688, respectively. Increasing in flowrates led to the decrease of NaCl and CaSO₄ concentration polarization (CP) module without vibration, owing to the sweeping effect of flow. In the vibration cases, shear stress was further increased by the vibration; CP modules decreased when the frequency changed from 20 to 50 Hz. Periodic oscillations caused the fluctuation in normalized permeate flux; the higher the vibration frequency is, the higher the permeate flux. CFD simulation also showed excellent agreement with the results over different Reynolds numbers.

3.3.2 Oscillating membrane module

3.3.2.1 *Oscillating rectangular membrane*

Compared with the oscillation filtration cell modules, another kind of device is realized by immersing the oscillating membrane in the filtered liquid. The principle of shear enhancement by the oscillating membrane is generally applied in a rectangular membrane. Different technics aimed to create the horizontal motion of membranes, and 4 modules are reported in recent publications.

The oscillatory flat surface membrane (OFSM) module was proposed by Goma et al. [137, 139, 206-209]. A flat membrane (filtration area of 0.06 m²) is mounted on a membrane frame, fixed with a metal mesh, and immersed in a yeast solution. A vacuum pump is used to collect permeate and control transmembrane pressure. Hydrophilic nylon membranes (0.22 μm) were used in the re-hydrated baker's yeast under the condition of 0-25 Hz (frequency), 3-30 mm (amplitude) and 0.2-0.6 bar (TMP). Increasing oscillation frequency or amplitude resulted in higher permeate flux; the effect of oscillation frequency was found to be stronger than the amplitude [137]. Using higher oscillation frequency and lower amplitude were found to be more effective for flux enhancement and energy utilization [139]. Furthermore, membrane surface equipped with both flat turbulence promoters and grooved turbulence

promoters has been proved to improve microfiltration flux further. The combined effect of oscillatory motion and turbulence promoters can result in substantial flux augmentation. Such an effect increased with increasing the oscillation frequency but decreased with its amplitude [139, 208, 209].

With the same concept, a magnetically induced membrane vibration (MMV) system [46, 211-215] consists of one or more flat sheet membranes and is mounted on a metal frame. The oscillation is created by the magnetic attraction/repulsion forces to alternate membrane modules that move up and down with a specific frequency and amplitude. For UF of bio-ethanol from the hydrolysate, 4 membranes were placed in series with a gap of 1 cm with a filtration area of 0.04 m². With undiluted feeds (extremely viscous), permeate and TMP showed the same trends with oscillation (frequency:10 Hz, amplitude: 6 mm) and without oscillation. However, these differences were enlarged with diluted feeds (dilution rate: 4 or 6 times). It also indicated that fouling control could be improved by suitable membranes (nature) and higher oscillating amplitude [214]. In other fields such as wastewater treatment, [46, 211, 212] microalgae harvesting [213, 215] has also been investigated.

Tongji University (China) has designed a constant-shear vibration device named the uniform shearing vibration membrane (USVM) [210] system. By the rotating shaft, the flat rectangular membrane (effective membrane area of 0.02 m²) installed on a cassette can be operated with a uniform circular motion (not rotating), which induces a constant shear rate at the membrane surface. On the membrane frame, there is an outlet connecting a tube, and the permeate can be taken away through the tube using a peristaltic pump. Another axial vibration membrane (AVM) [93, 217, 218] device that reduces membrane fouling by vibrating the shaft along the vertical axis was developed by the same lab. By controlling the servo motor and changing the structure of the rotating shaft, different vibration frequencies and amplitudes for both devices can be achieved. On a cassette, 1 to 100 flat membranes can be installed in the square frame (11 cm) with the distance between membranes from 1 to 50 mm. Zhao et al. [217] investigated AVM in microalgae harvesting; a 0.1 μm PVDF membrane was used to work at any frequency up to 15 Hz and amplitude from 5 to 40 mm. The critical flux is proportional to $\gamma_{max}^{0.2284}$; the motion not only prevents the deposition of algae cells on the membrane but also reduces the adsorption of extracellular organic matter on the membrane. The horizontal system (USVM) worked at a lower frequency (5 Hz) and amplitude of 20 mm; the same membrane was used. The TMP visibly reduced when the frequency increased from 1 to 5 Hz. Even at a relatively low frequency of 5 Hz, reversible and irreversible membrane fouling could also be limited [210].

3.3.2.2 *Oscillating cylinder membrane*

With the same concept, azimuthal or axial oscillation can be achieved with the cylinder membrane. 2 lab-scale modules were described, and the effect of oscillating frequency, amplitude or angle was investigated.

A cylinder membrane (14 mm outside diameter, 64 mm membrane working length) was immersed in calcite suspension, and two modes of oscillations were performed [219]. The axial oscillations can be operated with an adjustable displacement and frequency up to 100 Hz. The azimuthal movement oscillates at 3 degrees with 20 to 100 Hz, and the highest shear stress of 240 Pa is reached. The vibration mode did not influence the filtration performance, while it corresponded to the shear stress peak delivered by the oscillating system [219].

With a vibrating head, an axial oscillation of the slotted-pore nickel membrane is controlled up to 100 Hz (frequency) and 10 mm (amplitude) [79]. The fouling of the membrane pore area is reduced in the presence of the shear. Compared with crude oil, Tween 20-stabilized oil with decreasing interfacial tension and smaller droplet size, and led to a lower blocking area. The blocking constant at 1000 L/(m²·h) (permeate flux) was approximately five times smaller than 200 L/(m²·h), caused by the increased permeation of the deformable oil droplets [79].

3.3.2.3 *Oscillating hollow fibre membrane*

The principle of shear enhancement by oscillation has also been applied to hollow fiber membranes by attaching them to a sliding rod connected to a rotating head. 3 modules have investigated the oscillation of the HF membrane in the axial direction.

A Vibrating hollow fiber microfiltration (VHM) system [220] has 7 MF hollow fiber membranes (40 cm in length) with a surface area of 0.0057 m². They were potted in a cassette using Araldite glue and then submerged in a yeast suspension tank. This cassette vibrated using a 250 W electric motor at any frequency up to 10 Hz with an amplitude of 4 cm. A relatively monotonic increase in critical flux was observed during the frequency increase from 0 to 10 Hz. A two-step correlation between critical permeate flux and rotating frequency was established and separated in the frequency of 5 Hz [220]. A similar observation has been investigated by Jaffrin et al. [11] with RDM and VSEP. Specific critical flux was defined as the ratio between critical flux and specific power consumption. The peak value was observed at a low oscillating frequency below 2 Hz and followed by a subsequent drop to a low value as the specific power consumption increased [220].

The second module was described by the Technical University of Denmark [13, 136,

221]. The vibrating membrane bioreactor (VMBR) system consists of a module with hollow fibers fixed in parallel between a steel plate at the bottom of the module and a permeate gap at the top. Despite different versions of modules equipped with diverse membranes (filtration area range between 84 and 488 cm²) and liquid levels, these systems were almost identical. A total membrane area of 488 cm² is composed of 54 hollow fibers with a length of 12.5 cm; it oscillates with the displacement of 1.175 mm (the peak-to-peak amplitude is twice as big) and frequency up to 30 Hz. In yeast suspension, the PES membrane with a nominal pore size of 0.45 μm was tested, and the critical flux was improved up to the maximum oscillating degree. The correlation between shear rate and critical flux was similar to the oscillating rectangular membrane module [217, 221].

The last module was described by Li et al. [80]. Membrane modules (13 HFs with a length of 40 cm, inner/outer diameters of 1/1.7 mm and 1/2 mm) were aligned vertically in parallel, with the distance between two adjacent fibers of 15 mm, and driven by a rotating head. The vibration amplitude varied from 0 to 12 mm accurately, while the vibration frequency from 0 to 15 Hz. In a 4 g/L bentonite solution, experiments were conducted at both constants permeate flux and constant suction pressure conditions. In the constant permeate flux of 30 L/(m²·h), the fouling rate of 1.7 mm HFs was almost twice as in 2 mm HFs without oscillation. The fouling rate typically decreased when vibration was applied. There was an 85% reduction in the fouling rate when the 2 mm HFs vibrated with 5 mm amplitude and 5 Hz frequency, compared to no vibration. At constant suction pressure of -24 kPa, cake resistance implied that the larger fiber size could perform better in an oscillating system. As for the power consumption, 95% fouling reduction was observed with 8 mm amplitude and 10 Hz frequency, and consumed 16.6 W power. With the same setup, 21 W power was needed to achieve a 10% fouling reduction by 5 L/min bubbling rate [80].

3.3.3 Oscillating spacers module

Rotating or oscillating membrane/filtration cell involves the movement of membrane cassette and permeates inside of the membrane module. It requires a relatively high mechanical energy and a complicated membrane module. The alternative of a lightweight spacer in turbulence promoter permits to minimize the energy consumption regarding oscillation.

A submerged flat sheet membrane filtration system with vibrating spacers was introduced by Nanyang Technological University (Singapore) [223]. Two pieces of flat sheet membranes (8 cm×12 cm) with a total area of 70 cm² were mounted into a membrane module

and then submerged into a tank. With a distance of 0.1 or 1 mm, both spacers were placed at each side of the membrane module and enabled to oscillate at 1-2.5 Hz (frequency) and 0.8-2 cm (amplitude). At a distance of 0.1 mm between the spacers and membrane, the hill-like spacers more efficiently alleviated membrane fouling than smooth and grooved spacers. The increase in vibration frequency and amplitude led to the reduction of fouling, but the threshold operation presented to be 2 Hz and 1.2 cm with a hill-like spacer. As expected, spacer vibration consumed significantly less power ($<0.008 \text{ W/m}^2$) than gas sparging (5.7 W/m^2) under the comparable fouling control effectiveness [223].

3.4 Oscillating and vibrating system

A vibrating system is not helpful for the permeate flux due to the compacting/cleaning effect during the back-and-forth movement of the membrane, and a pure vibrating system does not exist yet. By the oscillation or vibration of HF membranes, transverse or axial movements may lead to a variety of flux directions, which correspond to the combination of oscillating and vibrating modes. Five devices at a lab-scale were investigated.

The transverse vibrating hollow fiber membrane system was reported and compared with the case of oscillating liquid [138]. The former one was driven by the rotor to vibrate the hollow fiber membrane, with the displacement varying from 0.5 to 5 mm. Another one performed the circular movement of a container (liquid) with an eccentric axis (fixed radius: 2.5 mm) and a frequency of up to 2200 oscillations per minute (36.6 Hz). MF of 100mg/L alginate solution with 0.2 μm HF membrane resulted in the permeate flux of $70 \text{ L}/(\text{m}^2 \cdot \text{h})$, increased to $105 \text{ L}/(\text{m}^2 \cdot \text{h})$ with the aid of a liquid oscillation frequency of 6.7 Hz. However, this method was limited to small-scale applications. Oscillating transverse motion via vibrating membranes was expected to be more practical for large-scale applications. The critical flux of 4 g/L yeast solution with the transverse membrane vibrations (10.3 Hz, displacement 2.5 mm) was found to be $40 \text{ L}/(\text{m}^2 \cdot \text{h})$, while it was $35 \text{ L}/(\text{m}^2 \cdot \text{h})$ under the oscillating liquid (at 10 Hz, displacement 2.5 mm) [138]. In the separation and concentration of milk proteins with 0.04 μm PVDF HF membrane, Chai et al. [224] summarized that the frequency of 10.3 Hz applied could fully reject the casein micelle and maintain very high transmission rates of whey proteins (α -LA and β -LG) and lactose.

Derived from the same institution (University of New South Wales, Australia), the axial vibration module was introduced [32]. 32 hollow fiber membranes (total membrane area: 0.0131 m^2) were arranged in a tube-like shaft, immersed in a 6 L filtration column and held in

place through a rod connected to an oscillation converter. This configuration allows the angular displacement to vary from 18.3° to 55°. Different yeast concentrations of 10, 100 and 200 g/L in MF had little effect on the permeate flux with the aid of oscillating or vibrating at 10.3 Hz. The critical flux was not sensitive to the packing density of HFs in the module but highly dependent on frequency [32].

The same idea was also applied in another module. Two ends of the hollow fiber membrane were potted together to access the permeable channel, 7 fibers with a length of 10 cm, resulting in a total membrane area of approximately 45 cm². Angular vibrations generated by the motor convertor worked with fixed angular displacement of 180°, and frequency controlled between 0 and 2 Hz. The results indicated the effects of angular vibrations on the fouling rate at the frequency of 2 Hz in the following order: algal cells (~97.4%) > debris (~93.6%) > intracellular organic matter (~81.8%) > extracellular organic matter (~52.3%). A poor effect was found on pore blocking due to a large portion of extracellular organic matter fouling [132].

Zhejiang University (China) introduced a vibrated submerged HF membrane module that achieved two motion modes by adjusting the vibrating shaft. The membrane was moved from forth and back in axial (mode-1) or left to right (mode-2) displacement through a sine wave pattern. Membrane oscillation could be vertical or parallel to the module, respectively. In the standard module (without oscillation), the steady-state membrane permeability was 3.27 L/(m²·h·bar), whereas mode-1 and mode-2 (optimal) were stabilized over 21 L/(m²·h·bar) at 20 rpm. Increasing the vibrating speed also helped reduce the permeability decline [227].

The San Bortolo Hospital (Italy) introduced the concept of mechanical vibration to the hollow fiber dialysis membrane system [225, 226]. Four types of shaking models were established to increase the shear rate at the membrane surface: i) longitudinal shaking produced the reverse flow in the central and peripheral region of a single hollow fiber; ii) transverse shaking developed a symmetric swirling to shaking direction and spiral flow path lines; iii) rotational shaking to longitudinal axis also developed symmetric swirling flow regimes inside the HF, but the local shear rate presented non-uniform distribution in the radial position of HF bundle; and iv) rotational shaking to the centroid resulted in lengthwise non-uniform hemodynamic enhancement and reached the maximum at the inlet and outlet [225].

4 Characterization of fluid flow in dynamic filtration

It is well known that the principle of dynamic filtration consists of creating relative motion between the membrane and its housing to generate a high shear rate at the membrane surface and/or oscillating flows. Among the advantages of DF devices, the ability to generate a high shear rate independently of the feed flow, the preservation of a high membrane permeability associated with the filtration at low TMP, and the reduction of the filtration loop volume can be highlighted. Combining all these factors limits the fouling propensity and compressibility at the membrane surface [15, 66, 88, 97, 106, 174], which appears as major advantages for UF and MF, especially for the filtration of biological matrices. Film theory stands as the most common theoretical approach to describe permeation flux independently of pressure for mass transfer limited system.

4.1 Global approaches

4.1.1 Dimensionless analysis

4.1.1.1 Reynolds number

The well-known Reynolds number, Re , is the most common number used in fluid mechanics to characterize the flow regime (laminar, transient or turbulent). It is defined as the ratio between the inertia forces and the viscous forces. For convenience, it is generally written in the form of a length scale, the so-called hydraulic diameter d_h , a velocity scale u and the kinematic viscosity ν of the fluid, as follows: $Re = \frac{ud_h}{\nu}$.

Due to the complex geometry and operating conditions encountered in dynamic filtration devices (enclosed rotating disc/ impeller, static or rotating membrane, oscillating and vibrating module), different expressions of the Reynolds were proposed (see Table II.7). Based on $\nu = \frac{\mu}{\rho}$, all equations are given with dynamic viscosity μ , where ρ is the fluid density.

Table II.7 Dimensionless numbers used to describe hydrodynamic within Dynamic Filtration device (d : diameter, u : velocity, Q : flowrate, r : radius, d_h : hydraulic diameter, r_h : hydraulic radius, d_o : outer diameter; d_i : inner diameter, u_z , axial flow velocity, N : mixing rate, d_m : rotor diameter, k : core velocity coefficient, ω : angular velocity, h : rotor height, α : inclination angle of conical rotor, s : characteristic length scale, F : oscillating/vibrating frequency, H : vertical distance).

Mode	Formula	Equation
Tube	$Re = \frac{\rho du}{\mu}$ or $Re_Q = \frac{\rho Q}{\mu \pi r}$	(II.1)
Equivalent tube	$Re = \frac{\rho d_h u}{\mu}$ or $Re_Q = \frac{\rho Q}{\mu \pi r_h}$	(II.2)
Annulus tube	$Re = \frac{\rho(d_o - d_i)u}{\mu}$	(II.3)
Axial flow in annulus	$Re_a = \frac{2\rho du_z}{\mu}$	(II.4)
Rotating system (mixing)	$Re_m = \frac{\rho N d_m^2}{\mu}$	(II.5)
Rotating system*	$Re_r = \frac{k\rho\omega r^2}{\mu}$	(II.6)
Rotating cone	$Re_s = \frac{\rho\omega(h + r\tan\alpha)^2}{\mu}$	(II.7)
Gap based Ekman number	$Ek = \frac{1}{Re_s} = \frac{\mu}{\rho\omega s^2}$	(II.8)
Oscillating/Vibrating system	$Re_v = \frac{2\pi FH^2}{\rho}$	(II.9)

As can be seen, the hydraulic diameter d_h is equal to the outer diameter of the tube minus inner diameter (d_o : outer diameter; d_i : inner diameter) for an annulus tube in Eq. (II.3). According to the different operating conditions, the velocity scale can be defined using flowrate Q , see Eqs. (II.1) and (II.2). However, when this annulus coaxial cylinder was fed by axial flow, it can be defined as the axial velocity [92, 235].

In the rotating system, the Reynolds number is calculated from the angular velocity ω as $Re = (\rho\omega r^2)/\mu$ or by mixing rate N as shown in Eq. (II.5). But in practical applications, angular velocity should be replaced by $k\omega$ considering the transmission of impeller velocity to the fluid. Reynolds number induced by rotating disk/impeller is described by Eq. (II.6). An axial Reynolds number of a rotating conical rotor system was given as Eq. (II.7), where the rotor height h and the inclination angle α were taken into account [144, 190]. And Reynolds number can be expressed as a reverse of the Ekman number Ek as Eq. (II.8) shows. Ekman number characterizes the ratio of viscous drag forces in a fluid to the Coriolis forces [236].

Four different flow patterns of rotating disk in a housing system were proposed by

researchers[7, 134]: Re_r is radial Reynolds number, z/R_m refers to the gap ratio (z is the distance between rotor and membrane, R_m is the radius of the rotor). With a flowrate equal to zero, four flow regimes (Table II.8) may appear in the filtration cell, and they have been described by Murkes & Carlsson (1988) [237]:

Table II.8 Four flow pattern in rotating system.

Re_r	z/R_m	Flow regime	Pattern
$<2-3 \times 10^5$	<0.05	Laminar	I
$<2-3 \times 10^5$	>0.05	Laminar	II
$>2-3 \times 10^5$	<0.05	Turbulent	III
$>2-3 \times 10^5$	>0.05	Turbulent	IV

Laminar regime I correspond to a small gap with Couette flow and pressure gradient. When it comes to laminar regime II, the gap is more critical, and limiting layers are developing at stator and rotor surfaces. Close to the rotor, centrifugal forces eject the fluid outwardly compared to the shaft, whereas, at the membrane surface (stator), radial velocity induced centripetal forces concerning the continuity equation. The thickness of the limiting layer on the stator surface is theoretically four times higher than on the rotor for an infinite disk. With this theory, limiting layers are separated in turbulent regime IV.

In the oscillating system, the flow is governed by various parameters (oscillation frequency, amplitude, gap). This system was early studied by Rosenblat [238], who used two parallel infinite plane disks, oscillate torsional driven by a common axis for a Newtonian fluid. The Reynolds number is defined as a function of oscillation frequency F and the distance between disks, shown as Eq. (II.9). It has been applied to a commercial VSEP system, and a Reynolds number could reach 3×10^5 [10, 125].

4.1.1.2 Taylor number

The flow between two concentric cylinders with the inner one is rotating, and an axial flow in the annulus cylinder. Due to the shear generated by the rotation, inertial forces tend to destabilize a system, whereas viscous forces tend to stabilize the turbulence. Taylor number (Ta) is defined as the centrifugal force due to rotation of a fluid relative to viscous forces, which is well discussed in Taylor-Couette flow [92, 173]. Taylor vortices would appear when the Ta reaches specific values. As shown in equation $Ta = \frac{\omega r_i z}{\nu} \left(\frac{2z}{r_i + r_o} \right)^{0.5}$, r_i and r_o indicate the radius of the inner cylinder and housing cylinder, respectively, z is the distance between them. When $z/r_i \ll 1$, it could be simplified with $Ta = \frac{\omega r_i^{0.5} z^{1.5}}{\nu}$. $Ta < 42$, the flow is in

laminar regime. Further increase the rotation speed, Taylor vortices start to form, and these vortices increase until 400 (as described in the transition zone) [239]. When the Taylor number is above 400, these vortices degenerate into fully developed turbulent flow.

4.1.1.3 Mass transfer

Dimension analysis of mass transfer (by analogy with heat transfer) lead to establishing the semi-empirical correlation between dimensionless numbers,

Sherwood (Sh), $Sh = \frac{k_m d_h}{D} = \frac{d_h}{\delta}$, Schmidt (Sc), $Sc = \frac{\nu}{D} = \frac{\mu}{\rho D}$ and Reynolds (Re), $Re = \frac{\rho d_h u}{\mu}$ such as $f(Sh, Re, Sc) = 0$, in laminar regime $Sh = A' Re^\alpha Sc^\beta \left(\frac{d_h}{L}\right)^\epsilon$ and in turbulent regime $Sh = A'' Re^\alpha Sc^\beta$ [18] (D : diffusion coefficient, k_m : transfer coefficient, d_h : hydraulic diameter, L : channel length, δ : thickness of limiting layer, μ : viscosity, u : velocity, ρ : density).

For laminar flow in a thin rectangular channel [240-242], Sherwood was presented with Graetz-Lévêque's correlation): $Sh = 1.62 \left(Re Sc \left(\frac{d_h}{L}\right) \right)^{1/3}$ with $100 < Re Sc \left(\frac{d_h}{L}\right) < 5000$. By rearranging, it becomes $k_m = 1.62 \left(\frac{u D^2}{d_h L}\right)^{1/3}$ and $k_m = 0.816 \left(\frac{\gamma}{L} D\right)^{1/3}$ with $\gamma = 8u/d_h$. In turbulent regime (Dittus-Boelter's equation): $Sh = 0.023 Re^{0.80} Sc^{1/3}$ with $Re > 10000$.

In an agitated cylindrical vessel, Colton [243] has proposed the following correlation: In laminar boundary layer, $8000 < \frac{\omega r^2}{\nu} < 32000$, $Sh = 0.285 \left(\frac{\omega r^2}{\nu}\right)^{0.55} \left(\frac{\nu}{D}\right)^{0.33}$. In turbulent boundary layer, $32000 < \frac{\omega r^2}{\nu} < 82000$, $Sh = 0.0443 \left(\frac{\omega r^2}{\nu}\right)^{0.75} \left(\frac{\nu}{D}\right)^{0.33}$. Both cases share the same exponent of Schmidt and similar Reynolds, but the slope is higher at mixing condition.

These relations make it possible to evaluate the mass transfer coefficient, k_m . It leads to determine how membrane geometry and operating conditions may be selected to improve the filtration flux. These expressions require the identification of diffusion coefficient, D of solutes retained by the membrane in water (solvent). These relations highlight that flux may increase if flowrate increases or the cross-section reduces. From a general standpoint, all hydrodynamics techniques to increase flow velocity and the shear rate at the membrane surface enable to increase flux [240]. In microfiltration, various recent theories take into account the hydrodynamics: i) lateral migration of particles (tubular pinch effect), ii) axial migration of deposit (flowing cake) or hydrodynamic diffusion generated by shear rate (shear-induced diffusion). To enhance the understanding of the transfer mechanism in the membrane process, it seems essential to investigate and characterize hydrodynamics (velocity field, shear rate, flow regime) at local and global scales.

4.1.2 Friction and power consumption curves

In a mixing device, the power consumption curve is the representation of the Power number, N_p (Eq. (II.10)) against the mixing Reynolds number, Re_m (Eq. (II.5)). The characteristic curve integrates the tank configurations, fluid rheological behaviors and operating conditions. The mixing Reynolds number informs about the flow regimes while the Power number N_p is associated with power consumption (P).

$$N_p = \frac{P}{\rho N^3 d_m^5} \quad (\text{II.10})$$

In a continuous process, the friction curve represents Darcy's number, Da (Eq. (II.12)) against Reynolds number, Re_Q (Eq. (II.11)). This curve predicts the frictional energy loss in a pipe or equivalent pipe based on the geometrical properties, fluid characteristics and operating conditions. The friction curve can be described using a unique expression (Eq. (II.13)) based on Churchill's model [244]. This general expression can be used for laminar, transitory or turbulent flow regimes.

$$Re_Q = \frac{\rho u d_h}{\mu} = \frac{2\rho Q}{\mu \pi d_h} \quad (\text{II.11})$$

$$Da = \frac{8\tau_p}{\rho u^2} = \frac{\Delta p d_h}{4L\rho u^2} \quad (\text{II.12})$$

$$Da = \left(((Da)_{tur}^{n1} + (Da)_{tran}^{n1})^{\frac{n2}{n1}} + (Da)_{lam}^{n2} \right)^{\frac{1}{n2}} \quad (\text{II.13})$$

The friction (Fig. II.7) and the power consumption (Fig. II.8) curves of the RVF module were previously established [6] and aim to predict the pressure drop and energy demand for mixing. Considering Churchill's model, a unique correlation between $Da/Da_{N=0}$ and $Re_Q^{0.72}/Re_m^{1.08}$ was proposed. It indicated that this friction is related to the mixing rate and flowrate (laminar flow regime: $Re_Q < 3$, $Re_m < 2000$, transition flow regime: $3 < Re_Q < 50$, $2000 < Re_m < 300000$ and turbulent flow regime: $Re_Q > 50$, $Re_m > 300000$). On the opposite, the power number seemed to be independent of the flowrate.

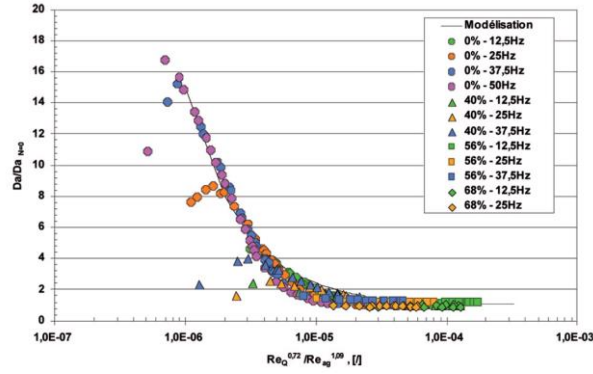


Fig. II.7 Friction curve established with RVF lab-scale module [6]

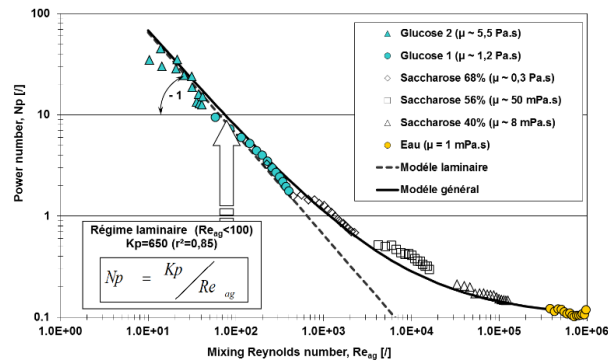


Fig. II.8 Power consumption curve established with RVF lab-scale module [6]

4.2 Semi-local approaches

4.2.1 Radial pressure and core velocity coefficient

In the rotational DF device, the mechanical pieces in rotation and fluid flow generate additional radial pressure. The core velocity coefficient appears as a critical parameter to define the additional pressure, whose value is a complex function of the gap, radial position, mixing rate and geometry of the rotating disk (smooth disk, modified surface disk, flat blade mixer).

4.2.1.1 Radial pressure

The impact of additional pressure due to mixing was studied previously [6, 111, 112]. Permeate flux J is calculated according to Darcy's law,

$$J = \frac{Q_p}{S} = \frac{\Delta P}{\mu_p R_h} = L_p \Delta P \quad \text{with} \quad \Delta P = \frac{(P_{in} + P_{out})}{2} - P_p \quad (\text{II.14})$$

where J : flux, Q_p : permeate flowrate, S : membrane surface area, ΔP : the transmembrane

pressure, μ_p : the permeate viscosity, R_h : the total hydraulic resistance, L_p : the permeability, P_{in} , P_{out} and P_p are respectively inlet, outlet and permeate pressures.

Bouzerar et al. [11, 174, 241] indicated that in the core fluid layer, fluid velocity could be calculated by $2\pi kN$, where k is the core velocity coefficient inferior to 1. The core velocity coefficient highly depends on system geometry, such as the configuration of the mixer, the distance from the mixer to the membrane. Therefore, the radial pressure gradient in the core layer can be expressed by:

$$\frac{\partial p}{\partial r} = \rho r (2\pi kN)^2 \quad (\text{II.15})$$

$$p(r) = p_0 + \rho g z(r) + 2\rho (k\pi N)^2 r^2 \quad (\text{II.16})$$

where p is the pressure and R is the radius.

The pressure field is then obtained by the integration of Eq. (II.15), and achieved the mean additional pressure by Eq. (II.16) over the membrane area from R_0 to R_{max} . Due to the specification of impeller design [111], the hydrodynamic perturbation generated by this three-blade impeller in the gap (membrane to impeller) is different from a full flat disk. This perturbation includes the contribution of rotation speed (N) and additional pressure fluctuation (ΔP_{ag}). Additional pressure ΔP_{ag} deduced by measuring the flux versus the radial position and the rotation speed (Fig. II.9). The flux was measured versus the frequency and compared to the case rotation speed equal to zero (Eqs. (II.17) and (II.18)):

$$J(0, R \text{ to } R + dR) = \frac{\Delta P}{\mu_p R_h} \quad (\text{II.17})$$

$$J(N, R \text{ to } R + dR) = \frac{(\Delta P + \Delta P_{ag}(N, R))}{\mu_p R_h} \quad (\text{II.18})$$

where R_h is the hydraulic resistance of the clean membrane. Transmembrane pressure can be expressed by $\Delta P = p(r) - \Delta P_{ag}(N, r)$.

TMP is related to the permeate flowrate in dynamic filtration. Fig. II.9 showed the linear relationship between the additional pressure induced by the rotating impeller with R^2 . The rotating disk equipped with 8 vans increases peripheral pressure in the filtration cell [174]. Fillaudeau et al. [111] have investigated the local pressure by replacing the membrane with radial permeable crowns in a rotating system. A 5 mm gap permits measurement of the radial pressure at the membrane surface. The final results agree with the empirical equation (Eq. (II.15)) and almost share the same core velocity coefficient with the same configuration [111, 174], indicating that the k value could help to estimate the local pressure. It means that local pressure is highly dependent on the configurations of devices and operating conditions.

Furthermore, many efforts (special-designed rotors [93, 124, 174], inserts [62, 104], turbulence promoters [139, 223], and aeration [215]) focused on the improvement of shear stress by generating the disturbance of flow, which resulted in the variation of local pressure over time. The fluctuation of local pressure should be further investigated to reveal the benefits of non-stationary effects on the improvement of filtration.

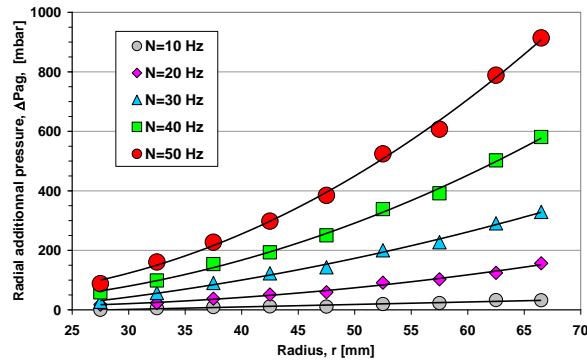


Fig. II.9 Determination of hydrodynamic performances, evolution of the radial pressure distribution versus the radius and the rotational speed [6]

4.2.1.2 Core velocity coefficient

Core velocity coefficient, k , the ratio of mean fluid velocity to impeller velocity, is one of the critical factors that present the mechanical efficiency of the rotating system as an indicator to quantify the mechanical efficiency. The k for different configurations of DF modules were displayed in Table II.9.

The flow between a stationary and a rotating disk system was early studied by Wilson et al. [245]. They proved that the flow pattern between these two disks was different. Radial flow close to the rotor was centrifugally outwards, and it was directly inwards close to the stator. Two cases had different boundary layers, and the suction effect reduced the thickness. Then a concept of rotation rate was presented and equal to 0.3131 at $Re=10^4$; it characterized the fluid rotating at an angular velocity of $0.3131 \times 2\pi N$ with the rotor rotating at $2\pi N$.

Most people are likely to be interested in improving k by increasing surface roughness or modifying device configurations. The flow field between a stationary membrane and a rotating disk was studied by Bouzerar et al. [174]. The velocity coefficient was influenced by system geometry and configuration, to be 0.34 for a smooth flat disk, and rise to 0.62 for a flat disk equipped with vanes. Furthermore, this influence was further investigated by Brou et al. [15] by modifying the distance of the disk to the membrane, and they found that the coefficient rises from 0.45 with the smooth disk in 17 mm gap to 0.65 in 15 mm gap for disk equipped with eight pairs of 2 mm thickness vanes. In addition, a disk equipped with more

vans or vans with larger height but with the same gap between disk and membrane has been confirmed to be useful in increasing the core velocity coefficient. The disk has reached a larger k value (0.84) with eight pairs of 6 mm thickness vanes [15, 183]. As for another rotor, a three-blade impeller in a 3 mm rotor-to-membrane gap has been performed in the RVF module with k equal to 0.71 [111].

Table II.9 Core velocity coefficient of different DF filters.

Module	Rotor	z (mm)	z/R_m	Flow regime	Testing fluid	k	Ref.
Rotating infinite disks	One disk rotates	/	/	/	Reynolds numbers $Re=10^4$	0.3131	[245]
RDM (154 mm housing)	Plexiglas flat disk (smooth)	10	0.13	Turbulent	CaCO ₃ suspension, 60 kg/m ³	0.32	[174]
	PVC flat disk			Turbulent		0.35	
	Disk with mesh	0.13	Turbulent	0.43			
	Smooth flat disk	Turbulent	0.44				
RDM (154 mm housing)	Disk with 8 pairs of 2mm rods	10	0.14	Turbulent	Water	0.62	[11]
	Smooth flat disk	8	0.11	Turbulent		0.45	
	Disk with 8 pairs of 6mm vanes		0.11	Turbulent		0.84	
RDM (154 mm housing)	Smooth flat disk	15	0.21	Turbulent	Water	0.42	[183]
	Disk with 8 pairs of 2mm vanes			Turbulent		0.65	
	Disk with 8 pairs of 4mm vanes			Turbulent		0.71	
	Disk with 8 pairs of 6mm vanes			Turbulent		0.79	
RDM (176 mm housing)	Flat disk	14	0.17	Turbulent	Water	0.44	[185]
	Disk with 6 of 2mm rectangular vanes	12	0.14	Turbulent		0.79	
	Smooth flat disk	17	0.23	Turbulent		0.45	
	Disk with 8 pairs of 2mm vanes	15	0.21	Turbulent		0.65	
RDM (154 mm housing)	Disk with 4 pairs of 4mm vanes	15	0.21	Turbulent	Baker yeast suspension, 3g/L	0.69	[15]
	Disk with 8 pairs of 4mm vanes	15	0.21	Turbulent		0.71	
	Disk with 8 pairs of 6mm vanes	15	0.21	Turbulent		0.84	
				Turbulent		0.71	
RVF (154 mm housing)	3 blades impeller	3	0.04	Laminar	Water	0.71	[111]
				Laminar	PIV	0.3	[8]
				Laminar	CFD	0.35	
RCF (352.6 mm housing)	Plastic flat disk	5	0.04	Laminar	CFD	0.895	[7]
				Turbulent	CFD	0.795	

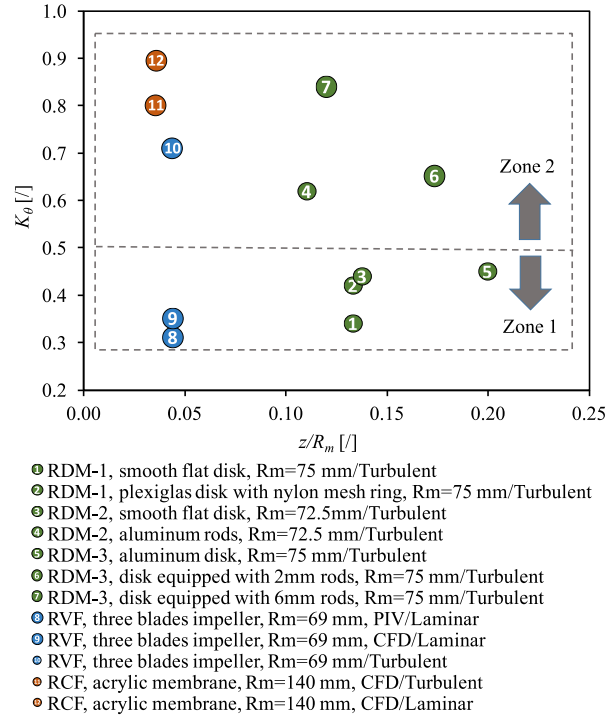


Fig. II.10 Evolution of core velocity coefficient, K_θ as a function of gap-to-radius ratio, z/R_m . Values are reported from literature for DF modules using confined rotating impeller close to the membrane and established under laminar or turbulent regimes [8].

Among the different rotating systems, the ratio z/R_m was used to characterize the geometry of the DF module, where z is the minimal distance between the impeller or the disk (considering geometrical modification) and the membrane, R_m is the radius of the rotor. The lowest values in Zone 1 ($k=0.3-0.5$) and the enhanced mechanical efficiency in Zone 2 ($k>0.5$) were described by Xie et al. [8].

Little researches are focused on the investigation of the core velocity coefficient in the laminar regime. Bentzen et al. [7] have conducted CFD simulations in laminar and turbulent regimes. They report $k=0.8$ (turbulent) and 0.9 (laminar) for a rotating cross-flow MBR installed with a plastic disk rotor ($z/R_m=0.0357$). These values are very close, which is unexpected for the laminar regime. In the RVF module (with a three blades impeller), the local flow was identified by PIV measurements and CFD simulation in the laminar regime, which provides a similar value of 0.3 and 0.35, respectively [8].

4.2.2 Shear rate and shear stress

In dynamic filtration, separation efficiency and productivity are highly dependent on the selection of membrane types and materials. However, as mentioned previously, the shear rate is one of the crucial factors which can control membrane fouling and enhance permeate flux.

Some theoretical and semi-empirical mathematical models for calculating the shear rate in different systems are presented in this section.

In general, the shear rate between two disks can be estimated according to viscosity law, with the flow velocity, u and the gap, y :

$$\gamma = \frac{du}{dy} \quad (\text{II.19})$$

Or by the shear stress, τ and the fluid viscosity, μ :

$$\gamma = \frac{\tau}{\mu} \quad (\text{II.20})$$

4.2.2.1 Rotating systems

In rotating systems, flow is governed by centrifugal forces generated by rotors, and it induces different flow patterns near the rotor and the stator. Considering the boundary theory, four different flow regimes were presented, according to azimuthal Reynolds number and the gap to radius ratio z/R_m , and shear rates at rotor (γ_R) and membrane (γ_S) surfaces were defined in Table II.10:

Table II.10 Shear rate of four flow regimes in a rotation system.

Regime	Rotor	Stator
I	$\gamma_R = \frac{\omega r}{z}$ (II.21)	$\gamma_S = \frac{\omega r}{z}$ (II.22)
II	$\gamma_R = 1.81 \frac{(k\omega)^{3/2} r}{\nu^{1/2}}$ (II.23)	$\gamma_S = 0.77 \frac{(k\omega)^{3/2} r}{\nu^{1/2}}$ (II.24)
III	$\gamma_R = 0.008 \frac{(\omega r)^{7/4} (\nu/z)^{1/4}}{\nu}$ (II.25)	$\gamma_S = 0.0115 \frac{(\omega r)^{7/4} (\nu/z)^{1/4}}{\nu}$ (II.26)
IV	$\gamma_R = 0.057 \frac{(k\omega)^{9/5} r^{8/5}}{\nu^{4/5}}$ (II.27)	$\gamma_S = 0.0296 \frac{(k\omega)^{9/5} r^{8/5}}{\nu^{4/5}}$ (II.28)

Bouzerar et al. [174] obtained the same expression of Eqs. (II.24) and (II.28) for laminar and turbulent flow for investigating the RDM system. By assuming a thinner gap between the rotor and membrane, boundary layers merged. The narrow gap, s represents the layer thickness, Eqs. (II.25) and (II.26) give the shear rates for rotor and stator, respectively [96, 237, 246]. Bendick et al. [156] assumed that steady-state flux J_{ss} evolves as a function of γ and Re in the rotating membrane system HSR-MS. They confirmed the $J_{ss}-Re$ and $J_{ss}-\gamma$ relationships and extended the model for further prediction with larger membranes. With this theory, shear rates on the rotating membrane surface with a membrane diameter of 267 mm were characterized using Eq. (II.23) in laminar flow and Eq. (II.27) in a turbulent flow.

Vogel et al. [144] considered the average shear rate γ_{av} in the gap between the conical rotor and the membrane in the CSF system. It could be estimated by the angular velocity ω ,

the radius of the rotating cone r , the distance between the cone and the membrane h , and the inclination angle of the cone α as Eq. (II.29) shown.

$$\gamma_{av} = \frac{\omega r}{h + r \tan \alpha} \quad (\text{II.29})$$

Lee et al. [63] calculated the shear rate in an annulus of coaxes cylindrical RO membrane system as Eq. (II.30) shows, where f was a velocity factor and depended on the flow regime. They considered the circumferential velocity was uniform in the center of the annulus at about $r_i \omega / 2$. The maximum shear rate was generated close to the rotating inner cylinder.

$$\gamma_{max} = f \left(\frac{\omega r_i}{r_o - r_i} \right) \quad (\text{II.30})$$

Atsumi et al. [247] described the shear rate in an annulus of a coaxed cylinder. The Couette-Taylor flow has been studied intensively and the wall shear stress, τ is given below:

$$\tau = f \rho \omega^2 r_i^2 / 2 \quad \text{for} \quad 0.03 \leq d/r_i \leq 1.0 \quad (\text{II.31})$$

where ω was angular velocity, r_i was the radius of the inner cylinder, d was the gap between two cylinders, f denoted the friction factor, was determined by the flow and could be described as the following equation Eqs. (II.32) and (II.33). Reynolds number is given in Eq. (II.3), while Re_c stands as the critical Reynolds number at which the Taylor vortex begins.

$$f = \frac{4(1 + \frac{d}{r_i})^2}{(2 + \frac{d}{r_i}) Re} \quad \text{for} \quad 20 \leq Re \leq Re_c \quad (\text{II.32})$$

$$f = 0.08 \left(\frac{d}{r_i} \right)^{0.35} Re^{-0.53} \quad \text{for} \quad Re_c \leq Re \leq 10^4 \quad (\text{II.33})$$

4.2.2.2 Oscillating systems

Azimuthal and axial oscillation are two strategies to reduce fouling by generating torsion or oscillating on the membrane. VSEP is a general module that has been largely reported.

Rosenblatt et al. early studied the flow between oscillating disks [238]. And Akoum et al. [10] calculated the local shear rate on the membrane in a lab-scale VSEP system by Eq. (II.34):

$$\gamma_w(r, t) = \frac{\partial V}{\partial Z} \Big|_{z=0} = \frac{\partial V}{\partial Z} \Big|_{z=h} = \frac{r \Omega}{h} \sqrt{\frac{Re}{2}} G(t) \quad (\text{II.34})$$

$$\gamma_w(r, t) = \frac{r}{R_2} d_r (\pi F)^{1.5} v^{-0.5} (\cos(2\pi Ft) - \sin(2\pi Ft)) \quad (\text{II.35})$$

With $G(t) = \cos(2\pi Ft) - \sin(2\pi Ft)$, wall shear stress represented as Eq. (II.35), where d_r was the membrane displacement at radius r , R_2 was the outer radius of the membrane, h was the gap between the disks, t was the operating times, F was oscillation frequency. The maximum shear rate occurred at the periphery ($r=R_2$), which generated the

maximum displacement d , and could be calculated by Eq. (II.36):

$$\gamma_{w \max} = 2^{0.5} d (\pi F)^{1.5} \nu^{-0.5} \quad (\text{II.36})$$

Moreover, the mean value of the shear rate can be defined by computing the absolute value over a specific area. For example, the annular limited by inner radius R_1 and outer radius R_2 , in this case, shown as Eq. (II.37).

$$\bar{\gamma}_w = \frac{2^{3/2} (R_2^3 - R_1^3)}{3\pi R_2 (R_2^2 - R_1^2)} \gamma_{w \max} \quad (\text{II.37})$$

For the VSEP system [10], the result showed that the maximum and mean shear rates at the membrane were 112000 and 37000 s^{-1} , respectively, with water at 20°C. These expressions were also used to estimate the maximum shear rates with Eq. (II.36) [101] and calculate the mean shear rate with Eq. (II.37) [68, 100] in 45°C milk solution.

Gomaa et al. [137] investigated a flat vertical vibrating membrane unit with turbulence promoters. They gave a surface shear rate expression in Eq. (II.38) and the maximum shear rate in Eq. (II.39).

$$\gamma(t) = \frac{A_w^{1.5}}{2\nu^{0.5}} \left(\cos \omega t + \frac{\pi}{4} \right) \quad (\text{II.38})$$

$$\gamma_{\max} = \frac{A_w^{1.5}}{2\nu^{0.5}} \quad (\text{II.39})$$

As described in the oscillating rectangular membrane, AVM [217] stands as a typical system; the membrane moves horizontally in a direction parallel to them. The local shear rate is evenly distributed on the membrane surface, which could be expressed by Eq. (II.40):

$$\gamma_w(t) = d(\pi F)^{1.5} \nu^{-0.5} (\cos(2\pi Ft) - \sin(2\pi Ft)) \quad (\text{II.40})$$

Zhao et al. [217] found the shear decreased with the increment of distance to the membrane. At 10 Hz frequency and 1 cm amplitude, the shear rate induced by the oscillation membrane could be ignored and decreased from 4000 to 0 s^{-1} at a distance of about 1 mm.

Another similar device described by Su et al. [56] achieved the oscillation frequency up to 50 Hz but with a lower amplitude (1.2 mm) in the desalination of simulated seawater. The membrane boundary shear rate was more than 6000 s^{-1} in this condition ($Re=344$).

Hollow fiber membranes are often applied in the oscillating system. The shear rate in this membrane module was calculated by Beier et al. [136]. They showed that the shear rates (Eq. (II.41)) at the membrane surface should be:

$$\gamma_s = v_0 \sqrt{\frac{\omega}{2\nu}} [\sin(\omega t) - \cos(\omega t)] \quad (\text{II.41})$$

where ω was angular velocity ($\omega=2\pi f$), v_0 was the amplitude of velocity ($v_0=A\omega$, A was the peak-to-peak amplitude), t was time.

Based on this expression, a time mean average of shear rate was computed as Eq. (II.42). At the frequency of 30 Hz and amplitude of 1.175 mm, it could reach up to approximately 2000 s^{-1} with the permeate flowrate of $68 \text{ L}/(\text{m}^2 \text{ h})$.

$$\bar{\gamma}_s = \frac{\sum_{i=0}^{1000} |\gamma_s(t = i/1000)|}{1000} \quad (\text{II.42})$$

$$\frac{\gamma_{max1}}{\gamma_{max2}} = \frac{d_1}{d_2} \left(\frac{\omega_1}{\omega_2} \right)^{1.5} \quad (\text{II.43})$$

The maximum shear rate of these kinds of systems was compared as follows in Eq. (II.43). The shear rate for VSEP (frequency 60 Hz, amplitude 30 mm) is 28-fold higher than the hollow membrane system (30 Hz, 3 mm) [4]. It is 33-fold higher than the VERO system (50 Hz, 1.2 mm). But what we also need to take into consideration is the distribution of shear rate at the membrane surface. The shear rate in VSEP increases with a higher radius of the disk membrane, while the other two modules are uniformly distributed at the membrane surface.

4.2.2.3 Oscillating and vibrating systems

Except for oscillating parallel to the HF membrane, other forms of movement applied with the HF membrane would be classified into Oscillating and vibrating, where the motion is perpendicular to the fiber axis [138] or with a defined angle [227]. The shear force is cylindrically asymmetric around the fiber, and using a simple equation to describe it is not available.

4.3 Local approaches

4.3.1 Local velocity and shear stress

In the DF system, the complexity of the flow field is of course expected to improve filtration performances. It is promoted by different phenomena related to the specific geometrical configuration and the associated moving walls. Indeed, the flow pattern is not only time-dependent but also highly influenced by the different length scales that exist in the system. Moreover, the rheological behaviors of the fluid that can be non-Newtonian in some applications may also affect the flow field. Global and semi-local approaches to getting quantitative information on velocity, pressure and shear stress show their limitation in revealing what really happens in the system.

From an experimental point of view, recent optical measurement/visualization techniques are becoming more and more popular for accurate and reliable local

measurements, resulting in the velocity field, concentration field, temperature field, etc.

4.3.1.1 Particle Image Velocimetry (PIV)/ Particle Tracking Velocimetry (PTV)

PIV allows the estimation of the velocity field by the average displacement of multiple small tracer particles in a given interval Δt . In comparison, PTV is developed in the case of low seeding densities to calculate the particle velocity by measuring the optical track length of the particle under a specific exposure time [248, 249]. Typically, the tested device needs to have a good light transmission to ensure a better acquisition of particle images by laser light scattering. Trace particles seeded in the flow are assumed to move with the fluid without any velocity lag, fluorescent, polystyrene, silver-coated particle, or other reflective particles are used [249]. Li et al. [80] seeded 0.1 g/L particles with a diameter of 20 μm in the oscillating system to establish a velocity vector map; the data acquisition system was performed at 6Hz. In a rotating system, Xie et al. [8, 198] investigated the velocity fields in radial and vertical profiles with BREOX solution. They found that velocity is highly organized and stable within the filtration cell and is mainly governed by the impeller shape.

4.3.1.2 Molecular Tagging Velocimetry (MTV)

MTV determines the velocity field in fluid flow by tagging specific molecular instead of macroscopic particles as in PIV, and tracking its displacement by imaging twice. There are three optical ways to visualize these tagged molecules: fluorescence, phosphorescence and laser-induced fluorescence [250]. This technology is achieved on a molecular basis to avoid the non-uniformed seeding and the impact of the suspended particle on the fluid itself. Simultaneously, the capital cost would increase sharply for the complex experimental system [251].

4.3.1.3 Laser Doppler Velocimetry (LDV)

LDV, also known as Laser Doppler Anemometry (LDA), is one of the techniques of using the Doppler shift in a laser beam to measure the velocity in transparent or semi-transparent fluid, or the linear or vibratory motion of opaque, reflecting, surfaces. The measurement with LDA is absolute, linear with speed, and requires no pre-calibration [252-254]. But the drawbacks are the high precise optical arrangement and bothersome signal processing [249]. Bentzen et al. [7] measured tangential velocity with the LDA system at the rotating speed between 50 and 350 rpm. Wall shear stress in 15 locations was achieved and indicated a good agreement with CFD simulation.

4.3.1.4 Electrochemical method

Electrochemical method is based on the redox reaction of the electrolyte combination.

The magnitude of the current was measured and derived from calculating the shear stress from the theoretical relationship. For most of these solutions, ferric and ferrocyanide is used as oxidizing and reducing ions, respectively [255]. A reaction is conducted at high enough voltages to reduce the concentration of the reacting species to zero at the surface of the working electrode. Therefore, the reaction rate is controlled by the speed of mass transfer, which is directly related to the local shear stress. What should be concerned are the non-uniform flow across the probe and the response of the instrument to fluctuations in the velocity field [256, 257].

4.4 Computational Fluid Dynamics (CFD)

As an alternative to the experimental studies, Computational fluid dynamics can be used to solve mass and momentum balances governing equations for fluid flow, the so-called Navier-Stokes equations, to determine the velocity and pressure fields in the geometrical domain. It is of great use to replenish our knowledge about increasing the filtration performances without further experimental verification. Although attractive, this theoretical approach is often complicated to implement in particular to take into account the mobile walls of the domain and the turbulent flow regime, especially in the complex-geometries modules. Moreover, a proper calculation mesh should adapt to the geometry and the numerical method according to the specific problem [258-260]. In laminar flow, with a relatively lower mixing rate of 2 Hz in the RVF module, CFD simulation was in good agreement with PIV regarding velocity fields and profile [8]. The simulated shear stress distributions indicated that the rotating speed and disk structure are the main factors affecting shear stress on the membrane surface [93, 124]. For the requirement of uniform surface shear stress, CFD simulation was used to optimize the design of the rotor in a rotating system, which permits the same mean shear stress with relatively low rotation speed [190].

5 Discussion

Dynamic filtration permits to reduce fouling and concentration polarization thanks to high local shear stress generated by rotating, oscillating or vibrating movements. Various systems have been described and investigated, but no instruction or procedure helps engineers select a suitable DF module.

As for conventional filtration, engineers should previously define the specifications of the application, including objectives (separation, concentration), expected performances and operating limitations. Capital expenditure (CAPEX) and operational expenditure (OPEX) associated with DF modules should be evaluated in the business plan. For CAPEX (equipment, land, construction, etc.), production capacity and scaling should be known. For OPEX, the main cost will be associated with DF energy demand. In this last situation, several approaches can be proposed to estimate total power consumption.

5.1 Energy demand associated with DF module

Compared with cross-flow filtration, dynamic filtration shows great performance in fouling control with higher critical flux, which leads to longer filtration run between cleaning steps. However, the power consumption is much more delicate to estimate in DF modules than in the conventional ones (DEF, CFF).

The total power P_T in the basic filtration unit includes mechanical power P_M and pumping power P_P (Eq. (II.44)). Energy consumption for the mixing, oscillating or vibrating movements is usually much higher than pumping energy. The driving force for filtration (TMP) is highly dependent on the filtration type: MF (0.2 to 3 bar), UF (1 to 10 bar), NF (10 to 40 bar) and RO (10 to 100 bar). Its magnitude for filtration will affect pumping powers in different ways for each filtration mode present in Fig. II.11. Two conventional filtration modes [261] are considered: single-pass continuous filtration and continuous filtration with partial retentate recycle (Feed & Bleed), as illustrated in Table II.11.

$$P_T = P_M + P_P \quad (\text{II.44})$$

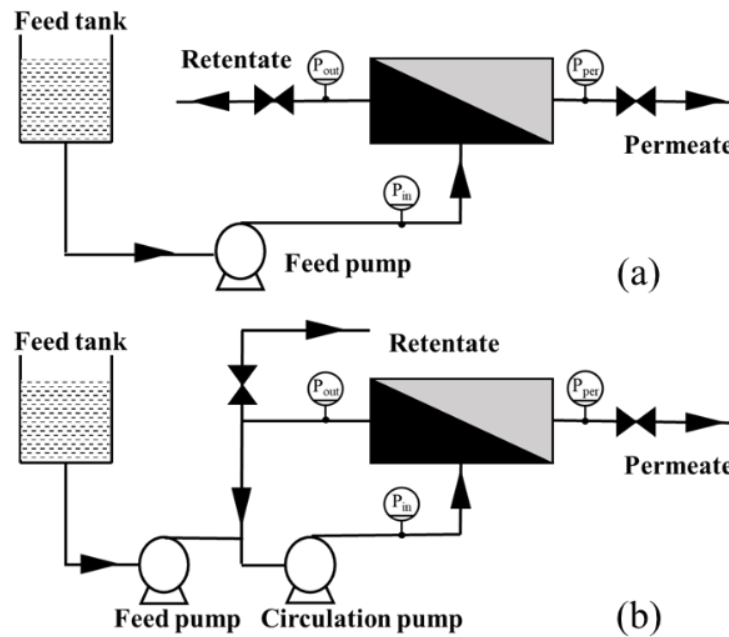


Fig. II.11 Filtration modes, (a). Single-pass continuous filtration (b). Continuous filtration with partial retentate recycle (Feed & Bleed)

5.1.1 Mechanical power

Considering a DF module, the mechanical power consumption can be estimated by generated movement (mixing, oscillating, vibrating) and the flow through the module. Therefore, three strategies are described: i) the global approach (power consumption curves, friction curves), ii) semi-local empirical correlation estimating the mean shear stress and iii) local measurements (or simulation) of the velocity field.

For global approach, power consumption curves and friction curves (friction factor or Euler) can be determined for each module, as reported by Fillaudeau et al. [6] for RVF lab-scale module. With mixing Reynolds numbers ranging from 10 to 10^6 , semi-empirical dimensionless correlations were established. The power number was calculated with the global electrical power of the motor, and the mechanical power was estimated by subtracting consumed power without charge. They demonstrated that the power consumption curve was independent of the flowrate. On the opposite, the friction curve was strongly affected by mixing conditions and a semi-empirical correlation was established to take it into account.

For semi-local approach, the mechanical power could be estimated by the local shear stress, which has been presented in § 4.2. In the RDM module (rotating system, type 5), the mechanical power P_M developed by friction force was given in Eq. (II.45) [15]. τ_d and τ_{db} are the shear stress on two sides of the disk (b : smooth backside); k_d and k_{db} are the core velocity

coefficients. Mechanical power was found to vary linearly with electric power (efficiency close to 0.39 for disks with vanes and 0.63 for smooth disks). Using Murkes and Carlson's equation (Table II.10, Eq. (II.27)), the turbulent shear stress was estimated. It implied that electrical power varied as $\omega^{14/5}$ [15], which was verified by Brou et al. [141]. In the SBM module [59] (rotating system, type 2), with a different configuration, it was reported that electrical power was proportional to ω . In laboratory oscillating (type 11, [139]) and/or vibrating (type 15, [138]) systems, time average values should be taken into account over a period for different frequencies, as seen in Eq. (II.46). The function $f(t)$ represents the force balance with the drag force, gravity, buoyancy and viscous force according to the motion; $v(t)$ is the local velocity in the time domain. It gives the maximum value of $2\pi FA$.

$$P_M = 2\pi \int_0^R (\tau_d + \tau_{db}) r^2 \omega dr = 0.0779 \rho v^{1/5} \omega^{14/5} R^{23/5} (k_d^{9/5} + k_{db}^{9/5}) \quad (\text{II.45})$$

$$\overline{P_M} = \frac{1}{T} \int_0^T f(t)v(t) dt \quad (\text{II.46})$$

For local approach, Xie [262] has investigated the local shear stress with PIV measurements at the static walls in the RVF module (rotating system, type 6). Considering the angular momentum balance, the torque along the rotor is equal to the torque on the surrounded housing. The corresponding mechanical power was lower than those estimated with the power consumption curve, due to the non-uniform distribution of torque on the lateral/external walls. The contribution of periodic motions and turbulence needs to be considered.

5.1.2 Pumping power

In industrial applications, the pumping power is represented by the electric consumption (Eq. (II.47)) by knowing current (U) and tension (I). Mechanical power can also be estimated from the pressure difference between the inlet and outlet and the flow rate. In both filtration modes (Fig. II.11), the contribution of pumping will significantly differ.

$$P_p = UI \quad (\text{II.47})$$

For single-pass continuous filtration, the power is calculated from feeding flowrate (Q_f) and pressure difference with Eq. (II.48). It is equivalent to the pressure differences associated with permeate and retentate flowrate. P_{in} , P_{out} and P_0 represent the inlet/outlet pressure of the DF module and the atmospheric pressure; Q_r and Q_p are the retentate and permeate flowrate. By neglecting the pressure drop in the DF module, it could be assumed that $(P_{out} - P_0) \approx \Delta P$. In NF and RO where TMP is maintained at high pressure (>10 bar), pumping power

cannot be neglected. But these powers are still greatly reduced for the relatively lower feeding flowrate applied compared with conventional CF, which needs a high shear rate produced by a high feeding flowrate. In DF modules, the uncoupling of flowrate and local shear rate is ensured by mechanical power. Feeding flowrate should satisfy permeate and retentate concentration and volume reduction ratio. Consequently, pumping power can be drastically reduced up to a negligible contribution.

$$P_P = Q_f(P_{in} - P_0) \approx Q_r(P_{out} - P_0) + Q_p \Delta P \quad (\text{II.48})$$

For Feed & Bleed mode, the pumping power is equal to the sum of feed and circulation powers associated with Q_f and Q_c , given in Eq. (II.49). In conventional filtration, this configuration enables uncouples of the feeding and circulation flowrate. Consequently, the pumping power can be significantly reduced for the high-pressure filtration process (NF, RO). With the DF module, this configuration will be simplified by eliminating the circulation pump. Feed & Bleed mode will have a negligible interest except if a pre-concentration of the fluid is used. The knowledge of the friction curves is required to estimate the pressure loss within the DF module [6]. However, the pumping power (feed) is expected to be lower than in a single-pass configuration.

$$P_P = Q_f(P_{out} - P_0) + Q_c(P_{in} - P_{out}) \quad (\text{II.49})$$

Luo et al. [176] proposed a linear relationship between pumping power and TMP, within the range of 0 to 40 bar, $P_{in}-P_0$ would approximate the transmembrane pressure in the open-loop when neglecting the pressure drop of DF. In the UF of PEG 6000 with SBM, the retentate flowrate was fixed at 10^{-4} m³/s, but the maximum permeate flowrate was 8×10^{-7} m³/s, which is negligible in comparison with the retentate flow [59]. These limited permeate flux would reduce the output of the feeding pump, especially in configuration (b) in Fig. II.11.

5.1.3 Specific energy demand

Specific energy demand, E (Eq. (II.50)) is defined as the total energetic consumption per m³ of permeate, equal to the ratio between total power and permeate flowrate. The total power is supposed to be the sum of pumping and mechanical power previously discussed. But in most publications, the pumping power is negligible or a very low concern in MF and UF. It could be ignored compared with mechanical power, as demonstrated in the RDM module for mixing rates up to 2000 rpm [176].

$$E = \frac{P_T}{Q_f} \approx \frac{P_M}{JS\eta} \quad (\text{II.50})$$

For laboratory or industrial DF devices, energy demand is rarely reported and resumed in Table II.11. Specific energy varies to a large extent from 0.29 to more than 1000 kWh/m³ due to the different configurations and scales. Other parameters such as disk design, fluid concentration and temperature also affect power consumption. Consequently, the comparison of DF modules is hardly reliable or feasible.

Table II.11 Specific energy demand in different modules.

Module	Fluid	Membrane	N (Hz, rpm)/ A (mm)	S (m ²)	J (L/m ² h)	TMP (bar)	E (kWh/m ³)	Ref.
RDM	1:2 diluted skim milk	NF	2000 rpm	0.0176	350	40	170	[176]
RDM	1:2 diluted skim milk	NF	1000 rpm	0.0176	135	40	303	[176]
RDM	1:2 diluted skim milk	UF	2000 rpm	0.019	/	/	65	[183]
RDM	1:2 diluted skim milk	UF	2000 rpm	0.019	/	/	30	[183]
RDM	Baker yeast	MF	2000 rpm	0.019	200	/	15	[15]
MSD	CaCO ₃	MF	1930 rpm	0.06	/	3	1.7	[87]
MSD	CaCO ₃	MF	1930 rpm	0.033	/	3	2.9	[87]
VSEP	Skim milk	RO	60.2 Hz	100	55	40	1.63	[69]
VSEP	Skim milk	UF	60.4 Hz	151	56	/	1.05	[101]
OFSM	baker's yeast	MF	25 Hz/ 1.5 mm	0.006	500	0.6	0.3	[139]
SBM	PEG 6000	UF	400 rpm	0.0286	411	5.884	80	[59]
MMV	Activated sludge	MF	/	0.016	16	/	12.2	[212]
MMV	Activated sludge	MF	/	0.096	16	/	2.03	[212]
VHM	Yeast	MF	1.7 Hz	0.0057	46	/	0.29	[220]
VERO	Silica colloids and sodium chloride	RO	/	0.006	/	/	~10 ³	[64]

For several rotating and oscillating DF modules (MSD, RDM, VSEP, VHFV), membrane type (NF, MF, UF with polymeric and ceramic membranes) and experimental fluids, Zsirai et al. [12] demonstrated that permeate steady-state flux increased as a power law of shear rate, $J = k\gamma^n$ with $0.186 < n < 1.560$ and $0.00003 < k < 6.7$. The empirical correlation of $n = (1.98 - \log k)/5.04$ was fitting well except for the high viscosity liquid and non-uniform shear rate distributed in MSD. However, confusion remains between the mean and maximal shear rates being applied.

In rotating RDM modules, since the maximum shear rate was proportional to $\omega^{9/5}$ (Eqs. (II.27) and (II.28)), and permeate flux increased as a power law of maximum shear rate, γ_{max} with an exponent of 0.5-1 [4, 11, 15, 99, 110, 183, 263]. Then the specific energy demand can be easily estimated knowing the mechanical power and the steady-state flux, indicating that E is proportional to $\omega^{1-1.9}$. In the concentration of skim milk with NF membrane, operating conditions at 2000 rpm and extreme TMP (40 bar) resulted in the lowest mean specific energy demand, around 170 kWh/m³. In comparison, it increased up to 303 kWh/m³ under

1000 rpm and 40 bar [176]. The same fluid was tested by Ding et al. [183] in UF, and specific energy demand increased from 30 kWh/m³ with smooth disk up to 65 kWh/m³ with disk equipped with vans. In MSD, a solution of 200 g/L CaCO₃ was filtered at 3 bar TMP. The maximum specific energy consumption was 2.9 kWh/m³ for the nylon membranes and 1.7 kWh/m³ for the ceramic ones [87].

In the oscillating VSEP (type 9) system, Frappart et al. [69] estimated the power consumed by the oscillation of the module at 60.2 Hz (amplitude: 2.5 cm). Specific energy demand was evaluated at 1.63 kWh/m³ by assuming a permeate flux equal to 55 L/(m²·h). With defined operating conditions ($Q_p=8.42$ m³/h, $S=151$ m², $TMP=1500$ kPa and $F=60.4$ Hz), the power demand for the oscillation and pumping are 8.83 kW and 6.58 kW, respectively. The estimated specific energy demand was below 1 kWh/m³ for oscillating [101]. Gomaa et al. [139] compared the specific energy consumption based on low and high-efficiency power recovery of 20% and 80% with the oscillating membrane (type 11); they were 0.3 kWh/m³ and 0.1 kWh/m³ at the highest frequency (25 Hz), respectively. In the VERO module (type 10), equipped with a small membrane area of 0.006 m² for desalination, the estimated specific energy demand was in the order of 10³ kWh/m³.

In oscillating and vibrating systems, Kola et al. [138] investigated the energy consumption in terms of productivity in a linear transverse vibration HF system (type 15) with the vibration frequency at 3.7 Hz and displacement of 2.5 mm for 0.04 μm PVDF membrane. The specific energy consumption for oscillation and vibration was around 0.0009 kWh/m³ at permeate flux of 30 L/(m²·h). It increased to 0.20 kWh/m³ at the same permeate flux for the highest frequency of 21.8 Hz and 2.5 mm displacement.

In conclusion, specific energy demand can be estimated if information about power consumption and permeate flux are known. However, the different configurations and scales do not allow the comparison of absolute values between different modules.

5.2 Specifications and decision tree for DF application

Dynamic filtration is a reliable alternative to the dead-end and the cross-flow filtrations as reported in the present documents. Their performances are associated with complex flow patterns generating high and fluctuating local shear rates and pressure at the membrane surface.

Considering the 15 types of DF devices (corresponding to 55 known modules), the overarching aims propose to elaborate the main criteria for helping engineers to select a DF

module or to identify the missing information about the DF module or fluid to be treated. The best choice for a given application will be driven by several basic questions:

- What is the limitation associated with the fluids?
- How to determine the operating conditions?
- What should we know about dynamic filtration equipment?

A framework (Fig. II.12) is proposed with criteria operating conditions and knowledge barriers in DF application, which would help to select a module with available information and identify the missing knowledge.

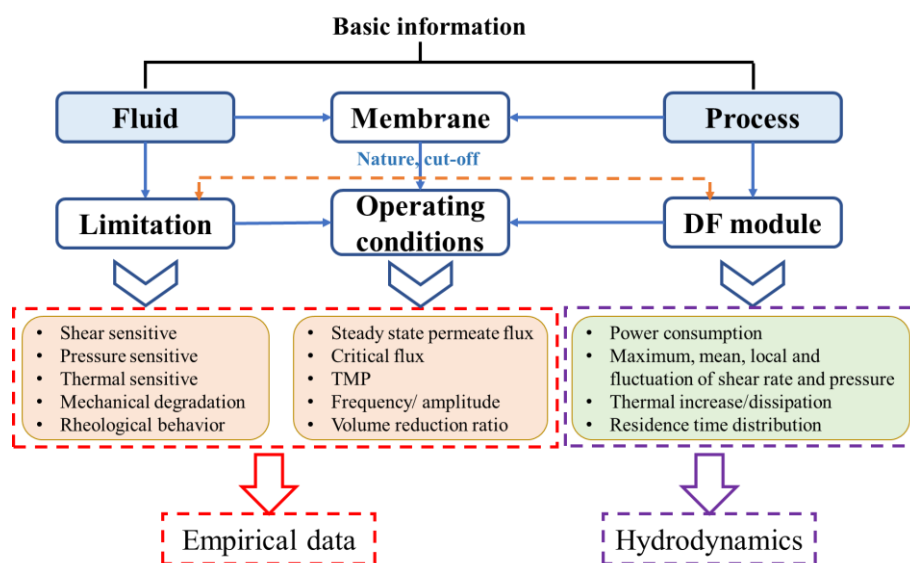


Fig. II.12 Main criteria and knowledge gap in DF application

Firstly, basic information about nature, composition, physico-chemical properties of the fluid to be treated (ex. rheological behaviors, density, temperature, pH, particle size distribution, concentration) and the objectives of the process (concentration, purification or separation), as well as the production capacity and mode (volume, time, batch, continuous...), should be known. This information will help to select the filtration type (MF, UF, NF or RO) and the membrane (cut-off and nature). Coupled with the limitation of fluid and DF module, the operating conditions can be defined in terms of steady-state/ critical flux, TMP, frequency/ amplitude and volume reduction ratio.

In the dynamic filtration module, the behaviors of experimental fluid under stringent hydrodynamics conditions should be investigated (ex. sensitivity to shear rate magnitude, temperature increase, mechanical degradation such as cell or particles...) before process design and scaling (filtration area, power consumption, acceptable operating conditions). Meanwhile, the knowledge of local hydrodynamics (velocity, shear or pressure field),

including maximum, average and time-dependent values, may enable to estimate performances as well as critical local operating conditions.

Finally, Table II.12 summarizes the empirical applicative and hydrodynamics data available for the 15 types of DF modules as discussed in § 3 and 4. It leads to highlight the knowledge gap for future scientific research and industrial applications.

Table II.12 Resume of available data about hydrodynamics and applications with the different types of DF modules.

Type	Empirical data							Hydrodynamics investigation					
	Application / Performances		Global approach					Semi-local approach (Membrane or rotor surface)			Local approach (Filtration cell volume)		
	Water treatment	Food processing	Bioprocess engineering	Dimensionless analysis	Dimensionless correlation	Pumping power	Mechanical power	Core velocity coefficient, k	$\bar{P}(x,y,z)$	$\gamma(x,y,z)$	$U(x,y,z,t)/\gamma(x,y,z,t)$	$P(x,y,z,t)$	CFD
1	X	X	X	X	X	n.a	n.a	X	X	X	n.a	n.a	X
2	X	n.a	X	X	n.a	X	X	n.a	n.a	n.a	n.a	n.a	X
3	X	n.a	X	X	X	n.a	n.a	n.a	X	X	n.a	n.a	X
4	X	n.a	n.a	X	n.a	n.a	n.a	n.a	n.a	n.a	n.a	n.a	n.a
5	X	X	X	X	n.a	X	X	X	X	X	X	n.a	X
6	X	X	X	X	X	X	X	X	X	X	X	n.a	X
7	X	n.a	n.a	X	n.a	n.a	n.a	n.a	X	X	n.a	n.a	n.a
8	X	X	X	X	X	n.a	n.a	n.a	X	X	n.a	n.a	n.a
9	X	X	X	X	X	n.a	n.a	n.a	n.a	X	n.a	n.a	X
10	X	n.a	n.a	X	X	n.a	n.a	n.a	n.a	X	n.a	n.a	X
11	X	n.a	X	X	X	X	X	n.a	n.a	X	n.a	n.a	X
12	X	n.a	n.a	n.a	n.a	n.a	n.a	n.a	n.a	X	n.a	n.a	n.a
13	X	n.a	X	X	n.a	n.a	X	n.a	n.a	X	X	n.a	n.a
14	X	n.a	n.a	n.a	n.a	n.a	X	n.a	n.a	X	n.a	n.a	X
15	X	X	X	X	n.a	n.a	X	n.a	n.a	n.a	n.a	n.a	X

X: investigated; n.a: not available at present time.

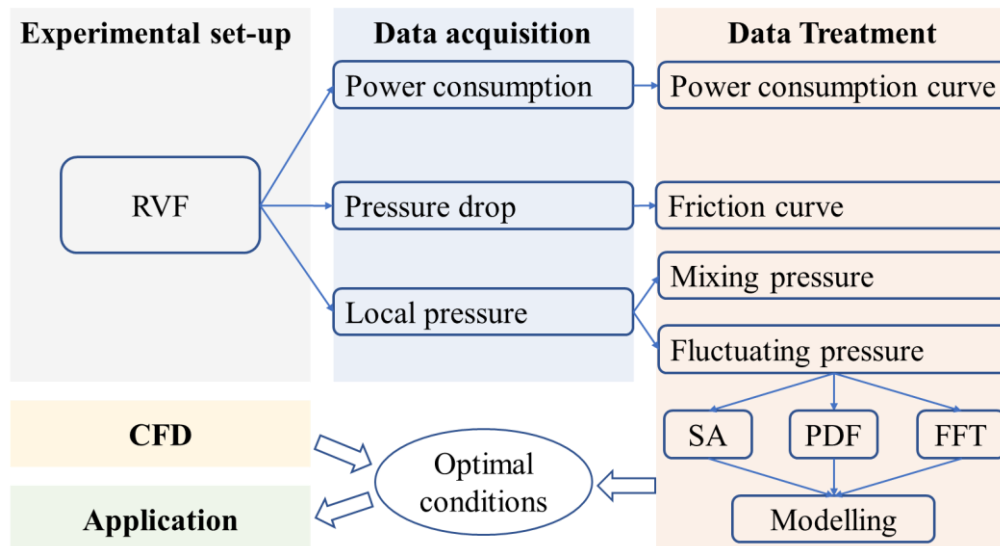
Chapter III: Materials and Method

The rotating and Vibrating Filtration (RVF) module was used to investigate their global performances (mixing and pumping power), local and instantaneous pressure. On the global scale, the effect of operating conditions was characterized by the thermal increase in the filtration cell, the pressure drop and the power consumption. Local measurements were carried out to quantify the continuous and fluctuating pressure.

The configuration of the RVF module (filtration cell and impeller geometry and number of blades) and its instrumentation were described with a focus on pressure measurement at the membrane surface. Data treatments were performed with Statistical Analysis (SA), Probability Distribution Function (PDF), Fast Fourier Transform (FFT) and then modeling to extract the amplitude and frequency of pressure fluctuation. The experiments were carried out with Newtonian fluids (water and BREOX solutions) in laminar and turbulent regimes. Afterward, the methodology associated with CFD simulation (COMSOL Multiphysics) was detailed.

Highlights:

- (1) Experimental set-up to acquire the local pressure at the membrane surface;
- (2) Data treatment of time-series pressure;
- (3) Optimization of impeller geometries and operating conditions based on numerical approaches.



1 Experimental set-up and instrumentation

1.1 RVF module

The lab-scale RVF module [8, 111] (Fig. III.1 a, b) consists of two filtration cells with a total volume of 1.5 L ($0.2 \times 2 + 1.1$ L). Four disk membranes (0.012 m² filtration area per membrane) can be mounted on the porous substrates, which collect permeate drained to lateral ducts. Each cell includes two crown membranes with a gap of 14 mm, between which is located an impeller that rotates with the central shaft (Fig. III.1 e). And it is driven by a motor that can be operated up to 50 Hz. The feeding fluid comes inside RVF from the inlet at the bottom and flows through the module along with the central shaft, finally leaving from the retentate outlet at the top.

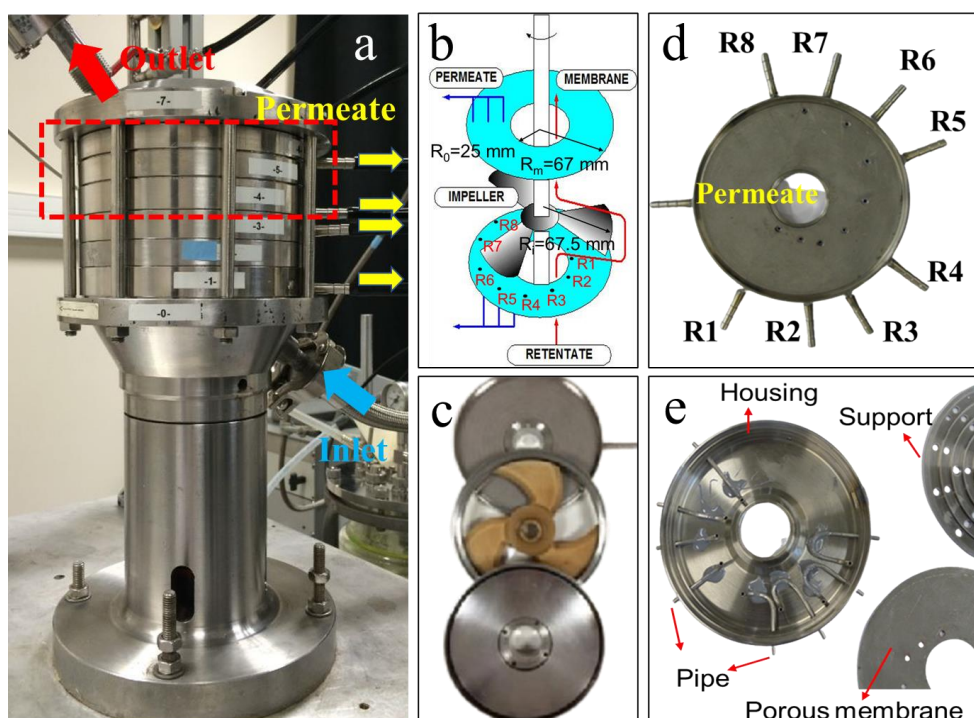


Fig. III.1 Schematic diagram of Rotating and Vibrating Filtration module. (a) RVF module; (b) one dismantled filtration cell; (c) and (d) home designed and instrumented porous substrate for local pressure measurements; (e) configuration of filtration cell.

Table III.1 Radial distribution of pressure taps at the membrane surface (porous substrate).

Radial position	Radius (mm)	Radial position	Radius (mm)
R1	26.2	R5	45.3
R2	29.3	R6	53.9
R3	34.8	R7	63.4
R4	38.2	R8	64.9

In Fig. III.1 c and d, a home-designed and instrumented porous substrate was used to measure the local pressure at the membrane surface. Eight pressure taps (2 mm) were connected to stainless tubes, with one extremity welded to the porous support and the other extremity located on the outer cell wall. The pressure taps were distributed between 26.2 mm (R1) up to 64.9 mm (R8), as indicated in Table III.1.

1.2 Impeller configuration

Three impellers with two shapes of blades (shape 1 has increased surface area and 8 mm thickness; shape 2 has decreased surface area and thickness) are applied in the tests, as shown in Fig. III.1 b and c. Imp 1 equips with three blades (shape 1); Imp 2 and 3 have six and three blades (shape 2), respectively. The surface area of the blades for three impellers follows the order: Imp 1 > Imp 2 > Imp 3.

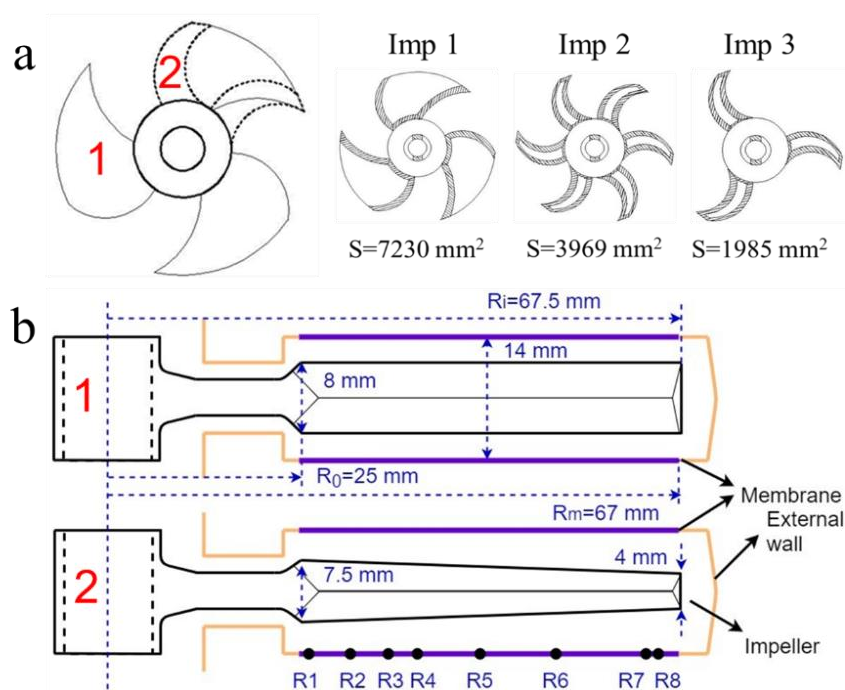


Fig. III.2 Impeller configuration.

1.3 Experimental set-up

The experimental set-up is displayed in Fig. III.3; it includes a feed tank, a circulation loop and the RVF module, as shown in Fig. III.1. In the circulation loop, water was pumped from a double-jacket tank (10 L), including thermal regulation at flowrate up to 300 L/h.

Flowrate was controlled by a volumetric pump and acquired with a mass flowmeter; it enabled the measurement of mass flowrate, density and temperature (associated with outlet temperature). The inlet temperature was recorded from the conductivity sensor, Cond, in the feeding tank. The back pressure in RVF was adjusted by a counter-pressure valve coupled with a pressure gauge (PG, 0/4 bar) and two relative pressure sensors (PR1 and PR2) located at the inlet and outlet. Before the experiments, the back pressure was maintained at 300 mbar to avoid cavitation caused by the high mixing rate. A Tachymeter was used to adjust the mixing rate (N) from 0 to 50 Hz. Both current (CU) and tension (TEN) of the motor were recorded for all the conditions. The differential pressure sensors (DP) were used to determine the pressure drop and local pressure of RVF. The relative pressure (PR3, maximum acquisition frequency 5 kHz) was measured at the membrane surface. All sensors and equipment used in the experiments are shown in Table III.2 and Table III.3.

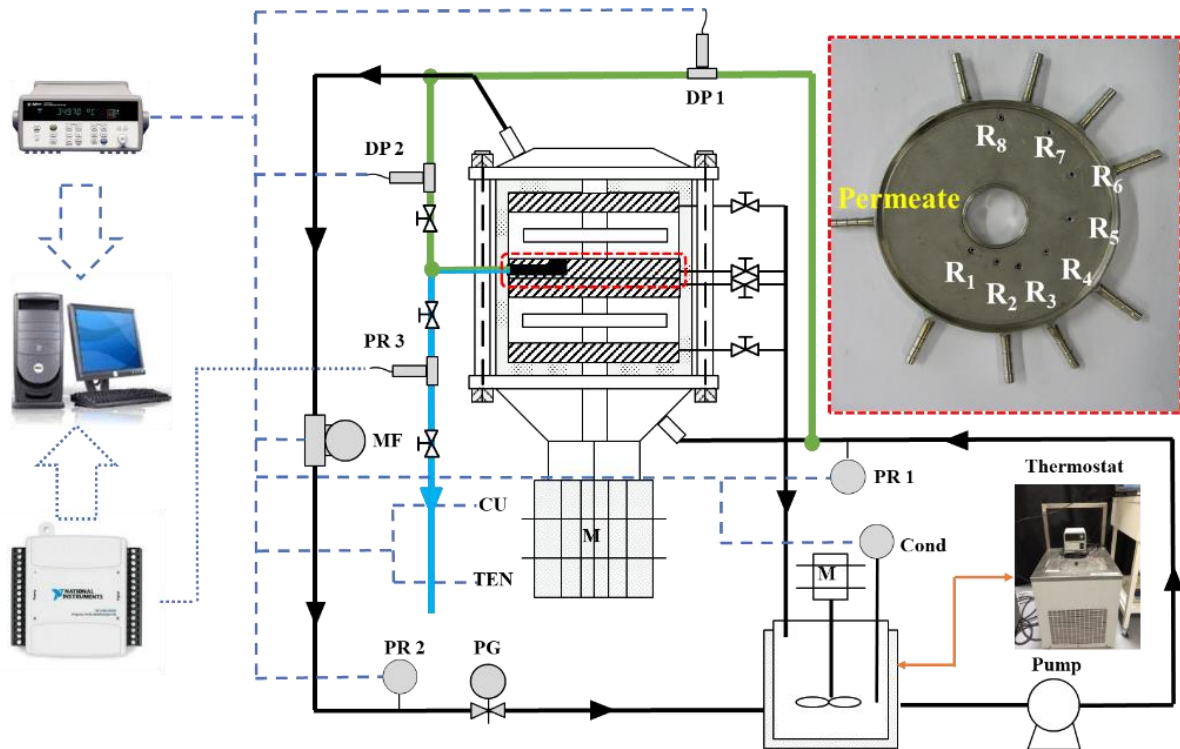


Fig. III.3 Experimental set-up.

Table III.2 All sensors used in the experiment.

Sensor	Ref	Measure	Range-precision	Application			
				Global	Semi-local	Local	Cell
Relative pressure sensor, Bourdon-Haenni E913	PR 1	P _{inlet}	0-10 bar, ±0.2%	×	×	×	×
Relative pressure sensor, Bourdon-Haenni Y913	PR 2	P _{outlet}	0-6 bar, ±0.2%	×	×	×	×
Relative pressure sensor, KELLER, PR 23	PR 3	P(N,r,t)	-1-1 bar, ±0.1%	/	/	×	
Conductivity meter Conducell 4USF-PG325	Cond	T _{inlet}	1-500000 µS/cm, ±1%; -20-150 °C, ±0.5 °C	×	×	×	
		T _{outlet}	0-130 °C, ±1 °C	×	×	×	
Mass flowmeter, KROHNE MFS-7050-S06	MF	ρ	500-2000 kg/m ³ , ±2 kg/m ³	×	×	×	
		Q _F	0-950 kg/h, ±0.1% Liq, ±0.5% Gas	×	×	×	
Differential pressure sensor, Honeywell STD 120	DP 1	ΔP _{RVF}	0-2.5/ 1000 mbar, ±0.075%	×	/	/	
Differential pressure sensor, Honeywell STD 120	DP 2	ΔP(N,r,t)	0-2.5/ 1000 mbar, ±0.075%	/	×	/	
Ammeter AT 20 B 10 LEM KR 02	CU	I	Input: 20 A, Output: 0-10 V, precision ±0.3 A	×	/	/	
Voltmeter Camille bauer Ref: SINEAX U 504	TEN	U	Tech. Info. Input: 0-250 V, 50 Hz, Output: 0-20 mA, R: 750 Ω, precision ±0.2V	×	/	/	

×: means selected; /: indicates not used.

Table III.3 All equipment used in the experiment.

Devices	Information	Notes
Tank	8 L double-jacket glass tank	With a thermal regulation
Pump	Head: TUTHILL CO., series A54739, Drive: GROSCHOPP CO., series PM8014, 3800 rpm, DC motor control unit: DART 250G series	Feeding pump
Rotor	94358 electronic, Heidolph	Mixing the fluid in the tank
Thermal balance	9105-BB, Polyscience, serial 615342, temperature range: -45-150 °C, reservoir capacity: 13 L	To maintain the temperature
Pressure gauge	Manometer, 0-6 bar	To control the counter pressure in the outlet
Motor	LSFMV80L, LEROY SOMER	To enhance the filtration in the RVF
Tachymeter	Testo 460, Germany, 100-29999 RPM, ±0.02% of mv, resolution 0.1 RPM (100-999.9 RPM) 1 RPM (1000 to 29999 RPM)	To measure the rotating speed of motor

1.4 Data acquisitions

There are two types of data acquisition systems applied in our tests (Fig. III.3). Global measurements along the circulation loop correspond to differential pressure (DP1 and DP2), flowrate, temperature, current and tension. All the sensors were connected to Agilent 34972A (Agilent Technologies, Loveland, USA) with a multiplexer acquisition card (34901A, 20 channels). The Bench View system (Keysight Technologies, Santa Rosa, California, USA) is used for data acquisition and monitoring during the experiments. Instantaneous pressure was measured with PR3 (shown in the blue line in Fig. III.3) at 1000 Hz, connected to the local radius. The pressure signal was recorded with NI USB-6009 (National Instruments, USA, 1 kHz) at a sampling frequency of 1000 Hz.

2 Experimental strategies and operating conditions

2.1 Experimental strategies

Two types of measurements were performed without permeate: (i) global measurement and (ii) instantaneous and local pressure measurement. Global measurements were conducted with 2 min stabilization, and then recorded at a 5 s time interval for 3 min; Instantaneous pressure was acquired with the NI instrument at the sampling frequency of 1000 Hz for 40 s, and the operating conditions were controlled with Agilent (3 s/sample). The relevant parameters are listed in the following Table III.4.

Table III.4 Data acquisitions in the experiments.

Sensor	Measure	Global	Instantaneous and local	
		Agilent	Agilent	NI
PR 1	Inlet pressure, P_{inlet}	×	×	/
PR 2	Outlet pressure, P_{outlet}	×	×	/
PR 3	Instantaneous pressure, $P(N,r,t)$	/	/	×
Cond	Inlet temperature, T_{inlet}	×	×	/
	Outlet temperature, T_{outlet}	×	×	/
MF	Density, ρ	×	×	/
	Flowrate, Q_F	×	×	/
DP 1	Pressure drop, ΔP_{RVF}	×	/	/
DP 2	Mixing pressure, ΔP_{mixing}	×	/	/
CU	Current, I	×	/	/
TEN	Tension, U	×	/	/

×: means selected; /: indicates not used.

2.2 Operating conditions and fluids

Table III.5 Operating conditions for global and local pressure measurements.

Fluids	Parameters				Impellers			
	Q_F (L/h)	N (Hz)	r (mm)	P_{outlet} (mbar)	Imp 1	R-Imp 1	Imp 2	Imp 3
Water (0.001 Pa.s)	50-300	0-50	R1-R8	0-500	×	×	×	×
BREOX 0.1 (0.01 Pa.s)	50-200	0-50	R1-R8	310	×	/	/	/
BREOX 0.2 (0.05 Pa.s)	50-130	0-40	R1-R8	440	×	/	/	/
BREOX 0.3 (0.2 Pa.s)	25-40	0-30	R1-R8	630	×	/	/	/
BREOX 0.4 (0.6 Pa.s)	12	0-20	R1-R8	890	×	/	/	/

The model fluids (water and BREOX solutions) were used for global and local measurements, with the flow from laminar to turbulent regimes. Several parameters,

including feeding flowrate, mixing rate, radius, back pressure and impeller configurations on the local pressure were introduced. The detailed information is shown in Table III.5.

2.2.1 Water

Tap water was used as the model fluid in the turbulent regime. The basic information on thermal-physical properties and their thermal dependency were reported in the literature. At 20 °C, the density of water is $\rho = 998.2 \text{ kg/m}^3$, specific heat capacity at constant pressure $C_p=4181.8 \text{ J/(kg}\cdot\text{°C)}$, viscosity $\mu=1.0 \text{ Pa}\cdot\text{s}$. (under 100 kPa).

2.2.2 BREOX solutions

In order to change the fluid viscosity, a water-soluble Newtonian fluid with stable properties, called BREOX (BREOX® Polyalkylene Glycol 75 W 55000, BASF), whose dilutions were used as the model fluid. Their thermal-physical properties at different temperatures are shown below versus the mass concentration C (w/w, %).

$$\begin{cases} Cp = aT + b \\ a = -14.8C^2 + 16.3C - 1.5 \quad (R^2 = 0.9735) \\ b = -1202C^2 - 948C + 4113 \quad (R^2 = 0.9997) \end{cases} \quad (\text{III.1})$$

$$\begin{cases} \ln\mu(T) = \ln\mu(20^\circ\text{C}) + 4 \times 10^6 c^2 + 2811.3c - 0.0161 \quad (R^2 = 0.9905) \\ c = \frac{1}{T + 273} - \frac{1}{T_{20^\circ\text{C}} + 273} \\ \ln\mu(20^\circ\text{C}) = -8.90 \times C^2 + 18.03C - 6.17 \quad (R^2 = 0.9998) \end{cases} \quad (\text{III.2})$$

where a and b are concentration-dependent coefficients that can be represented by the concentration of BREOX, c is the temperature coefficient. Thus, heat capacity C_p can be presented as Eq (III.1). At the constant temperature (20 °C), the viscosity $\mu(20^\circ\text{C})$ is the function of concentration. The thermal dependent viscosity $\mu(T)$ is estimated using Eq (III.2).

3 Global investigation: friction and power consumption curve

For dynamic filtration devices, power consumption is the critical point that needs to be considered during practical work. The first case is the pumping power for the feeding fluid, which is the key element in cross-flow filtration. However, the mechanical power (rotating, oscillating and/or vibrating) is much more important than the pumping power in the dynamic filtration module. The energy consumption can be evaluated comprehensively by means of the empirical equations.

3.1 Raw data

For global measurement, the counter pressure is kept around 300 mbar, as shown in Fig. III.4 a. The pressure drop of the RVF module can be estimated with DP 1; DP 2 indicates the mixing pressure at the membrane surface, which shows to increase with radius. Other global parameters are displayed in Fig. III.4 b. The mixing of the impeller resulted in the thermal increase, the experiments were carried out at the temperature between 20 and 40°C.

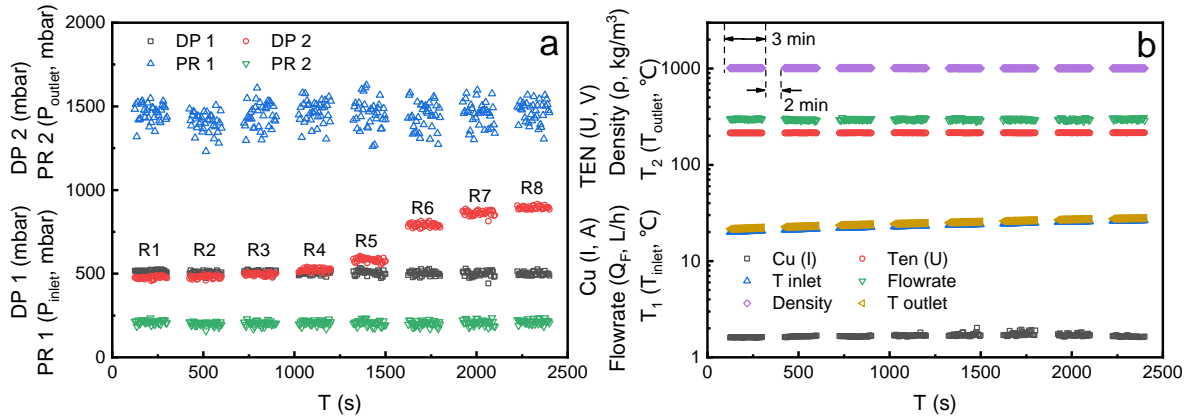


Fig. III.4 Global measurement with water at 300 L/h and 40 Hz.

3.2 Friction curve

From a global standpoint, RVF modules can be assimilated to a hydraulic singularity generating a pressure drop and as a mixing device. Linear pressure drops in the RVF module (ΔP_{RVF}) are attributed to the friction loss, which can be expressed by Euler dimensionless number, Eu , given by Eq. (III.3).

$$Eu = \frac{\Delta P_{RVF}}{1/2\rho u^2} \quad (\text{III.3})$$

where ΔP_{RVF} is pressure drop, ρ is the fluid density, u is the velocity at the inlet of RVF module. The Reynolds number for feeding ($Re_{feeding}$) and mixing (Re_{mixing}) are defined as follows:

$$Re_{feeding} = \frac{\rho du}{\mu} \quad (\text{III.4})$$

$$Re_{mixing} = \frac{\rho N d_i^2}{\mu} \quad (\text{III.5})$$

where d is the inlet diameter (12 mm), d_i is the diameter of the rotating impeller (135 mm), μ is dynamic viscosity, N represents the mixing rate of the impeller.

3.3 Power consumption curve

In the rotating system, the mixing power is highly affected by the configuration of the impeller sharp. In 1963, Bates et al. [264] reported the power consumption curve in the baffled tanks with Newtonian fluids. The great changes of the Power number from laminar to turbulent regimes. In contrast with the RVF module, the impeller rotates within a narrow gap in order to generate high shear stress at the membrane surface, which needs further investigation.

Power consumption of the rotor is given by the current I and tension U of the motor. The electrical power needed to drive the shaft was measured without fluid, considered shaft loss ($U_0 I_0$). Thus, the net power Φ_N consumed by the rotating impeller is equal to the difference between total power and shaft losses [15], as displayed in Eq. (III.6). It can be described by the Power number Np in Eq. (III.7).

$$\Phi_N = UI - U_0 I_0 \quad (\text{III.6})$$

$$Np = \frac{\Phi_N}{\rho N^3 d_i^5} \quad (\text{III.7})$$

3.4 Energy balance

For incompressible fluids, gravity is neglected. A non-slip condition is imposed on the walls, and the inlet speed profile is the same as the outlet profile. It gives:

$$\Delta P \cdot Q + \iint_A \sum_{j=1}^3 \sum_{i=1}^3 \tau_{if} n_i U_j ds + \iint_A \sum_{i=1}^3 (-P) n_i U_i ds = \iiint_D \rho \varepsilon_V dv \quad (\text{III.8})$$

1st term: necessary pumping power to drive the fluid in the circulation loop;

2nd term: external viscous forces (surface shear stress) on the impeller;

3rd term: external forces of the pressure on the impeller;

4th term: total power dissipation in the cell.

3.4.1 Thermal power

We assume the uniform temperature at the inlet and outlet sections, the heat capacity (C_P) is independent of T . Thus, the heat dissipation can be simplified by thermal power (Φ_T) during the insulation of the boundary walls:

$$\Phi_T = \iiint_D \rho \varepsilon_V dv = \rho C_p (T_{inlet} - T_{outlet}) Q_F \quad (III.9)$$

where T_{inlet} and T_{outlet} are the inlet and outlet temperature, respectively, Q_F is the feeding flowrate.

3.4.2 Mechanical power

In the turbulent regime ($Re_r > 3 \times 10^5$), the boundary layers merge together at a narrow gap ($s = 3$ mm), and the local shear stress τ on the rotating disk in Eq. (III.10) illustrates the linear relation with $N^{1.75}$ [96, 246]. As mentioned by Brou et al. [15], the mechanical power Φ_M generated by the friction force on the plate disk is calculated by Eq. (III.11). R_0 and R_i are the inner and outer radius of the impeller, respectively.

$$\tau = 0.008 \rho^{0.75} (2\pi N \cdot r)^{1.75} \left(\frac{\mu}{s}\right)^{0.25} \quad (III.10)$$

$$\Phi_M = 2 \int_{R_0}^{R_i} 2\tau (2\pi N \cdot r) (2\pi r) dr = 6.632 \rho^{0.75} \left(\frac{\mu}{s}\right)^{0.25} (R_i^{4.75} - R_0^{4.75}) N^{2.75} \quad (III.11)$$

In the laminar flow regime ($Re_r < 3 \times 10^5$), the local shear rate is equal to the angular velocity divided by the gap. Thus, the mechanical power for a full disk system is shown as:

$$\begin{aligned} \Phi_M &= 2 \int_{R_0}^{R_i} 2\tau (2\pi N \cdot r) (2\pi r) dr = 248 \left(\frac{\mu}{s}\right) (R_i^4 - R_0^4) N^2, s/R_i < 0.05 \\ \Phi_M &= 1125 \mu^{0.5} \rho^{0.5} k^{1.5} (R_i^4 - R_0^4) N^{2.5}, s/R_i \geq 0.05 \end{aligned} \quad (III.12)$$

4 Semi-local investigation: core velocity coefficient

Since the impeller is installed with a narrow gap to the membrane, assuming the inviscid core layer rotates at the mixing rate of N , it results in the angular velocity of $2\pi kN$. According to Bernoulli's equation in Eq. (III.13) [174], the mean local pressure $\bar{P}(N, r)$ at the membrane surface equals the sum of P_0 and ΔP_{mixing} . P_0 is the pressure at the centre of membrane or be given by the pressure when the absence of mixing, while ΔP_{mixing} is the additional pressure driven by the rotating impeller.

$$\bar{P}(N, r) = P_0 + \Delta P_{mixing} = P_0 + \frac{1}{2}\rho(k \cdot 2\pi N)^2 r^2 \quad (\text{III.13})$$

where r is the radius at the membrane surface. In the previous study, the local pressure was measured with the radial permeable crowns, and the mean values at the large gap (5 mm) were overestimated [6]. In this study, using a pressure tap of 1 mm radius to measure the local pressure can be more accurate, and the number of measurement points is increased to 8. It is yet important for the analysis of local k value.

5 Local investigation: instantaneous pressure

Assuming the three blades impeller was used in the experiments, which will result in a 150 Hz signal when rotating at 50 Hz. The instantaneous pressure has been measured with a 1000 Hz sampling frequency. Considering the vibrating flow induced by the pressure fluctuations, the instantaneous pressure can be expressed as Eq. (III.14), with $\bar{P}(N, r)$ and $\tilde{P}(N, r, t)$ represent the mean and fluctuating pressure, respectively. Fig. III.5 a and b illustrate the time evolution of absolute pressure and its fluctuating component. Pressure fluctuation and its amplitude can be treated by i) statistical analysis, SA; ii) probability distribution function, PDF and iii) Fast Fourier transform, FFT.

$$P(N, r, t) = \bar{P}(N, r) + \tilde{P}(N, r, t) \quad (\text{III.14})$$

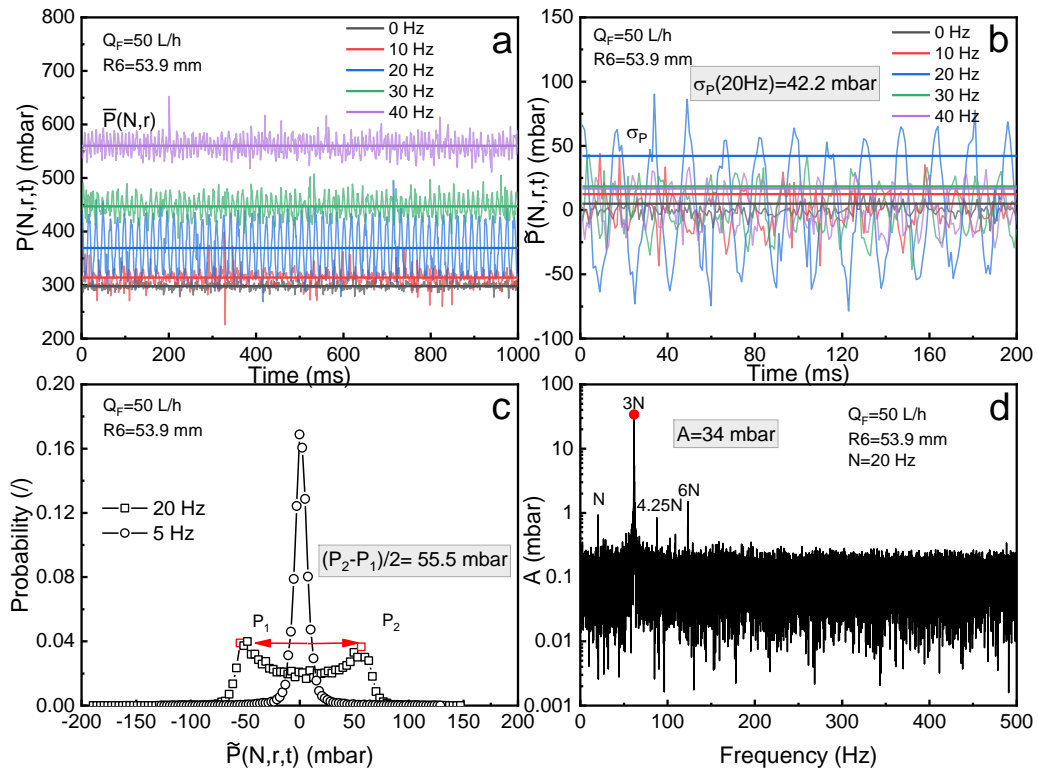


Fig. III.5 The spectrum of instantaneous pressure and data treatment. (a) instantaneous and mean pressure; (b) fluctuating pressure and its standard deviation; (c) probability analysis at 5 and 20 Hz; (d) fluctuating pressure on frequency domain at 20 Hz.

5.1 Statistical analysis (SA)

The standard deviation of the signal has been widely accepted to quantify fluctuating

intensity [265-267]. In our condition, a total number of sampling ($m=2^{15}$) is acquired at a constant time interval (1 ms), as illustrated in Fig. III.5b. The mean pressure $\bar{P}(N, r)$ and standard deviation σ_p are expressed as the moment of first order and the square root of the central moment of second order, respectively. Their mathematical definitions for continuous and discrete functions are given in Eq. (III.15) and (III.16). The coefficient of variation, β is defined as the ratio between σ_p and $\bar{P}(N, r)$, and give the relative standard deviation.

$$\bar{P}(N, r) = \frac{1}{T} \int_0^T P(N, r, t) dt \approx \frac{1}{m} \sum_{i=1}^m P(N, r, t_i) \quad (\text{III.15})$$

$$\sigma_p^2 = \frac{1}{T} \int_0^T (P(N, r, t) - \bar{P}(N, r))^2 dt \approx \frac{1}{m} \sum_{i=1}^m (P(N, r, t_i) - \bar{P}(N, r))^2 \quad (\text{III.16})$$

$$\beta = \frac{\sigma_p}{\bar{P}(N, r)} \times 100\% \quad (\text{III.17})$$

The normalised central moment of the third order, known as skewness (S), determines the symmetry of the signal in the probability distribution, and zero means a symmetrical distribution.

$$S = \frac{1}{T\sigma_p^3} \int_0^T (P(N, r, t) - \bar{P}(N, r))^3 dt \approx \frac{1}{m\sigma_p^3} \sum_{i=1}^m (P(N, r, t_i) - \bar{P}(N, r))^3 \quad (\text{III.18})$$

The flatness (F) is represented by the normalised central moment of the fourth order, indicating the sharpness of distribution.

$$F = \frac{1}{T\sigma_p^4} \int_0^T (P(N, r, t) - \bar{P}(N, r))^4 dt \approx \frac{1}{m\sigma_p^4} \sum_{i=1}^m (P(N, r, t_i) - \bar{P}(N, r))^4 \quad (\text{III.19})$$

5.2 Probability distribution function (PDF)

Another method for obtaining the intensity of fluctuating pressure can be carried out with probability analysis. By subtracting the average pressure, the deviation signal is divided into 100 classes considering 2^{15} of raw data. The probability of each class can be calculated based on its occurrence. In Fig. III.5c, the probability is illustrated against the fluctuating pressure. The unimodal (dominant random contribution) distribution of probability is observed at 5 Hz while extended to bimodal (dominant periodic contribution) at 20 Hz. These PDF widths are defined by peak-to-peak differences divided by 2, $(P_2 - P_1)/2$, finally resulting in the pressure intensity of 55.5 mbar at 20 Hz.

5.3 Fast Fourier transform (FFT)

The Fast Fourier Transform decomposes a signal into a series of sinusoid waves to be analyzed and given by the frequency domain signal. It has been used to extract information about fluctuation (amplitude and frequency) from the time-series signal. Continuous and discrete Fourier transform can be represented by:

$$P(f) = \int_{-\infty}^{+\infty} \tilde{P}(N, r, t) e^{-j2\pi ft} dt \approx \sum_{i=0}^{m-1} \tilde{P}(N, r, t_i) e^{-\frac{j2\pi fi}{m}}, \quad (III.20)$$

$$f = 0, 1, \dots, m - 1$$

where $\tilde{P}(N, r, t_i)$ is the deviation of pressure at point i , f is the frequency. This formula is associated with the complex plane, composed of real and imaginary parts, and its amplitude (A) can be expressed as follows:

$$A = \frac{2}{m} \sqrt{P(f)^2} \quad (III.21)$$

The time-dependent fluctuating pressure can be converted into the frequency domain with FFT [265, 266, 268-270]. 2^{15} sample points were chosen to get a sufficient precision of the fluctuated signal. The amplitude and frequency, driven by the rotating impeller, are discussed in the next part. Fig. III.5d shows the typical result of FFT at 20 Hz. The peak amplitude (A) is defined as the intensity of fluctuation pressure.

5.4 Reconstruction of PDF with periodic and random functions

The fluctuating signal consists of two parts: periodic and random contributions (Table III.6). The periodic signal can be simplified as a single sinusoidal fluctuation with $f=3N$, whose intensity is determined by the amplitude A . Since only one peak is considered, the A presented here is higher than the FFT amplitudes at the same frequency. The random signal conforms to a normal distribution with a zero mean, and σ denotes the standard deviation. The energy input in each contribution is given by their root mean square (RMS).

Table III.6 Signal decomposition into periodic and random contributions ($P_P(t)$: periodic signal, $P_R(t)$: random signal, A : amplitude, f : frequency, φ : phase, σ : standard deviation, $E_P(x)$ and $E_R(x)$ are the PDF.).

Contribution	Function	Parameters	PDF (mbar ⁻¹)	Energy input (mbar)
Periodic	$P_P(t) = A \sin(2\pi ft + \varphi)$	$A, f=3N, \varphi$	$E_P(x) = \frac{1}{\pi \sqrt{A^2 - x^2}}$	$A/\sqrt{2}$
Random	$P_R(t) \sim N(\bar{x}, \sigma^2)$	$\bar{x} = 0, \sigma$	$E_R(x) = \frac{1}{\sigma \sqrt{2\pi}} e^{-\frac{1}{2}(\frac{x-\bar{x}}{\sigma})^2}$	σ

In theory, the continuous model of pressure fluctuation distribution results from the convolution of $E_P(x)$ with $E_R(x)$, as reported in Eq. (III.22). Comparison between experimental data and model is realized by identifying amplitude, A for periodic component, and standard deviation (σ) for a random term. Considering the statistical convergence, phase lag has no effect on PDF building. Both optimal parameters, A and σ are obtained by minimizing the cumulative error function, Δ with Eq. (III.23), thanks to Excel solver (Suite Office Microsoft 2013, Excel, GRG non-linear) for each operating condition. Fig. III.6 illustrates the experimental and simulated PDF at R6 and 20 Hz.

$$PDF = E_P(x) * E_R(x) \quad (III.22)$$

$$\Delta = \text{Min} \left(\sum_{i=0}^{100} \sqrt{(Experiment - Model)^2} \right) \quad (III.23)$$

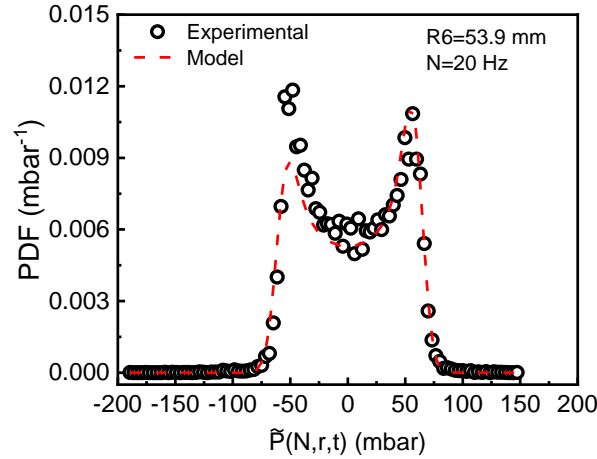


Fig. III.6 PDF at 20 Hz. Model reconstruction of PDF with periodic and random functions.

6 Computational Fluid dynamic (CFD)

CFD techniques are used to predict the flow field by solving basic governing equations such as mass, momentum and continuity equations instead of requiring complex experiments and high expenses. The numerical simulations of the fluid flow in the RVF module were carried out in laminar and turbulent regimes with the commercial software COMSOL Multiphysics (Version 5.5). Since the permeation rate in DF is generally below 10^{-3} m/s, which is much lower than the impeller rotation speed (8.16 m/s can be reached at 20 Hz) [59, 271], thus, all the numerical simulations were performed without permeation at the membrane surface.

6.1 Laminar regime

6.1.1 Computational domain

The RVF module consists of two cylindrical filtration cells in series. Each of them comprises an impeller with three blades regularly spaced of 120° . Assuming that the two cells work identically, only one cell is considered. Moreover, the computational domain is limited to one-third of the cell with periodic boundary conditions, as shown in Fig. III.7.

6.1.2 Model

It is assumed that the test fluid is Newtonian (BREOX solutions), incompressible, and isothermal in the simulation, the steady-state flow is solved under the laminar regime. The local mass and momentum balances are governed by the Navier Stokes (N-S) equations expressed in a fixed reference frame as follows:

$$\nabla \cdot \mathbf{u} = 0 \quad (\text{III.24})$$

$$\rho(\mathbf{u} \cdot \nabla \mathbf{u}) = -\nabla P + \mu \nabla^2 \mathbf{u} \quad (\text{III.25})$$

where ρ is the fluid density in kg/m^3 , μ is the fluid dynamic viscosity in Pa·s, P is the pressure in Pa, and \mathbf{u} is the velocity vector in m/s.

6.1.3 Boundary conditions

Fig. III.7 shows the configurations of RVF, and the 3D models are developed using AutoCAD according to the lab-scale RVF parameters. An impeller ($r=67.5$ mm) rotates with the central shaft ($r=12$ mm) at a constant mixing rate inside a cylindrical housing ($r=71$ mm). The fluid flows along the central shaft at the bottom and leaves at the upper end. We define the xy -axis parallel to the plane of the impeller and the z -axis along the direction of rotation. On the other hand, the cylindrical coordinate is also defined in the geometry: θ and r indicate the angular and radial components, respectively, and a along the shaft direction.

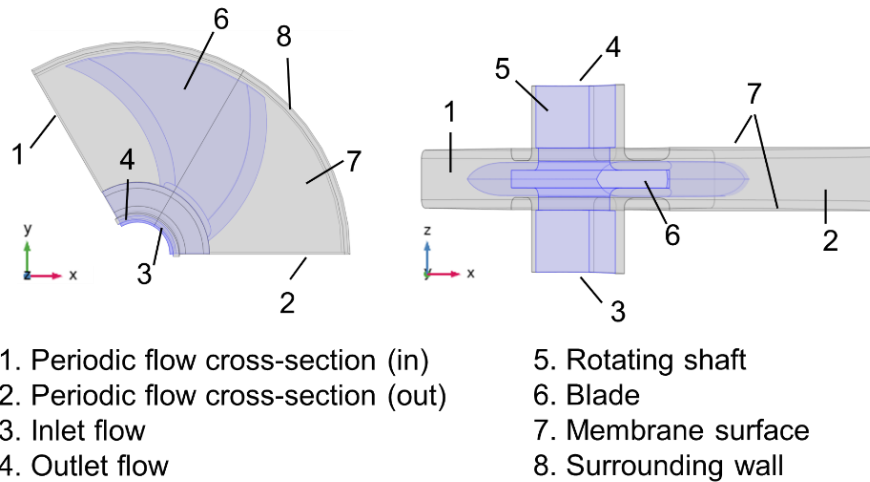


Fig. III.7 Schematic of RVF cell. (a) is the top view and (b) is the side view.

The simulations are carried out under the following conditions:

- The flow is assumed to be periodic in the angular direction (sections 1 and 2);
- Periodic boundary conditions are also used at the inlet and outlet faces (3-4). Here an average pressure gradient in the z -direction is imposed, which magnitude is adjusted to get the expected flowrate;
- A reference pressure constraint point at the outlet face (4) is set as the back pressure, P_b ;
- A no-slip boundary condition is imposed at both walls: the velocity is zero at membrane surfaces (7) and cell walls (8), the velocity is equal to $2\pi Nr$ in the θ direction at both blade and shaft walls (5-6) to account for the rotation of the impeller.

6.1.4 Mesh

The so-called “normal” mesh (Fig. III.8) is generated automatically with COMSOL 5.5 based on the physics. Different element types such as tetrahedral, pyramid, prism, triangular, quadrilateral, edge and vertex elements are then generated, resulting in the 299510 domain

cells, 32242 boundary elements and 2401 edge cells for Imp 1.

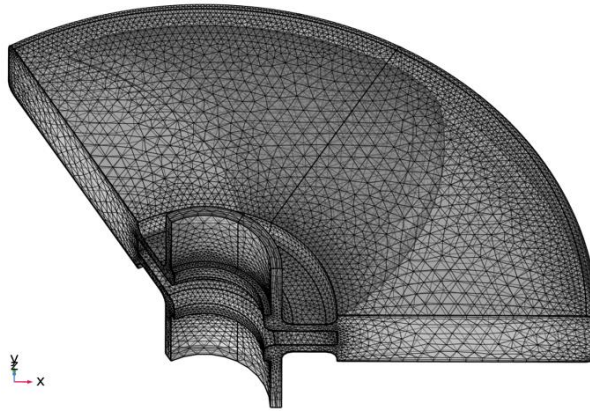


Fig. III.8 Mesh geometry

6.2 Turbulent regime

6.2.1 Computational domain

In turbulence simulations, the solution of the flow field requires simplifying the computational model as much as possible. Due to the comparatively complex structure of Imp 1, it is difficult to converge even with a very fine mesh. Therefore, we simulate a 60° three-blade impeller instead, which shares the same surface area and impeller thickness as Imp 1. The computational domain was defined as one-third of the cell. In addition, we also simplified the rotating full disk, and a 10° ($1/36$) structure was used for the simulation.

6.2.2 Model

In laminar flow, the flow field is predicted by solving the steady-state N-S equations. As the fluid velocity (Reynolds number) increases, vortices appear in the flow field. Large-eddy simulation (LES) is to solve the filtered N-S equations directly under a large eddy scale grid, and the small eddy is simulated according to their similarity, which needs more time and space for the calculation. The Reynolds-averaged N-S (RANS) equations are based on the time-averaged solution of the flow field, which limits the turbulence fluctuations to some extent but reduces the time for the simulation. The RANS-based model helps us to solve the periodic fluctuations of the flow field induced by the impeller rotation under the turbulent regime.

The standard k - ε model was employed to determine stationary turbulence flow. Thus, the transport equations for the turbulent kinetic energy (k) and its dissipation rate (ε) were solved.

Since the variation of the pressure is determined by the main fluid velocity, this turbulence model has been applied in the simulation of pressure at the membrane surface in RD modules [148, 169, 272]. Another two-equation model ($k-\omega$) substitutes the turbulent kinetic energy dissipation rate (ε) by ratio dissipation (ω), which is also available for solving the pressure in the RD modules [70, 230]. The wall function was used to approximate the flow field close to the wall for these two models, while the flow field of the viscous sublayer cannot be solved perfectly. Yu et al. [273] used the shear-stress transport (SST) $k-\omega$ model to solve the pressure fluctuation in pump-jet propulsor. The mesh near the wall surface is enhanced and offers a superior resolution [62]. That can be applied in the simulation of wall pressure and shear stress variation [7, 274].

6.2.3 Boundary conditions

In turbulent flow, the configuration of impeller and disk in the cell can be seen in Fig. III.7. The boundary conditions are similar to those under laminar flow; only the inlet and outlet conditions are redefined:

- Inlet is imposed with constant normal phase velocity;
- Uniform outlet pressure is maintained at 300 mbar.

6.2.4 Mesh

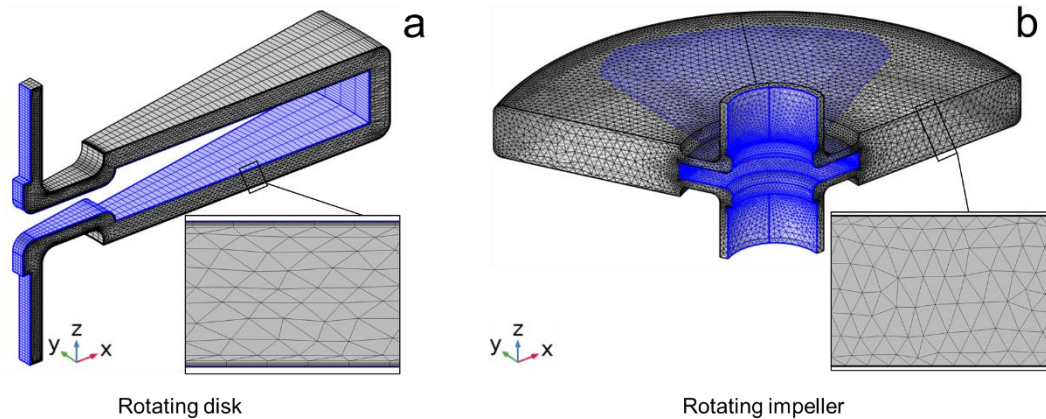


Fig. III.9 Mesh geometry. (a) 1/36 of rotating disk and (b) 1/3 of rotating impeller.

Based on the axisymmetric design of the rotating disk, a structured grid is formed by sweeping (Fig. III.9). The boundary layer mesh is defined with a minimum mesh size of 0.005 mm, and increases layer by layer at a ratio of 1.2. Thus, the final mesh contains 34044 domain cells, 19402 boundary elements and 1310 edge cells. Due to the complex structure of

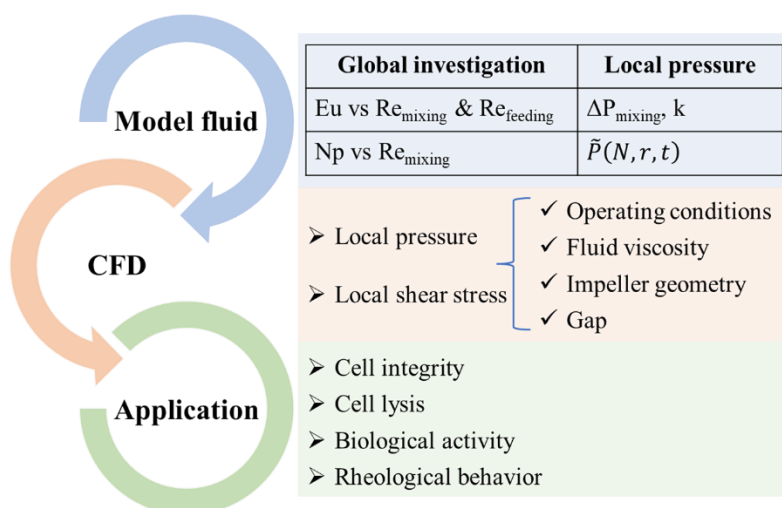
the impeller (Fig. III.9), the mesh is segmented by free tetrahedra. When encrypting the boundary layer, the resulting mesh includes 1166910 domain cells, 63018 boundary elements and 3336 edge cells.

Chapter IV: Results and Discussion

Dynamic filtration exhibits high performance by generating wall shear stress (tangential to the membrane) and pressure stress (normal to the membrane) by mechanical movements, such as rotating, oscillating or vibrating systems. The rotating and Vibrating Filtration (RVF) module includes rotating flat blade impellers which generate high and fluctuating shear stress and pressure at the membrane surface.

To optimize the operating conditions, global parameters (power consumption, pressure drop) and driving forces (mean, instantaneous and local pressure at the membrane surface) were characterized. For global approach, friction and mixing power in the RVF module were described by semi-empirical correlations. For semi-local and local approaches, the local pressure at the membrane surface was measured with a specially designed and instrumented porous substrate. Mean radial pressure and core velocity coefficients were quantified versus flowrate and mixing rate. For fluctuating components, pressure fluctuation and its amplitude were treated by SA, PDF and FFT. Based on the PDF modeling, periodic and random contributions are extracted by deconvolution. Then, the empirical correlations are established to estimate their intensities as a function of rotation frequency and radial position.

For further optimization of the cell configuration, CFD techniques are used to simulate the flow field within the RVF. The mean and fluctuating values of local pressures and shear forces are compared.



1 Global investigations

Due to the presence of additional movement, the power consumption in RVF should be quantified, including pumping and mixing power. For industrial applications, it is useful to establish effective empirical equations for estimating energy consumption based on the operating conditions.

1.1 Pumping power

1.1.1 Pressure drop

If energy loss is not considered, the pumping power can be estimated with the pressure drop of the RVF module. Fig. IV.1 shows the evolution of pressure drop with the mixing rate. In the turbulent regime, the pressure drop increase with the mixing rate and the feeding flowrate. By increasing the fluid viscosity, the pressure drop at lower mixing rate (<20 Hz) for BREOX 0.2 (0.05 Pa.s) higher than that of BREOX 0.1 (0.01 Pa.s). The opposite result is obtained when N is superior to 20 Hz. At high viscous fluid (BREOX 0.4, 0.6 Pa.s), a decrease of ΔP_{RVF} can be observed with the mixing rate. This phenomenon indicates that the high shear force contributes to the flow of fluid through the RVF module.

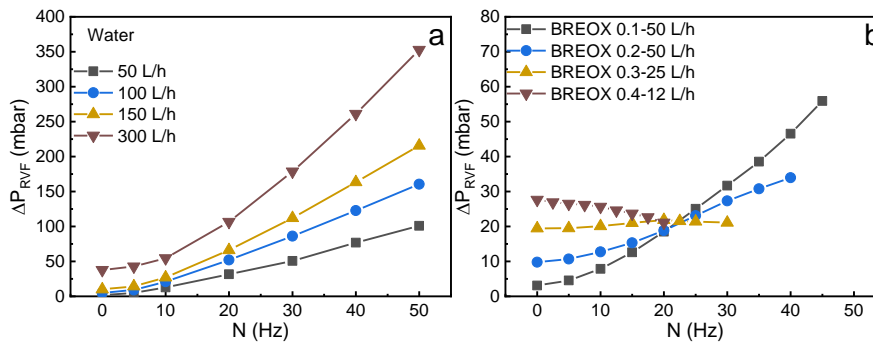


Fig. IV.1 The pressure drop of the RVF module as a function of the mixing rate. (a) the pressure drop for different flowrate (Q_F : 50-300 L/h); (b) the pressure drop for different viscosity (μ : 0.001-0.6 Pa.s).

1.1.2 Friction curve

At the process scale, the RVF module can be identified as a hydraulic singularity (generating pressure drop) or a confined mixing device (power consumption). The evolution of Euler number versus feeding ($0.6 < Re_{feeding} < 9000$) and mixing ($80 < Re_{mixing} < 1200000$) Reynolds numbers are shown in Fig. IV.2.

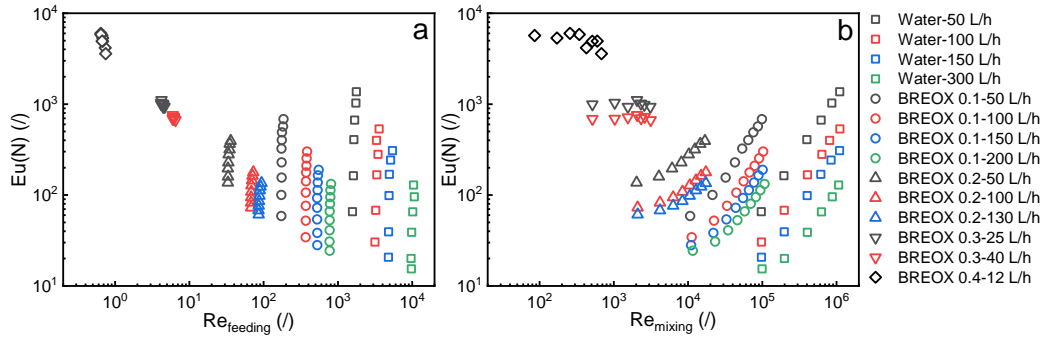


Fig. IV.2 Euler number with mixing versus feeding (a) and mixing (b) conditions, respectively.

In the absence of rotation, $Eu(N=0 \text{ Hz})$ shows a decrease with increasing $Re_{feeding}$ from 6200 to 13. These values are almost constant when $Re_{feeding}$ exceeds 1000, as seen with water in Fig. IV.3. At the same condition (water, 50-300 L/h), the values of $Eu(N=0 \text{ Hz})$ for Imp 1 are almost equal to that of Imp 2, but inferior to Imp 3. The empirical equation for Imp 1 is achieved as $Eu(N = 0 \text{ Hz}) = \frac{3924}{Re_{feeding}} + 14$, with $0.6 < Re_{feeding} < 11000$.

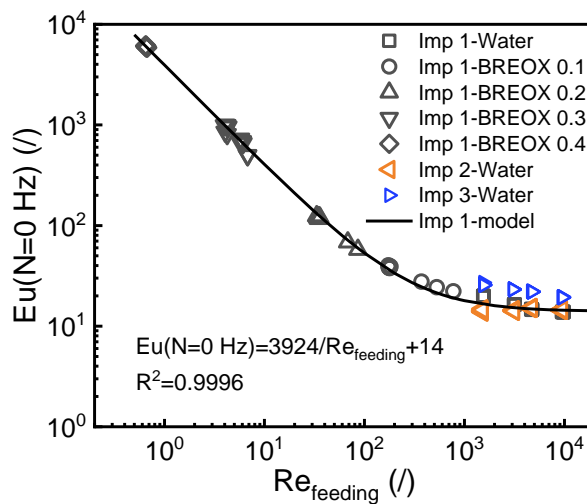


Fig. IV.3 Euler number without mixing versus feeding condition (0.001-0.6 Pa.s for Imp 1, 0.001 Pa.s for Imp 2 and 3).

For process engineering and scaling, it appears useful to establish simple semi-empirical correlations to estimate the pressure drop and power consumption in such a module. By subtracting $Eu(N=0 \text{ Hz})$, the Euler number increment is plotted as a function of mixing and feeding conditions in Fig. IV.4. The semi-empirical correlations for three impellers are displayed in Table IV.1:

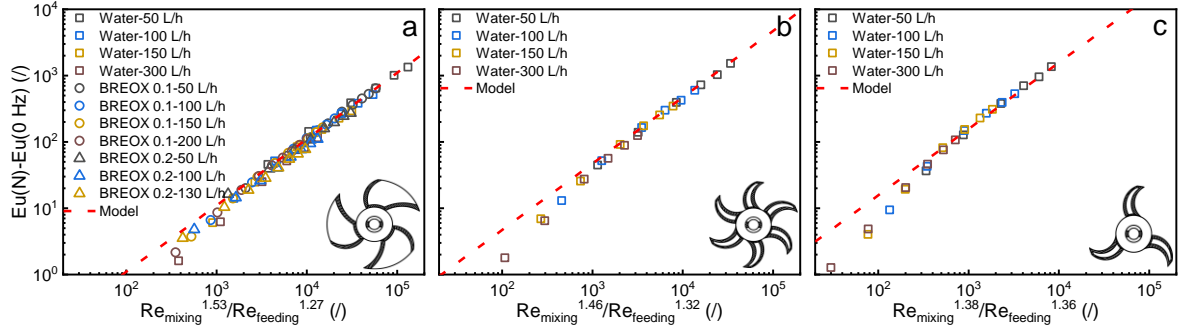


Fig. IV.4 Friction curve for different impeller configuration. (a) Imp 1 (μ : 0.001-0.6 Pa.s), (b) Imp 2 (μ =0.001 Pa.s) and (c) Imp 3 (μ =0.001 Pa.s).

For Imp 1, a general model shown in Fig. IV.4 a indicates the evolution of Euler number increment for different flow conditions. Some of the results in the laminar flow regime are not shown because the $Eu(N)$ values are lower than $Eu(N=0 \text{ Hz})$. The effect of shear on fluid flow promotion departs from the model at lower values of $Re_{mixing}/Re_{feeding}$. Under the turbulent regime, similar results are observed for the fitting of the other two impellers. In the previous work, two domains were proposed in turbulent regimes in order to give an accurate estimation of pressure drop [275].

Table IV.1 Established friction curves for three impellers.

Impeller	Conditions	Equation	R ²
Imp 1	2000 < Re_{mixing} < 1200000, 30 < $Re_{feeding}$ < 11000	$Eu(N) - Eu(0 \text{ Hz}) = \frac{0.0111 Re_{mixing}^{1.53}}{Re_{feeding}^{1.27}}$	0.9934
Imp 2	90000 < Re_{mixing} < 1200000, 1500 < $Re_{feeding}$ < 11000	$Eu(N) - Eu(0 \text{ Hz}) = \frac{0.047 Re_{mixing}^{1.46}}{Re_{feeding}^{1.32}}$	0.9985
Imp 3	90000 < Re_{mixing} < 1200000, 1500 < $Re_{feeding}$ < 11000	$Eu(N) - Eu(0 \text{ Hz}) = \frac{0.157 Re_{mixing}^{1.38}}{Re_{feeding}^{1.36}}$	0.9983

1.2 Mixing power

In order to generate sufficient shear on the membrane surface, the mixing power is dominant compared to the pumping power. The power consumption curves can be established based on the mixing condition with Re_{mixing} ranging from 10^2 to 10^6 .

1.2.1 Net power

Fig. IV.5 shows the net power for Imp 1 as a function of the mixing rate. With low viscous fluid, the net power for water and BREOX 0.1 follows the same model, and is

proportional to $N^{2.9}$, slightly higher than the exponent ($N^{2.75}$) estimated from the local shear stress [15]. By increasing the viscosity, the regression of Φ_N versus mixing rate is presented in Fig. IV.5 b, with the exponent count decreasing to 1.9. This value is very close to the N^2 in the laminar regime ($s/R < 0.05$).

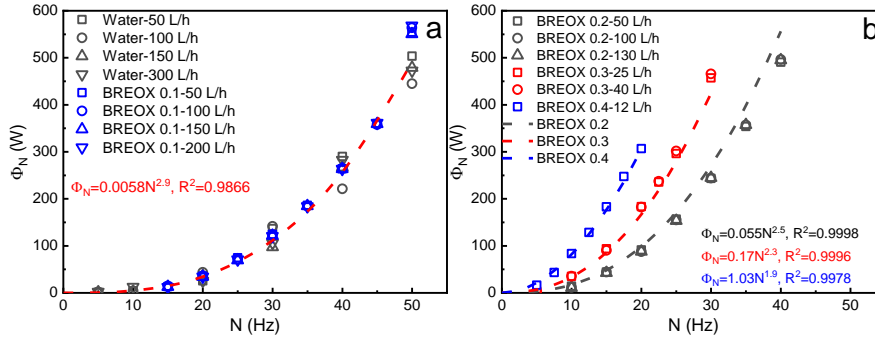


Fig. IV.5 Net power for Imp 1 as a function of mixing rate. (a) turbulent regime ($\mu=0.001, 0.01$ Pa.s); (b) laminar regime ($\mu=0.05, 0.2, 0.6$ Pa.s).

1.2.2 Power consumption curve

Just like the mixing tank, the net power of the rotor can be estimated by the power consumption curve, as shown in Fig. IV.6. Two separate regimes are observed at the Re_{mixing} equal to 30000, which is consistent with the investigation of flow conditions in the rotating dynamic filtration module. In the laminar regime ($Re_{mixing} < 30000$), Np is proportional to $Re_{mixing}^{-0.57}$, with the viscosity of fluid from 0.05 to 0.6 Pa.s. During the Re_{mixing} superior to 30000, Np tends to be constant whatever the mixing rates, and shows 0.09, 0.006 and 0.005 for Imp 1, Imp 2 and Imp 3, respectively.

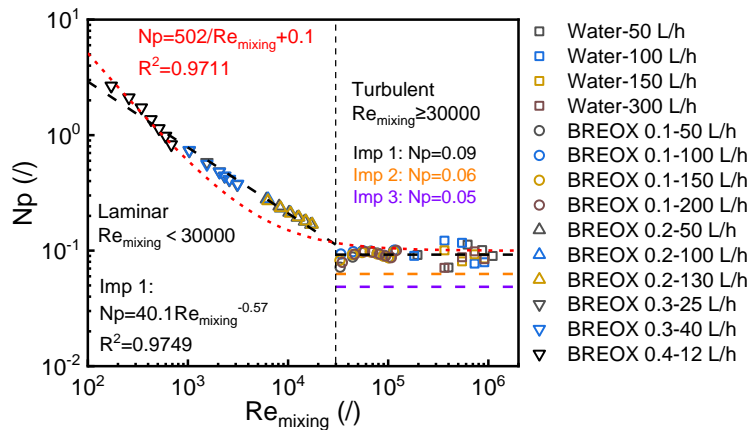


Fig. IV.6 Power consumption curves for three impellers from laminar to turbulent regime.

1.3 Thermal balance

The mechanical power is dissipated during the mixing of the impeller. If heat loss at the surrounding wall is not considered, the energy dissipation in the filtration cell is equal to the input power, which can be identified by the inlet and outlet temperature.

1.3.1 Thermal increase

Fig. IV.7 shows the thermal increase of the lab-scale RVF module as a function of the mixing rate. The relationship between ΔT and N can be represented by the parabolic representation. In the turbulent regime, Fig. IV.7a demonstrates that ΔT drops with the increase of feeding flowrate. The slight changes of ΔT can be observed at a constant flowrate (100 L/h) for three impellers, and it follows the order: Imp 2 > Imp 1 > Imp 3. By increasing the viscosity (Fig. IV.7), ΔT for water (0.001 Pa.s) and BREOX 0.1 (0.01 Pa.s), in the turbulent regime, are almost constant at the same flowrate. However, ΔT is higher in the laminar regime (BREOX 0.2, 0.05 Pa.s) at the same mixing rate. For high viscous fluid (BREOX 0.4, 0.6 Pa.s), only 12 L/h of flowrate can be reached with our equipment, and the thermal increase can reach more than 10°C at 20 Hz. The variation of fluid temperature is correlated with the flowrate, and it can be further explained by the thermal balance.

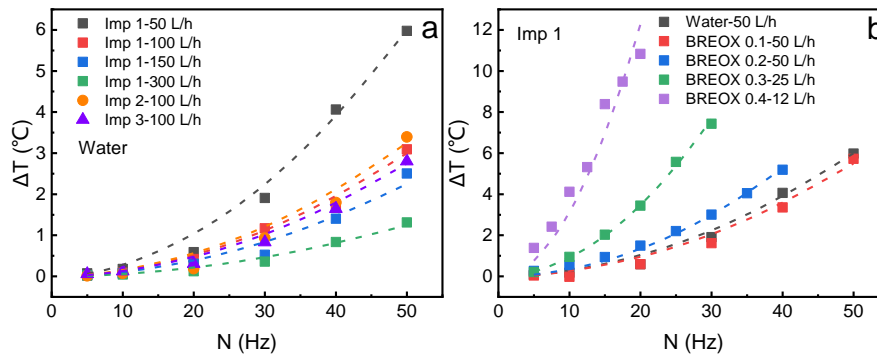


Fig. IV.7 Thermal increase of the fluid in the RVF as a function of mixing rate. (a) Different flowrate (water) for Imp 1 and 100 L/h for Imp 2 and 3; (b) different fluid (μ : 0.001-0.6 Pa.s) for Imp 1.

1.3.2 Thermal power

The thermal power Φ_T is shown in Fig. IV.8. For Imp 1 at 50 Hz, Φ_T increases by 30% at 300 L/h than 50 L/h, while these values are limited below 10% for Imp 2 and 3. The same phenomenon can be seen with BREOX 0.1, which shows more than a 45% of increase at 50 Hz. With the increase of viscosity, even at a very low flowrate (12 L/h), the thermal power increase dramatically. The numerical coefficient a by the regression of thermal power is

presented in Table IV.2.

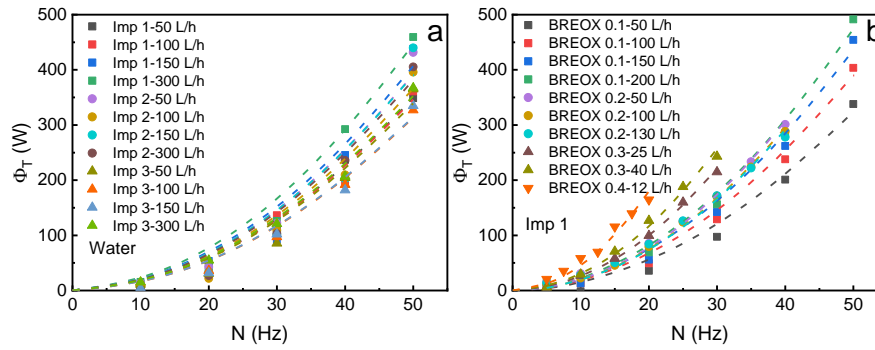


Fig. IV.8 Thermal dissipation in the RVF as a function of mixing rate for Imp 1. (a) Different flowrate (water, μ : 0.001 Pa.s, Q_F : 50-300 L/h,) and impeller; (b) different flowrate (Q_F : 12-200 L/h) and viscosity (BREOX solution, μ : 0.01-0.6 Pa.s).

Table IV.2 Numerical coefficient for the thermal dissipation based on the equation: $\Phi_T = aN^2$.

Fluids	Q_F (L/h)	N (Hz)	Imp 1	Imp 2	Imp 3
Water, $\mu=0.001$ Pa.s	50	0-50	0.1395	0.2565	0.1358
	100	0-50	0.1386	0.1463	0.1253
	150	0-50	0.1627	0.1561	0.1259
	300	0-50	0.1786	0.1527	0.141
BREOX 0.1, $\mu=0.01$ Pa.s	50	0-50	0.1295	/	/
	100	0-50	0.156	/	/
	150	0-50	0.1743	/	/
BREOX 0.2, $\mu=0.05$ Pa.s	50	0-40	0.1896	/	/
	100	0-40	0.1916	/	/
	130	0-40	0.1842	/	/
BREOX 0.3, $\mu=0.2$ Pa.s	25	0-30	0.1821	/	/
	40	0-30	0.2453	/	/
BREOX 0.4, $\mu=0.6$ Pa.s	12	0-20	0.2854	/	/

1.3.3 Energy balance

Considering the energy balance in the RVF module, the thermal dissipation should equal to the power input (pumping and mixing power). Fig. IV.9 presents the linear relation between thermal dissipation and net power for Imp 1. Due to the heat loss at the wall surface, the Φ_T constitutes 87% of the electrical power consumed by the mixing in the turbulent regime, whereas it decreases to 57% in laminar during the test with BREOX 0.4.

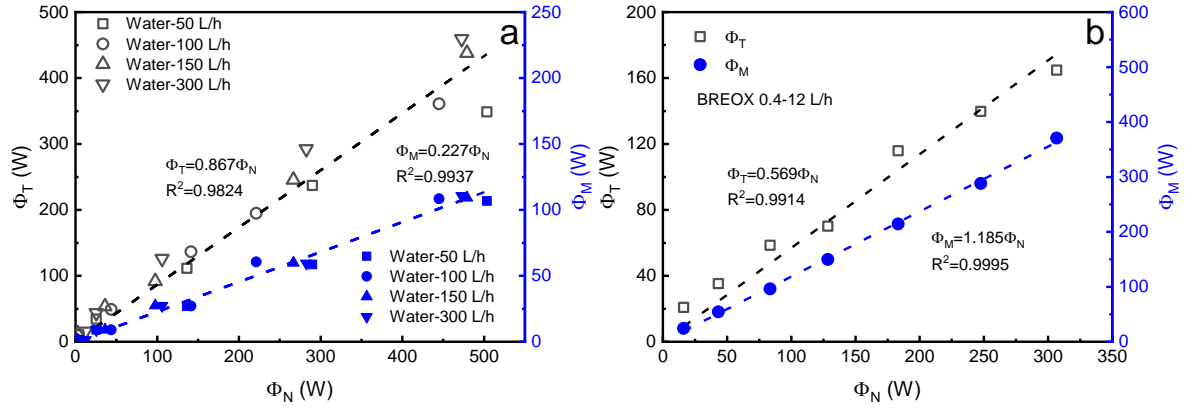


Fig. IV.9 Comparison of thermal dissipation and mechanical power as a function of net power for Imp 1. (a) turbulent regime ($\mu=0.001$ Pa.s, $N: 0-50$ Hz) (b) laminar regime ($\mu=0.6$ Pa.s, $N: 0-30$ Hz).

In a turbulent regime (Fig. IV.9a), the boundary layers merge together in a narrow gap (3 mm), and the local shear stress τ on the rotating disk is the linear relation with $N^{1.75}$ [96, 246]. As mentioned by Brouet al. [15], the mechanical power Φ_M generated by the friction force on the plate disk is calculated. With this model, Φ_M varies linearly with the nominal power, and it is underestimated by 22.7%. If the impeller surface area is considered, this ratio reduces to 11%. It demonstrates that the local shear stress on the blades only corresponds to a minor fraction of the torque. The major contribution of driving force contributes to the pressure difference between the leading and trailing edge of blades, which needs to be further investigated. In the laminar flow regime (Fig. IV.9b), the local shear stress is calculated using the classical model as Eq. (II.19). However, the mechanical power is overestimated (119%) during the integration on a full disk. Thus, approximately 60% of power can be achieved at the blade surface. The pressure driving force on the leading and trailing edge is not considered.

❖ Summary of Global investigation

Objectives:

- (1) To evaluate the pumping and mixing power in the RVF module during different mixing conditions (flowrate Q_F and mixing rate N);
- (2) To distinguish the flow pattern (laminar and turbulent regimes);
- (3) To estimate power consumption (mixing, pumping and thermal power) with established empirical equations;

Contents:

(1) Pumping power

The effective pumping power can be estimated with feeding and mixing conditions. For high viscosity fluids, the rotation of the impeller can even reduce the pumping power; and as the viscosity decreases, the increase in speed is positive to the pumping power.

(2) Mixing power

In the turbulent regime, the net power for the rotor indicates a linear with $N^{2.9}$ for both water and 10% BREOX solution. In comparison, the exponent of N reduces with the increase of viscosity due to the different boundary layers in the laminar regime. The feeding flowrate shows no effect on net power.

Compared with the mixing tank system, the relation between Np and Re_{mixing} in RVF shows the same shape. It illustrates that the transition from laminar to turbulent regime occurs at the Re_{mixing} around 30000. The constant values of Np for three impellers in the turbulent regime follow the order: Imp 1 > Imp 2 > Imp 3.

(3) Thermal balance

Due to the heat dissipation, the thermal increase of fluid should be considered in the biotic application. Properly increasing the flowrate or limiting the mixing rate contributes to the control of the fluid temperature.

After the integration of local shear stress with the empirical equations based on the merged boundary layer, the mechanical power shows a linear relation with net power. It indicates 22.7% and 118.5% of mechanical efficiency in the turbulent and the laminar regimes, respectively. The merged boundary layer theory is not suitable in the RVF module due to the large gap between the two blades. On the other hand, thermal power also can be used to estimate net power. But the slope is higher in the turbulent than in the laminar regime.

2 Local pressure at the membrane surface

In RVF, TMP is another essential factor affecting membrane filtration in addition to local shear stress. According to Eq. (III.13), the TMP can be estimated with back pressure and mixing conditions during the rotation of the impeller. The additional pressure is the function of the mixing rate, indicating a linear with N^2 . In microfiltration, TMP can be maintained at very low values (~ 100 mbar), and then high-pressure fluctuation (same order of magnitude as TMP), as an additional component, could contribute to surface cake layer and internal reversible fouling destabilization. The local pressures include the mean and fluctuating components at the membrane surface were measured at different radii (26.2-64.9 mm), mixing rates (0-50 Hz), flowrates (12-300 L/h) and viscosities (0.001-0.6 Pa.s).

2.1 Mean pressure

2.1.1 Mixing pressure

The mixing pressures as a function of mixing rates and radius are presented in Fig. IV.10. In the global overview, it can be seen that Imp 1 and 2 generate the same level of additional pressure and are superior to Imp 3.

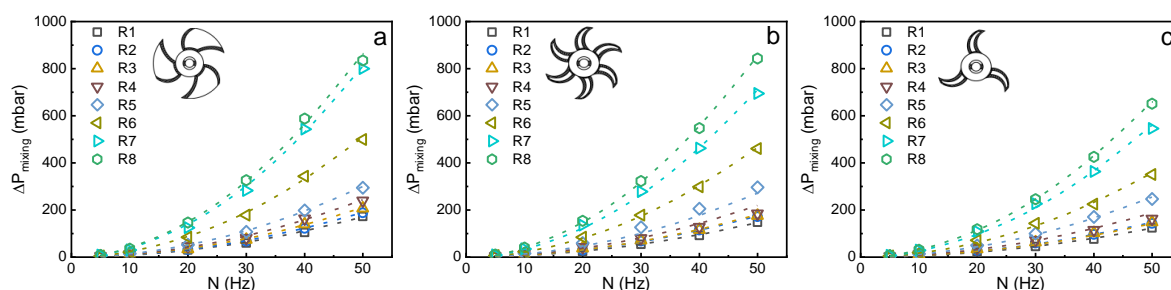


Fig. IV.10 Mixing pressure as a function of mixing rate and radius for three impellers. (a) Imp 1, (b) Imp 2 and (c) Imp 3. Operating conditions: $\mu=0.001$ Pa.s, N : 0-50 Hz, $Q_F=50$ L/h.

In Fig. IV.11, with an increase in flowrate, the mixing pressure is slightly increased, whatever the laminar and turbulent regime. For the change in viscosity, the water mixing pressure was slightly higher than that of BREOX 0.1 below 40 Hz under turbulent conditions. However, the mixing pressures of both were close at 50 Hz, probably due to the fact that the BREOX solution was then easily bubbled under high shear conditions. In the laminar regime, the viscosity increases from 0.05 to 0.6 Pa.s, and no visible distinction at mixing pressures below 20 Hz can be found. Above 20 Hz, a small decrease in mixing pressure can be noted as

the viscosity increases. However, from a global perspective, the mixing pressure of each regime can be represented by a single equation, respectively.

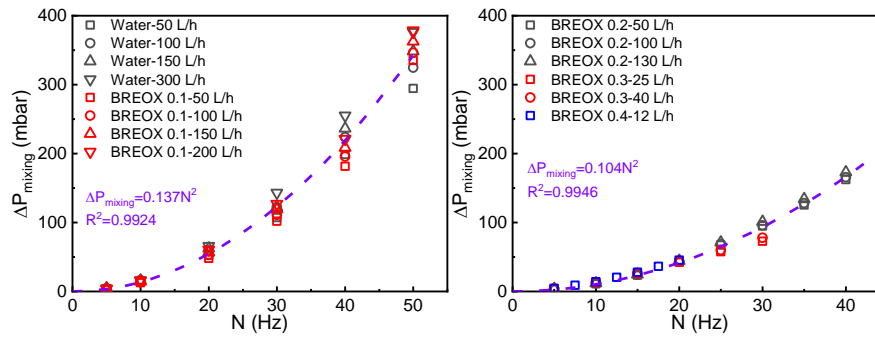


Fig. IV.11 Mixing pressure as a function of mixing rate at R5. (a) turbulent regime (μ : 0.001, 0.01 Pa.s, N : 0-50 Hz, Q_F : 50-300 L/h, Imp 1, r : 53.9 mm); (b) laminar regime (μ : 0.05, 0.2, 0.6 Pa.s, N : 0-40 Hz, Q_F : 12-130 L/h, Imp 1, r : 53.9 mm).

2.1.2 Core velocity coefficient

2.1.2.1 Impeller geometry

In rotating systems, the angular velocity in the main fluid can be written as $2\pi kN$. As the tangential velocity is considered as the dominant component of the velocity vector, the additional pressure due to mixing can be approximated as the proportion of N^2r^2 , i.e., the square of the tangential velocity component. Therefore, it appears that the value of k is larger than the actual value.

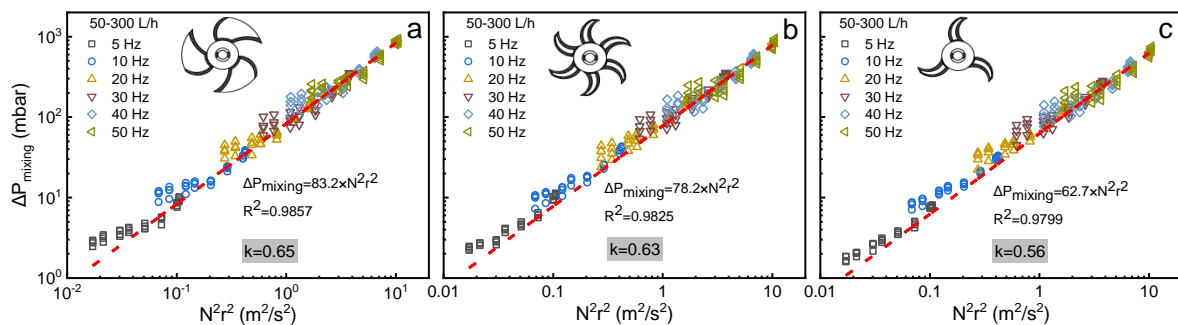


Fig. IV.12 Mean core velocity coefficient for three impellers. (a) Imp 1, (b) Imp 2 and (c) Imp 3. Operating conditions: water, μ : 0.001 Pa.s, N : 0-50 Hz, Q_F : 50-300 L/h, r : R1-R8.

Fig. IV.12a shows the regression of mixing pressure in water for Imp 1 as a function of N^2r^2 from 50 to 300 L/h. The great correlation indicates a core velocity coefficient equal to 0.65, which is lower than 0.71, as reported by Fillaudeau et al. [6]. Previously, the mixing pressure at a defined radius was measured with the permeable crowns. With large gaps (5 mm)

in the annular cavity, the k value was overestimated using the mean radius. By the regression of mixing pressure at all the conditions (rotation frequencies and radii), Fig. IV.12 indicates the k follows the order: Imp 1 > Imp 2 > Imp 3 ($0.65 > 0.63 > 0.56$). It can be concluded that more blades and a larger surface area seem to increase the k value. Similar results can be found in the rotating disk with vans [15, 183].

2.1.2.2 Flowrate

The ideal conditions based on a full disk system assume that mean local velocity (horizontal) results from radial and tangential velocities, $U_r(r)$ is determined by feeding flowrate and local cross-section, and $U_\theta(r)$ by mixing rate and core velocity coefficient. The horizontal velocity is shown as:

$$U_{r\theta}^2(r) = (k_{theo} 2\pi N r)^2 + \left(\frac{Q_F}{2\pi r s}\right)^2 = (k_{exp} 2\pi N r)^2 \quad (IV.1)$$

For example, during the circulation of water in the RVF module, the radial velocity at R1 is around 0.028 m/s at 50 L/h, and the impeller angular velocity is equal to 0.823 m/s at 5 Hz. Under this condition, the ratio between radial and angular velocities is limited to 3%. At the highest feeding flowrate (300 L/h), this ratio reaches more than 20%. It indicates that the contribution of feeding is more important with the lowest radii and mixing rates, as described by Eq. (IV.1).

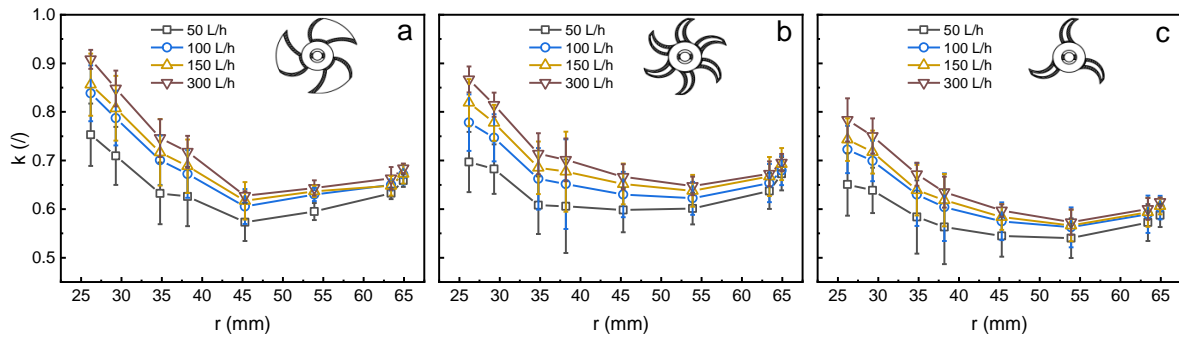


Fig. IV.13 Core velocity coefficient for different flowrates. (a) Imp 1, (b) Imp 2 and (c) Imp 3. Operating conditions: water, μ : 0.001 Pa.s, N : 0-50 Hz, Q_F : 50-300 L/h, r : R1-R8.

In order to clarify the radial velocity component on the effect of k value, the mean local k values for different flowrate were plotted as a function of radius in Fig. IV.13. It is clear that k increases with a higher feeding flowrate. The k values tend to decrease with the rise of radius before the plateau value ($R5=45.3$ mm) is reached; these phenomena can be seen from three impellers. It is also interesting to find that the mean k values at R6 are approximately

the global k -value estimated from the previous section (§ 2.1.2.1). By the integration of the same data at one flowrate, Fig. S 4 shows the k value increase with flowrate (50 to 300 L/h) by 7.8% for Imp 1, 9.8% for Imp 2 and 10.8% for Imp 3.

2.1.2.3 Mixing rate

The mixing rate effect on the k values also can be explained by Eq. (IV.1). In a constant flowrate, the contribution of angular velocity increase with the mixing rate, which indicates the experimental k values will be closer to the theoretical one. The local k values for three impellers are presented in Fig. IV.14. An increase of k can be observed at a lower radius due to the highest contribution of radial velocity at the entrance of the cell (close to the shaft). However, the changes of k at R8 (close to the external wall) are not yet known.

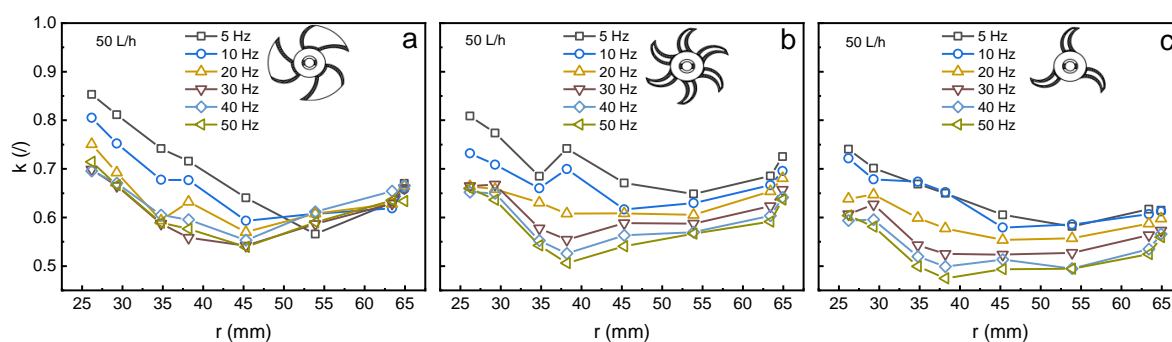


Fig. IV.14 Core velocity coefficient for different mixing rates. (a) Imp 1, (b) Imp 2 and (c) Imp 3. Operating conditions: water, μ : 0.001 Pa.s, N : 0-50 Hz, Q_F : 50 L/h, r : R1-R8.

2.1.2.4 Rotation direction

Due to the special shape of the impeller (leading edge protruding, trailing edge concave), the effect of rotation direction on k values of Imp 1 was investigated and shown in Fig. IV.15. It can be found that at R5 and R7, the impeller rotation direction has no effect on the k value. Curiously, at low radii (R2 and R4), the clockwise rotation of the impeller, its k -value is significantly higher than that with the counter-clockwise rotation. The effect of flowrate on k also can be observed at a lower radius during counter-clockwise rotation.

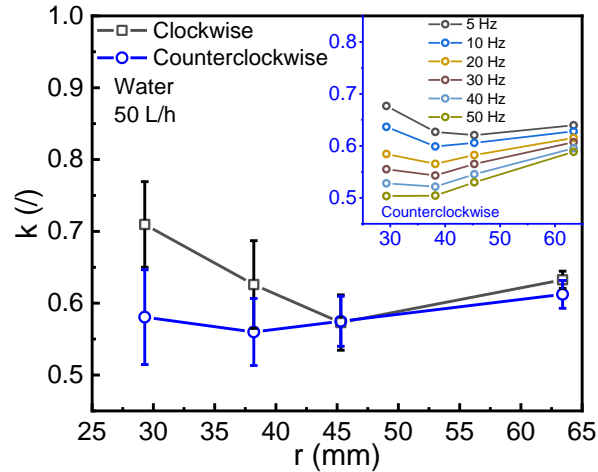


Fig. IV.15 Core velocity coefficient for the different rotation directions. Operating conditions: water, μ : 0.001 Pa.s, N : 0-50 Hz, $Q_F=50$ L/h, r : R2, R4, R5, R7.

2.1.2.5 Viscosity

It is of interest to observe the variation of k -value when altering the viscosity of the fluid. Fig. IV.16a shows that the k -value decreases with increased viscosity when r is close to the rotation shaft; the result is exactly the opposite when it is close to the impeller outer edge. Especially at high viscosity conditions, the k shows to increase with r , even reaching 0.7 at R7. Another point worth mentioning is that in the middle part of the membrane surface (R5), the change of viscosity shows little effect on the k value. The same data are represented in Fig. IV.16b, with the laminar and the turbulent flow as the distinction. In the turbulent regime, k tends to decrease with viscosity. But the mean k values are almost constant in the laminar regime among the test range, and the standard deviation of k shows to increase with viscosity due to the large range of k for different radii.

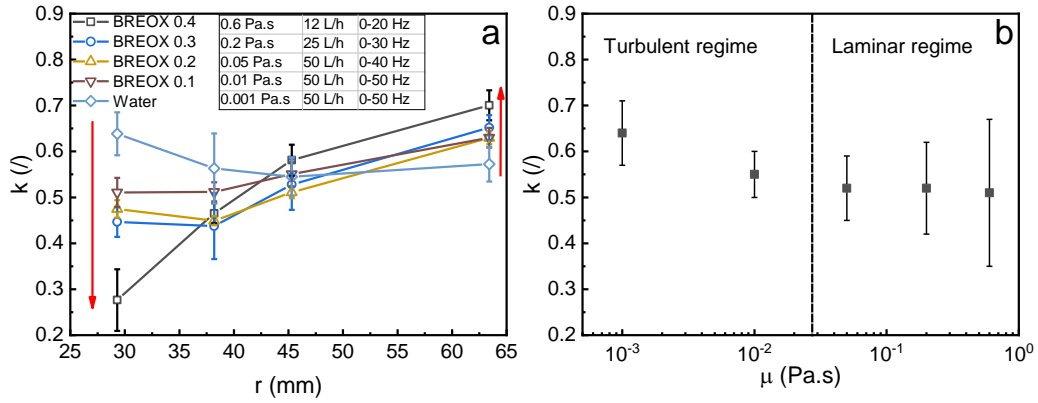


Fig. IV.16 Core velocity coefficient of different fluids. Operating conditions: μ : 0.001-0.6 Pa.s, N : 0-50 Hz, Q_F : 12-50 L/h, r : R2, R4, R5, R7.

2.2 Instantaneous pressure

2.2.1 Data convergence

As preliminary verification, the evolutions of $\bar{P}(N, r)$, σ_P , S and F as a function of sampling number in Fig. IV.17 demonstrate that statistical convergence of raw data is reached at $m > 1000$. The sampling number m (2^{15}) may be sufficient to be analysed with the following methods.

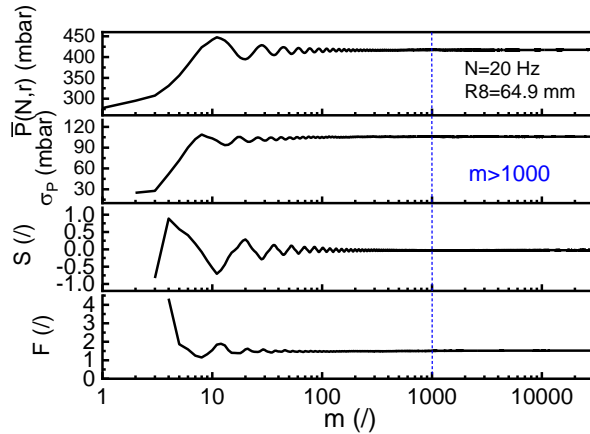


Fig. IV.17 Statistical convergence of raw data.

2.2.2 Raw data

Instantaneous pressures were locally measured at eight radii (R1 to R8) and different mixing rates from 0 to 50 Hz. They are shown in Fig. IV.18, indicating the increase of steady or mean pressure versus N and r for three impellers. But their magnitudes of fluctuation are

very different for each condition (N , r and impeller shape).

Interestingly, Imp 1 and 2 have similar steady pressure values, both higher than Imp 3. In addition, the magnitudes of pressure fluctuations follow the order: Imp 1 > Imp 3 > Imp 2. In Fig. IV.18d, it can be observed that the instantaneous pressure for Imp 1 varies with a period around 60 Hz, which is consistent with three times the mixing rate. This can be attributed to the number of blades. Whereas in Fig. IV.18f, the periodic amplitude of Imp 3 at 20 Hz is relatively small, its period is also in accordance with $3N$. For Imp 2 at 20 Hz, the periodic variation cannot be achieved from Fig. IV.18e, and the pressure fluctuations are much weaker.

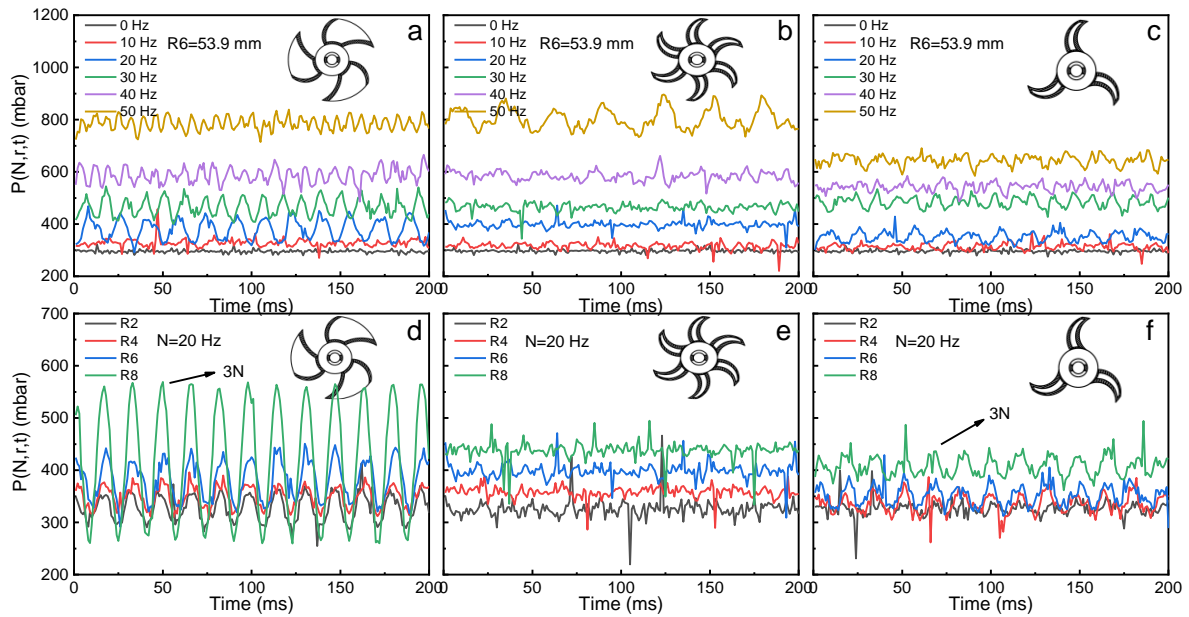


Fig. IV.18 Raw data analysis for three impellers with water. (a), (b) and (c) are the evolution of instantaneous pressure versus mixing rate for three impellers at R_6 ; (d), (e) and (f) are the evolution of instantaneous pressure versus local radius for three impellers at 20 Hz.

For different fluids, with the increase of viscosity from 0.001 Pa.s (water) to 0.6 Pa.s (BREOX 0.4), the instantaneous pressure for Imp 1 is shown in Fig. IV.19. At 10 Hz, there is no obvious periodic variation in pressure values for all viscosities. When N is equal to 20 Hz, the maximum steady pressure can be reached with BREOX 0.4 due to the increased back pressure, but the pressure signal is also disordered. For other viscosities, it can be seen that the pressure varies with a period approximately equivalent to $3N$. Similar cases can be observed at 30 Hz. The tests of water and BREOX 0.1 trend to be in the turbulent regime at 50 Hz. Assuming that $3N$ is the frequency of the signal, this would indicate a period of 6.7 ms when $N=50$ Hz. Due to the limitations of the pressure measurement frequency, there are only 6-7 points in each period, which is hard to achieve the fluctuating information (intensity and frequency). Further analysis associated with the continuous component of the signal (mixing

pressure) and the pressure fluctuations defined in Eq.(III.14) need to be investigated.

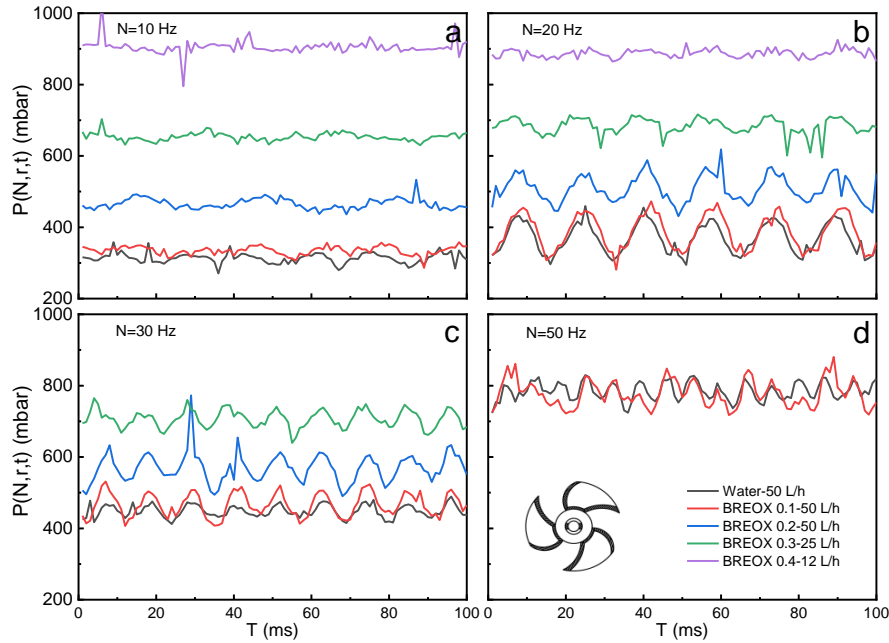


Fig. IV.19 Raw data analysis for different fluids with Imp 1. (a), (b) (c) and (d) are the evolution of instantaneous pressure at R6 and mixing rate of 10, 20, 30 and 50 Hz, respectively.

2.2.3 Turbulent regime

The pressure fluctuation can be analyzed with SA, PDF, FFT and modeled to illustrate the fluctuating intensity and frequency of the signal. Same treatments are carried out to compare the fluctuations with three different impellers.

2.2.3.1 SA

The standard deviation σ_P has been used to describe the fluctuation intensity of the signal. As shown in Fig. IV.20, σ_P is independent of back pressure and flowrate, but influenced by mixing rate. On the contrary, the local pressure P_0 is influenced by these parameters. Of course, the change in these parameters will affect the mean local pressure.

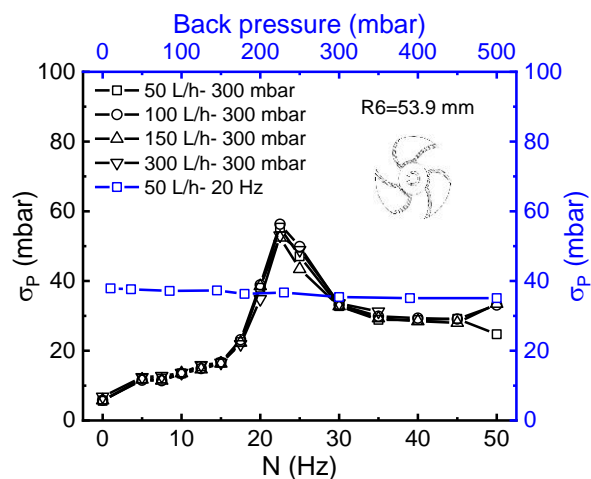


Fig. IV.20 Standard deviation of instantaneous pressure for Imp 1 at different conditions (flowrates, mixing rates and back pressures) with water.

Fig. IV.21a, b and c present the evolution of σ_P under different conditions. For Imp 1, a large increase of σ_P with N can be observed below 20 Hz and followed by a decrease until 50 Hz. The maximum σ_P varies in the range of mixing rate between 20 and 25 Hz. It increases with local radius and even reaches more than 100 mbar at R8. For Imp 2, σ_P exhibits a constant value below 20 mbar, and then slightly increases with a mixing rate from 40 to 50 Hz. While the increase of σ_P occurs at 20 Hz with Imp 3, it is relatively lower than Imp 1. With the same shape of blades, the highest deviations for Imp 2 and 3 are limited to a value below 50 mbar, almost negligible when compared with Imp 1. It can be concluded that more blades contribute positively to a higher mixing pressure but negatively to the generation of pressure fluctuations. Comparing the standard deviation of instantaneous pressure relative to steady pressure, the coefficients of variation β are shown in Fig. IV.21d, e and f. It can be noticed that the β value of Imp 2 is limited to less than 7%; Imp 3 shows an increase, reaching 13% at R4. However, these values are inferior to Imp 1, which achieved 25.3% of local pressure at R8 and 20 Hz. It indicates that the pressure fluctuations cannot be neglected with Imp 1 in microfiltration applications. An intensive fluctuating area with high-pressure fluctuations at the membrane surface is promoted at the range of mixing rate from 15 to 30 Hz.

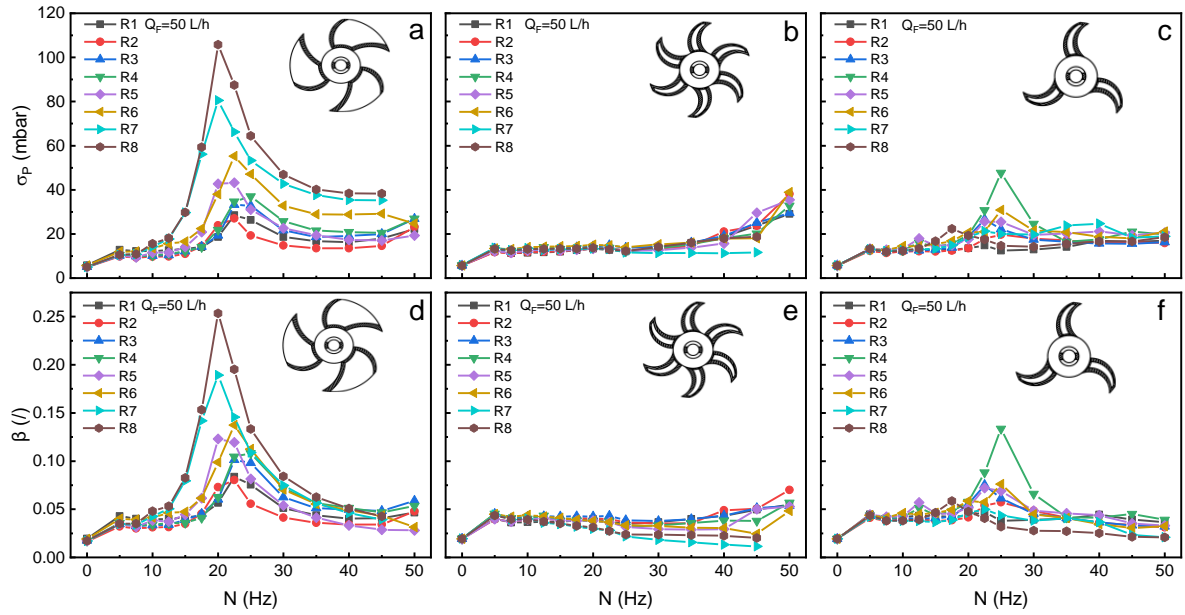


Fig. IV.21 Statistical Analysis. (a), (b) and (c) are the evolution of standard deviation versus mixing rate for three impellers; (d), (e) and (f) are the coefficient of variation versus mixing rate for three impellers.

The high order moment distributions from 0 to 50 Hz and R1 to R8 are shown in Fig. IV.22. Fig. IV.22a, b and c present the skewness under different conditions, with values varying from -0.8 to 0.8 and showing disorder versus mixing rate and local radius. The flatness indicates the degree of peakedness of PDF, as shown in Fig. IV.22d, e and f. Compared with F in a normal distribution ($F=3$, dashed blue lines), the value of F superior to 3 informs that a sharp distribution with a narrow fluctuation intensity, while $F>1$ indicates the extension of PDF and results in a large deviation. For Imp 2, F shows a decrease with the mixing rate, and its value is consistent with a normal distribution when the maximum N of 50 Hz is reached. That can be explained by the increase in pressure fluctuations. The same results are also achieved from Imp 1 and 3. Comparison with the normal distribution gives an indication of the fluctuations in the data to some extent, but the magnitude of the fluctuations still needs further analysis.

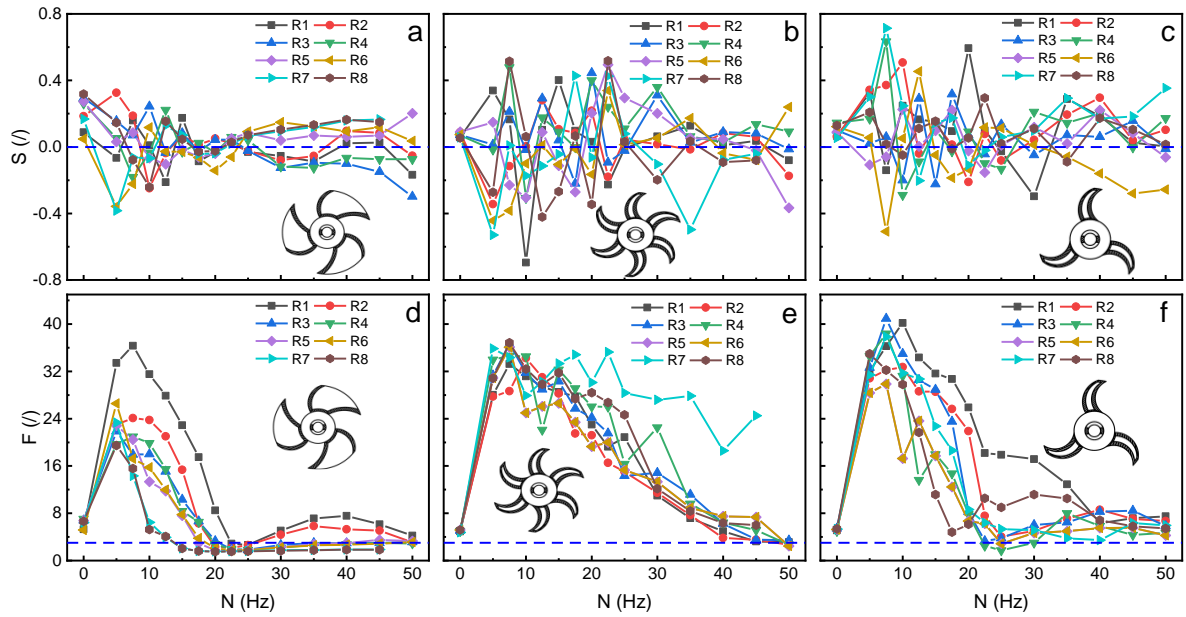


Fig. IV.22 High order items distribution. (a), (b) and (c) are the skewness distribution for three impellers; (d), (e) and (f) are the flatness distribution for three impellers. The dashed line indicates the S and F in a normal distribution.

2.2.3.2 PDF

PDF provides a more explicit profile of pressure fluctuations. Fig. IV.23 presents the PDF of three impellers under different conditions. At R6, a strong fluctuation occurs at a mixing rate around 20 Hz for Imp 1. The same observation can be found for Imp 3, but with lower fluctuation intensity. While the large extension of PDF for Imp 2 is only found at 50 Hz. At the same mixing rate (20 Hz), Imp 1 shows two peaks in the PDF, with an increase of fluctuations from 40 to 160 mbar with radius. The pressure fluctuations are limited below 40 mbar for Imp 2 and 3; only one peak is found for Imp 2 at all the radius, while two peaks can be observed for Imp 3 at a mixing rate ≥ 20 Hz. These results are consistent with the fluctuation intensity represented by standard deviation.

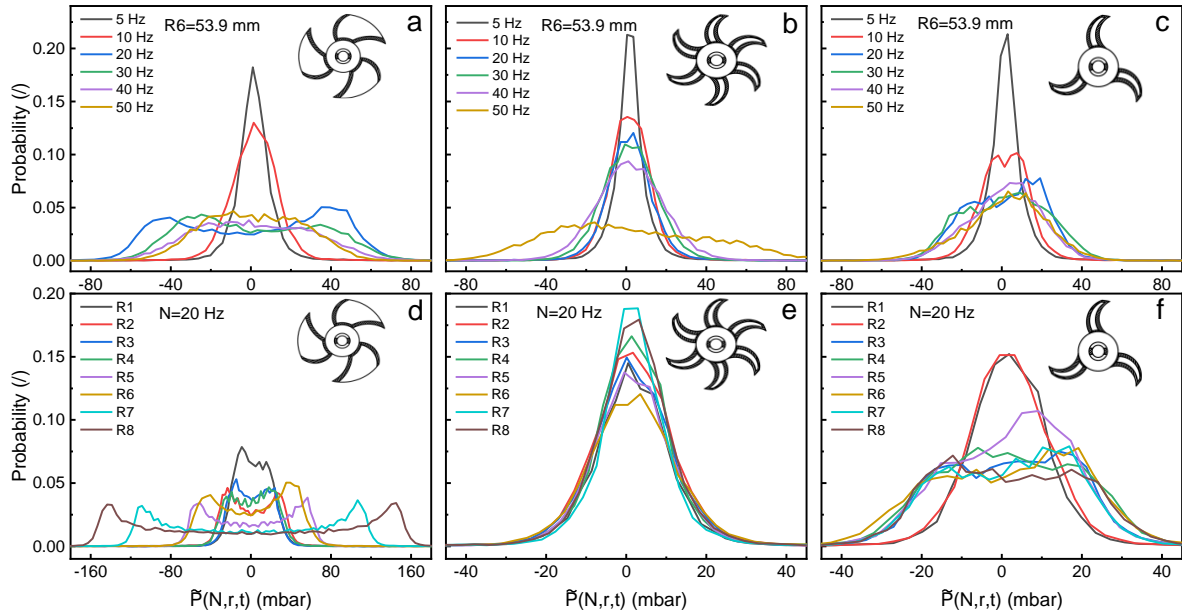


Fig. IV.23 PDF at different conditions. (a), (b) and (c) are the PDF versus mixing rate for three impellers; (d), (e) and (f) are the PDF versus radius for three impellers.

In order to provide additional insights into the pressure fluctuations, the PDF analysis for Imp 1 is shown in Fig. IV.24a, with the mixing rates from 0 to 50 Hz at R6. When N is below 10 Hz, the spectrum displays as unimodal, confined to a narrow fluctuating signal. When $N > 10$ Hz, the peak at the zero deviations sinks downward and expands to the sides, forming a bimodal and reaching the highest deviation at 20 Hz. Nevertheless, The PDF at 10, 40 and 45 Hz can be defined as the transition zone. In general, the probability distribution of a sinusoidal signal has a U-shaped structure, while a random signal tends to be normally distributed. The transition from unimodal to bimodal will occurs with the increased contributions of the sinusoidal wave relative to the random component.

Considering the peak-to-peak values in Fig. IV.24b, the magnitude of pressure fluctuation evolves with the mixing rate and radius. The unimodal region occurs below 10 Hz, whose intensity cannot be achieved due to only one peak value observed. The dash lines demonstrate the transition areas in the range from 10 to 17.5 Hz and 30 to 50 Hz. However, at a large radius, such as R8, the intensive fluctuation (bimodal) happens at $N > 10$ Hz and reaches the maximum peak-to-peak value of 144 mbar at 20 Hz. Due to the fact that Imp 2 and 3 generate a very low-pressure fluctuation for most conditions, this method is inappropriate.

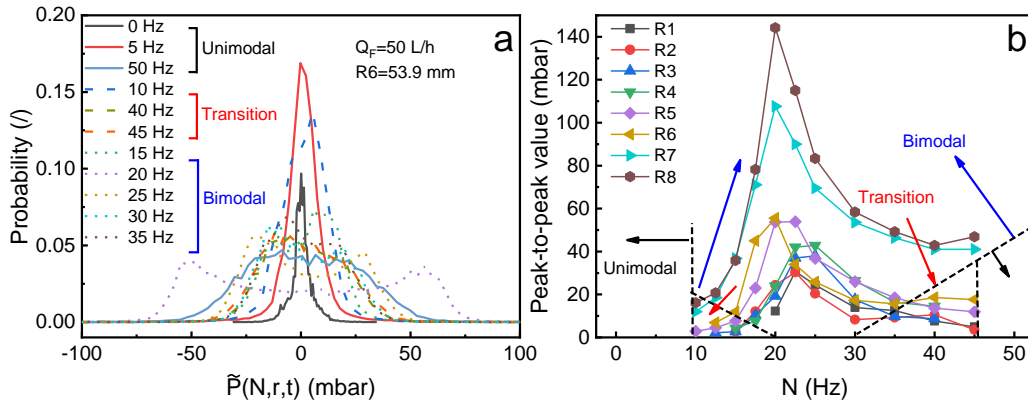


Fig. IV.24 PDF analysis for Imp 1. (a) the probability distribution of fluctuating pressure at R6; (b) the evolution of PDF width (peak-to-peak/2) versus mixing rate.

2.2.3.3 FFT

With FFT, the time variations of pressure are presented on the frequency domain. A mixing rate of 20 Hz is selected as the representative to display in Fig. III.5. For three blades impellers (Imp 1 and 3), the significant peak amplitudes are found at N , $2N$, $3N$, $4.25N$ and $6N$, where N is the mixing rate. The value of $3N$ demonstrates that the main frequency can be associated with the mixing rate and the number of blades. N and $2N$ indicate the effects of one and two blades, while $6N$ is linked to twice the number of blades. The same peaks can be observed with six blades impeller, but $12N$ amplitude is almost negligible in the spectrum. In addition, another peak amplitude can be found at $4.25N$ for the three different impellers, with intensities around 1 mbar. It remains unclear for the pressure fluctuations during mixing. Compared to the amplitude at $3N$, there is an increase in the radius for Imp 1, even reaching up to 100 mbar at R8. Imp 3 also shows the same behaviour but with a lower amplitude. Whereas the amplitude for Imp 2 is almost constant at all the radii.

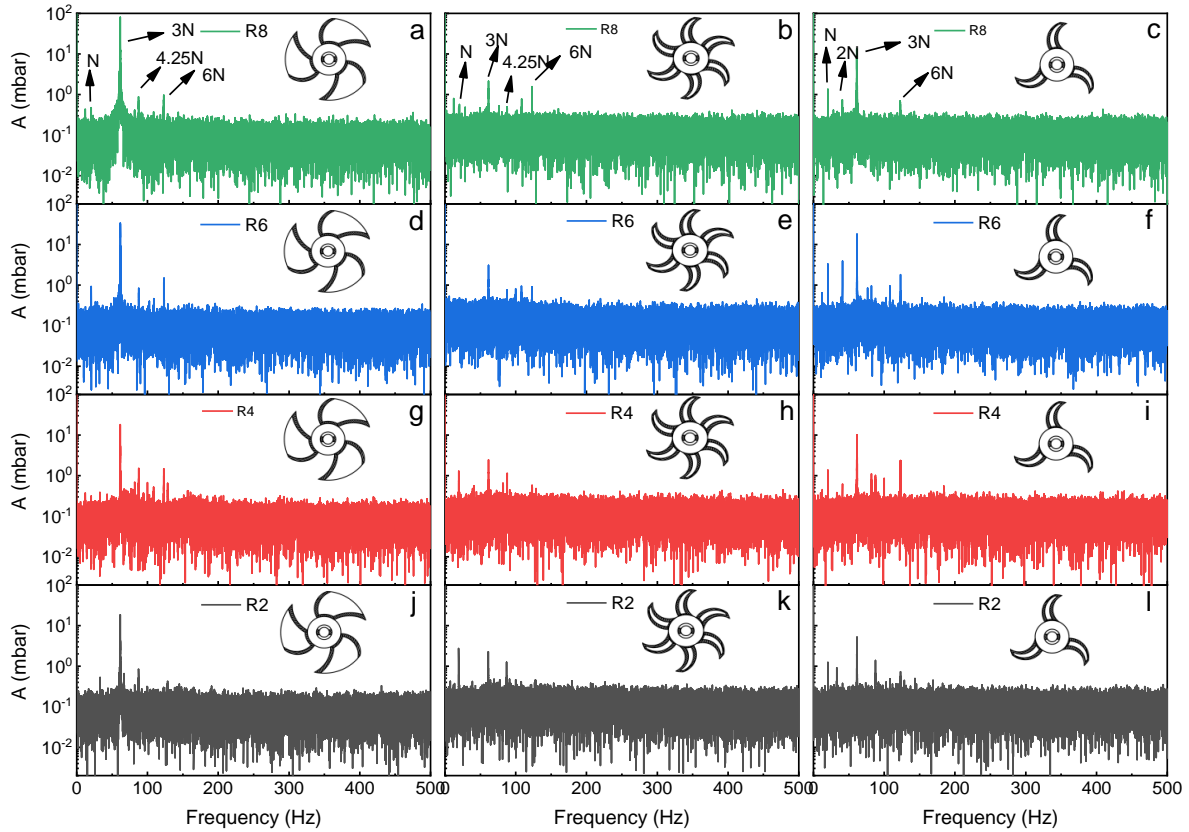


Fig. IV.25 Frequency domain analysis with FFT at 20 Hz. (a), (d), (g) and (j) are Imp 1; (b), (e), (h) and (k) are Imp 2; (c), (f), (i) and (l) are Imp 3.

Fig. IV.26 shows the cumulative amplitude of pressure fluctuations at the frequency of N , $2N$, $3N$, $4.25N$ and $6N$ at R6 for the three impellers. This type of representation appears to be very useful for exploring the dominant frequencies, i.e., the frequencies associated with the higher amplitudes in FFT analysis plotted in Fig. IV.25. It can be seen in Fig. IV.26a that the cumulative amplitude increases significantly with the mixing rate until 22.5 Hz, and then decreases for Imp 1. This behaviour is similar to one of the standard deviations plotted in Fig. IV.21a. The dominant frequencies are $6N$ below 10 Hz and $3N$ above 10 Hz. For Imp 2 (Fig. IV.26b), the cumulative amplitude is very weak, below 10 mbar. We find that the dominant frequencies are $6N$ from 5 to 15 Hz, change to $3N$ from 17.5 to 35 Hz, and finally to be N from 40 to 50 Hz. It indicates that there is an increase in the contribution of the frequency N (one-blade effect) at higher mixing rates. Furthermore, it should be noted that the cumulative amplitude does not increase at 50 Hz as it appears in σ_P , which means that this increase of pressure fluctuations is generated by a random component instead of a periodic signal. For Imp 3 (Fig. IV.26c), with the increase in mixing rate, the dominant frequencies evolve from $6N$ (5-10 Hz) to $3N$ (12.5-30 Hz) and $2N$ (35 Hz), finally by N (40-50 Hz). The cumulative

amplitudes also differ somewhat from σ_P , especially for the value of N associated with the maximum fluctuations (cumulative amplitude at 30 Hz, σ_P at 25 Hz). It can be concluded that the random signal is not so important in the pressure fluctuations for Imp 1, while it has a greater effect in the case of Imp 2 and 3.

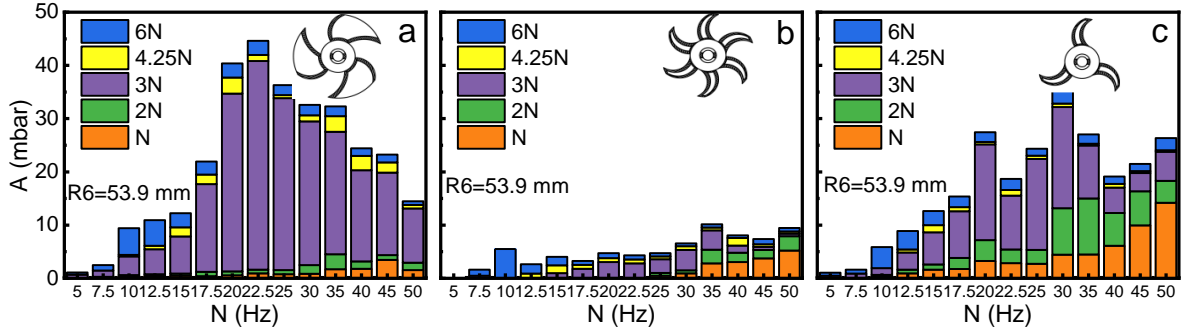


Fig. IV.26 Cumulative amplitudes at R6. (a) Imp 1; (b) Imp 2; (c) Imp 3.

2.2.3.4 Modelling

As explained in Eq.(III.22), a model is proposed to reconstruct the PDF of pressure fluctuations from the convolution of a periodic and a random signal. The model parameters are determined from the minimisation of the cumulative error function: $\Delta \leq 0.35$. The plots of Fig. IV.27a, b and c show the phase diagram of total intensities versus mixing rate and radius at the membrane surface. With the same legend, the total energy input for Imp 1 can reach up to 100 mbar at 20 Hz, which is much higher than the maximum value from Imp 2 and 3. The more intensive fluctuations occur at a high mixing rate ($N > 40$ Hz) for Imp 2, and from 20 to 40 Hz for Imp 3. These total energy inputs are consistent with σ_P , indicating a high degree of model validity. For random signals, the I_R is limited below 30 mbar for the three impellers. The relative periodic contribution $I_P/(I_P+I_R)$ is presented in Fig. IV.27d, e and f. It is found that the periodic fluctuations for Imp 1 dominate for most conditions (15-40 Hz), while they only appear at 20 to 30 Hz for Imp 3. Due to the weak amplitude observed in Fig. IV.27b for Imp 2, the periodic contribution remains below 50%. Thus, the use of Imp 1 is more appropriate than Imp 2 and 3 to intensify the pressure fluctuations at the membrane surface.

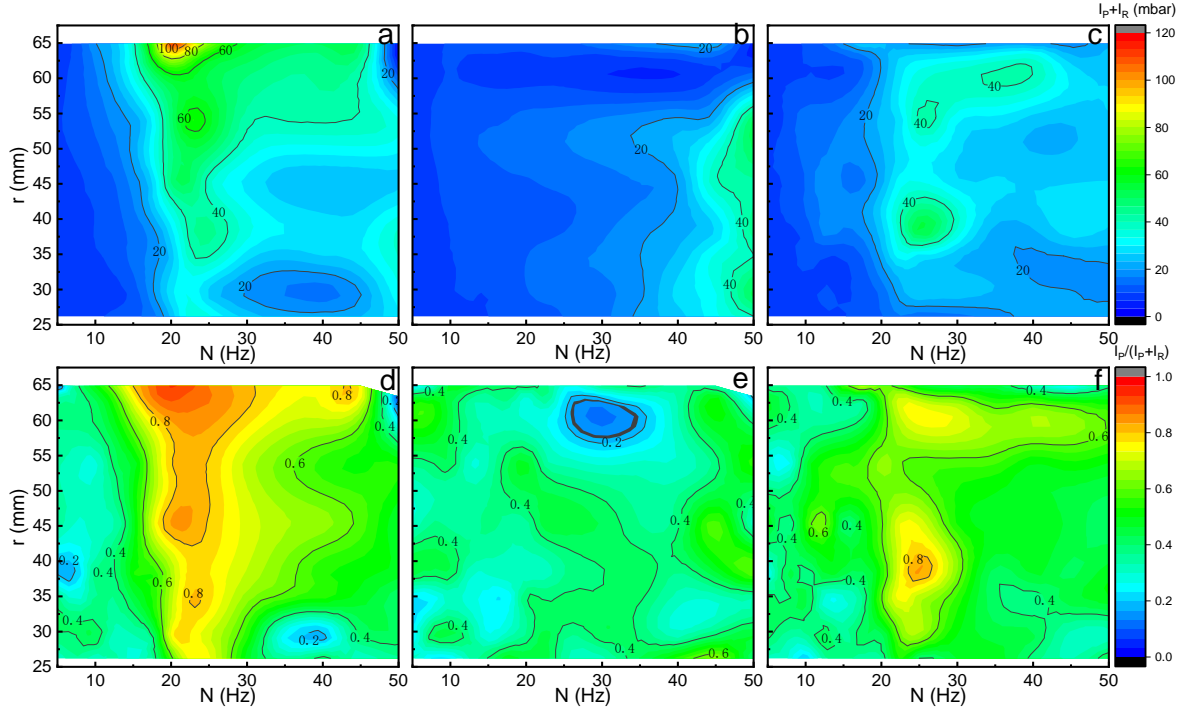


Fig. IV.27 Total energy input $I_P + I_R$ (a, b, c) and periodic contribution $I_P / (I_P + I_R)$ (d, e, f) as a function of mixing rate and radius for Imp 1, Imp 2 and Imp 3, respectively.

The regression of intensity versus mixing rate (N , Hz) and radius (r , m) can be a useful way to estimate the pressure fluctuations. It is plotted in Fig. IV.28. For periodic fluctuations (I_P , mbar), the fluid flow resonates under the periodic rotation of the impeller. On the membrane surface, the periodic pressure fluctuations evolve similarly to the response amplitude $U(\omega)$ of a second-order linear system to a periodic input force $F = F_0 \sin(\omega t)$ [276], which follows the equation:

$$U(\omega) = \frac{GF_0}{\sqrt{(1-s^2)^2 + (2\epsilon s)^2}} \quad (IV.2)$$

where $s = \omega / \omega_0$ is the pulsation ratio. Here, we recognise the three parameters of the second-order system: G is the gain, ω_0 is the intrinsic pulsation and ϵ the damping coefficient. However, the input signal $F' = F_0 \omega r \sin(\omega t)$ varies as a function of ω and r in our system; Eq. (IV.2) was then modified to obtain a new function $U'(\omega)$. It can be written as:

$$U'(\omega) = \frac{GF_0 r^2 s^2}{\sqrt{(1-s^2)^2 + (2\epsilon s)^2}} \quad (IV.3)$$

With slight modifications, a new model based on mixing rate and local radius is proposed as in Eq. (IV.4); the corresponding resonance frequency (N_r) of the system is calculated using Eq. (IV.5).

$$I_P(N, r) = \frac{K}{\sqrt{(1-s^2)^2 + (2\epsilon s)^2}} \times \rho N^2 r^2 \quad (IV.4)$$

$$= \frac{KN_0^2}{\sqrt{(N_0^2 - N^2)^2 + (2\epsilon N_0 N)^2}} \times \rho N^2 r^2$$

$$N_r = \frac{N_0}{\sqrt{1-2\epsilon^2}} \quad (IV.5)$$

where $K = \frac{GF_0}{\rho N_0^2}$ and ϵ are constants, N_0 is the intrinsic frequency of the fluid in the cell. After the regression, N_0 is equal to 20.6 Hz, which is slightly lower than the resonance frequency (21.1 Hz). Meanwhile, the values of K and ϵ are solved as 1.5 and 0.15, respectively.

For the random signal, I_R is found to be independent of the radius and to increase with the mixing rate slightly. Then a linear regression is used to approximate the variations of random intensity as a function of N , which give a 90% prediction band with $I_R \pm 3.4$ mbar.

$$I_R = 0.21N + 4.8 \quad (IV.6)$$

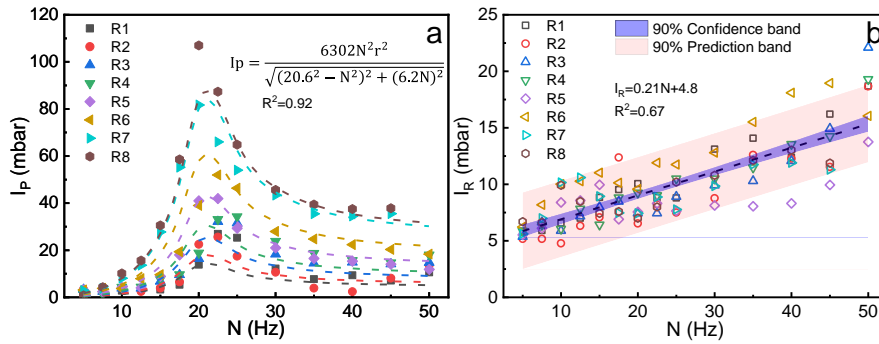


Fig. IV.28 Fluctuating intensities for Imp 1 as a function of mixing rate and radius. (a) periodic intensity; (b) random intensity.

2.2.3.5 Comparison of fluctuating intensity

The signal reconstruction of instantaneous pressure can be seen in Table IV.3. Since membrane surface pressure includes periodic signals generated by impellers and random signals induced by turbulent flow, coupled with sensor errors, it is not accurate to describe pressure fluctuations by standard deviation only. The different methods are compared below.

Table IV.3 Information on the data treatment.

Method	Mean pressure	Fluctuating pressure		
		Periodic + Random	Periodic	Random
SA	$\bar{P}(N, r)$	σ_p, S, F	/	/
PDF	/	Peak-to-peak	/	/
FFT	/	/	A_i, f_i	/
Model	/	/	A_I, f_I	σ

The evolution of fluctuating intensity for three strategies and modelling are compared in Fig. IV.29. From a global perspective, the deviations of the curves almost share the same trends with increasing mixing rates. The results from PDF are higher than other methods, around 1.04 (± 0.17) times of σ_p above 15 Hz. Nevertheless, the former case contains information about fluctuations in all ranges, which can be useful in signal reconstruction. Meantime, the amplitude from FFT at $3N$ indicates 0.72 (± 0.18) times of σ_p . This ratio increases to 0.9 if the contributions of other peaks (N , $2N$, $4.25N$ and $6N$) are considered. When it comes to the model, fluctuating intensity is composed of the period and random contributions. The total energy input is higher than σ_p and reaches 126%. As shown as a grey zone in Fig. IV.29, the intensive fluctuation occurs in the range from 15 to 30 Hz.

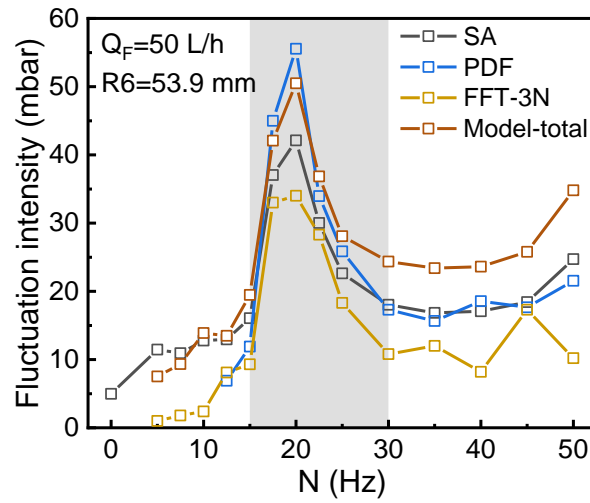


Fig. IV.29 The evolution of pressure fluctuations (standard deviation, peak-to-peak/2, amplitude from FFT at $3N$ and total energy from modelling) as a function of mixing rate.

2.2.3.6 Signal reconstruction

At different mixing rates, the local pressure close to the central shaft (P_0) is almost constant with the same back pressure (300 mbar) and flowrate (50 L/h). ΔP_{mixing} is calculated with the k value equal to 0.59 obtained previously. The model parameters A and σ are determined from experimental data as explained in section § 2.2.3.4. The dominant frequency is chosen equal to $3N$. φ does not affect the signal fluctuations and can be ignored. These parameters are shown in Table IV.4.

The time variations of pressure calculated from the model are compared with the experimental data and shown in Fig. IV.30. It can be noticed that the reconstructed signal provides a good description of the instantaneous pressure. Thus, this indicates that we can make use of this simplified model or estimate the time variations of the local pressure.

Table IV.4 Signal reconstruction for Imp 1 at R6, with the value of the two parameters to estimate the instantaneous pressure. A and σ are calculated from the convolution of PDF functions.

N (Hz)	P_0	ΔP_{mixing}	$\overline{P}_P(t)$		$\overline{P}_R(t)$
	Constant (mbar)	k (/)	A (mbar)	f (Hz)	σ (mbar)
10	294.5	0.59	5.5	3N	6.9
20			58	3N	9
30			32.3	3N	11.1
40			24.4	3N	13.2
50			21.8	3N	15.3

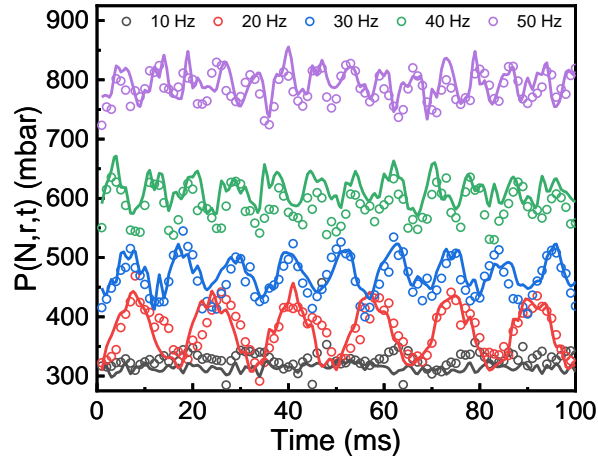


Fig. IV.30 Signal reconstruction of instantaneous pressure with empirical correlations (continuous and fluctuating components at R6). Dots and lines correspond to the experimental and reconstructed signal, respectively.

2.2.4 Laminar regime

In the measuring range, the pressure fluctuations within the laminar flow conditions are much lower than those under the turbulent flow. Although the distribution of fluctuating pressure can be visually characterized by PDF, it is difficult to quantify their intensities. In this section, the pressure fluctuation in laminar flow conditions (BREOX 0.3) will be characterized by SA and FFT.

2.2.4.1 SA

The standard deviation (σ_P) of pressure fluctuation versus mixing rate and radius is shown in Fig. IV.31. The variation of pressure is almost negligible (below 20 mbar) during the mixing rate inferior to 15 Hz and $r < 40$ mm. The highest value is observed at 30 Hz and R5, which is approximately one-fourth in the turbulent regime.

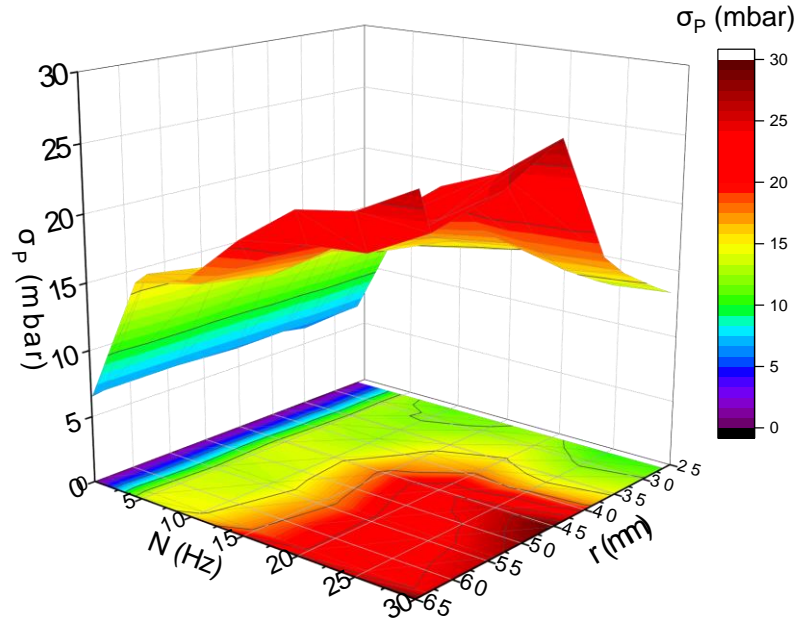


Fig. IV.31 Standard deviation of pressure fluctuation at different mixing rates and radii.

2.2.4.2 FFT

Following FFT analysis, in the laminar regime, the evolution of cumulative amplitudes versus mixing rate at R6 is displayed in Fig. IV.32. The same peak amplitude at N , $2N$, $3N$, $4.25N$ and $6N$ as in the turbulent regime can be found. Amplitudes at $3N$ still dominate at the test range of mixing rate from 0 to 30 Hz. Contrary to the turbulent conditions, no extreme values of the amplitude were observed. The value of A at $3N$ demonstrates a linear relation with a mixing rate up to 30 Hz.

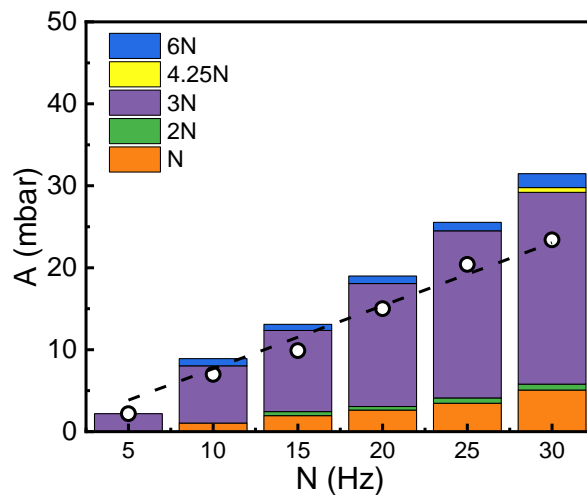


Fig. IV.32 Evolution of cumulative amplitude from FFT versus mixing rate.

2.2.4.3 Modelling

Modelling and quantifying periodic and random contributions of fluctuating pressure

have been determined by identifying their amplitude (A) and standard deviation (σ). In Fig. IV.33a, the total energy evolves with radius (R1 to R8) and the mixing rate (5 to 30 Hz) is presented. Similar to the SA and FFT results, the total energy input is limited to less than 40 mbar, reaching a maximum of 35 mbar at 30 Hz, R5 and R8. Among them, the maximum value of the periodic pressure intensity is 24 mbar, which is higher than the random signal intensity of 13 mbar. Fig. IV.33b shows the map of the ratio between periodic and total energy input for the pressure fluctuation. It indicates that the periodic signal is dominant (more than 50%) at higher radii ($r > 45.3$ mm) and mixing rates ($N > 20$ Hz).

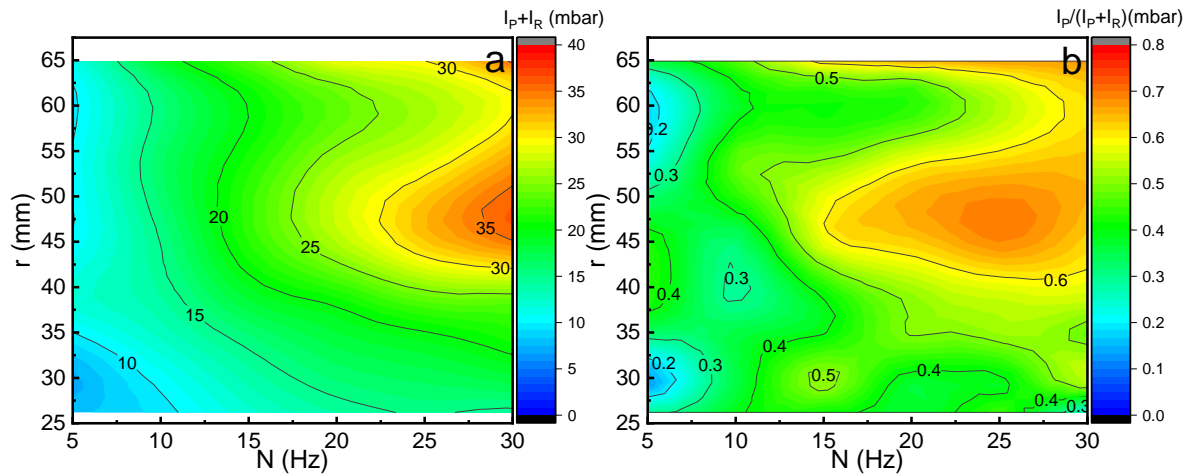


Fig. IV.33 Spectrum of total energy input and periodic contribution as a function of mixing rate and radius.

2.2.5 Viscosity

2.2.5.1 SA

Fluid viscosity is also an important factor affecting the magnitude of pressure fluctuation. According to statistical analysis, the standard deviation of pressure was plotted as a function of viscosity in Fig. IV.34. Below 10 Hz, σ_P is almost independent of viscosity both at R6 and R8, the values of which are limited below 20 mbar. With the increase in mixing rate, especially at 20 Hz, σ_P reaches the maximum in the turbulent regime (μ : 0.001, 0.01 Pa.s) and is poorly influenced by viscosity. When it comes to 30 Hz, similar trends of σ_P can be observed with low viscosity fluid. However, in the laminar regime (μ : 0.05, 0.2 and 0.6 Pa.s), σ_P can be neglected with respect to the mean pressure value. It can be observed that σ_P decreases with increasing viscosity at a mixing rate superior to 20 Hz, while the change in mixing rate then becomes less influential on σ_P instead.

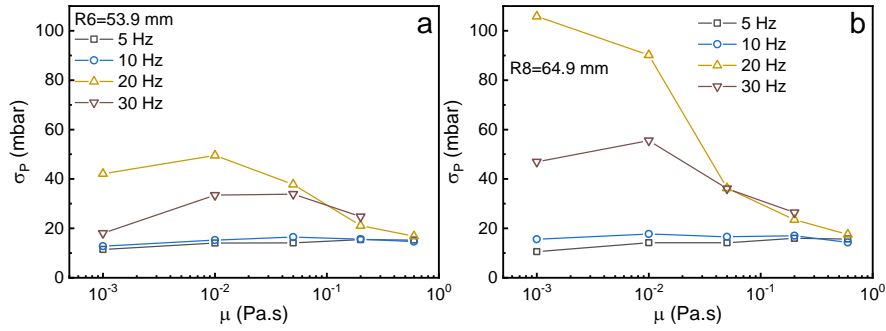


Fig. IV.34 Viscous effect on the standard deviation of pressure fluctuation. Operating conditions: μ : 0.001-0.6 Pa.s, N : 0-30 Hz, r : R6 and R8.

2.2.5.2 FFT

From turbulent to laminar flow, the same frequencies of peak amplitudes can be found by FFT, which has been described in sections § 2.2.3.3 and 2.2.4.2. The dominant contribution of amplitude at $3N$ was extracted and plotted versus viscosity in Fig. IV.35. These results are similar to σ_P but slightly decreased.

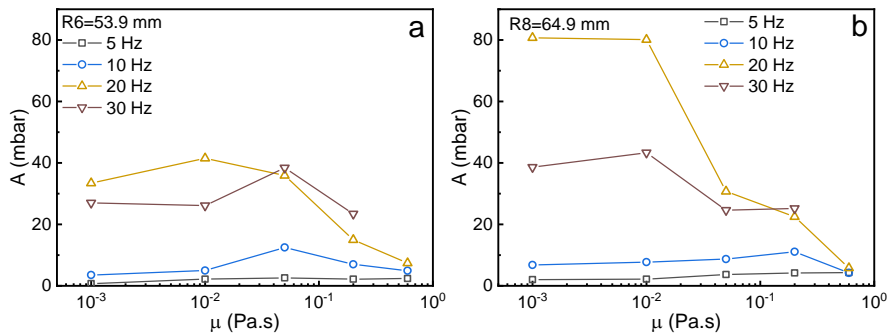


Fig. IV.35 Viscous effect on the amplitude at $3N$ of pressure fluctuation. Operating conditions: μ : 0.001-0.6 Pa.s, N : 0-30 Hz, r : R6 and R8.

❖ Summary of local pressure investigation

Objectives:

- (1) To decompose the local pressure into mixing and fluctuating components;
- (2) To evaluate the impeller geometries and operating conditions (N , Q_F and μ) on local pressure;
- (3) To compare the pressure fluctuation based on SA, PDF, FFT and modelling;
- (4) To decompose and model the periodic and random intensities of pressure fluctuation.

Contents:

- (1) Mean pressure (k values)

Mean pressure is a function of the k value, which is positive to the number of blades, impeller surface area, and feeding flowrate. The effect of flow on the k -value mainly occurs at the entrance of the filtration cell. The average value of k at R6 (Imp 2 and 3) or R7 (Imp 1) can be used to represent the whole cell.

- (2) Instantaneous pressure (fluctuating components)

The analysis of instantaneous pressure indicates that the effect of flowrate and back pressure on pressure fluctuation can be neglected; the impeller shape and mixing rate shows to be the main factors. The results are divided into laminar and turbulent regimes.

Turbulent regime:

- The pressure fluctuations show periodic variations;
- The PDF of pressure displayed as unimodal to bimodal distribution;
- The periodic signal occurs at the frequencies of N , $2N$, $3N$ (dominant), $4.25N$, and $6N$, and their intensity is dominant compared to the random intensity.
- Resonance frequencies were found to be around 20 Hz (water or BREOX 0.1 solution), resulting in a maximum pressure fluctuation of more than 100 mbar.

Laminar regime:

- The pressure fluctuation is limited below 30 mbar and increases with the mixing rate;
- The periodic signal occurs at the frequencies of N , $2N$, $3N$ (dominant), $4.25N$, and $6N$; their intensities constitute more than 50% at higher radii and mixing rates;

The magnitude of pressure fluctuation is almost constant under the turbulent regime, while it drops with higher viscosity under the laminar regime.

3 CFD

The main purpose of CFD simulation is to study in detail the fluid flow within the filtration cell to interpret the performance changes arising from different operating conditions and parameters. The membrane filtration effectiveness depends on the TMP and shear magnitude. The trend of fluid velocity variation needs to be solved, thus helping to answer the pressure and shear fluctuations.

Model		Cell Geometry		Boundary conditions		Mesh		Solve	
Model		L	T	Boundary conditions		L	T		
Laminar		<input checked="" type="checkbox"/>		Rotating impeller/ disk		<input checked="" type="checkbox"/>	<input checked="" type="checkbox"/>		
Turbulent	k- ϵ		<input checked="" type="checkbox"/>	Stationary cell wall		<input checked="" type="checkbox"/>	<input checked="" type="checkbox"/>		
	k- ω		<input checked="" type="checkbox"/>	Pressure gradient		<input checked="" type="checkbox"/>	<input checked="" type="checkbox"/>		
	SST k- ω		<input checked="" type="checkbox"/>	Velocity inlet, pressure outlet			<input checked="" type="checkbox"/>		
Cell geometry		L	T	Mesh		L	T		
1/36	disk		<input checked="" type="checkbox"/>	Structured	Normal/ fine/ finer		<input checked="" type="checkbox"/>		
1/3	disk	<input checked="" type="checkbox"/>	<input checked="" type="checkbox"/>	Unstructured	Normal/ fine/ finer	<input checked="" type="checkbox"/>	<input checked="" type="checkbox"/>		
Full	disk	<input checked="" type="checkbox"/>	<input checked="" type="checkbox"/>	Boundary layer	1 μ m*1.2 (20 layers)		<input checked="" type="checkbox"/>		
1/3	60° blade	<input checked="" type="checkbox"/>	<input checked="" type="checkbox"/>		1 μ m*1.3 (20 layers)		<input checked="" type="checkbox"/>		
Full	60° blade		<input checked="" type="checkbox"/>		5 μ m*1.2 (20 layers)		<input checked="" type="checkbox"/>		
1/3	Imp 1	<input checked="" type="checkbox"/>	<input checked="" type="checkbox"/>		5 μ m*1.2 (15 layers)		<input checked="" type="checkbox"/>		
Full	Imp 1	<input checked="" type="checkbox"/>	<input checked="" type="checkbox"/>		5 μ m*1.2 (10 layers)		<input checked="" type="checkbox"/>		

Fig. IV.36 Explorations and actions in CFD approach within RVF module (L: laminar regime, T: turbulent regime)

In order to achieve an accurate simulation, the CFD works were carried out as Fig. IV.36 to optimize the model, cell geometry, boundary conditions and mesh property. In the laminar regime, 1/3 and the full geometries of the cell have been compared based on the unstructured mesh, and the normal mesh is fine enough to model the pressure. The periodic flow (1/3 of the cell) is well solved for a full disk and a three blades impeller (60° blades). In the turbulent regime, different models have been compared to simulate the pressure. The full disk system has been realised to validate the pressure and velocity. While the simulation converged only in 1/3 of the cells (simplified 60° blades) due to the complex geometry. And we also compared the mesh of the boundary layer in order to get access to the local pressure at the

membrane surface.

3.1 Laminar regime

In this study, a Newtonian fluid, BREOX solution with a viscosity ranging from 0.05 to 0.6 Pa.s, is assumed to be incompressible and independent of temperature. The back pressure and flowrate were fixed at constant values of 300 mbar and 25 L/h, respectively. The impeller mixing rate varied from 0 to 50 Hz so that the maximum Re_{mixing} could reach 18800, which in the laminar regime (§ 1.2). For the impact of impeller geometry on the flow fields (velocity, pressure and shear stress), new-designed impellers (Imp 4, Fig. S 1 and Fig. S 2) with different configurations were achieved with Auto CAD (2021), then performed with the same simulation.

In order to determine the appropriate mesh size, physical-controlled meshes formed automatically with COMSOL from normal, fine to refine meshes with 299510, 694091 and 1617468 elements, respectively. Their tangential velocity along the z-axis, pressure and shear stress distribution at the membrane surface were compared in Fig. S 3. The finer meshes result in similar velocity, pressure and shear stress distributions to the normal one but take more time to converge. Thus, the simulations in the following part use the normal mesh to solve the fluid dynamics.

3.1.1 Validation of numerical simulation

In order to verify the reliability of COMSOL for the flow simulation within the RVF, we compared the fluid flow velocity and pressure obtained numerically with the experimental results, respectively. Table IV.5 presents the operating conditions for the validation.

Table IV.5 Validation of CFD simulation based on velocity and pressure field.

Simulation	Fluid properties		Operating parameters		
	ρ (kg/m ³)	μ (Pa.s)	N (Hz)	P _b (mbar)	Q _F (L/h)
Velocity	1060	0.81	2	300	45
Pressure	1060	0.18	0-30	625	25

The velocity profile in the RVF module has been investigated with PIV technology in a previous study [5]. The magnitude of the horizontal velocity component (xy plane) along the z-axis, which is mainly in the θ direction, is shown in Fig. IV.37. Different θ positions were explored regarding the impeller position: leading, middle and trailing. The horizontal velocity

significantly increases when close to the blades. Considering the PIV measurements as the reference, the velocity is well calculated by the CFD model at the leading edge, while it is slightly overestimated between two blades and at the trailing edge. It should be noted that the numerical results also show large deviations in the impeller zone ($-4 < z < 4$ mm). This can be explained by the influence of the impeller on the laser during the PIV measurement, where the velocity values can only be determined between the two blades. Nevertheless, it can be claimed that the numerical velocity profiles are in great agreement with the experimental results if the deviations in the laser installation process are taken into account.

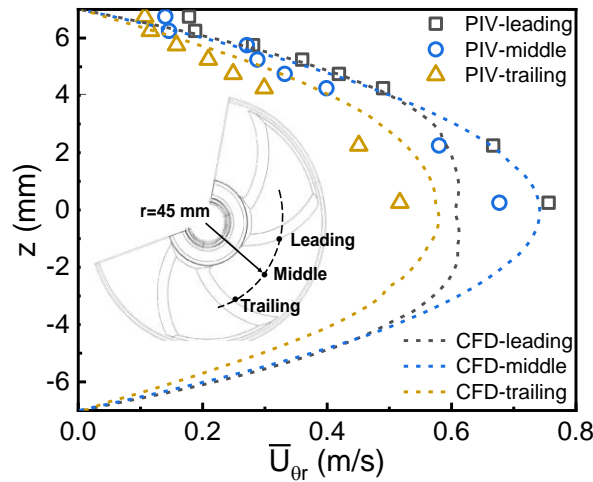


Fig. IV.37 Horizontal velocity profile at z -direction and $r=45$ mm for PIV measurement and CFD simulation. Operating conditions: μ : 0.81 Pa.s, N : 2 Hz, Q_F : 45 L/h.

The comparison of the pressure obtained numerically and the experimental measurements can be seen in Fig. IV.38. With the increase in the mixing rate, the so-called mixing pressure tends to increase, the gap between CFD results and experimental data also increases, as can be seen in Fig. IV.38a. It should be mentioned that the simulations were carried out in ideal conditions, and the temperature variations due to high friction were not taken into account. For pressure fluctuation, three periods ($3T_0$) of experimental data and CFD results are presented in Fig. IV.38b. Here the angle θ variable was replaced by the time t variable according to the following equation: $t = \frac{3\theta}{2\pi}T_0$, where T_0 is equal to $\frac{1}{N}$. The pressure fluctuations including the amplitude and the period of the signal, appears to be well reproduced by the model.

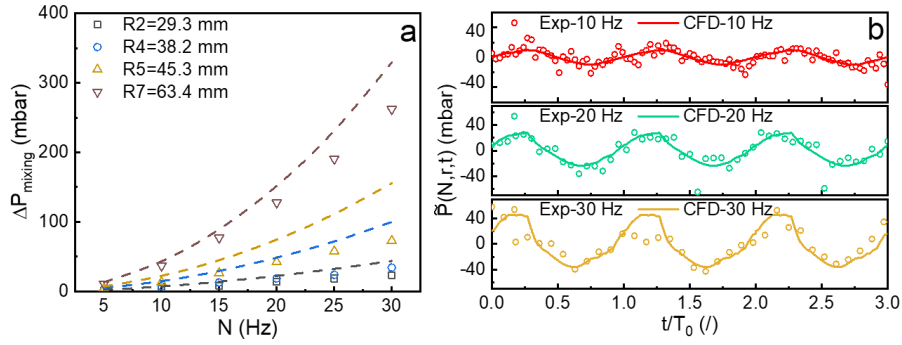


Fig. IV.38 Comparison of pressure profile for experimental results and numerical simulation. (a) Mixing pressure as a function of mixing rate; (b) pressure fluctuation for different mixing rates at R6. Operating conditions: μ : 0.18 Pa.s, N : 0-30 Hz, Q_F : 25 L/h. Dots are experimental data and curves show CFD simulation.

According to the comparison of experimental and numerical pressure and velocity distribution at different locations done above, the model developed using COMSOL provides a correct agreement for the simulation of the laminar fluid flow field within the RVF. Then further simulations can be carried out for a large range of operating conditions and different geometrical parameters.

3.1.2 Local velocity

Fig. IV.39 shows the velocity field within the filtration cell, especially the vertical velocity profile in selected specific regions of the cell. Of course, the velocity distribution differs from the rotating full disk system as the gap through which the fluid passes vary with the position of the impeller. The gap s between the blade and the membrane is 3 mm ($s/R=0.04$); it is seen that the two boundary layers merge together (Fig. IV.39b and c). In the middle of the space between two blades, the boundary layer appears to be separated in a large gap of 14 mm ($s/R=0.21$), as shown in Fig. IV.39a and d.

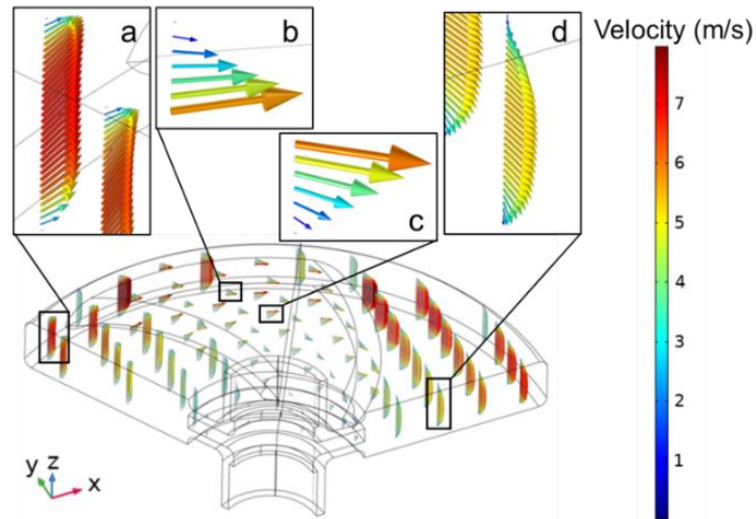


Fig. IV.39 Velocity field in the filtration cell. Operating conditions: μ : 0.2 Pa.s, N : 20 Hz, Q_F : 25 L/h.

Fig. IV.40a depicts the vertical profiles (z -axis) of the tangential velocity component U_θ at different locations in the cell relative to the position of the impeller (points A-G can be seen in the figure). At the same radius (points A, B and D, $r=60$ mm), the tangential velocity varies with the location relative to the position of the impeller. The fluid velocity at the leading edge (point B) remains identical to the impeller velocity close to the centre of the cell ($z=0$ mm). On the contrary, it reaches its minimum value close to the centre of the cell ($z=0$ mm) at the trailing edge (point D). In the region of the narrow gap between the membrane and the blade, the vertical profile of the tangential velocity is roughly linearly from the membrane to the blade surface (points C, E, F and G). A perfectly straight line would correspond to a Couette flow. Between the two blades, the velocity profile is almost parabolic (point A). An exact parabolic shape would correspond to a Poiseuille flow. The maximum velocity value is around 7.5 m/s at point B. It is close to the value of $2\pi Nr$, which is the linear velocity of the blade at this radial position.

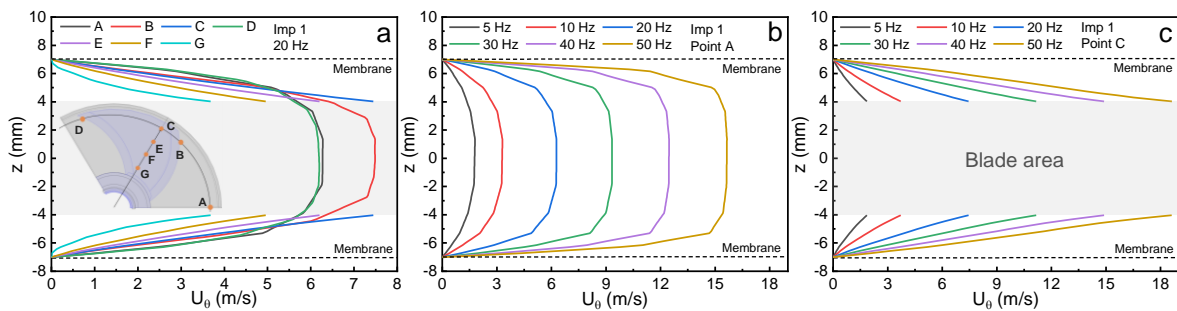


Fig. IV.40 Tangential velocity along the z -direction. (a) is the velocity distribution at different positions; (b) and (c) are the velocity distribution for different mixing rates at A and C, respectively. A

(between two blades), B (leading edge), C (on the blade) and D (trailing edge) with a radius of 60 mm; E, F and G with a radius of 50, 40 and 30 mm, respectively. Operating conditions: μ : 0.2 Pa.s, N : 20 Hz, Q_F : 25 L/h.

Now let us look at the effect of the mixing rate of the impeller on the velocity profile. Fig. IV.40b presents the velocity profile along the z -axis between two blades (point A) for a large range of N . It is really interesting to notice that the flow is not always fully developed; it depends on the N magnitude. At 5 or 10 Hz, it is fully developed (Poiseuille flow); this is proved by the perfect parabolic velocity profile. But it is not true for higher N values, and this can be deduced from the classical shape of the corresponding velocity profile: boundary layer profile close to the wall and uniform velocity in the core region. The same analysis can be done in the region above/ below the blade (point C). Fig. IV.40c well exhibits that the fluid flow is not fully developed (Couette flow). One can physically understand that the higher N , the shorter time for the fluid flow to develop.

As we know that the kinematic viscosity is the momentum diffusion coefficient, we can simply deduce that the higher the viscosity, the easier the fluid to develop. This physical phenomenon is exactly reported in Fig. IV.41 a and b, where the vertical profiles of the tangential velocity are plotted for a large range of viscosity (0.05 to 0.6 Pa.s). At point A, the shape of the velocity profile progressively changes when the viscosity is increased to get a parabolic profile at 0.6 Pa.s. The separation of the boundary layers can be seen with lower viscosity. Whereas, when the viscosity is higher, the two boundary layers clearly merge within the 3 mm small gap between the blade and the membrane (point C). This is the same as for the full disk, which results are plotted in Fig. IV.41c.

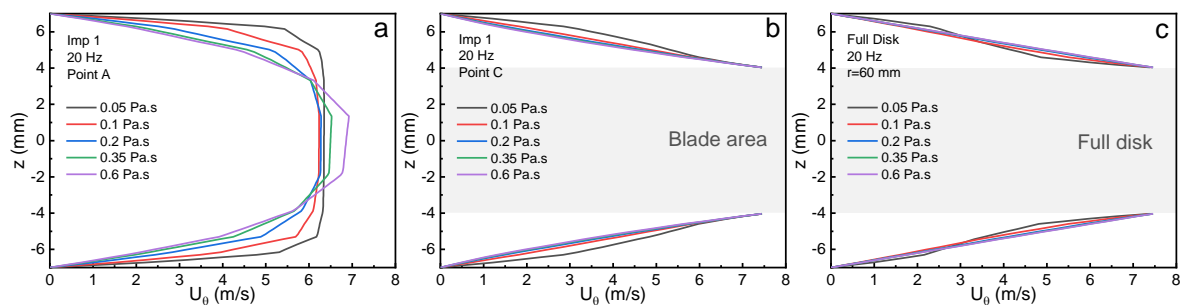


Fig. IV.41 Tangential velocity along the z -direction. (a) and (b) are velocity distribution at different positions for Imp 1; (c) is the velocity distribution for the full disk. Operating conditions: μ : 0.05-0.6 Pa.s, N : 20 Hz, Q_F : 25 L/h, Imp1 and full disk.

3.1.3 Local pressure

The effect of the operating conditions on the pressure variations has been clearly

exemplified experimentally. However, this phenomenon can be more deeply explored using CFD simulations. It is true that CFD can be a useful tool for further optimization of the operating parameters. We denote the mixing pressure and the magnitude of pressure fluctuations induced by the impeller with ΔP_{mixing} and σ_P , respectively. At a given mixing rate, the mean local pressure varies linearly with the back pressure (Fig. S 5) and feeding flowrate (Fig. S 6), and these two parameters do not affect the σ_P . Then the mixing rate and the fluid viscosity appear as the key factors in controlling pressure fluctuations for process intensification in the application of the RVF module.

3.1.3.1 Mixing rate

Fig. IV.42 shows the pressure field at the membrane surface and two different angular cross-sectionals (0 and 60°). From the top view (Fig. IV.42a, b and c), the pressure at the membrane surface increases with the mixing rate, and the maximum value occurs between two blades and close to the external wall. The pressure variation increases with the higher mixing rates. It is also seen that the pressure distribution is uniform in the vertical direction (Fig. IV.42d-i) according to the type of flows occurring within the RVF (laminar boundary layer, Couette, Poiseuille) already discussed in § 3.1.2.

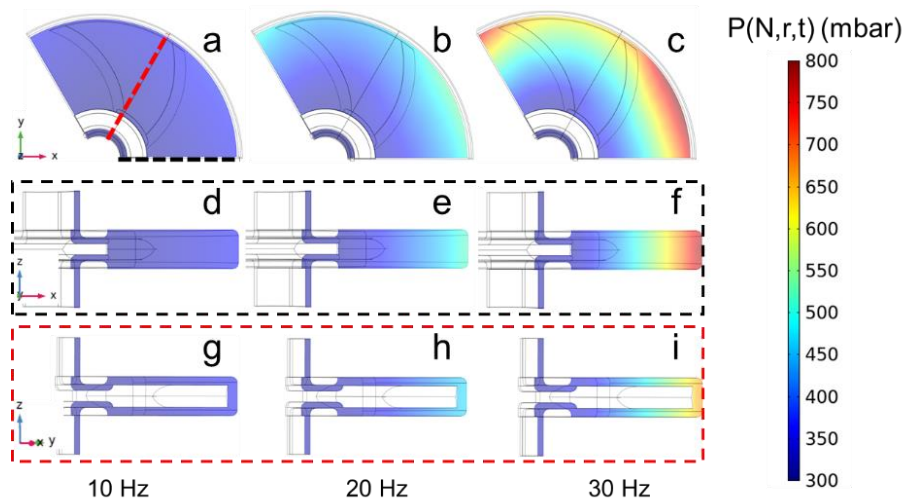


Fig. IV.42 Pressure field for different mixing rates with Imp 1. (a), (b) and (c) are on the membrane surface; (d), (e) and (f) are the cross-section with 0° to x-axis (black dashed line); (g), (h) and (i) are the cross-section with 60° to x-axis (red dashed line). Operating conditions: μ : 0.2 Pa.s, N : 10, 20 and 30 Hz.

Two impellers with similar blade surface area (1090 mm² for one blade) are compared. The first impeller has the exact shape of Imp 1 used experimentally, while the second impeller called Imp 4-60° is fan-shaped with three blades.

The mixing pressure and the magnitude of pressure fluctuation as a function of the

mixing rate are presented in Fig. IV.43. The value of k increases with increasing radius. And the k values of the two impellers are very close to each other, except at R2, where the k value of Imp 4-60° is significantly lower than that of Imp 1. By the integration of all mixing pressure versus radii (R1 to R8) and mixing rates (0 to 50 Hz), the mean k value for Imp 1 is 0.65, and almost the same value for Imp 4-60° (0.64). In comparison, these values are very close to the k -value at R6. To facilitate the calculation, the value of k at R6 is assumed to be the average value across from the full disk.

In Fig. IV.43c and d, the magnitude of pressure fluctuations, σ_P , increases with N , even up to 50 Hz. Interestingly, σ_P is almost linear with N at a lower radius (Imp 1: $r \leq R6$; Imp 4: $r \leq R4$), while it is proportional to N^2 at a higher radius. The two impellers with the same surface areas exhibit both similar mixing and fluctuating pressures. This indicates that the effect of impeller shape on global pressure is not remarkable.

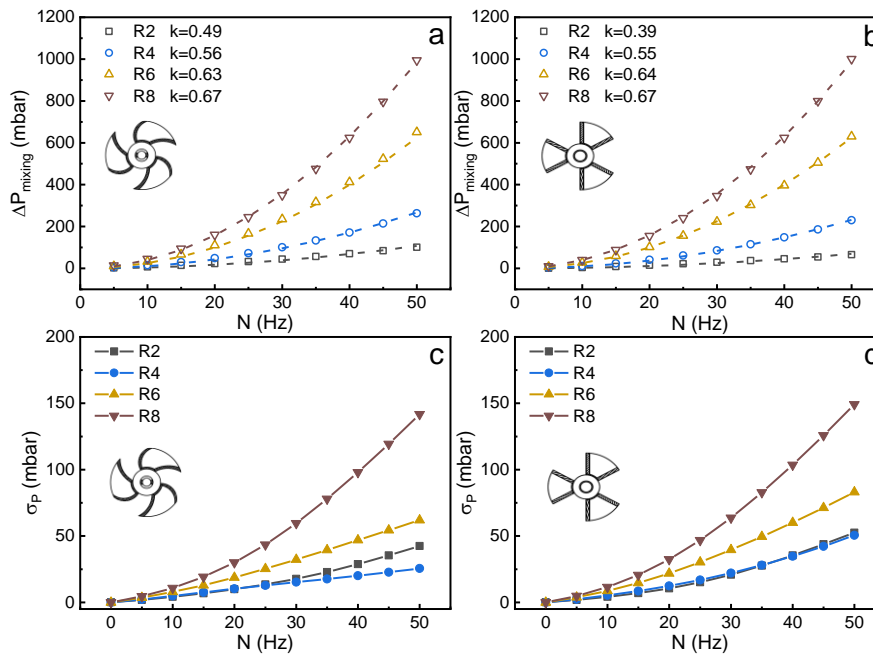


Fig. IV.43 Pressure distribution as a function of mixing rate. (a) and (b) are the mixing pressure; (c) and (d) are the standard deviation of pressure fluctuation. Operating conditions: μ : 0.2 Pa.s, N : 0-50 Hz, r : R2, R4, R6 and R8, Imp 1 for (a) and (c), Imp 4-60° (three blades) for (b) and (d).

The pressure distribution as a function of the radius is shown in Fig. IV.44. The integration of mixing pressure as a function of radius resulted in the decreased k value with the mixing rate for Imp 1. It can be explained by the increased contribution of feeding flow at lower mixing rates. For Imp 4-60°, the mixing rates have a minor effect on the value of k due to the uniform surface area distribution along the radial direction.

The σ_P for two impellers versus radius are shown in Fig. IV.44c and d. It can be found

that σ_P is not increasing monotonically for Imp 1. When r is less than 45 mm, the σ_P value is limited to 50 mbar for both impellers, then followed by the increase with radius.

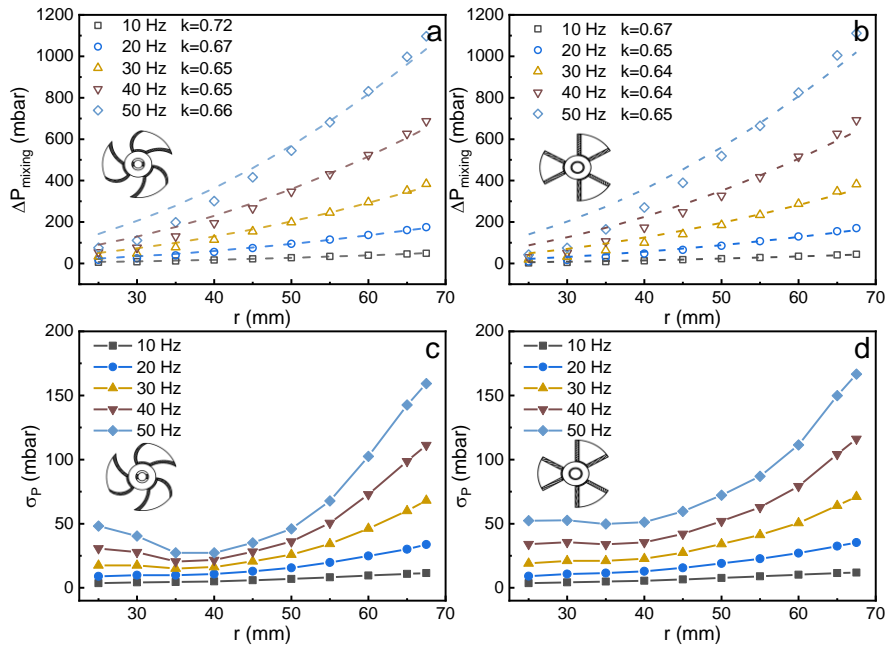


Fig. IV.44 Pressure distribution as a function of radius. (a) and (b) are the mixing pressure; (c) and (d) are standard deviation of pressure fluctuation. Operating conditions: μ : 0.2 Pa.s, N : 0-50 Hz, r : 25-67.5 mm, Imp 1 for (a) and (c), Imp 4-60° (three blades) for (b) and (d).

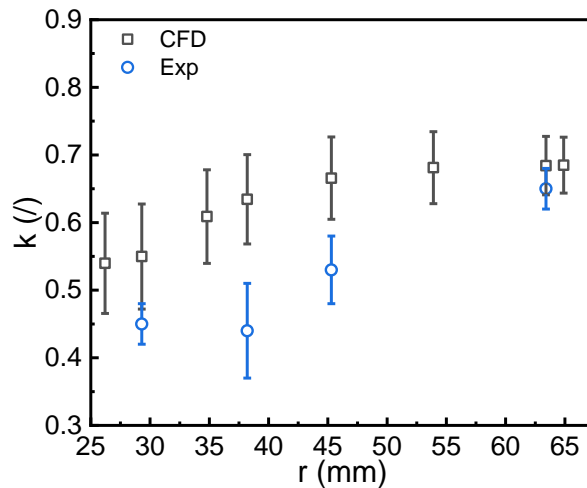


Fig. IV.45 Core velocity coefficient for different radii. Operating conditions: μ : 0.2 Pa.s, N : 0-50 Hz, Q_F : 25 L/h, r : R1-R8.

By comparing the numerical simulations with experimental results, the local k values at 25 L/h are presented in Fig. IV.45. Since the heat dissipation is not taken into account during the simulation, the obtained k values are higher than the experimental results. Whereas, these values are very close at R7.

3.1.3.2 Viscosity

The viscous effects on local pressure are illustrated in Fig. IV.46. At R6, the mixing pressures show a minimum value with the viscosity around 0.2 Pa.s. After integration, k values for the laminar regime from 0.05 to 0.6 Pa.s are achieved as 0.69 ± 0.03 , which can be assumed as independent of viscosity. However, σ_P increases with the increasing viscosity, which is opposite to the experimental results. There are several potential explanations for this result: i) increase of temperature in the experiments due to high viscous dissipation, this phenomenon is non-uniform within the cell; ii) cavitation during the mixing that could significantly reduce the apparent viscosity; iii) formation of bubbles in the measuring tube that promotes wrong pressure measurements and iv) dumping effect in the cell as in turbulent regime. Thus, all these considerations appear to interpret the difference between experiments and numerical simulations.

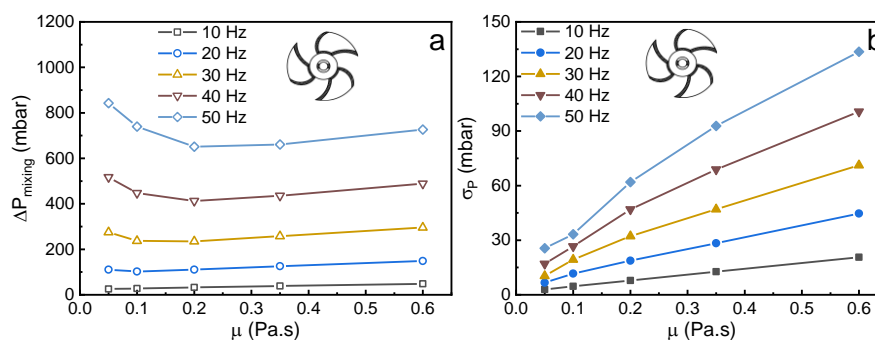


Fig. IV.46 Pressure distribution as a function of viscosity. (a) is the mixing pressure; (b) is the standard deviation of pressure fluctuation. Operating conditions: μ : 0.05-0.6 Pa.s, N : 10-50 Hz, r : R6.

3.1.3.3 Blades surface area

To compare the effect of impeller surface area on local pressure, Imp 4, already used in the previous section, is the fan-shaped three-blade impeller and has the same thickness (8 mm) as Imp 1. Here its blade surface area varied thanks to angle length, from 0° (no blade) to 120° (full disk), as shown in Fig. S 1. The pressure field for the different cases is shown in Fig. IV.47. As already found in the previous section, the maximum pressure takes place between two blades. When there is no blade (Fig. IV.47b), a uniform pressure distribution along the θ direction is achieved. The same phenomenon can be observed with the full disk (Fig. IV.47 i) but induced higher pressure. In addition, one can see that the pressure distribution in the area below the blade varies with the blade surface area.

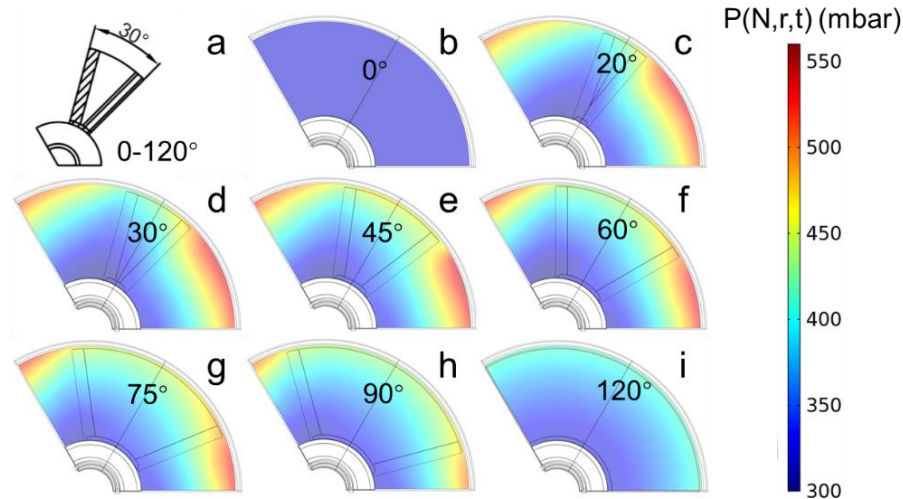


Fig. IV.47 Pressure field at the membrane surface for different impeller geometries. (a) is the geometry 30° blade, which angle length varies from 0 to 120° ; from (b) to (h) are the three blades impeller with the increased surface area from 0 to 90° ; (i) is the full disk. Operating conditions: μ : 0.2 Pa.s, N : 20 Hz.

The variations of ΔP_{mixing} and σ_P with the angle length of the blades can be seen in Fig. IV.48. As could be expected, when there are no blades, the additional pressure generated by the rotation of the shaft is small, only 30 mbar at 30 Hz and R6. The existence of the blades significantly increases the additional pressure. It is notable that the increase of the angle length from 20° to 75° does not significantly change the mixing pressure magnitude. Asymptotic cases tend to exhibit a lower mixing pressure. At R6, the core velocity coefficient for each case is shown in Table S 1. Moreover, there are no obvious pressure fluctuations with 0° (no blades) and 120° (full disk) of blades. It is also shown that the ΔP_{mixing} and σ_P strongly increased with the rotation of the impeller. It is found that σ_P does not vary between 20° and 30° angle length, then decreases with increasing angle length, i.e., blade surface area. At R6, the maximum ratio between σ_P and ΔP_{mixing} is 22% during the mixing rates of 30 Hz. If 300 mbar of back pressure is considered, the contribution of pressure fluctuation (10%) can be neglected.

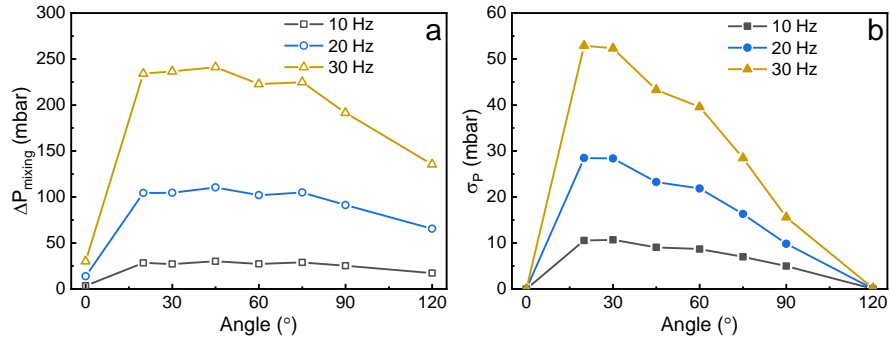


Fig. IV.48 Pressure distribution with the increased angle of blades. (a) is the mixing pressure; (b) is the standard deviation of pressure fluctuation. Operating conditions: μ : 0.2 Pa.s, N : 0-30 Hz, r : R6.

Fig. IV.49 illustrates the evolution of pressure fluctuation as a function of θ at the membrane surface for the different angle lengths of blades, showing irregular sinusoidal waves. A quasi-linear decrease of pressure can be seen above the blade, and the minimum pressure occurs at the trailing edge of the blade.

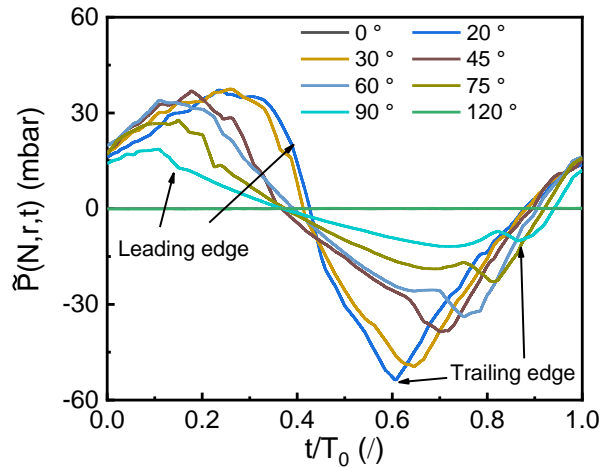


Fig. IV.49 Evolution of pressure fluctuation for different kinds of blades. Operating conditions: μ : 0.2 Pa.s, N : 20 Hz, r : R6.

3.1.3.4 Number of blades

The local pressure for different numbers of blades is investigated. Imp 4 is designed at a 30° angle length but with an increased number of blades, as shown in Fig. S 2. Each simulation is carried out with a geometrical domain of one blade. The pressure fields at 20 Hz for each case are given in Fig. IV.50. As previously described, the maximum value of pressure appears at the leading edge of the blades for all impeller geometry. Among them, the pressure distribution of the two-blade impeller shows a larger fluctuation in the θ direction.

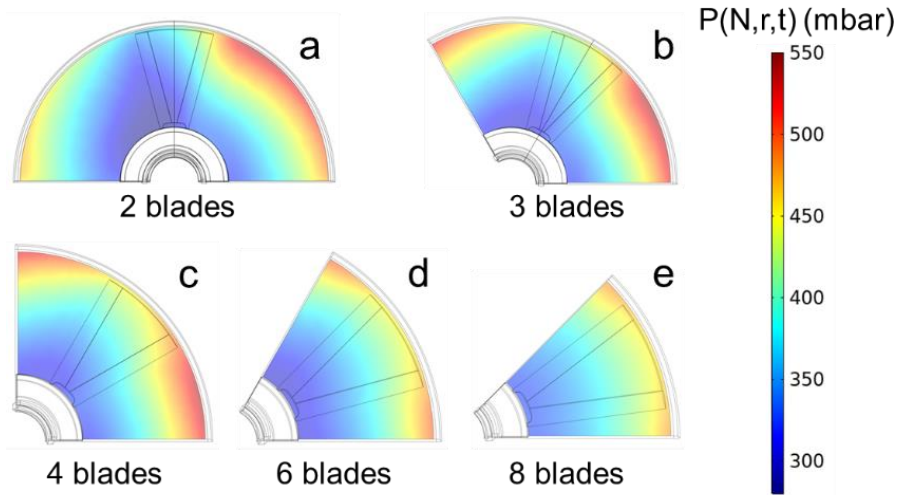


Fig. IV.50 Pressure field at the membrane surface for different impeller geometries. From (a) to (e) are the impeller with the increased number of blades (30°) from 2 to 8. Operating conditions: μ : 0.2 Pa.s, N : 20 Hz.

Fig. IV.51 shows the mixing pressure and its standard deviation at the membrane surface. The impeller with four blades seems to induce the maximum mixing pressure, or we can say that there is a maximum k value. In a rotating disk system, Brou et al. found that a disk with eight vans (4 mm thickness) presents a large k value (0.71) than four vans (0.69) [15]. This result is opposite to the k value obtained from our rotating impeller system. There are two possible reasons for this result. One is that the fluid flow between the impellers is different than the one for a full disc, and the second is that the gap between the impeller and the membrane is smaller in the present study. The local k -value at R6 is presented in Table S 2. It is likely that σ_P is independent of k value and decreases with the number of blades. A two-blade impeller tends to be an optimal device regarding pressure fluctuations.

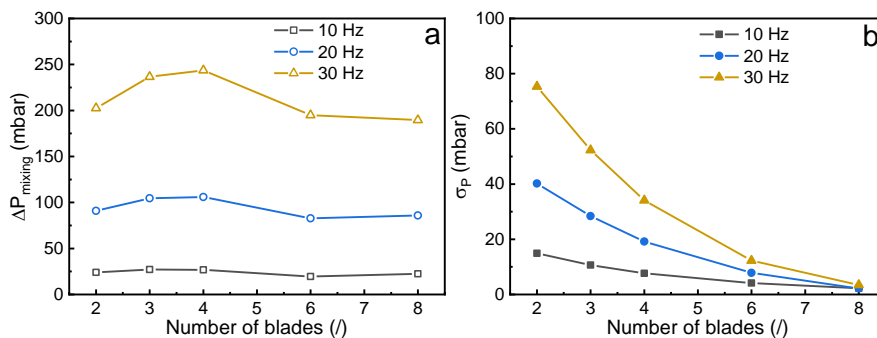


Fig. IV.51 Pressure distribution with the increased number of blades. (a) is the mixing pressure; (b) is the standard deviation of pressure fluctuation. Operating conditions: μ : 0.2 Pa.s, N : 0-30 Hz, r : R6.

The effect of the number of blades on the pressure fluctuation is also illustrated in Fig.

IV.52. The change in the number of blades does not affect the trend of pressure fluctuation, but its intensity decreases rapidly with the number of blades. As can be seen from Fig. IV.51b, for the two-blade impeller at R6, σ_P can reach 75 mbar at 30 Hz, while this value for the eight-blade impeller is only 2 mbar.

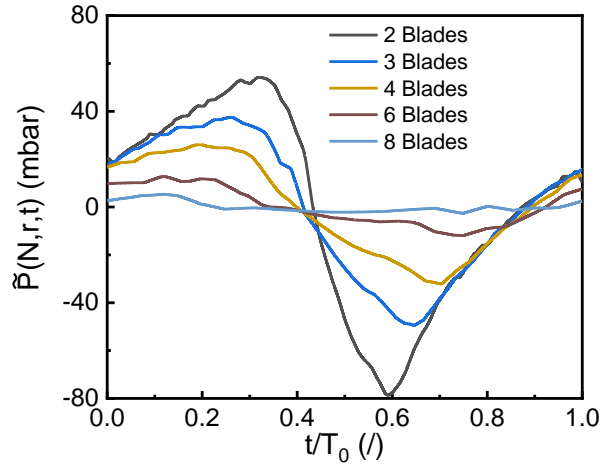


Fig. IV.52 Evolution of pressure fluctuation for different numbers of blades. Operating conditions: μ : 0.2 Pa.s, N : 20 Hz, r : R6.

3.1.3.5 Impeller/membrane gap

The impeller/membrane gap (s) is defined as the distance between the impeller and the membrane surface, as shown in Fig. IV.53a. Fig. IV.53b-h presents the pressure field at the surface of the membrane for a large range of s (2 to 10 mm). It is clear and obvious that pressure fluctuations are expected to be significantly reduced as the gap is increased. Indeed, the shear effect due to the passage of the blade is progressively less felt by the fluid that flows close to the membrane surface.

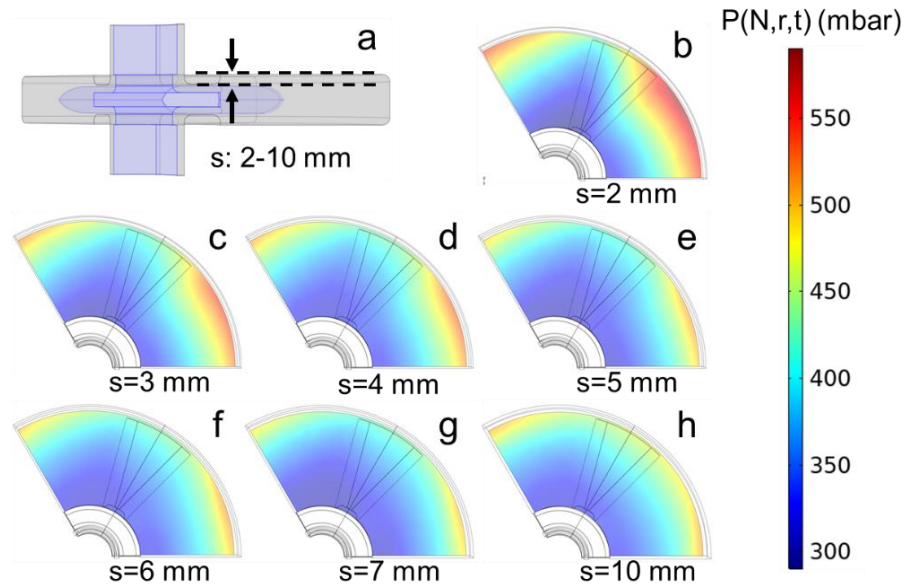


Fig. IV.53 Pressure field at the membrane surface with different gaps between impeller and membrane. (a) is the illustration of cell geometry; from (b) to (h) are the increased gap from 2 to 10 mm. Operating conditions: μ : 0.2 Pa.s, N : 20 Hz.

From the data represented in Fig. IV.54, with the increase in gap, the mixing pressure shows a decrease and then increases with the gap. Table S 3 shows the local k -value varied in the range between 0.59 and 0.71. The reason why there is an increase of k with a large gap (10 mm) can be attributed to the separation of the boundary layer in the filtration cell. The pressure fluctuation distribution (σ_P) is similar to that of the number of blades effect. A small gap not only contributes to the generation of mixing pressure but also yields a larger pressure fluctuation.

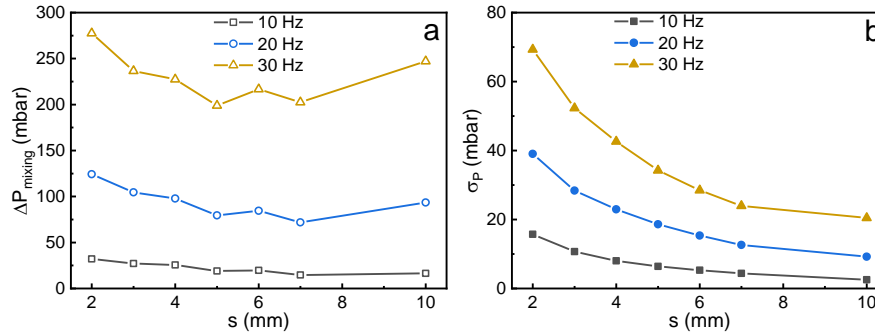


Fig. IV.54 Pressure distribution with the different gaps. (a) is the mixing pressure; (b) is the standard deviation of pressure fluctuation. Operating conditions: μ : 0.2 Pa.s, N : 0-30 Hz, r : R6.

3.1.4 Local shear stress

It is commonly admitted that the shear stress at the membrane surface is one of the major factors affecting filtration performance. Thanks to the CFD approach, the local shear stress at the membrane surface can be achieved and then compared.

3.1.4.1 Mixing rate

Unlike pressure, local shear stress is proportional to the velocity gradient for a Newtonian fluid. The shear stress fields in different cross-sections of the filtration cell are shown in Fig. IV.55. In the lab-scale RVF module, the gap between the impeller and the membrane is 3 mm, corresponding to a gap ratio of s/R_i equal to 0.04. In this narrow gap, the boundary layer can merge together depending on the magnitude of N , resulting in slight variations of the shear stress along the z -direction (Fig. IV.55g-i). While between the two blades, the large gap (14 mm) allows the separating boundary layer. The shear stress appears to reach the maximum at the membrane surface, and it is obviously about 0 close to the center of the cell between two blades (Fig. IV.55d-f). At the membrane surface (Fig. IV.55a-c), the maximum shear stress occurs at the trailing edge of the blades, which is exactly opposite to the pressure distribution.

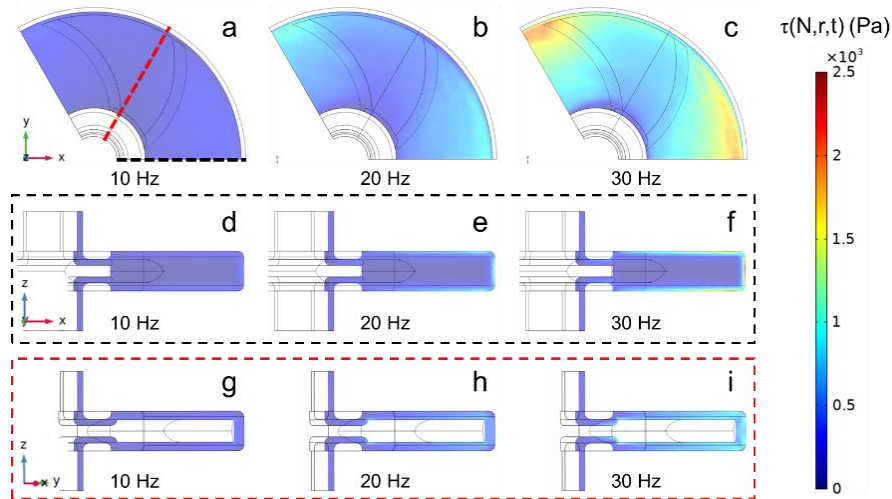


Fig. IV.55 Shear stress field for different mixing rates with Imp 1. (a), (b) and (c) are on the membrane surface; (d), (e) and (f) are the cross-section with 0° to x -axis (black dashed line); (g), (h) and (i) are the cross-section with 60° to x -axis (red dashed line). Operating conditions: μ : 0.2 Pa.s, N : 10, 20 and 30 Hz.

In the rotating full disk system, the shear stress at the membrane surface is proportional to the mixing rate in a narrow gap. But this relation is not applicable to the rotating impeller device. The shear stress variations as a function of the mixing rate are shown in Fig. IV.56, which indicates that the mean shear stress is linear with $N^{1.5}$. As can be seen from Fig. IV.57, the mean shear stress grows linearly with the radius, and this variation remains consistent with Eq. (II.20). However, at small radii (close to $r=25$ mm), the calculated shear stress is higher than the CFD simulation results. This may be explained by the sudden increase of the surface area at the inlet, where the fluid generates vortices in this region, and thus the velocity gradient decreases. It is also interesting to note that the calculated values of membrane surface shear stresses are overestimated at low mixing rates ($N \leq 20$ Hz) when r is close to the impeller edge. In comparison, the results are completely opposite at high mixing rates ($N > 20$ Hz).

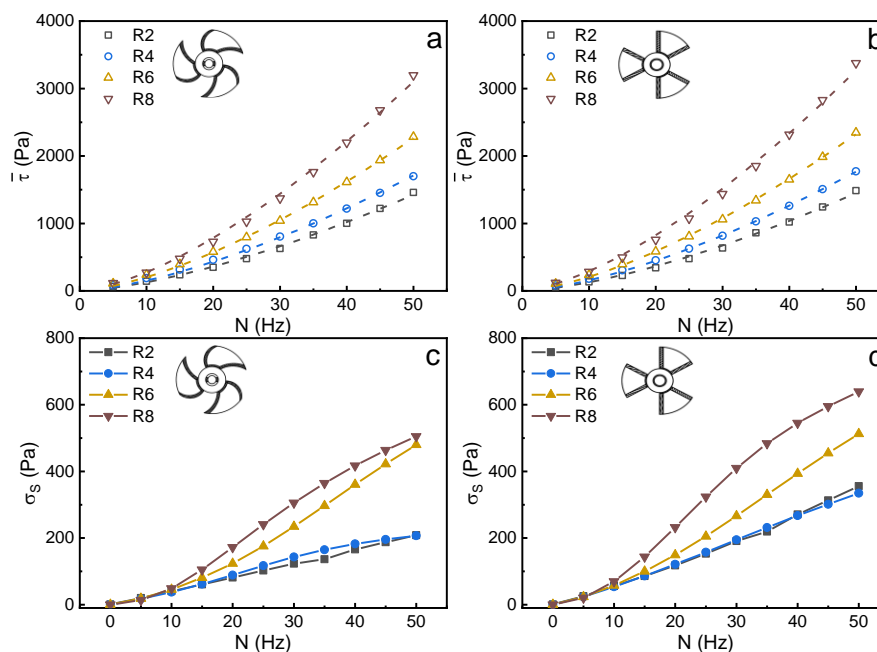


Fig. IV.56 Shear stress distribution as a function of mixing rate. (a) and (b) are the mean shear stress; (c) and (d) are the standard deviation of local shear stress. Operating conditions: μ : 0.2 Pa.s, N : 0-50 Hz, Imp 1 for (a) and (c), Imp 4-60° (three blades) for (b) and (d).

Analog to pressure fluctuations, the local shear stress variations become larger as the mixing rate increases, which can be seen in Fig. IV.56c and d. The magnitude of the shear stress fluctuation (σ_s) is higher with Imp 4-60°, which indicates 640 Pa of fluctuation amplitude at R8 and 30 Hz, but only 505 Pa for Imp 1. Fig. IV.57c and d provide the evolution of σ_s versus radius. When $r < 45$ mm, the value of σ_s is independent of the radius and increases rapidly at $45 \leq r < 60$ mm. When it is close to the impeller edge, σ_s increase at mixing rates below 20 Hz, but decrease as the mixing rates exceed 20 Hz. The relative standard deviation of shear stress at 20 Hz is 18-29% for Imp 1 and 25-38% for Imp 4-60°. It demonstrates that the local shear stress variation during the mixing with the impeller should be taken into account to better explained the benefits of dynamic filtration.

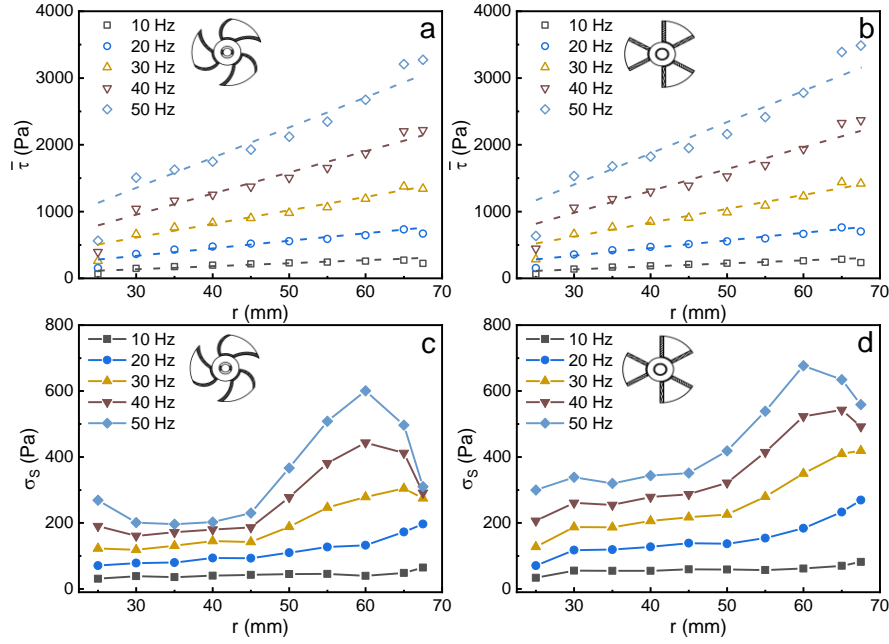


Fig. IV.57 Shear stress distribution as a function of radius. (a) and (b) are the mean shear stress; (c) and (d) are the standard deviation of local shear stress. Operating conditions: μ : 0.2 Pa.s, N : 0-50 Hz, Imp 1 for (a) and (c), Imp 4-60° (three blades) for (b) and (d).

3.1.4.2 Viscosity

Contrary to pressure, the time-mean shear stress increases with fluid viscosity in the rotating impeller device. It is proportional to $\mu^{0.5}$, as shown in Fig. IV.58. Thus, the following equation can be stated in the rotating impeller system, Eq. (IV.7). Meantime, σ_s also increases with higher viscosity, as can be seen in Fig. IV.58b.

$$\bar{\tau} = 0.96\rho^{0.5}\mu^{0.5}(2\pi kN)^{1.5}r, k=0.69 \quad (\text{IV.7})$$

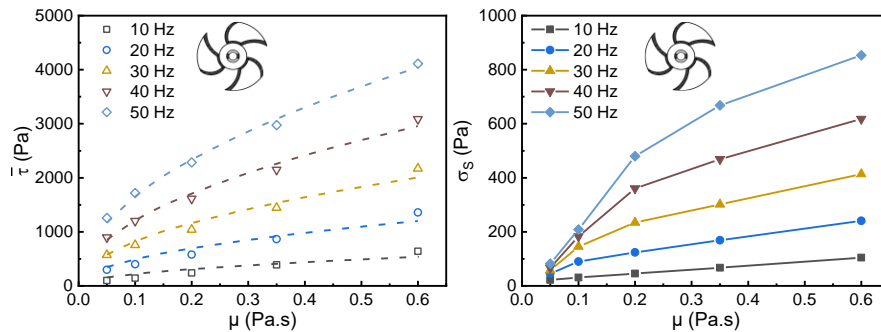


Fig. IV.58 Shear stress distribution as a function of viscosity. (a) is the mean shear stress; (b) is the standard deviation of local shear stress. Operating conditions: μ : 0.05-0.6 Pa.s, N : 0-50 Hz, r : R6.

As explained at the beginning of this section (§ 3.1.2), the boundary layers that exist at

the walls of the cell (membrane surface and impeller surface) highly depend on fluid properties (viscosity) and operating conditions (mixing rate of the impeller). Recall that the wall shear stress for a Newtonian fluid in the present flow conditions can be expressed as $\tau_W = \mu \left(\frac{\partial U_\theta}{\partial z} \right)_W$. Increasing N leads to increase $\left(\frac{\partial U_\theta}{\partial z} \right)_W$ at all the walls of the cell. That can be seen in the plots of the velocity profiles presented in the previous section (Fig. IV.39 and Fig. IV.40). The development of the boundary layer is less important in this situation, in particular in the region between two blades. (Fig. IV.40b). In the region above the blade, the shear rate is obviously increased according to the increase of N (Fig. IV.40c). Therefore, increasing N significantly increases the wall shear stress. On the contrary, increasing μ leads to a decrease $\left(\frac{\partial U_\theta}{\partial z} \right)_W$ at all the walls due to the more important development of the boundary layer (Fig. IV.41a and b). But the corresponding value of the wall shear stress still increases due to the higher value of viscosity that compensates for this phenomenon.

The linear relation between the local shear stress and $\rho^{0.5} \mu^{0.5} (2\pi k N)^{1.5} r$ was achieved in Fig. IV.59. When the average k value of 0.69 under laminar flow is used, the calculated slope is 0.96. This value is higher than 0.77, which was proposed in the full disk system and large gap [174].

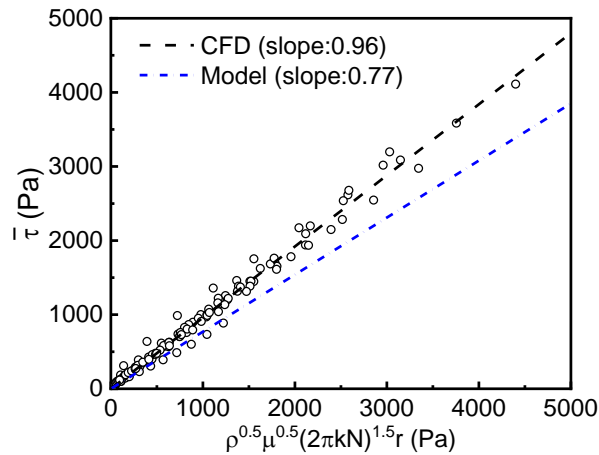


Fig. IV.59 Estimation of local shear stress at the membrane surface. Operating conditions: μ : 0.05-0.6 Pa.s, N : 0-50 Hz, r : R1-R8.

3.1.4.3 Blades surface area

Fig. IV.60 provides the shear stress field at the membrane surface with increased angle length of blades from 0° to 120° . At 20 Hz, the maximum shear stress is approximately 1200 Pa, which occurs behind the trailing edge of the blades. For the full disk, the uniform shear stress can be observed at the same radius, and the value of which is lower than that of

impellers (20-90°).

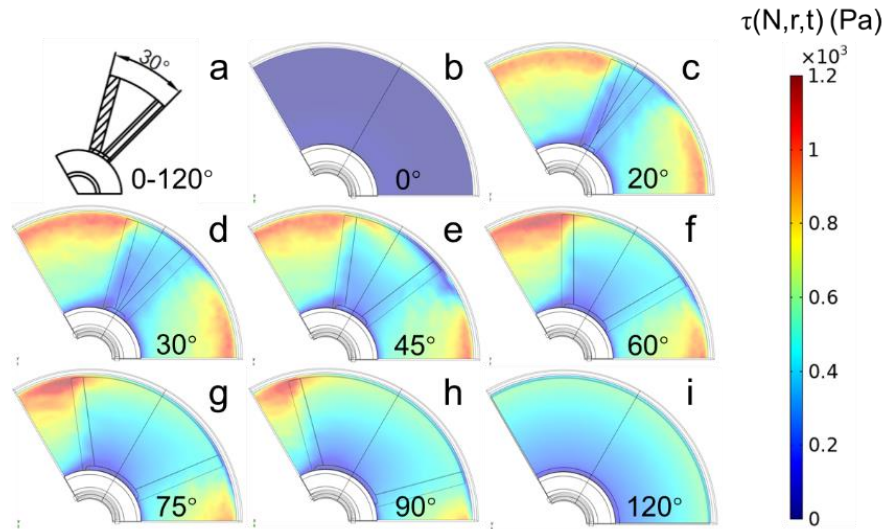


Fig. IV.60 Shear stress field at the membrane surface for different impeller geometries. (a) is the geometry of a blade; from (b) to (h) are the three blades impeller with the increased surface area from 0 to 90°; (i) is the full disk. Operating conditions: μ : 0.2 Pa.s, N : 20 Hz.

Fig. IV.61 shows the variation of membrane surface shear stress with blade surface area. The local shear stress slightly decreases as the blade's area increases and reaches the minimum when it is a full disc. For shear stress fluctuations, σ_s reach their maximum value with three blades impeller of 30° and 60°. At R6 and 20 Hz, the relative standard deviation of local shear stress reaches 23.4% with 30° blades, and 25.1% with 60° blades.

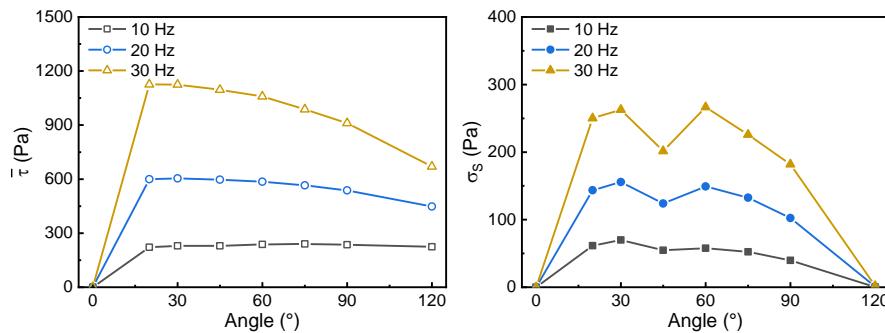


Fig. IV.61 Shear stress distribution with the increased angle of blades. (a) is the mean shear stress; (b) is the standard deviation of local shear stress. Operating conditions: μ : 0.2 Pa.s, N : 0-30 Hz, r : R6.

3.1.4.4 Number of blades

When Imp 4 was designed as a 30° angle length blade, different CFD simulations were carried out by changing the number of blades (Fig. IV.62). With the increase in the gap between the two blades, the maximum region of shear stress still appears at the trailing edge

of the blade. However, the shear stress in the area above or below the blade also appears to enhance with more blades.

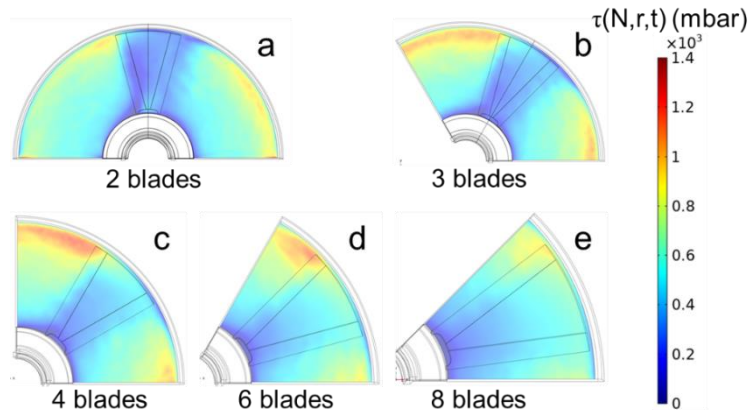


Fig. IV.62 Shear stress field at the membrane surface for different impeller geometries. From (a) to (e) are the impeller with the increased number of blades (30°) from 2 to 8. Operating conditions: $\mu=0.2$ Pa.s, $N=20$ Hz.

In Fig. IV.63, the shear stress variations at a given radius are illustrated as a function of the blades' number. Consistent with the trend in k values, three or four blades are optimal for generating high shear stress. But the σ_s reaches its maximum when the number of blades is three. More blades are negative to the generation of shear stress fluctuation at the membrane surface.

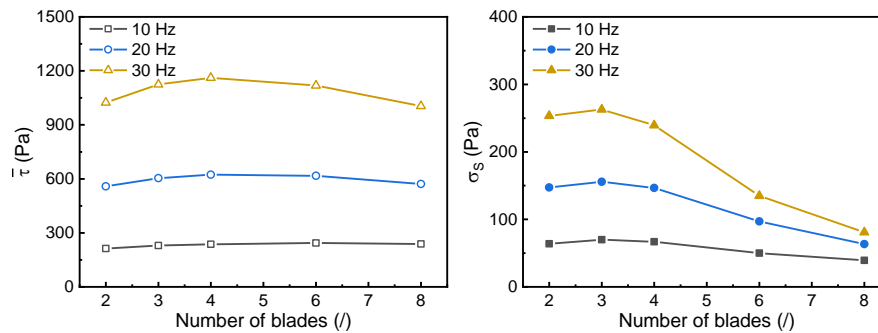


Fig. IV.63 Shear stress distribution with different numbers of blades. (a) is the mean shear stress; (b) is the standard deviation of local shear stress. Operating conditions: $\mu=0.2$ Pa.s, $N: 0-30$ Hz, $r: R6$.

3.1.4.5 Impeller/membrane gap

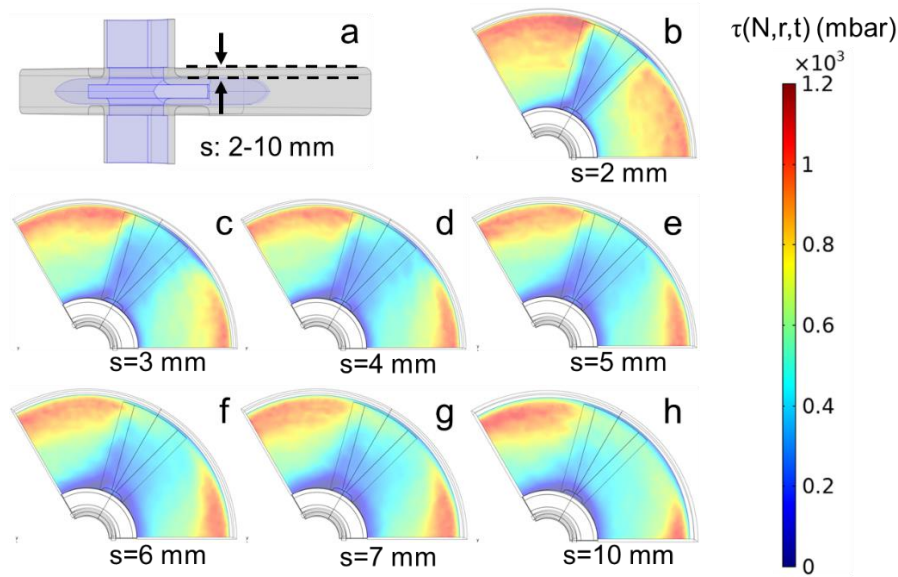


Fig. IV.64 Shear stress field at the membrane surface with different gaps between impeller and membrane. (a) is the illustration of cell geometry; from (b) to (h) are the increased gap from 2 to 10 mm. Operating conditions: $\mu=0.2$ Pa.s, $N=20$ Hz.

Fig. IV.64 and Fig. IV.65 show the effect of the gap, s , between the blade and the membrane surface on shear stress distribution. The maximum shear stress occurs at the gap of 2 mm, further increase in the gap value shows little effect on mean local shear stress. As s increases from 2 to 10 mm, σ_s is decreasing and are constant with pressure fluctuation observed in Fig. IV.54b. This means that a smaller gap is not only beneficial for the pressure effect but also creates higher shear stress. However, considering the accessibility of the device manufacturing, a gap of 3 mm seems to be the optimal value. This corresponds to the existing lab-scale RVF module.

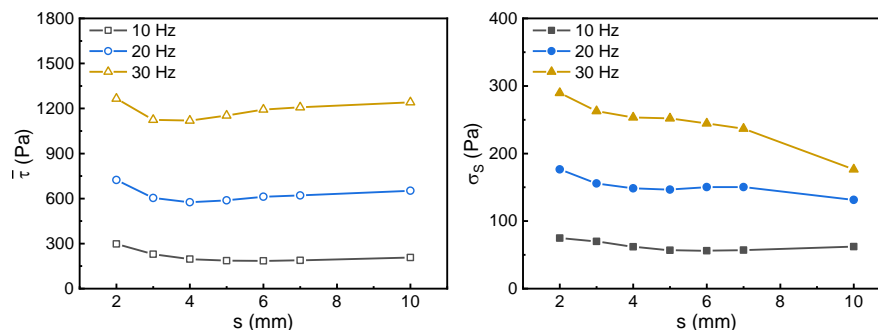


Fig. IV.65 Shear stress distribution with different gaps. (a) is the mean shear stress; (b) is the standard deviation of local shear stress. Operating conditions: $\mu=0.2$ Pa.s, $N: 0-30$ Hz, $r: R6$.

3.2 Turbulent regime

According to the experiment, water is selected as the model fluid for the simulation in the turbulent regime. The fluid is assumed to be incompressible and independent of the temperature. A constant inlet flowrate (50 L/h) and a uniform outlet pressure (300 mbar) are imposed, and the mixing rate from 0 to 50 Hz is defined.

The convergence and accuracy of the simulation are highly dependent on the quality of the mesh. Considering the complexity of the impeller design, unstructured meshes are constructed based on free tetrahedra. With respect to the physics of turbulent flow, the boundary layers and local grids are both refined. In order to achieve the local stress at the membrane surface, $y^+ < 1$ is recommended for the simulation. According to the equation: $y^+ = \frac{\rho u_\tau y}{\mu}$, the velocity u_τ can be expressed as $\sqrt{\frac{\tau_w}{\rho}}$ (τ_w , wall shear stress). Thus, the first node over the membrane surface y at 0.005 mm would be appreciated to fulfil the requirement. This corresponds to the maximum y^+ value being slightly higher than 1 (about 1.1).

To validate the model, the simulation results with rotating disk module have been compared with the publications. The structured mesh (Fig. S 7) generated with sweeping surface to simplified the simulation.

3.2.1 Validation of numerical simulation

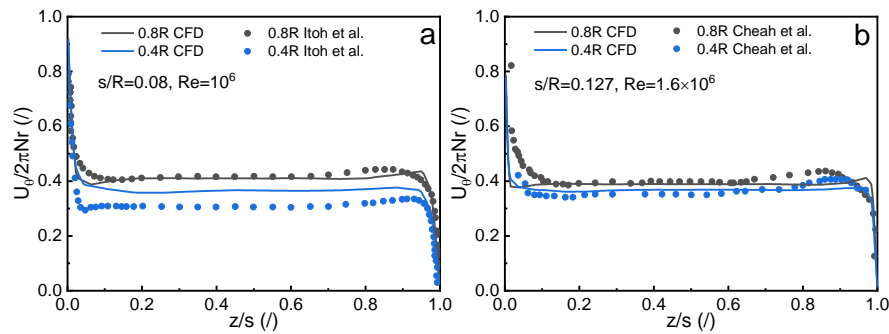


Fig. IV.66 Angular velocity profile at z direction. (a) $s/R=0.08$, $Re=10^6$, (b) $s/R=0.127$, $Re=1.6 \times 10^6$. Operating conditions: μ : 0.001 Pa.s, N : 35/56 Hz, Q_F : 0 L/h.

First, a rotating disk system with structural parameters of $s/R=0.08$ ($s=5.4$ mm, $R=67.5$ mm, corresponds to the increase of gap from 3 to 5.4 mm in the RVF module) and Reynolds number ($Re = \frac{2\pi NR^2}{\nu}$) of 10^6 is simulated. The objective of this preliminary work is to

validate the turbulent model (SST) with experimental data from Iron et al. [277]. As shown in Fig. IV.66a, the numerical simulation of the angular velocity profile along the z -axis matches correctly at the radius of $0.8R$ but is slightly higher at $0.4R$. This is mainly attributed to the simulation of the device ($R=67.5$ mm) being much smaller than the experimental one ($R=250$ mm). It can also be noticed that the location at $0.4R$ is close to the central part of the device. Another rotating disk module ($s/R=0.127$, $Re=1.6 \times 10^6$) has been investigated with LDA technology [278], which is related to the gap of 8.6 mm in the RVF module. It can be seen in Fig. IV.66b that the velocity profile at the same position shows a better agreement with the numerical simulation. This result is also similar to the CFD results from Torras et al. for the classical RD model [230].

3.2.2 Local velocity

Once validated, the model is used to study turbulent flow in the RVF with a simplified three blades impeller. The velocity field for the 60° three-blade impeller is shown in Fig. IV.67. In contrast to laminar flow, the separation of the boundary layers at both sides of the domain is maintained in turbulent flow, even within the narrow gap between the membrane and the blade.

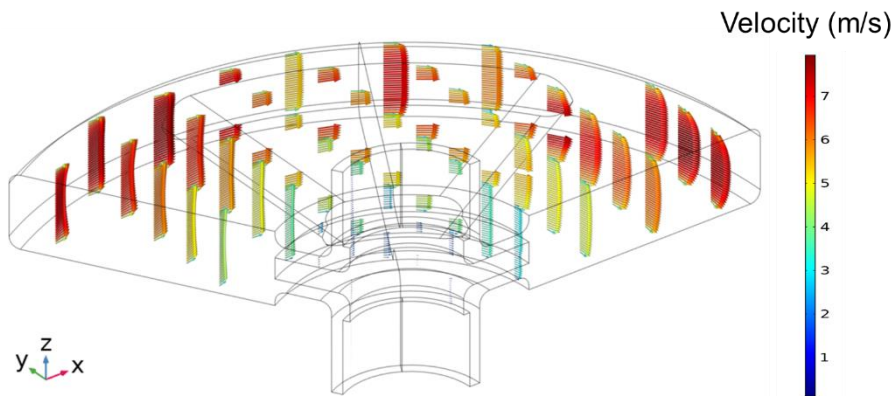


Fig. IV.67 Velocity field in the filtration cell. Operating conditions: 60° three-blade impeller, μ : 0.001 Pa.s, N : 20 Hz, Q_F : 50 L/h.

The angular velocity profiles along the z -axis at different locations in RVF are compared in Fig. IV.68. According to the turbulent regime, a sharp increase in velocity is observed for each local position (A-G) when close to the wall. Due to the rotation of the blade, the angular velocity between two blades (A, B, D) varies in the gap and reaches its maximum value close to the blade. Between the membrane and the blade, the flow is not fully developed in the small gap ($s=3$ mm), which is different from the same case in the laminar regime. The

velocity distributions at different mixing rates are plotted in Fig. IV.69, which confirm the existence of two separate boundary layers, whatever the mixing rate, even in the narrow gap. In contrast, the boundary layers appear to separate with the increase of the mixing rate, or the decrease of the viscosity (Fig. IV.40 and Fig. IV.41). Considering the rotating full disk (Fig. IV.68), the separation of the boundary layers is also noted, but the magnitude of the velocity at the same radius was lower than the one with the rotating impeller. This explains why the k value of the rotating full disk is lower. Another interesting phenomenon is that the symmetry of flow is lost in the rotating full disk, i.e., the velocity in the upper region (outlet side) of the disk is slightly higher than in the lower region (inlet side), which is not appeared during the feeding flowrate equals to 0. This is not the case if the physical problem is symmetric (neither inlet nor outlet, or without flowrate). On the contrary, it does not occur with the rotating impeller.

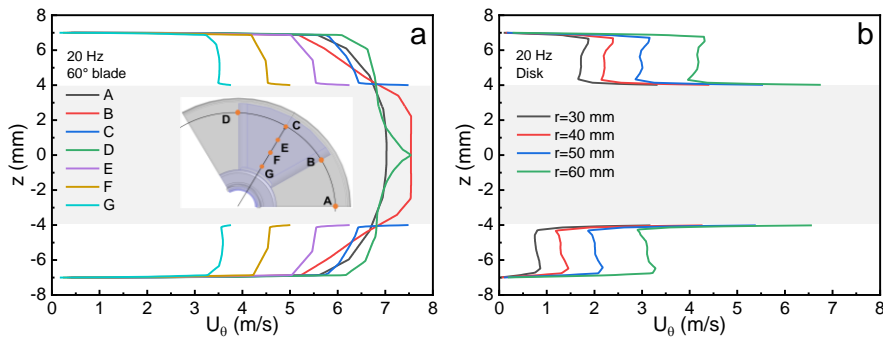


Fig. IV.68 Tangential velocity along the z -direction. (a) velocity distribution at different positions (radius, angle) for 60° three-blade impeller; (b) velocity distribution at different radii for the disk (between two blades), B (leading edge), C (on the blade) and D (trailing edge) with a radius of 60 mm; E, F and G with a radius of 50, 40 and 30 mm, respectively. Operating conditions: μ : 0.001 Pa.s, N : 20 Hz, Q_F : 50 L/h.

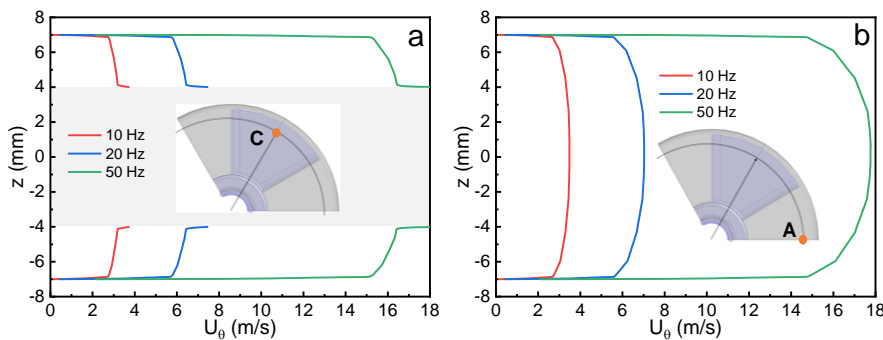


Fig. IV.69 Tangential velocity along the z -direction. (a) velocity distribution between the membrane

and the blade; (b) velocity distribution between two membranes. Operating conditions: μ : 0.001 Pa.s, N : 10, 20, 50 Hz, Q_F : 50 L/h.

3.2.3 Local pressure

The mixing pressure as a function of local radius is plotted in Fig. IV.70. The different mixing rates yielded k values close to 0.86, which is higher than the experimental results (0.65). As for the pressure fluctuations, the linear correlation between σ_P and the local radius differs from the laminar flow regime (Fig. IV.44). A possible explanation is that the boundary layer is separated at low radii with viscous fluid. Since the simulations are performed with the RANS model, the results for fluid fluctuations only take into account the periodic contribution. Thus, σ_P can be compared with the FFT result (Fig. IV.26). From 10 to 50 Hz, σ_P increase with mixing rates, while A reach the maximum around 20 Hz, corresponding to the resonance frequency. Apparently, this simulation did not confirm the resonance phenomenon within the RVF.

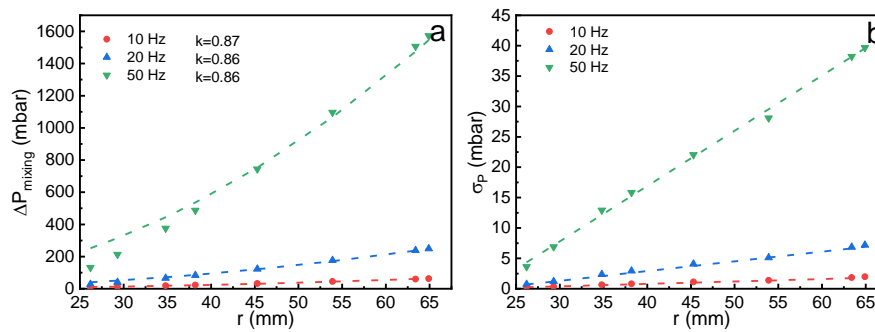


Fig. IV.70 Pressure distribution as a function of radius. (a) is the mixing pressure, (b) is the standard deviation of pressure fluctuation. Operating conditions: μ : 0.001 Pa.s, N : 10, 20, 50 Hz, Q_F : 50 L/h.

3.2.4 Local shear stress

Fig. IV.71 shows the shear stress distribution at the membrane surface. As described in the laminar regime, the maximum shear stress occurs at the trailing edge of the blade. By extracting the mean shear stress along the angle direction, mean shear stress as a function of local radius is plotted in Fig. IV.72. Interestingly, the shear stress is not as expected by the Eqs (II.26) and (II.28). Instead, it is linearly related to the radius and the same to the laminar regime (Fig. IV.57). This can also be explained as a result of the unique configuration of the impeller. As for the magnitude of shear stress fluctuation (σ_s), it is also similar to laminar flow. However, its relative standard deviation is limited below 10%, which is smaller than that of laminar flow.

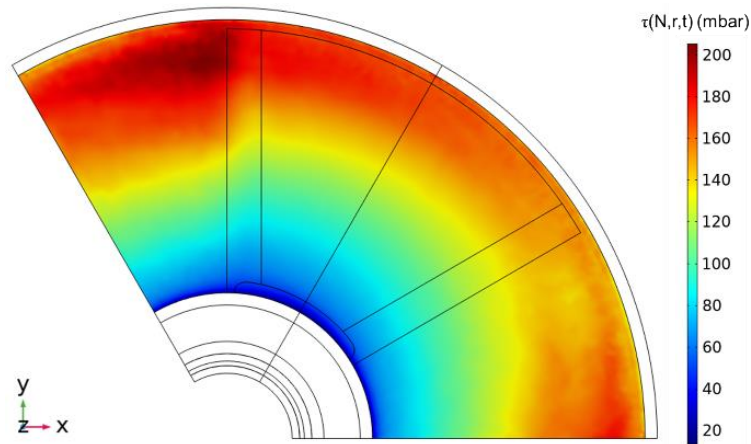


Fig. IV.71 Shear stress field at the membrane surface. Operating conditions: μ : 0.001 Pa.s, N : 20 Hz, Q_F : 50 L/h.

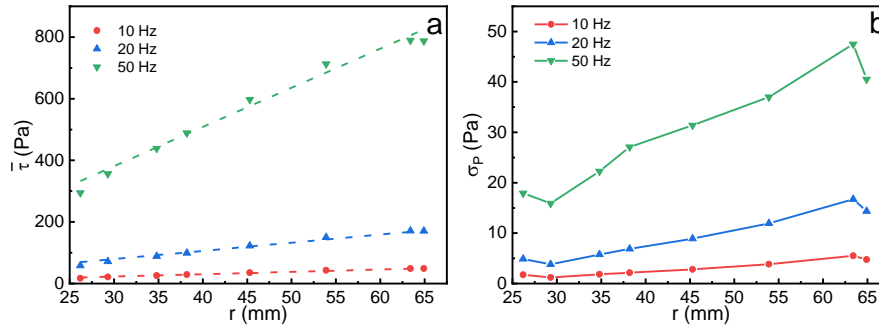


Fig. IV.72 Shear stress distribution as a function of radius. (a) is the mean shear stress, (b) is the standard deviation of shear stress fluctuation. Operating conditions: μ : 0.001 Pa.s, N : 10, 20, 50 Hz, Q_F : 50 L/h.

Based on statistical treatment, the linear relation to estimating the mean shear stress is plotted in Fig. IV.73. In this way, the k value of 0.86 was used, yielding a slope of 2.8.

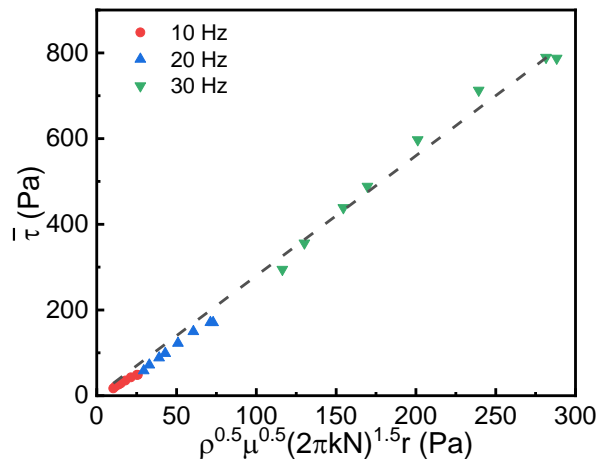


Fig. IV.73 Estimation of local shear stress at the membrane surface. Operating conditions: μ :

0.001 Pa.s, N: 10, 20, 50 Hz, Q_F : 50 L/h.

Due to the limited experimental conditions and time, the CFD simulation is currently limited to 3 mixing rates. More works will be carried out to reconstruct the pressure and shear stress distribution at the membrane surface. In that case, the optimal impeller design will be developed to enhance the dynamic filtration performance.

❖ Summary of CFD investigation

Objectives:

- (1) To clarify the operating conditions (Q_F , P_b , N and μ) on the pressure and shear stress distribution (mean and fluctuating components);
- (2) To expand the range of experiments (Q_F , P_b , N and μ);
- (3) To optimize the filtration cell (impeller geometry and gap s).

Contents:

The filtration performances are associated with the local shear stress ($\bar{\tau}$ and σ_s) and TMP (k -value and σ_P) at the membrane surface, which has been compared based on different operating parameters and cell geometries.

(1) Laminar regime

Operating parameters:

- Feeding flowrate shows a slight effect on local pressure due to the contribution of radial velocity, which can be neglected in dynamic filtration;
- Back pressure has no effect on pressure and shear stress;
- ΔP_{mixing} and σ_P are positively correlated with mixing rate and radius, but the contribution of σ_P is limited to less than 12% when the back pressure is 300 mbar;
- The ratio between σ_s and $\bar{\tau}$ can reach up to 39%.

Filtration cell geometries:

- The optimal impeller geometry is a 30° three blades impeller;
- The maximum pressure and shear stress can be achieved with a 3 and 4 blades impeller, but the increase in blade number is negative to pressure and shear stress fluctuation;
- Reducing impeller/membrane gap contributes to improving local pressure and shear at the membrane surface.

(2) Turbulent regime

- The simulated k value is overestimated;
- The increase of σ_P is quasi-linear as a function of local radius;
- The $\bar{\tau}$ can be estimated with the empirical equation, and the contribution of σ_s is limited below 10%.

The simulation in the turbulent regime needs to be further investigated in order to give the optimum cell geometry.

Chapter V: Conclusions and Perspectives

1 Scientific context

In order to investigate the intensification of membrane bioreactors with dynamic filtration (DF), our group has conducted a wide range of studies to characterize the hydrodynamics in RVF modules and their performances in biotechnology. With the knowledge gaps, this doctorate was devoted to gaining insight into the complex hydrodynamics of RVF module at global and local scales, scrutinizing the local and instantaneous measurements of the driving force (pressure), and accessing a better understanding of the limiting mechanisms that take place close to the membrane during the filtration operation.

Firstly, in this framework, an extensive review was realized, describing the DF techniques and the related hydrodynamic investigations, providing the scientific background of this research, and raising its application prospects and limitations.

Secondly, RVF, as shear-enhanced membrane filtration, has demonstrated better performance than DE and CF filtrations. Due to the rotation of the impeller, high shear stress is generated at the membrane surface, uncoupling from the feeding flowrate. The instrumentation and experimental set-up to measure the global parameters (current, tension, pressure drop, temperature and flowrate), local and instantaneous pressure were achieved. The time series pressure has been treated with SA, PDF and FFT in order to extract the mean and fluctuating (amplitude and frequency) components. Furthermore, the simulation of the same geometry (one cell) with CFD technology (COMSOL Multiphysics) was detailed in the laminar and turbulent regimes.

Thirdly, at the global scale, the empirical correlations to estimate the mixing and pumping power have been established with dimensionless numbers. The laminar and turbulent regimes were identified. For local approach, mean radial pressure and core velocity coefficient were quantified at different flowrates and mixing rates. The local k -value is highly dependent on the contribution of the angular velocity. But in the laminar regime, especially for high viscous fluid, the variation of the boundary layer also needs to be taken into account. Pressure fluctuations have been treated with several strategies to compare their amplitude (periodic and random components) and frequency. In the turbulent regime, a “resonance frequency” close to 20 Hz (21.1 Hz) is clearly identified for Imp 1, at which frequency the magnitude of pressure fluctuation is significantly higher than the other two impellers (Imp 2

and 3). In the laminar regime, this resonance phenomenon was not observed due to the limitations of the experimental equipment. By using the CFD technique, the simulation is more flexible and can be operated with higher mixing rates and flowrates. The evolution of the fluid boundary layer is fully demonstrated during the rotation of the impeller. The pressure fluctuations at the membrane surface are independent of the feeding flowrate and back pressure. The effect of the mixing rate from the simulations is similar to the experimental measurements, while a divergence appears with viscosity. Based on the magnitude of pressure and shear stress (mean and fluctuating components), a 30° three-blade impeller has been selected. In the turbulent regime, the RANS-based Shear Stress Transport (SST) model has been validated with the rotating full disk system. The flow field induced by a rotating impeller (60° three-blade) was successfully solved. Thus, this model can be used for further optimization of the operating conditions and impeller geometries.

2 Answer to our initial scientific questions

Researches were dedicated to answering the scientific questions raised in the first part:

(1) How to estimate the global parameters (pumping and mechanical power)?

For global investigation, friction and power consumption curves in laminar and turbulent regimes have been completed and validated with different impeller configurations. The pumping power can be represented as the dimensionless Euler number by the feeding and mixing conditions. Similarly, the motor power can be estimated using the mixing Reynolds number. We also recorded the thermal increase of the RVF module, which allows for evaluating the heat dissipation of the fluid (thermal dissipation on the shell is not considered). According to the empirical equations regarding the local shear stress, the mechanical power of the impeller can be approximated with the operating conditions.

(2) How to know the local and instantaneous pressure and shear stress, what are their intensity and frequency?

A specially designed porous substrate instrumentation was used to get access to the local and instantaneous pressure at the membrane surface, which provides more accurate measurements, including the mean and fluctuating components. However, the local shear stress was only achieved from the CFD simulation, and the experimental measurements will be implemented in future work.

In the laminar regime, the experimental and simulated local pressures exhibit similar results. The magnitude of the pressure fluctuation is relatively small (<30 mbar) and can be neglected when the TMP is higher than 300 mbar. In contrast, the shear stress increased with the mixing rate, and its fluctuations could reach more than 30%. The frequency of pressure

and shear correlates with the number of blades.

In the turbulent regime, we found the resonance phenomenon of pressure fluctuations generated by Imp 1. The resonance frequency is about 20 Hz (water or BREOX 0.1 solution), thus, producing a maximum pressure fluctuation that exceeds more than 100 mbar. This is not negligible under low-pressure microfiltration conditions. This phenomenon was also found for Imp 3, but its pressure fluctuations were much smaller than those of Imp 1 due to decreased surface area and thickness. No significant resonance phenomenon was observed for Imp 2.

(3) What are the best operating conditions (flow regime, mixing rate, flowrate and back pressure)?

Optimal operating conditions not only contribute to lower energy consumption but also accelerate the membrane filtration process. Considering the mass and heat transfer process of low viscosity fluids, more dynamic membrane filtration is applied to dilute fluids (turbulent flow conditions). Therefore, pressure fluctuation is also a key parameter in intensifying filtration performance, especially for resonant frequency applications. Both flowrate and back pressure has been confirmed to show nothing to the local pressure and shear force, including mixing and fluctuating components. Generally, the flowrate in DF can be controlled at a low level as the shear stress is driven by the rotating impeller rather than the feeding flowrate. Moreover, the back pressure is associated with the TMP, and the appropriate pressure value can be selected according to the filtration type and critical flux.

(4) What is the best filtration cell configuration (membrane/impeller gap and impeller geometry)?

In the laminar flow regime, CFD simulations were performed to obtain the best cell configuration. Based on local pressure and shear stress magnitudes, Imp 1 yielded similar results to the 60° three-blade impeller. Whereas the best impeller design is a 30° three-blade impeller for its high pressure, shear stress and their fluctuations. Reducing the membrane/impeller gap also helps to increase the k -value and shear stress due to the merged boundary layer.

In the turbulent regime, the instantaneous pressures generated by the three impellers were compared. Imp 1 and Imp 2 produced higher mixing pressures, while Imp 2 induced negligible fluctuating pressures. With the pressure fluctuations, resonance is observed for Imp 1 and Imp 3. Therefore, Imp 1 is the best configuration. Further simulation needs to be carried out to optimize the cell geometries.

(5) How do the mean/ fluctuating values of pressure and shear stress impact on filtration performance?

To answer this question, the instantaneous pressure and shear stress should be compared between the rotating impeller and full disk, which will be the future work. Of course, another similar structure may be able to answer this question. In the RD module, a rotating disk with vans yields higher permeate fluxes than a smooth disk, even at the same average shear rate.

(6) How do the microorganisms react to the increase in temperature and mechanical stress inside the filtration cell (cell lysis)?

There are several issues that need to be solved for this question, including RTD, thermal increase and tests in extreme conditions:

In the previous work, RTD was achieved to indicate the mean residence time is dependent on the feeding flowrate rather than the mixing rate in the laminar regime. However, in the turbulent flow regime, mean residence time varies as a function of the mixing rate, independent of the feeding flow rate.

Due to the heat dissipation, the temperature inside the RVF will increase, which shows to be linear with N^2 . The microorganism will suffer a great thermal increase (more than 10 °C at 20 Hz) with high viscous fluid. The temperature can be limited by the increase of flowrate, decrease of viscosity and mixing rate, or by the installation of a cooling system.

Xiaomin has tested the *E.coli* cell suspension (*Prokaryote*) react on the extreme mixing conditions (50 Hz). The results indicate that cells were damaged and disrupted under the mechanical shear stress and appeared as clusters and aggregates. Another representative of yeast suspension (*Eukaryote*) also needs to be applied for the filtration test to acquire their biological behaviour with mixing.

Before selecting the appropriate filtration conditions, the interaction of cells with shear and temperature variations needs to be investigated.

(7) How to enhance the filtration performance during bioprocess (flow regime, operating conditions and device configuration)?

As illustrated in Fig. II.12, the decision tree is proposed to select the appropriate DF module. The basic information (fluid, membrane, and process) associated with the empirical data and hydrodynamics were required before the selection. These knowledge gaps in scientific research should be highlighted.

3 Our highlights and perspectives

Based on the RVF module, as an example, the local hydrodynamic variation during the impeller rotation was investigated in a confined dynamic filtration chamber. It provides the

basic and determinant information for bioprocess application. Several results from this PhD work can be highlighted:

- (1) Extensive review of DF to raise main criteria and knowledge gap;
- (2) Technical strategies and methods to acquire and then treat the time-series pressure;
- (3) Investigate and interpret the local hydrodynamics in the RVF module;
- (4) Identify pressure resonance phenomena and propose an empirical equation for estimating pressure fluctuations;
- (5) Optimize the operating conditions and impeller geometries based on local pressure and shear magnitudes using the CFD approach.

This work provides a better fundamental knowledge for the characterization and the modelling of instantaneous pressure at the membrane surface in a DF module. It highlights the potential of pressure fluctuations as an additional driving force to intensify microfiltration. Certainly, the identified “resonance phenomena” may not be limited to pressure but also to shear stress. To better utilize and interpret this phenomenon, future work related to DF will be focused on:

- (1) Investigation of local and instantaneous shear stress at the membrane surface;
- (2) Exploring the contribution of mean and fluctuating values of pressure and shear on filtration performance;
- (3) Characterizing the flow field within the RVF under the turbulent regime and optimizing the cell geometries with the aid of the CFD approach;
- (4) Extending the application of RVF to bioprocesses, which will involve more complex fluids and more limitations (thermal increase, cell lysis, membrane pore plugging, etc.).

References

- [1] W.H. Smith, Germination of *Macrophomina phaseoli* sclerotia as effected by *Pinus lambertiana* root exudate, *Can J Microbiol*, 15 (1969) 1387-1391.
- [2] P. Aimar, G. Daufin, *Séparations par membrane dans l'industrie alimentaire*, F3250, *Techniques de l'ingénieur*, (2004) 1-23.
- [3] G. Daufin, J.P. Escudier, H. Carrère, S. Bérot, L. Fillaudeau, M. Decloux, Recent and Emerging Applications of Membrane Processes in the Food and Dairy Industry, *Food and Bioproducts Processing*, 79 (2001) 89-102.
- [4] M.Y. Jaffrin, Dynamic shear-enhanced membrane filtration: A review of rotating disks, rotating membranes and vibrating systems, *Journal of Membrane Science*, 324 (2008) 7-25.
- [5] X. Xie, Investigation of Local and Global Hydrodynamics of a Dynamic Filtration Module (RVF Technology) for Intensification of Industrial Bioprocess, in: LISBP, INSA Toulouse, 2017.
- [6] L. Fillaudeau, B. Boissier, S. Ermolaev, N. Jitariouk, Etude hydrodynamique d'un module de filtration dynamique, *Ind. Alim. Agri.*, 124 (2007) 8-16.
- [7] T.R. Bentzen, N. Ratkovich, S. Madsen, J.C. Jensen, S.N. Bak, M.R. Rasmussen, Analytical and numerical modelling of Newtonian and non-Newtonian liquid in a rotational cross-flow MBR, *Water Sci Technol*, 66 (2012) 2318-2327.
- [8] X. Xie, C. Le Men, N. Dietrich, P. Schmitz, L. Fillaudeau, Local hydrodynamic investigation by PIV and CFD within a Dynamic filtration unit under laminar flow, *Separation and Purification Technology*, 198 (2018) 38-51.
- [9] A. Chaudhuri, A. Jogdand, Permeate flux decrease due to concentration polarization in a closed roto-dynamic reverse osmosis filtration system, *Desalination*, 402 (2017) 152-161.
- [10] O.A. Akoum, M.Y. Jaffrin, L. Ding, P. Paullier, C. Vanhoutte, An hydrodynamic investigation of microfiltration and ultrafiltration in a vibrating membrane module, *Journal of Membrane Science*, 197 (2002) 37-52.
- [11] M.Y. Jaffrin, L.-H. Ding, O. Akoum, A. Brou, A hydrodynamic comparison between rotating disk and vibratory dynamic filtration systems, *Journal of Membrane Science*, 242 (2004) 155-167.
- [12] T. Zsirai, H. Qiblawey, M.J. A-Marri, S. Judd, The impact of mechanical shear on membrane flux and energy demand, *Journal of Membrane Science*, 516 (2016) 56-63.
- [13] S.P. Beier, G. Jonsson, Critical flux determination by flux-stepping, *AIChE Journal*, 56 (2009) 1739-1747.
- [14] J. Luo, L. Ding, Y. Wan, M.Y. Jaffrin, Threshold flux for shear-enhanced nanofiltration: Experimental observation in dairy wastewater treatment, *Journal of Membrane Science*, 409-410 (2012) 276-284.
- [15] A. Brou, L. Ding, P. Boulnois, M.Y. Jaffrin, Dynamic microfiltration of yeast suspensions using rotating disks equipped with vanes, *Journal of Membrane Science*, 197 (2002) 269-282.
- [16] M. Cheryan, *Ultrafiltration and Microfiltration Handbook*, Taylor & Francis, 1998.

- [17] L. Bachus, A. Custodio, 4 - The affinity laws, in: L. Bachus, A. Custodio (Eds.) *Know and Understand Centrifugal Pumps*, Elsevier Science, Oxford, 2003, pp. 39-43.
- [18] G. Daufin, J.-P. Labbé, *Equipment Fouling in the Dairy Application: Problem and Pretreatment*, in: Z. Amjad (Ed.) *Calcium Phosphates in Biological and Industrial Systems*, Springer US, Boston, MA, 1998, pp. 437-463.
- [19] R.J. Wakeman, E.S. Tarleton, Experiments using electricity to prevent fouling in membrane filtration, *Filtration & Separation*, 23 (1986) 174-176.
- [20] L. Fillaudeau, M. Lalande, A Practical Method to Predict Steady-State Flux and Fouling in the Crossflow Microfiltration of Rough Beer with 1.40 μm Tubular Ceramic Membranes, *Food and Bioproducts Processing*, 76 (1998) 217-223.
- [21] V.G.J. Rodgers, R.E. Sparks, Effect of transmembrane pressure pulsing on concentration polarization, *Journal of Membrane Science*, 68 (1992) 149-168.
- [22] I.G. Wenten, Mechanisms and control of fouling in crossflow microfiltration, *Filtration & Separation*, 32 (1995) 252-253.
- [23] H. Mallubhotla, G. Belfort, Flux enhancement during Dean vortex microfiltration. 8. Further diagnostics, *Journal of Membrane Science*, 125 (1997) 75-91.
- [24] H. Mallubhotla, S. Hoffmann, M. Schmidt, J. Vente, G. Belfort, Flux enhancement during dean vortex tubular membrane nanofiltration. 10. Design, construction, and system characterization, *Journal of Membrane Science*, 141 (1998) 183-195.
- [25] H. Mallubhotla, M. Schmidt, K. Hyun Lee, G. Belfort, Flux enhancement during Dean vortex tubular membrane nanofiltration: 13. Effects of concentration and solute type, *Journal of Membrane Science*, 153 (1999) 259-269.
- [26] T. Horie, S. Shiota, T. Akagi, N. Ohmura, S. Wang, V. Eze, A. Harvey, Y. Hirata, Intensification of hollow fiber membrane cross-flow filtration by the combination of helical baffle and oscillatory flow, *Journal of Membrane Science*, 554 (2018) 134-139.
- [27] T. Akagi, T. Horie, H. Masuda, K. Matsuda, H. Matsumoto, N. Ohmura, Y. Hirata, Improvement of separation performance by fluid motion in the membrane module with a helical baffle, *Separation and Purification Technology*, 198 (2017).
- [28] B.B. Gupta, P. Blanpain, M.Y. Jaffrin, Permeate flux enhancement by pressure and flow pulsations in microfiltration with mineral membranes, *Journal of Membrane Science*, 70 (1992) 257-266.
- [29] M. Mercier, C. Fonade, C. Lafforgue-Delorme, Influence of the flow regime on the efficiency of a gas-liquid two-phase medium filtration, *Biotechnol. Tech.*, 9 (1995) 853-858.
- [30] L. Borea, V. Naddeo, M.S. Shalaby, T. Zarra, V. Belgiorno, H. Abdalla, A.M. Shaban, Wastewater treatment by membrane ultrafiltration enhanced with ultrasound: Effect of membrane flux and ultrasonic frequency, *Ultrasonics*, 83 (2018) 42-47.
- [31] L. Ding, M.Y. Jaffrin, J. Luo, Dynamic Filtration with Rotating Disks, and Rotating or Vibrating Membranes, (2015) 27-59.
- [32] M. Chai, Y. Ye, V. Chen, Application of rotational vibration in a submerged hollow fibre membrane system for bioseparation of high concentration yeast suspensions, *Journal of Membrane Science*, 573 (2019) 145-156.
- [33] L. Villafana-Lopez, E. Clavijo Rivera, S. Liu, E. Couallier, M. Frappart, Shear-

enhanced membrane filtration of model and real microalgae extracts for lipids recovery in biorefinery context, *Bioresour Technol*, 288 (2019) 121539.

[34] M. Hapońska, E. Clavero, J. Salvadó, C. Torras, Application of ABS membranes in dynamic filtration for *Chlorella sorokiniana* dewatering, *Biomass and Bioenergy*, 111 (2018) 224-231.

[35] P. Mikulasek, Methods to reduce concentration polarization and fouling in membrane filtration, *Collect. Czech. Chem. Commun.*, 59 (1994) 737-755.

[36] S. Lee, R.M. Lueptow, Rotating Membrane Filtration and Rotating Reverse Osmosis, *J. Chem. Eng. Jpn.*, 37 (2004) 471-482.

[37] M.Y. Jaffrin, Hydrodynamic Techniques to Enhance Membrane Filtration, *Annual Review of Fluid Mechanics*, 44 (2012) 77-96.

[38] M.Y. Jaffrin, Dynamic filtration with rotating disks, and rotating and vibrating membranes: an update, *Current Opinion in Chemical Engineering*, 1 (2012) 171-177.

[39] L.H. Ding, M.Y. Jaffrin, Benefits of High Shear Rate Dynamic Nanofiltration and Reverse Osmosis: A Review, *Separation Science and Technology*, 49 (2014) 1953-1967.

[40] C. Chen, CiteSpace II: Detecting and visualizing emerging trends and transient patterns in scientific literature, *Journal of the American Society for Information Science and Technology*, 57 (2006) 359-377.

[41] C. Bhattacharjee, P. Bhattacharya, Ultrafiltration of black liquor using rotating disk membrane module, *Separation and Purification Technology*, 49 (2006) 281-290.

[42] S. Bhattacharjee, S. Datta, C. Bhattacharjee, Performance study during ultrafiltration of Kraft black liquor using rotating disk membrane module, *Journal of Cleaner Production*, 14 (2006) 497-504.

[43] J. Luo, L. Ding, Y. Wan, M.Y. Jaffrin, Flux decline control in nanofiltration of detergent wastewater by a shear-enhanced filtration system, *Chemical Engineering Journal*, 181-182 (2012) 397-406.

[44] C.M. Wisniewski, C.S. Slater, M.J. Savelski, Dynamic vibratory membrane processing for use in water recovery from soluble coffee product manufacturing wastewater, *Clean Technologies and Environmental Policy*, 20 (2018) 1791-1803.

[45] S. Kertész, Á. Veszprémi, Z. László, J. Csanádi, G. Keszthelyi-Szabó, C. Hodúr, Investigation of module vibration in ultrafiltration, *Desalination and Water Treatment*, 55 (2014) 2836-2842.

[46] M. Mertens, M.R. Bilad, A.Y. Gebreyohannes, L. Marbelia, I.F.J. Vankelecom, Membrane development for improved performance of a magnetically induced vibration system for anaerobic sludge filtration, *Separation and Purification Technology*, 200 (2018) 120-129.

[47] I. Ruigómez, L. Vera, E. González, G. González, J. Rodríguez-Sevilla, A novel rotating HF membrane to control fouling on anaerobic membrane bioreactors treating wastewater, *Journal of Membrane Science*, 501 (2016) 45-52.

[48] B. Gao, L. Liu, J. Liu, F. Yang, A photo-catalysis and rotating nano-CaCO₃ dynamic membrane system with Fe-ZnIn₂S₄ efficiently removes halogenated compounds in water, *Applied Catalysis B: Environmental*, 138-139 (2013) 62-69.

- [49] B. Gao, L.F. Liu, J.D. Liu, F.L. Yang, Photocatalysis and rotating dynamic membrane hybrid system with Fe-ZnIn₂S₄ efficiently removes 2,4,6-Tribromophenol in water: effect of dynamic membrane, in: X. Quan (Ed.) 2013 International Symposium on Environmental Science and Technology, 2013, pp. 509-514.
- [50] Y. Choi, H. Oh, S. Lee, Y. Choi, T.M. Hwang, J.C. Jeon, Y.K. Choung, Removal of taste and odor model compounds (2-MIB and geosmin) with the NF membrane, *Desalination and Water Treatment*, 15 (2010) 141-148.
- [51] A. Sarkar, D. Sarkar, M. Gupta, C. Bhattacharjee, Recovery of Polyvinyl Alcohol from Desizing Wastewater Using a Novel High-Shear Ultrafiltration Module, *CLEAN - Soil Air Water*, 40 (2012).
- [52] G. Zakrzewska-Trznadel, M. Harasimowicz, A. Miśkiewicz, A. Jaworska, E. Dłuska, S. Wroński, Reducing fouling and boundary-layer by application of helical flow in ultrafiltration module employed for radioactive wastes processing, *Desalination*, 240 (2009) 108-116.
- [53] C. Cojocar, G. Zakrzewska-Trznadel, A. Miskiewicz, Removal of cobalt ions from aqueous solutions by polymer assisted ultrafiltration using experimental design approach Part 2: Optimization of hydrodynamic conditions for a crossflow ultrafiltration module with rotating part, *J. Hazard. Mater.*, 169 (2009) 610-620.
- [54] Z. Tu, L. Ding, M. Frappart, M.Y. Jaffrin, Studies on treatment of sodium dodecyl benzene sulfonate solution by high shear ultrafiltration system, *Desalination*, 240 (2009) 251-256.
- [55] N. Moulai-Mostefa, L.H. Ding, M. Frappart, M.Y. Jaffrin, Treatment of Aqueous Ionic Surfactant Solutions by Dynamic Ultrafiltration, *Separation Science and Technology*, 42 (2007) 2583-2594.
- [56] X. Su, W. Li, A. Palazzolo, S. Ahmed, Concentration polarization and permeate flux variation in a vibration enhanced reverse osmosis membrane module, *Desalination*, 433 (2018) 75-88.
- [57] K.J. Hwang, S.Y. Wang, E. Iritani, N. Katagiri, Fine particle removal from seawater by using cross-flow and rotating-disk dynamic filtration, *Journal of the Taiwan Institute of Chemical Engineers*, 62 (2016) 45-53.
- [58] D. Sarkar, S. Bardhan, A. Bandyopadhyay, M. Chakraborty, C. Bhattacharjee, Simulation of continuous stirred ultrafiltration process: an approach based on surface renewal theory, *Asia-Pac. J. Chem. Eng.*, 7 (2012) 279-294.
- [59] A. Sarkar, D. Sarkar, C. Bhattacharjee, Design and performance characterization of a new shear enhanced module with inbuilt cleaning arrangement, *Journal of Chemical Technology & Biotechnology*, 87 (2012) 1121-1130.
- [60] D. Sarkar, C. Bhattacharjee, Modeling and analytical simulation of rotating disk ultrafiltration module, *Journal of Membrane Science*, 320 (2008) 344-355.
- [61] S. Ri, Z. Xu, Y. Zhou, G.e. Chen, Y. Kim, Experimental Study on Revolving Cross-flow Microfiltration of Highly Viscous Liquids, *Chinese Journal of Chemical Engineering*, 16 (2008) 961-964.
- [62] H.S. Marke, M.P. Breil, E.B. Hansen, M. Pinelo, U. Krühne, Investigation of the

velocity factor in a rotational dynamic microfiltration system, *Separation and Purification Technology*, 220 (2019) 69-77.

[63] S. Lee, R.M. Lueptow, Control of scale formation in reverse osmosis by membrane rotation, *Desalination*, 155 (2003) 131-139.

[64] X. Su, W. Li, A. Palazzolo, S. Ahmed, Permeate flux increase by colloidal fouling control in a vibration enhanced reverse osmosis membrane desalination system, *Desalination*, 453 (2019) 22-36.

[65] M. Frappart, M.Y. Jaffrin, L.H. Ding, V. Espina, Effect of vibration frequency and membrane shear rate on nanofiltration of diluted milk, using a vibratory dynamic filtration system, *Separation and Purification Technology*, 62 (2008) 212-221.

[66] W. Zhang, L. Ding, Investigation of membrane fouling mechanisms using blocking models in the case of shear-enhanced ultrafiltration, *Separation and Purification Technology*, 141 (2015) 160-169.

[67] M. Frappart, O. Akoum, L. Ding, M. Jaffrin, Treatment of dairy process waters modelled by diluted milk using dynamic nanofiltration with a rotating disk module, *Journal of Membrane Science*, 282 (2006) 465-472.

[68] O. Akoum, M.Y. Jaffrin, L.H. Ding, M. Frappart, Treatment of dairy process waters using a vibrating filtration system and NF and RO membranes, *Journal of Membrane Science*, 235 (2004) 111-122.

[69] M. Frappart, M. Jaffrin, L.H. Ding, Reverse osmosis of diluted skim milk: Comparison of results obtained from vibratory and rotating disk modules, *Separation and Purification Technology*, 60 (2008) 321-329.

[70] S. Ladeg, Z. Zhu, N. Moulai-Mostefa, L. Ding, M.Y. Jaffrin, CFD Simulation of the Distribution of Pressure and Shear Rate on the Surface of Rotating Membrane Equipped with Vanes for the Ultrafiltration of Dairy Effluent, *Arabian Journal for Science and Engineering*, 43 (2017) 2237-2245.

[71] W. Zhang, L. Ding, M.Y. Jaffrin, B. Tang, Membrane cleaning assisted by high shear stress for restoring ultrafiltration membranes fouled by dairy wastewater, *Chemical Engineering Journal*, 325 (2017) 457-465.

[72] S. Lee, R.M. Lueptow, Experimental verification of a model for rotating reverse osmosis, *Desalination*, 146 (2002) 353-359.

[73] M. Ebrahimi, O. Schmitz, S. Kerker, F. Liebermann, P. Czermak, Dynamic cross-flow filtration of oilfield produced water by rotating ceramic filter discs, *Desalination and Water Treatment*, 51 (2013) 1762-1768.

[74] L. Li, L. Ding, Z. Tu, Y. Wan, D. Clause, J.-L. Lanoisellé, Recovery of linseed oil dispersed within an oil-in-water emulsion using hydrophilic membrane by rotating disk filtration system, *Journal of Membrane Science*, 342 (2009) 70-79.

[75] N. Moulai-Mostefa, O. Akoum, M. Nedjihoui, L. Ding, M.Y. Jaffrin, Comparison between rotating disk and vibratory membranes in the ultrafiltration of oil-in-water emulsions, *Desalination*, 206 (2007) 494-498.

[76] N. Moulai-Mostefa, M. Frappart, O. Akoum, L. Ding, M.Y. Jaffrin, Separation of water from metal working emulsions by ultrafiltration using vibratory membranes, *J Hazard*

Mater, 177 (2010) 978-982.

[77] T. Murase, T. Ohn, K. Kamimura, Dynamic microfiltration of dilute O/W emulsion in rotating cylindrical membrane filter, *Kag. Kog. Ronbunshu*, 22 (1996) 120-126.

[78] T. Murase, A.-W. Yosufu, Microfiltration-Rate Increase of O/W Emulsion by Use of Rotating Membrane Filter with Additional Suspended Solids, *Kag. Kog. Ronbunshu*, 23 (1997) 452-454.

[79] A. Ullah, J. Ahmad, H. Khan, S.W. Khan, F. Zamani, S.W. Hasan, V.M. Starov, J.W. Chew, Membrane oscillation and slot (pore) blocking in oil-water separation, *Chem. Eng. Res. Des.*, 142 (2019) 111-120.

[80] T. Li, A.W.-K. Law, M. Cetin, A.G. Fane, Fouling control of submerged hollow fibre membranes by vibrations, *Journal of Membrane Science*, 427 (2013) 230-239.

[81] T. Murase, C. Pradistsuwana, E. Iritani, K. Kano, Dynamic microfiltration of dilute slurries with a rotating ceramic membrane, *Journal of Membrane Science*, 62 (1991) 187-199.

[82] K.-J. Hwang, S.-E. Wu, Y.-L. Hsueh, Analysis on the nonuniformity of cake formation in rotating-disk dynamic microfiltration, *Separation and Purification Technology*, 198 (2018) 16-24.

[83] T. Murase, D.-W. Yang, E. Iritani, Microfiltration Characteristics of High-Viscosity Slurries in Rotating Dynamic Filter, *Kag. Kog. Ronbunshu*, 18 (1992) 708-713.

[84] K. Takata, K. Tanida, Structure of shear-enhanced flow on membrane surface with horizontal vibration and its effect on filtration performance, *Chemical Engineering Research and Design*, 134 (2018) 130-139.

[85] R.B. Aim, S. Vigneswaran, H. Prasanthi, V. Jegatheesan, Influence of particle size and size distribution in granular bed filtration and dynamic microfiltration, *Water Sci. Technol.*, 36 (1997) 207-215.

[86] L. Ding, M. Jaffrin, M. Mellal, G. He, Investigation of performances of a multishaft disk (MSD) system with overlapping ceramic membranes in microfiltration of mineral suspensions, *Journal of Membrane Science*, 276 (2006) 232-240.

[87] Z. Tu, L. Ding, Microfiltration of mineral suspensions using a MSD module with rotating ceramic and polymeric membranes, *Separation and Purification Technology*, 73 (2010) 363-370.

[88] R. Bouzerar, L. Ding, M.Y. Jaffrin, Local permeate flux–shear–pressure relationships in a rotating disk microfiltration module: implications for global performance, *Journal of Membrane Science*, 170 (2000) 127-141.

[89] G. He, L.H. Ding, P. Paullier, M.Y. Jaffrin, Experimental study of a dynamic filtration system with overlapping ceramic membranes and non-permeating disks rotating at independent speeds, *Journal of Membrane Science*, 300 (2007) 63-70.

[90] M. Loginov, N.I. Lebovka, O. Larue, L.H. Ding, E. Vorobiev, Dead-End Dynamic Filtration of Highly Concentrated CaCO₃ Suspensions in the Presence of a Dispersant, *Chem. Eng. Technol.*, 33 (2010) 1260-1268.

[91] D.E. Hadzismajlovic, C.D. Bertram, Flux enhancement in laminar crossflow microfiltration using a collapsible-tube pulsation generator, *Journal of Membrane Science*, 142 (1998) 173-189.

[92] J.Y. Park, C.K. Choi, J.J. Kim, A study on dynamic separation of silica slurry using a rotating membrane filter 1. Experiments and filtrate fluxes, *Journal of Membrane Science*, 97 (1994) 263-273.

[93] S.-E. Wu, K.-J. Hwang, T.-W. Cheng, K.-L. Tung, E. Iritani, N. Katagiri, Structural design of a rotating disk dynamic microfilter in improving filtration performance for fine particle removal, *Journal of the Taiwan Institute of Chemical Engineers*, 94 (2019) 43-52.

[94] C. Kyun Choi, J. Yong Park, W. Cheol Park, J. Jin Kim, A study on dynamic separation of silica slurry using a rotating membrane filter: 2. Modelling of cake formation, *Journal of Membrane Science*, 157 (1999) 177-187.

[95] R. Ben Aim, M.G. Liu, S. Vigneswaran, Recent Development of Membrane Processes for Water and Waste Water Treatment, *Water Sci. Technol.*, 27 (1993) 141-149.

[96] R. Bouzerar, M.Y. Jaffrin, A. Lefevre, P. Paullier, Concentration of ferric hydroxide suspensions in saline medium by dynamic cross-flow filtration, *Journal of Membrane Science*, 165 (2000) 111-123.

[97] R. Bouzerar, P. Paullier, M.Y. Jaffrin, Concentration of mineral suspensions and industrial effluents using a rotating disk dynamic filtration module, *Desalination*, 158 (2003) 79-85.

[98] P. Ji, A. Motin, W. Shan, A. Bénard, M.L. Bruening, V.V. Tarabara, Dynamic crossflow filtration with a rotating tubular membrane: Using centripetal force to decrease fouling by buoyant particles, *Chemical Engineering Research and Design*, 106 (2016) 101-114.

[99] L. Ding, O. Al-Akoun, A. Abraham, M.Y. Jaffrin, Milk protein concentration by ultrafiltration with rotating disk modules, *Desalination*, 144 (2002) 307-311.

[100] O. Al-Akoun, L. Ding, R. Chotard-Ghodsniya, M.Y. Jaffrin, G. Gésan-Guiziou, Casein micelles separation from skimmed milk using a VSEP dynamic filtration module, *Desalination*, 144 (2002) 325-330.

[101] O. Akoun, M.Y. Jaffrin, L.-H. Ding, Concentration of total milk proteins by high shear ultrafiltration in a vibrating membrane module, *Journal of Membrane Science*, 247 (2005) 211-220.

[102] V. Espina, M. Jaffrin, M. Frappart, L. Ding, Separation of casein micelles from whey proteins by high shear microfiltration of skim milk using rotating ceramic membranes and organic membranes in a rotating disk module, *Journal of Membrane Science*, 325 (2008) 872-879.

[103] V. Espina, M.Y. Jaffrin, M. Frappart, L.H. Ding, Separation of casein from whey proteins by dynamic filtration, *Desalination*, 250 (2010) 1109-1112.

[104] P. Meyer, A. Mayer, U. Kulozik, High concentration of skim milk proteins by ultrafiltration: Characterisation of a dynamic membrane system with a rotating membrane in comparison with a spiral wound membrane, *International Dairy Journal*, 51 (2015) 75-83.

[105] J. Schäfer, R. Bast, Z. Atamer, S. Nöbel, R. Kohlus, J. Hinrichs, Concentration of skim milk by means of dynamic filtration using overlapping rotating ceramic membrane disks, *International Dairy Journal*, 78 (2018) 11-19.

[106] V.S. Espina, M.Y. Jaffrin, L.H. Ding, Comparison of rotating ceramic membranes

and polymeric membranes in fractionation of milk proteins by microfiltration, *Desalination*, 245 (2009) 714-722.

[107] V. Espina, M.Y. Jaffrin, L. Ding, Extraction and Separation of α -lactalbumin and β -Lactoglobulin from Skim Milk by Microfiltration and Ultrafiltration at High Shear Rates: A Feasibility Study, *Separation Science and Technology*, 44 (2009) 3832-3853.

[108] V. Espina, M.Y. Jaffrin, L. Ding, B. Cancino, Fractionation of pasteurized skim milk proteins by dynamic filtration, *Food Research International*, 43 (2010) 1335-1346.

[109] V. Espina, M.Y. Jaffrin, P. Paullier, L.H. Ding, Comparison of permeate flux and whey protein transmission during successive microfiltration and ultrafiltration of UHT and pasteurized milks, *Desalination*, 264 (2010) 151-159.

[110] O. Akoum, D. Richfield, M.Y. Jaffrin, L.H. Ding, P. Swart, Recovery of trypsin inhibitor and soy milk protein concentration by dynamic filtration, *Journal of Membrane Science*, 279 (2006) 291-300.

[111] L. Fillaudeau, B. Boissier, A. Moreau, P. Blanpain-Avet, S. Ermolaev, N. Jitariouk, Investigation of rotating and vibrating filtration for clarification of rough beer, *Journal of Food Engineering*, 80 (2007) 206-217.

[112] Y.E. Rayess, Y. Manon, N. Jitariouk, C. Albasi, M.M. Peuchot, A. Devatine, L. Fillaudeau, Wine clarification with Rotating and Vibrating Filtration (RVF): Investigation of the impact of membrane material, wine composition and operating conditions, *Journal of Membrane Science*, 513 (2016) 47-57.

[113] Z. Zhu, H. Mhemdi, L. Ding, O. Bals, M.Y. Jaffrin, N. Grimi, E. Vorobiev, Dead-End Dynamic Ultrafiltration of Juice Expressed from Electroporated Sugar Beets, *Food and Bioprocess Technology*, 8 (2014) 615-622.

[114] W. Zhang, N. Grimi, M.Y. Jaffrin, L. Ding, Leaf protein concentration of alfalfa juice by membrane technology, *Journal of Membrane Science*, 489 (2015) 183-193.

[115] W. Zhang, L. Ding, N. Grimi, M.Y. Jaffrin, B. Tang, Application of UF-RDM (Ultrafiltration Rotating Disk Membrane) module for separation and concentration of leaf protein from alfalfa juice: Optimization of operation conditions, *Separation and Purification Technology*, 175 (2017) 365-375.

[116] Z.Z. Zhu, X. Luo, F.F. Yin, S.Y. Li, J.R. He, Clarification of Jerusalem Artichoke Extract Using Ultra-filtration: Effect of Membrane Pore Size and Operation Conditions, *Food and Bioprocess Technology*, 11 (2018) 864-873.

[117] M. Frappart, A. Massé, M.Y. Jaffrin, J. Pruvost, P. Jaouen, Influence of hydrodynamics in tangential and dynamic ultrafiltration systems for microalgae separation, *Desalination*, 265 (2011) 279-283.

[118] S.D. Ríos, J. Salvadó, X. Farriol, C. Torras, Antifouling microfiltration strategies to harvest microalgae for biofuel, *Bioresour. Technol.*, 119 (2012) 406-418.

[119] S.D. Rios, E. Clavero, J. Salvadó, X. Farriol, C. Torras, Dynamic Microfiltration in Microalgae Harvesting for Biodiesel Production, *Industrial & Engineering Chemistry Research*, 50 (2011) 2455-2460.

[120] C. Nurra, E. Clavero, J. Salvado, C. Torras, Vibrating membrane filtration as improved technology for microalgae dewatering, *Bioresour Technol*, 157 (2014) 247-253.

- [121] K.J. Hwang, S.J. Lin, Filtration flux-shear stress-cake mass relationships in microalgae rotating-disk dynamic microfiltration, *Chemical Engineering Journal*, 244 (2014) 429-437.
- [122] C. Nurra, C. Torras, E. Clavero, S. Rios, M. Rey, E. Lorente, X. Farriol, J. Salvado, Biorefinery concept in a microalgae pilot plant. Culturing, dynamic filtration and steam explosion fractionation, *Bioresour Technol*, 163 (2014) 136-142.
- [123] K. Kim, J.-Y. Jung, J.-H. Kwon, J.-W. Yang, Dynamic microfiltration with a perforated disk for effective harvesting of microalgae, *Journal of Membrane Science*, 475 (2015) 252-258.
- [124] K.-J. Hwang, S.-E. Wu, Disk structure on the performance of a rotating-disk dynamic filter: A case study on microalgae microfiltration, *Chemical Engineering Research and Design*, 94 (2015) 44-51.
- [125] C.S. Slater, M.J. Savelski, P. Kostetsky, M. Johnson, Shear-enhanced microfiltration of microalgae in a vibrating membrane module, *Clean Technologies and Environmental Policy*, 17 (2015) 1743-1755.
- [126] K. Kim, J.-Y. Jung, H. Shin, S.-A. Choi, D. Kim, S.C. Bai, Y.K. Chang, J.-I. Han, Harvesting of *Scenedesmus obliquus* using dynamic filtration with a perforated disk, *Journal of Membrane Science*, 517 (2016) 14-20.
- [127] E. Lorente, M. Haponska, E. Clavero, C. Torras, J. Salvado, Microalgae fractionation using steam explosion, dynamic and tangential cross-flow membrane filtration, *Bioresour Technol*, 237 (2017) 3-10.
- [128] J.Y. Jung, K. Kim, S.A. Choi, H. Shin, D. Kim, S.C. Bai, Y.K. Chang, J.I. Han, Dynamic filtration with a perforated disk for dewatering of *Tetraselmis suecica*, *Environ Technol*, 38 (2017) 3102-3108.
- [129] J. Ye, Q. Zhou, X.Z. Zhang, Q. Hu, Microalgal dewatering using a polyamide thin film composite forward osmosis membrane and fouling mitigation, *Algal Res.*, 31 (2018) 421-429.
- [130] E. Lorente, M. Haponska, E. Clavero, C. Torras, J. Salvado, Steam Explosion and Vibrating Membrane Filtration to Improve the Processing Cost of Microalgae Cell Disruption and Fractionation, *Processes*, 6 (2018).
- [131] M. Hapońska, E. Clavero, J. Salvadó, X. Farriol, C. Torras, Pilot scale dewatering of *Chlorella sorokiniana* and *Dunaliella tertiolecta* by sedimentation followed by dynamic filtration, *Algal Research*, 33 (2018) 118-124.
- [132] Y. Zhang, X. Li, R. Xu, C. Ma, X. Wang, Q. Fu, Algal fouling control in a hollow fiber module during ultrafiltration by angular vibrations, *Journal of Membrane Science*, 569 (2019) 200-208.
- [133] M. Mateus, J.M.S. Cabral, Steroid recovery by a rotary membrane system, *Biotechnol. Tech.*, 5 (1991) 43-48.
- [134] S.S. Lee, A. Burt, G. Russotti, B. Buckland, Microfiltration of recombinant yeast cells using a rotating disk dynamic filtration system, *Biotechnol. Bioeng.*, 48 (1995) 386-400.
- [135] A. Adach, S. Wroński, M. Buczkowski, W. Starosta, B. Sartowska, Mechanism of microfiltration on the rotating track membrane, *Separation and Purification Technology*, 26

(2002) 33-41.

[136] S. Beier, M. Guerra, A. Garde, G. Jonsson, Dynamic microfiltration with a vibrating hollow fiber membrane module: Filtration of yeast suspensions, *Journal of Membrane Science*, 281 (2006) 281-287.

[137] H.G. Goma, S. Rao, A.M. Al-Taweel, Intensification of membrane microfiltration using oscillatory motion, *Separation and Purification Technology*, 78 (2011) 336-344.

[138] A. Kola, Y. Ye, A. Ho, P. Le-Clech, V. Chen, Application of low frequency transverse vibration on fouling limitation in submerged hollow fibre membranes, *Journal of Membrane Science*, 409-410 (2012) 54-65.

[139] H.G. Goma, R. Sabouni, Energetic consideration and flux characteristics of roughed-surface membrane in presence of reversing shear, *Chemical Engineering Research and Design*, 92 (2014) 1771-1780.

[140] A. G. Georges, J. Pierson, *Flow Dynamic Effect in Cake Shape and Resistance in Membrane Filtration*, 2011.

[141] A. Brou, M.Y. Jaffrin, L.H. Ding, J. Courtois, Microfiltration and ultrafiltration of polysaccharides produced by fermentation using a rotating disk dynamic filtration system, *Biotechnol Bioeng*, 82 (2003) 429-437.

[142] C. Harscoat, M.Y. Jaffrin, R. Bouzerar, J. Courtois, Influence of fermentation conditions and microfiltration processes on membrane fouling during recovery of glucuronane polysaccharides from fermentation broths, *Biotechnol. Bioeng.*, 65 (1999) 500-511.

[143] M. Mellal, M.Y. Jaffrin, L.H. Ding, C. Delattre, P. Michaud, J. Courtois, Separation of oligoglucuronans of low degrees of polymerization by using a high shear rotating disk filtration module, *Separation and Purification Technology*, 60 (2008) 22-29.

[144] J.H. Vogel, K.-H. Kroner, Controlled shear filtration: A novel technique for animal cell separation, *Biotechnol. Bioeng.*, 63 (1999) 663-674.

[145] J. Cole, J.D. Brantley, Dynamic membrane filtration in cell and protein production, *Biopharm-Technol. Bus. Biopharm.*, 9 (1996) 66-&.

[146] L.R. Castilho, F.B. Anspach, CFD-aided design of a dynamic filter for mammalian cell separation, *Biotechnol. Bioeng.*, 83 (2003) 514-524.

[147] D. Sarkar, D. Datta, D. Sen, C. Bhattacharjee, Simulation of continuous stirred rotating disk-membrane module: An approach based on surface renewal theory, *Chemical Engineering Science*, 66 (2011) 2554-2567.

[148] A. Sarkar, S. Moulik, D. Sarkar, A. Roy, C. Bhattacharjee, Performance characterization and CFD analysis of a novel shear enhanced membrane module in ultrafiltration of Bovine Serum Albumin (BSA), *Desalination*, 292 (2012) 53-63.

[149] M. Naskar, K. Rana, D. Chatterjee, T. Dhara, R. Sultana, D. Sarkar, Design, performance characterization and hydrodynamic modeling of intermeshed spinning basket membrane (ISBM) module, *Chemical Engineering Science*, 206 (2019) 446-462.

[150] J. Gursch, R. Hohl, G. Toschkoff, D. Dujmovic, J. Brozio, M. Krumme, N. Rasenack, J. Khinast, Continuous Processing of Active Pharmaceutical Ingredients Suspensions via Dynamic Cross-Flow Filtration, *J. Pharm. Sci.*, 104 (2015) 3481-3489.

- [151] Y.-F. Maa, C.C. Hsu, Investigation on fouling mechanisms for recombinant human growth hormone sterile filtration, *J. Pharm. Sci.*, 87 (1998) 808-812.
- [152] L. Fernandez-Cerezo, A. Rayat, A. Chatel, J.M. Pollard, G.J. Lye, M. Hoare, An ultra scale-down method to investigate monoclonal antibody processing during tangential flow filtration using ultrafiltration membranes, *Biotechnol. Bioeng.*, 116 (2019) 581-590.
- [153] U. Frenander, A.S. JÖNsson, Cell harvesting by cross-flow microfiltration using a shear-enhanced module, *Biotechnol. Bioeng.*, 52 (1996) 397-403.
- [154] Spin Tek- Model ST- II- Rotary Membrane system, in, <https://www.environmental-expert.com/products/spintek-model-st-ii-rotary-membrane-system-97370>.
- [155] M.M. Dal-Cin, C.N. Lick, A. Kumar, S. Lealess, Dispersed phase back transport during ultrafiltration of cutting oil emulsions with a spinning membrane disc geometry1, *Journal of Membrane Science*, 141 (1998) 165-181.
- [156] J. Bendick, B. Reed, P. Morrow, T. Carole, Using a high shear rotary membrane system to treat shipboard wastewaters: Experimental disc diameter, rotation and flux relationships, *Journal of Membrane Science*, 462 (2014) 178-184.
- [157] J. Bendick, B. Reed, P. Morrow, T. Carole, Effect of Backpulsing and Continuous Surface Cleaning on High-Shear Rotary Membrane System Permeate Flux Performance for Naval Shipboard Wastewaters, *Journal of Environmental Engineering*, 140 (2014) 04014004.
- [158] B.E. Reed, W. Lin, R. Viadero, J. Young, Treatment of Oily Wastes Using High-Shear Rotary Ultrafiltration, *Journal of Environmental Engineering*, 123 (1997) 1234-1242.
- [159] R. Viadero, R. Jr, B. Reed, Study of series resistances in high-shear rotary ultrafiltration, *Journal of Membrane Science*, 162 (1999) 199-211.
- [160] R.C.V. Jr, B.E. Reed, Rotation and Concentration Effects in High-Shear Ultrafiltration, *Journal of Environmental Engineering*, 125 (1999) 638-646.
- [161] R.C. Viadero, D.A. Masciola, B.E. Reed, R.L. Vaughan, Two-phase limiting flux in high-shear rotary ultrafiltration of oil-in-water emulsions, *Journal of Membrane Science*, 175 (2000) 85-96.
- [162] F. Liebermann, Dynamic cross flow filtration with Novoflow's single shaft disk filters, *Desalination*, 250 (2010) 1087-1090.
- [163] Modular Spin Disk Filter MSDF, in, <https://divaenvitec.com/divaenvitec/products/modular-spin-disk-filter-msdf>.
- [164] Rotating disk filter, in, <https://www.igb.fraunhofer.de/en/research/water-technologies/wastewater-treatment/water-purification-and-bioreactor-concepts/cost-optimized-filtration.html>.
- [165] ROCKET CERAMIC FILTER, in, <http://www.vinimat.fr/produit/3/2/83/filtre-ceramique-rocket.html>.
- [166] R. Alnaizy, A. Aidan, H. Luo, Performance assessment of a pilot-size vacuum rotation membrane bioreactor treating urban wastewater, *Applied Water Science*, 1 (2011) 103-110.
- [167] HUBER Membrane Filtration VRM, in, <https://www.huber.de/products/membrane-filtration-mbr/huber-membrane-filtration-vrmmr.html>.

- [168] M.Y. Jaffrin, G. He, L.H. Ding, P. Paullier, Effect of membrane overlapping on performance of multishaft rotating ceramic disk membranes, *Desalination*, 200 (2006) 269-271.
- [169] D. Sarkar, A. Sarkar, A. Roy, C. Bhattacharjee, Performance characterization and design evaluation of spinning basket membrane (SBM) module using computational fluid dynamics (CFD), *Separation and Purification Technology*, 94 (2012) 23-33.
- [170] L. Liu, B. Gao, J. Liu, F. Yang, Rotating a helical membrane for turbulence enhancement and fouling reduction, *Chemical Engineering Journal*, 181-182 (2012) 486-493.
- [171] G. Rock, P. Tittley, N. McCombie, Plasma collection using an automated membrane device, *Transfusion*, 26 (1986) 269-271.
- [172] A. Salama, Investigation of the problem of filtration of oily-water systems using rotating membranes: A multicontinuum study, *Colloids and Surfaces A: Physicochemical and Engineering Aspects*, 541 (2018) 175-187.
- [173] K.H. Kroner, V. Nissinen, Dynamic filtration of microbial suspensions using an axially rotating filter, *Journal of Membrane Science*, 36 (1988) 85-100.
- [174] R. Bouzerar, M. Jaffrin, L.-H. Ding, P. Paullier, Influence of Geometry and Angular Velocity on Performance of a Rotating Disk Filter, *AIChE Journal*, 46 (2000) 257-265.
- [175] L. Ding, W. Zhang, A. Ould-Dris, M.Y. Jaffrin, B. Tang, Concentration of Milk Proteins for Producing Cheese Using a Shear-Enhanced Ultrafiltration Technique, *Industrial & Engineering Chemistry Research*, 55 (2016) 11130-11138.
- [176] J. Luo, L. Ding, Y. Wan, P. Paullier, M.Y. Jaffrin, Application of NF-RDM (nanofiltration rotating disk membrane) module under extreme hydraulic conditions for the treatment of dairy wastewater, *Chemical Engineering Journal*, 163 (2010) 307-316.
- [177] J. Luo, W. Cao, L. Ding, Z. Zhu, Y. Wan, M.Y. Jaffrin, Treatment of dairy effluent by shear-enhanced membrane filtration: The role of foulants, *Separation and Purification Technology*, 96 (2012) 194-203.
- [178] J. Luo, L. Ding, Y. Wan, P. Paullier, M.Y. Jaffrin, Fouling behavior of dairy wastewater treatment by nanofiltration under shear-enhanced extreme hydraulic conditions, *Separation and Purification Technology*, 88 (2012) 79-86.
- [179] Z. Zhu, J. Luo, L. Ding, O. Bals, M.Y. Jaffrin, E. Vorobiev, Chicory juice clarification by membrane filtration using rotating disk module, *Journal of Food Engineering*, 115 (2013) 264-271.
- [180] J. Luo, L. Ding, Influence of pH on treatment of dairy wastewater by nanofiltration using shear-enhanced filtration system, *Desalination*, 278 (2011) 150-156.
- [181] Z. Zhu, S. Ladeg, L. Ding, O. Bals, M.-M. Nadji, M.Y. Jaffrin, E. Vorobiev, Study of rotating disk assisted dead-end filtration of chicory juice and its performance optimization, *Industrial Crops and Products*, 53 (2014) 154-162.
- [182] Z. Zhu, H. Mhemdi, W. Zhang, L. Ding, O. Bals, M.Y. Jaffrin, N. Grimi, E. Vorobiev, Rotating Disk-Assisted Cross-Flow Ultrafiltration of Sugar Beet Juice, *Food and Bioprocess Technology*, 9 (2015) 493-500.
- [183] L.-H. Ding, O. Akoum, A. Abraham, M.Y. Jaffrin, High shear skim milk

ultrafiltration using rotating disk filtration systems, *AIChE Journal*, 49 (2003) 2433-2441.

[184] J. Luo, Z. Zhu, L. Ding, O. Bals, Y. Wan, M.Y. Jaffrin, E. Vorobiey, Flux behavior in clarification of chicory juice by high-shear membrane filtration: Evidence for threshold flux, *Journal of Membrane Science*, 435 (2013) 120-129.

[185] L. Chen, Y. Qiu, Removal of Cd (II) from dilute aqueous solutions by complexation-ultrafiltration using rotating disk membrane and the shear stability of PAA-Cd complex, *Chinese Journal of Chemical Engineering*, 27 (2019) 519-527.

[186] S.Y. Tang, Y.R. Qiu, Removal of Zn (II) by complexation-ultrafiltration using rotating disk membrane and the shear stability of PAA-Zn complex, *Korean J. Chem. Eng.*, 35 (2018) 2078-2085.

[187] F. Meyer, I. Gehmlich, R. Guthke, A. Górak, W.A. Knorre, Analysis and simulation of complex interactions during dynamic microfiltration of *Escherichia coli* suspensions, *Biotechnol. Bioeng.*, 59 (1998) 189-202.

[188] FMX: Anti-Fouling Membrane Filtration System, in, <https://bkt21.com/fmx-technology-index>.

[189] LIFE 18™- disk separator, in, <https://www.miltenyibiotec.com/FR-en/products/therasorb-therapeutic-apheresis/disposables/disposables-for-life-18/life-18tm-disk-separator.html#330-000-038>.

[190] P. Francis, D.M. Martinez, F. Taghipour, B.D. Bowen, C.A. Haynes, Optimizing the rotor design for controlled-shear affinity filtration using computational fluid dynamics, *Biotechnol Bioeng*, 95 (2006) 1207-1217.

[191] R. Bott, T. Langeloh, E. Ehrfeld, Dynamic cross flow filtration, *Chemical Engineering Journal*, 80 (2000) 245-249.

[192] J. Nuortila-Jokinen, A. Kuparinen, M. Nyström, Tailoring an economical membrane process for internal purification in the paper industry, *Desalination*, 119 (1998) 11-19.

[193] T. Huuhilo, P. Väisänen, J. Nuortila-Jokinen, M. Nyström, Influence of shear on flux in membrane filtration of integrated pulp and paper mill circulation water, *Desalination*, 141 (2001) 245-258.

[194] M. Mänttari, J. Nuortila-Jokinen, M. Nyström, Evaluation of nanofiltration membranes for filtration of paper mill total effluent, *Filtration & Separation*, 34 (1997) 275-280.

[195] M. Mänttari, K. Viitikko, M. Nyström, Nanofiltration of biologically treated effluents from the pulp and paper industry, *Journal of Membrane Science*, 272 (2006) 152-160.

[196] J. Nuortila-Jokinen, M. Nyström, Comparison of membrane separation processes in the internal purification of paper mill water, *Journal of Membrane Science*, 119 (1996) 99-115.

[197] X.M. Xie, C. Andre, N. Dietrich, P. Schmitz, L. Fillaudeau, Flow investigation in an innovating dynamic filtration module using tracing methods, *Separation and Purification Technology*, 227 (2019).

[198] X. Xie, N. Dietrich, L. Fillaudeau, C. Le Men, P. Schmitz, A. Liné, Local

hydrodynamics investigation within a dynamic filtration unit under laminar flow, *Chemical Engineering Research and Design*, 132 (2018) 954-965.

[199] N. Jitariouk, Apparatus, system and method for separating liquids, in, Google Patents, 2003.

[200] RVF-filtration, in, <http://rvf-filtration.com/>.

[201] H. Balavi, Y. Boluk, Dynamic filtration of drilling fluids and fluid loss under axially rotating crossflow filtration, *Journal of Petroleum Science and Engineering*, 163 (2018) 611-615.

[202] A. Zouboulis, E. Peleka, A. Ntolia, Treatment of Tannery Wastewater with Vibratory Shear-Enhanced Processing Membrane Filtration, *Separations*, 6 (2019) 20.

[203] Vibratory Shear Enhanced Processing VSEP, in, <https://www.vsep.com/product/series-i/>.

[204] J. Postlethwaite, S.R. Lamping, G.C. Leach, M.F. Hurwitz, G.J. Lye, Flux and transmission characteristics of a vibrating microfiltration system operated at high biomass loading, *Journal of Membrane Science*, 228 (2004) 89-101.

[205] Vibrating Membrane Filtration (VMF) Pallsep Systems, in, <https://shop.pall.com/us/en/biotech/tangential-flow-filtration/automated-systems/zidgri78lfv?CategoryName=BP0703&CatalogID=Biopharmaceuticals&tracking=searchterm:PallSep+Biotech+PS400>.

[206] H.G. Gomaa, S. Rao, Analysis of flux enhancement at oscillating flat surface membranes, *Journal of Membrane Science*, 374 (2011) 59-66.

[207] H. Gomaa, A.M. Al Taweel, Dynamic analysis of mass transfer at vertically oscillating surfaces, *Chemical Engineering Journal*, 102 (2004) 71-82.

[208] H.G. Gomaa, Flux characteristics at oscillating membrane equipped with turbulent promoters, *Chemical Engineering Journal*, 191 (2012) 541-547.

[209] H.G. Gomaa, S. Rao, M.A. Taweel, Flux enhancement using oscillatory motion and turbulence promoters, *Journal of Membrane Science*, 381 (2011) 64-73.

[210] F. Zhao, Y. Zhang, H. Chu, S. Jiang, Z. Yu, M. Wang, X. Zhou, J. Zhao, A uniform shearing vibration membrane system reducing membrane fouling in algae harvesting, *Journal of Cleaner Production*, 196 (2018) 1026-1033.

[211] M. Mertens, M. Quintelier, I.F.J. Vankelecom, Magnetically induced membrane vibration (MMV) system for wastewater treatment, *Separation and Purification Technology*, 211 (2019) 909-916.

[212] M.R. Bilad, G. Mezohegyi, P. Declerck, I.F. Vankelecom, Novel magnetically induced membrane vibration (MMV) for fouling control in membrane bioreactors, *Water Res*, 46 (2012) 63-72.

[213] Z. Zhao, M. Mertens, Y. Li, K. Muylaert, I.F.J. Vankelecom, A highly efficient and energy-saving magnetically induced membrane vibration system for harvesting microalgae, *Bioresour Technol*, 300 (2020) 122688.

[214] Y. Li, M.R. Bilad, I.F.J. Vankelecom, Application of a magnetically induced membrane vibration (MMV) system for lignocelluloses hydrolysate filtration, *Journal of Membrane Science*, 452 (2014) 165-170.

- [215] M.R. Bilad, V. Discart, D. Vandamme, I. Foubert, K. Muylaert, I.F. Vankelecom, Harvesting microalgal biomass using a magnetically induced membrane vibration (MMV) system: filtration performance and energy consumption, *Bioresour Technol*, 138 (2013) 329-338.
- [216] F. Zhao, H. Chu, Y. Zhang, S. Jiang, Z. Yu, X. Zhou, J. Zhao, Increasing the vibration frequency to mitigate reversible and irreversible membrane fouling using an axial vibration membrane in microalgae harvesting, *Journal of Membrane Science*, 529 (2017) 215-223.
- [217] F. Zhao, H. Chu, X. Tan, L. Yang, Y. Su, X. Zhou, J. Zhao, Y. Zhang, Using axial vibration membrane process to mitigate membrane fouling and reject extracellular organic matter in microalgae harvesting, *Journal of Membrane Science*, 517 (2016) 30-38.
- [218] F. Zhao, H. Chu, Y. Su, X. Tan, Y. Zhang, L. Yang, X. Zhou, Microalgae harvesting by an axial vibration membrane: The mechanism of mitigating membrane fouling, *Journal of Membrane Science*, 508 (2016) 127-135.
- [219] R. Holdich, K. Schou, M. Dragosavac, S. Kellet, H. Bandulasena, A comparison of azimuthal and axial oscillation microfiltration using surface and matrix types of microfilters with a cake-slurry shear plane exhibiting non-Newtonian behaviour, *Journal of Membrane Science*, 550 (2018) 357-364.
- [220] G. Genkin, T. Waite, A. Fane, S. Chang, The effect of vibration and coagulant addition on the filtration performance of submerged hollow fibre membranes, *Journal of Membrane Science*, 281 (2006) 726-734.
- [221] S. Beier, G. Jonsson, Separation of enzymes and yeast cells with a vibrating hollow fiber membrane module, *Separation and Purification Technology*, 53 (2007) 111-118.
- [222] S. Prip Beier, G. Jonsson, A vibrating membrane bioreactor (VMBR): Macromolecular transmission—influence of extracellular polymeric substances, *Chemical Engineering Science*, 64 (2009) 1436-1444.
- [223] B. Wu, Y. Zhang, Z. Mao, W.S. Tan, Y.Z. Tan, J.W. Chew, T.H. Chong, A.G. Fane, Spacer vibration for fouling control of submerged flat sheet membranes, *Separation and Purification Technology*, 210 (2019) 719-728.
- [224] M. Chai, Y. Ye, V. Chen, Separation and concentration of milk proteins with a submerged membrane vibrational system, *Journal of Membrane Science*, 524 (2017) 305-314.
- [225] J.C. Kim, F. Garzotto, D.N. Cruz, A. Clementi, F. Nalesso, J.H. Kim, E. Kang, H.C. Kim, C. Ronco, Computational modeling of effects of mechanical shaking on hemodynamics in hollow fibers, *Int. J. Artif. Organs*, 35 (2012) 301-307.
- [226] J. Kim, F. Garzotto, D. Cruz, C. Goh, F. Nalesso, J. Kim, E. Kang, H.C. Kim, C. Ronco, Enhancement of Solute Removal in a Hollow-Fiber Hemodialyzer by Mechanical Vibration, *Blood purification*, 31 (2011) 227-234.
- [227] L. Qin, Z. Fan, L. Xu, G. Zhang, G. Wang, D. Wu, X. Long, Q. Meng, A submerged membrane bioreactor with pendulum type oscillation (PTO) for oily wastewater treatment: membrane permeability and fouling control, *Bioresour Technol*, 183 (2015) 33-41.
- [228] O.T. Komesli, C.F. Gökçay, Investigation of sludge viscosity and its effects on the performance of a vacuum rotation membrane bioreactor, *Environ. Technol.*, 35 (2014) 645-

652.

[229] T.K. Sherwood, P.L.T. Brian, R.E. Fisher, Desalination by Reverse Osmosis, *Industrial & Engineering Chemistry Fundamentals*, 6 (1967) 2-12.

[230] C. Torras, J. Pallares, R. Garcia-Valls, M.Y. Jaffrin, Numerical simulation of the flow in a rotating disk filtration module, *Desalination*, 235 (2009) 122-138.

[231] M. Mellal, L. Hui Ding, M. Y. Jaffrin, C. Delattre, P. Michaud, J. Courtois, Separation and Fractionation of Oligouronides by Shear-Enhanced Filtration, *Separation Science and Technology*, 42 (2007) 349-361.

[232] S.-Y. Tang, D.-Y. Wu, Y.-R. Qiu, Computation fluid dynamic simulation and experimental validation of shear induce dissociation coupling ultrafiltration technology for the treatment of lead contained wastewater, *Separation and Purification Technology*, 241 (2020) 116750.

[233] M. Mänttari, J. Nuortila-Jokinen, M. Nyström, Influence of filtration conditions on the performance of NF membranes in the filtration of paper mill total effluent, *Journal of Membrane Science*, 137 (1997) 187-199.

[234] W. Li, X. Su, A. Palazzolo, S. Ahmed, E. Thomas, Reverse osmosis membrane, seawater desalination with vibration assisted reduced inorganic fouling, *Desalination*, 417 (2017) 102-114.

[235] S. Chandrasekhar, S. Chandrasekhar, L. Lee, The stability of spiral flow between rotating cylinders, *Proceedings of the Royal Society of London. Series A. Mathematical and Physical Sciences*, 265 (1962) 188-197.

[236] D. Cébron, P. Maubert, M. Le Bars, Tidal instability in a rotating and differentially heated ellipsoidal shell, *Geophysical Journal International*, 182 (2010) 1311-1318.

[237] J. Murkes, C.G. Carlsson, *Crossflow filtration: Theory and practice*, (1988).

[238] S. Rosenblat, Flow between torsionally oscillating disks, *Journal of Fluid Mechanics*, 8 (2006) 388-399.

[239] M. Mori, I. Seyssiecq, N. Roche, Rheological measurements of sewage sludge for various solids concentrations and geometry, *Process Biochemistry*, 41 (2006) 1656-1662.

[240] M.C. Porter, Concentration Polarization with Membrane Ultrafiltration, *Product R&D*, 11 (1972) 234-248.

[241] E.M.V. Hoek, A.S. Kim, M. Elimelech, Influence of Crossflow Membrane Filter Geometry and Shear Rate on Colloidal Fouling in Reverse Osmosis and Nanofiltration Separations, *Environmental Engineering Science*, 19 (2002) 357-372.

[242] W.F. Blatt, A. Dravid, A.S. Michaels, L. Nelsen, Solute Polarization and Cake Formation in Membrane Ultrafiltration: Causes, Consequences, and Control Techniques, in: J.E. Flinn (Ed.) *Membrane Science and Technology: Industrial, Biological, and Waste Treatment Processes*, Springer US, Boston, MA, 1970, pp. 47-97.

[243] C.K. Colton, Permeability and transport studies in batch and flow dialyzers with applications to hemodialysis, in: *Chem. Eng. M.I.T., Massachusetts Institute of Technology*, 1969.

[244] Y. Manon, L. Fillaudeau, D. Anne-Archard, J.-L. Uribe Larrea, C. Molina-Jouve, On-line rheology of cell cultures in a bioreactor, in: *8. World Congress of Chemical*

Engineering (WCCE8), Montreal, Canada, 2009, pp. np.

[245] L.O. Wilson, N.L. Schryer, Flow between a stationary and a rotating disk with suction, *Journal of Fluid Mechanics*, 85 (2006) 479-496.

[246] R. Bouzerar, Filtration dynamique dans un module plan à disque rotatif : Application à des suspensions minérales, in: *Génie des procédés*, Université de Technologie de Compiègne, 1999, pp. 181 p.

[247] K. Atsumi, T. Makino, K. Kato, T. Murase, E. Iritani, P. Chidphong, M. Shirato, Frictional resistance of grooved rotor in cylindrical dynamic filter chamber without permeation or throughflow, *Kag. Kog. Ronbunshu*, 14 (1988) 14-19.

[248] R. Adrian, *Bibliography of Particle Image Velocimetry Using Imaging Methods: 1917–1995*, DLR Deutsches Zentrum für Luft- und Raumfahrt e.V. - Forschungsberichte, (2011).

[249] T. Yoshizawa, *Handbook of optical metrology: Principles and Applications*, CRC Press, 2017.

[250] C.P. Gendrich, M.M. Koochesfahani, D.G. Nocera, Molecular tagging velocimetry and other novel applications of a new phosphorescent supramolecule, *Experiments in Fluids*, 23 (1997) 361-372.

[251] R.W. Johnson, *Handbook of fluid dynamics*, Crc Press, 2016.

[252] A. Cenedese, G. Doglia, G.P. Romano, G. De Michele, G. Tanzini, LDA and PIV velocity measurements in free jets, *Experimental Thermal and Fluid Science*, 9 (1994) 125-134.

[253] L.E. Drain, *The laser Doppler technique*, John Wiley, 1980.

[254] J. Kilander, A. Rasmuson, Energy dissipation and macro instabilities in a stirred square tank investigated using an LE PIV approach and LDA measurements, *Chemical Engineering Science*, 60 (2005) 6844-6856.

[255] L. Böhm, S. Jankhah, J. Tihon, P. Berube, M. Kraume, Application of the Electrodiffusion Method to Measure Wall Shear Stress: Integrating Theory and Practice, *Chem. Eng. Technol.*, 37 (2014) 1-14.

[256] J.E. Mitchell, T.J. Hanratty, A study of turbulence at a wall using an electrochemical wall shear-stress meter, *Journal of Fluid Mechanics*, 26 (1966) 199.

[257] S. Toyama, Y. Tanaka, S. Shirogane, T. Nakamura, T. Umino, R. Uehara, T. Okamoto, H. Igarashi, Development of Wearable Sheet-Type Shear Force Sensor and Measurement System that is Insusceptible to Temperature and Pressure, *Sensors (Basel)*, 17 (2017) 1752.

[258] J. Günther, D. Hobbs, C. Albasi, C. Lafforgue, A. Cockx, P. Schmitz, Modeling the effect of packing density on filtration performances in hollow fiber microfiltration module: A spatial study of cake growth, *Journal of Membrane Science*, 389 (2012) 126-136.

[259] L. Oxarango, P. Schmitz, M. Quintard, Laminar flow in channels with wall suction or injection: a new model to study multi-channel filtration systems, *Chemical Engineering Science*, 59 (2004) 1039-1051.

[260] M. Linkès, P. Fede, J. Morchain, P. Schmitz, Numerical investigation of subgrid mixing effects on the calculation of biological reaction rates, *Chemical Engineering Science*,

116 (2014) 473-485.

[261] Z. Kovács, *Continuous Diafiltration: Cocurrent and Countercurrent Modes*, Springer Berlin Heidelberg, 2016.

[262] X. Xie, Investigation of local and global hydrodynamics of a dynamic filtration module (RVF technology) for intensification of industrial bioprocess, in, 2017.

[263] O. Akoum, D. Richfield, M. Jaffrin, L. Ding, P. Swart, Recovery of trypsin inhibitor by soy milk ultrafiltration using a rotating disk system, *Desalination*, 191 (2006) 438-445.

[264] R.L. Bates, P.L. Fondy, R.R. Corpstein, Examination of some geometric parameters of impeller power, *Industrial & Engineering Chemistry Process Design and Development*, 2 (1963) 310-314.

[265] S.M. Okhovat-Alavian, J. Behin, N. Mostoufi, Investigating the flow structures in semi-cylindrical bubbling fluidized bed using pressure fluctuation signals, *Advanced Powder Technology*, 30 (2019) 1247-1256.

[266] F. Johnsson, R. Zijerveld, J.v. Schouten, C. Van den Bleek, B. Leckner, Characterization of fluidization regimes by time-series analysis of pressure fluctuations, *International journal of multiphase flow*, 26 (2000) 663-715.

[267] S.A. Wassie, A. Zaabout, F. Gallucci, S. Cloete, M. van Sint Annaland, S. Amini, Detecting densified zone formation in membrane-assisted fluidized bed reactors through pressure measurements, *Chemical Engineering Journal*, 308 (2017) 1154-1164.

[268] C. Kang, H. Liu, Pressure fluctuation and surface morphology induced by the high-pressure submerged waterjet confined in a square duct, *International Journal of Heat and Fluid Flow*, 77 (2019) 134-143.

[269] K. Hirata, Y. Iida, A. Takushima, J. Funaki, Instantaneous pressure measurement on a rotating blade of a cross-flow impeller, *Journal of Environment and Engineering*, 3 (2008) 261-271.

[270] Z. Wang, Z. Qian, J. Lu, P. Wu, Effects of flow rate and rotational speed on pressure fluctuations in a double-suction centrifugal pump, *Energy*, 170 (2019) 212-227.

[271] Z. XU, CFD Simulation of Dynamic Filtration System with Rotating Disks, in, *Dalian University of Technology*, 2009, pp. 26.

[272] S.S. Hoseini, G. Najafi, B. Ghobadian, A.H. Akbarzadeh, Impeller shape-optimization of stirred-tank reactor: CFD and fluid structure interaction analyses, *Chemical Engineering Journal*, 413 (2021) 127497.

[273] H. Yu, Z. Zhang, H. Hua, Numerical investigation of tip clearance effects on propulsion performance and pressure fluctuation of a pump-jet propulsor, *Ocean Engineering*, 192 (2019) 106500.

[274] N. Ratkovich, C.C.V. Chan, T.R. Bentzen, M.R. Rasmussen, Experimental and CFD simulation studies of wall shear stress for different impeller configurations and MBR activated sludge, *Water Sci. Technol.*, 65 (2012) 2061-2070.

[275] M. Cheng, C. Le Men, A. Line, P. Schmitz, L. Fillaudeau, Methodology to investigate instantaneous and local transmembrane pressure within Rotating and Vibrating Filtration (RVF) module, *Separation and Purification Technology*, (2021) 118955.

[276] S.G. Kelly, Mechanical vibrations: theory and applications, Cengage learning, 2012.

[277] M. Itoh, Y. Yamada, S. Imao, M. Gonda, Experiments on turbulent flow due to an enclosed rotating disk, *Experimental thermal and fluid science*, 5 (1992) 359-368.

[278] S. Cheah, H. Iacovides, D. Jackson, H. Ji, B. Launder, Experimental investigation of enclosed rotor-stator disk flows, *Experimental thermal and fluid science*, 9 (1994) 445-455.

Annexes

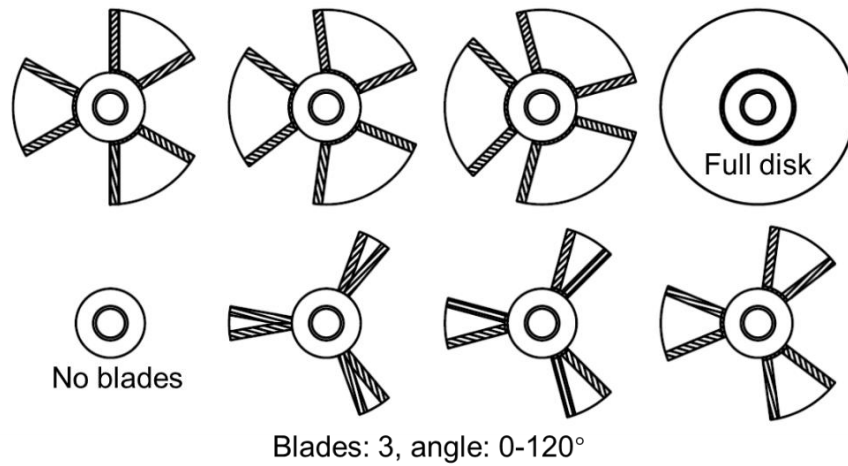
Figures:

Fig. S 1 Impeller geometry with difference surface area. No blades and full disk indicate 0 and 120°, other three impellers equip with three blades and the angle from 20 to 90°.

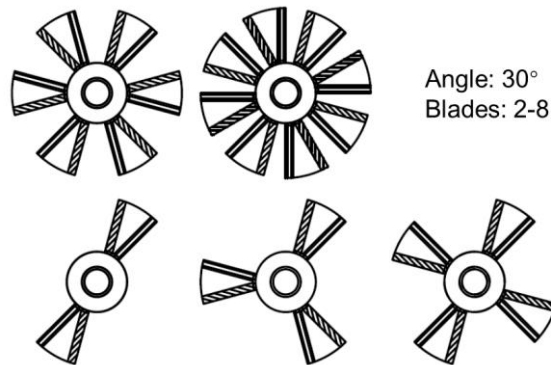


Fig. S 2 Impeller geometry with difference number of blades. The impellers equip with 2 to 8 blades (30°).

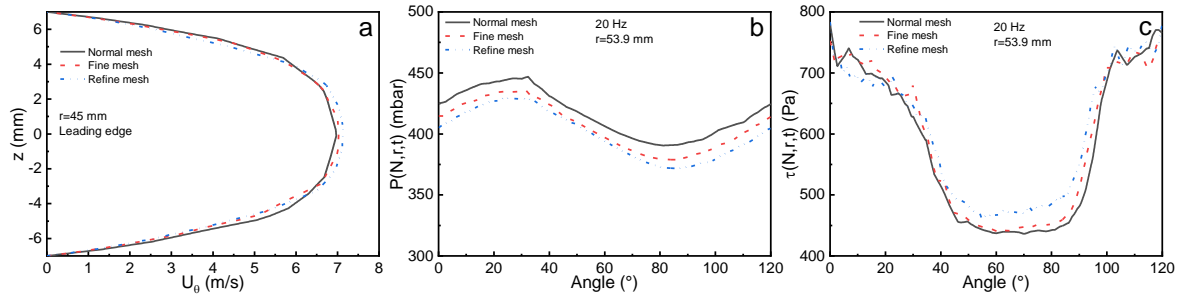


Fig. S 3 The comparison of velocity, pressure and shear stress for different meshes. (a) tangential velocity along the z -axis; (b) and (c) are the pressure and the shear stress along the θ direction.

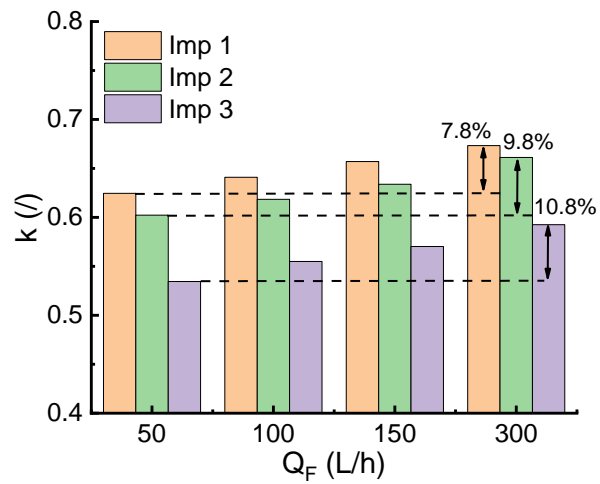


Fig. S 4 Core velocity coefficient for different flowrates. Operating conditions: water, $\mu=0.001$ Pa.s, N : 0-50 Hz, Q_F : 50-300 L/h, r : R1-R8.

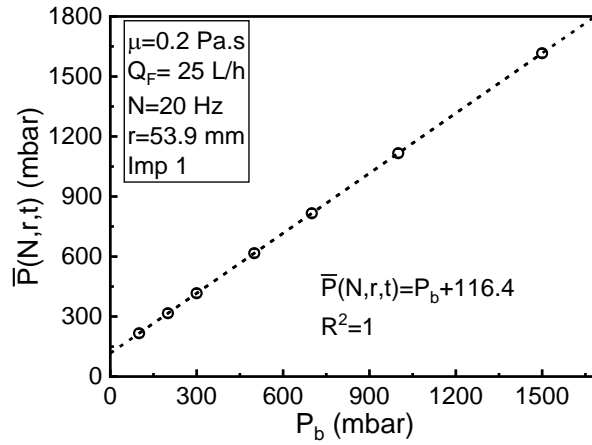


Fig. S 5 Local pressure as a function of back pressure. Operating conditions: $\mu = 0.2$ Pa.s, $N = 20$ Hz, r : R6, $Q_F = 25$ L/h.

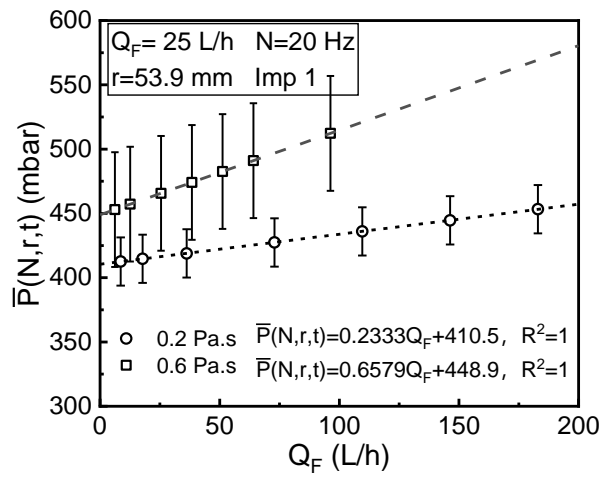


Fig. S 6 Local pressure as a function of feeding flowrate. Operating conditions: $\mu = 0.2$ and 0.6 Pa.s, $N = 20$ Hz, r : R6, Q_F : 6-183 L/h.

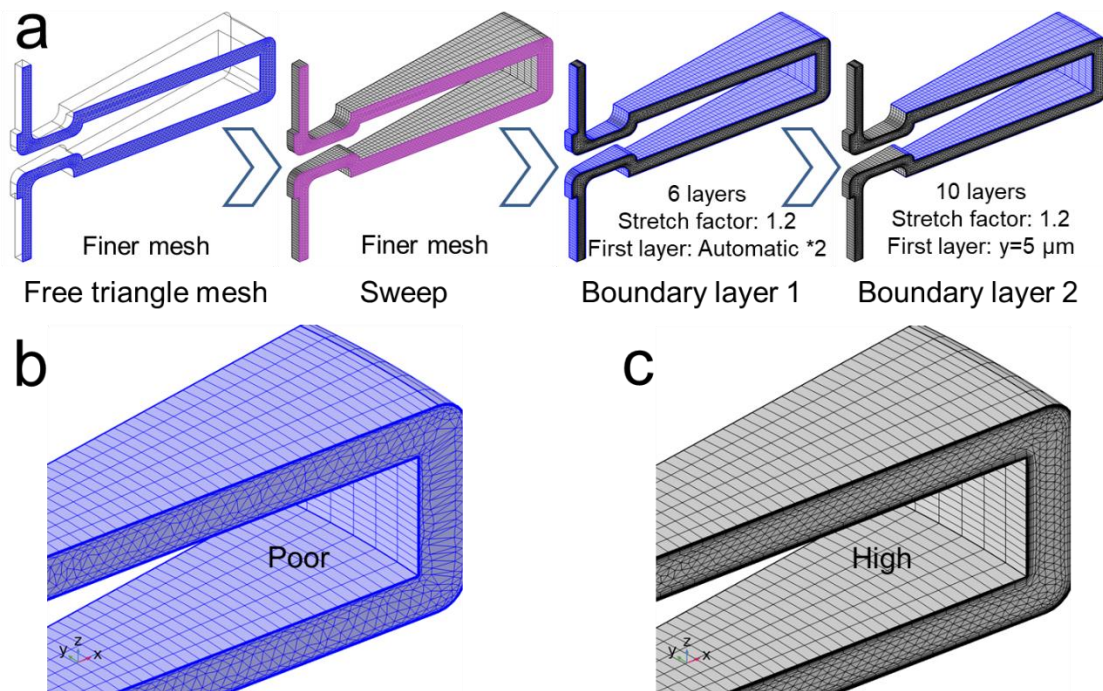


Fig. S 7 Structured mesh of rotating disk system (10° of the disk). (a) is the formation of structured mesh, (b) and (c) are the poor (boundary layer 1) and high (boundary layer 1 and 2) quality of mesh, respectively.

Tables:

Table S 1 Effect of blade surface area on core velocity coefficient.

Operating conditions	Angle of blades ($^\circ$)	k (/)
$\mu=0.2$ Pa.s, N: 0-30 Hz, r=53.9 mm	0 (no blades)	0.23
	20	0.65
	30	0.65
	45	0.66
	60	0.64
	75	0.64
	90	0.6
	120 (full disk)	0.5

Table S 2 Effect of blade number on core velocity coefficient.

Operating conditions	Number of blades (/)	k (/)
$\mu=0.2$ Pa.s, N: 0-30 Hz, r=53.9 mm	2	0.61
	3	0.65
	4	0.66
	6	0.59
	8	0.59

Table S 3 Effect of impeller/membrane gap on core velocity coefficient.

Operating conditions	Impeller/membrane gap (/)	k (/)
$\mu=0.2$ Pa.s, N: 0-30 Hz, r=53.9 mm	2	0.71
	3	0.65
	4	0.64
	5	0.59
	6	0.61
	7	0.59
	10	0.65